Advances in Planetary Geology

June 1980

NASA

NASA TM-81979

Advances in Planetary Geology

NASA Scientific and Technical Information Branch 1980
National Aeronautics and Space Administration
Washington, DC

For sale by the National Technical Information Service
Springfield, Virginia 22161

FOREWORD

This document is a compilation of reports from Principal Investigators (and their Associates) of NASA's Office of Space Science, Planetary Division, Planetary Geology Program. The reports presented in this document are research that add to our knowledge of the origin and evaluation of the solar system and to our understanding of the earth as a planet. Advances in Planetary Geology was established as a complement to the abstract document "Reports of Planetary Geology Program" and to professional journals. This document provides a method of publishing research results which are in a form that would not normally be published elsewhere. The research reports may be in the form of lengthy research reports, progress reports, Ph. D. dissertations, or master's theses.

Joseph M. Boyce
Discipline Scientist
Planetary Geology Program
Office of Space Science

Advances in Planetary Geology is a new series intended to serve the planetary geology community with a form for quick communication. There are no set lists of acceptable topics or types of presentations, and submitted manuscripts will not undergo a formal review. All submissions should be single spaced in a camera-ready form, and submitted to the Editor.

Alex Woronow, Editor

CONTENTS

SECTION I

GEOMORPHOLOGY OF MARTIAN VALLEYS

A Thesis

Presented to the Faculty of the Graduate School
of Cornell University
in Partial Fulfillment for the Degree of
Doctor of Philosophy

by

David Christopher Pieri
May 1979

GEOMORPHOLOGY OF MARTIAN VALLEYS

David Christopher Pieri, Ph.D.
Cornell University 1979

This dissertation covers a broad range of topics related to martian valleys: terminology, classification, distribution, morphology, age, quantitative analysis of pattern, physics of flow, origin, and the relation of martian valleys to climatic change. Channels are distinguished from valleys on the basis of: (1) the greater size of the "large channels", and (2) presence of flow erosion morphology in channels. Valleys generally are small (less than 5km wide, less than 1km deep), show little direct evidence of erosion by flow, and form ramified networks which coalesce down regional slopes.

Data on morphology and planimetric characteristics of 240 martian valley networks reveal seven network patterns (e.g. digitate, parallel, stem, centrifugal, centripetal (interior and exterior), and fragmented), and three major system assemblage categories (i.e. reoccurring juxtapositions of network patterns: integrated, longitudinal and slope valley systems). Integrated networks (e.g. combinations of parallel and digitate networks) are most like terrestrial dendritic networks, but well-organized, space efficient, true dendritic patterns are markedly absent on Mars.

From orbit, at similar resolution there are no terrestrial features which are as comparably obvious as the martian valley networks. Terrestrial river networks observed at this scale have a fine subtle filigreed texture, in contrast to the crudely integrated, deeply entrenched, and coarse martian networks.

Crater size-frequency distributions show that valley systems are as old as the oldest heavily cratered terrains on Mars, but are no younger than the oldest Lunae Planum terrain (3.5 B.Y. using the Soderblom et al. (1974) impacting flux model).

A simple physical model was devised to correlate rate of decrease of slope down-network with increasing tributary junction angles, in order to infer longitudinal profile from planimetric pattern. Dendritic terrestrial networks are consistent with this model with exponentially decreasing slopes. Martian valley networks, often termed "dendritic" in the literature exhibited no such systematic behavior in their junction angle distribution. On Mars, low unsystematic junction angles coupled with (1) large cross-sections for low magnitude (Shreve, 1967) tributaries, (2) commom amphitheater terminations, (3) lack of shallow feeder tributaries above amphitheater terminations, (4) widespread evidence of mass wasting on

slopes, (5) downhill coalescence of networks on low regional slopes, and (6) marked lack of intervalley dissection or drainage basin development, imply immature drainage from restricted source regions as a result of mobilization of volatiles in the subsurface (e.g. sapping or seepage through permeable strata).

Further, operative physics of flow predict that gravity scaling should not produce a vastly different morphology for river erosion on Mars as compared to observed terrestrial river morphology. Thus, there is at present no compelling evidence on Mars for erosion by rivers fed by rainfall runoff.

Little beyond speculation can be offered about the mechanism of emplacement of water into the subsurface although the presence of substantial amounts of water in the regolith suggests the introduction of volatiles during a previous, more erosionally active period, with a thicker atmosphere. Subsequent valley formation ensued only by exploitation of the regolith reservoir, generally ceasing before the formation of both Lunae Planum and much of the intercrater plains. Finally, valley obliteration has occurred by formation of intercrater plains and by superposition of impact craters.

Martian valley systems are ancient landforms which show little evidence of having been formed by rainfall erosion. Truth table analysis of various alternative formation processes finds flow from lithospheric source accompanied by sapping as the most likely mechanism.

BIOGRAPHIC SKETCH

David Christopher Pieri, the author, was born February 23, 1949 in New Haven, Connecticut. He is oldest of seven children born to Nazareth and Margaret Pieri. He attended Great Valley Senior High School in Malvern, Pennsylvania, graduating in June 1966, and graduated from Villanova University in September 1972 with the degree of Bachelor of Science in Physics. He attended graduate school at the University of Pennsylvania in the Department of Geology and worked as a geologist for the United States Geological Survey, Branch of Astrogeology in Flagstaff, Arizona before entering Cornell in 1974. He has been a graduate student in the Department of Geological Sciences since then, being supported as a Graduate Research Assistant under Professor Sagan at the Center for Radiophysics and Space Research. The author has participated in two recent planetary exploration missions. As a member of the Viking Lander Imaging Flight Team, he was in residence at the Jet Propulsion Laboratory in Pasadena, California for 18 months. He is now again at JPL participating in the Voyager Mission to the outer planets as a sponsored investigator under Dr. Sagan. He has been a Research Associate with C.R.S.R., at Cornell, is currently a National Academy of Sciences-National Research Council Postdoctoral Associate at J.P.L.

DEDICATION

. . . to friends of the Mars Room, wherever they may be.

ACKNOWLEDGEMENTS

During the course of this research I have had the privilege of receiving help and encouragement from many people. In particular I would like to thank Professor Carl Sagan for his unstinting support during my years at Cornell, and to acknowledge the constant support and guidance of Professor Joseph Veverka. I'd like to thank Professor Arthur Bloom for his thorough critiques and discussions and Professor William Travers for his helpful advice. I would also like to acknowledge the help and valued friendship, and intellectual stimulation of Dr. Michael Malin in many extensive discussions. His persistence and unselfish help will always be appreciated.

I would also like to thank Dr. Peter Thomas, Dr. Maura Weathers, Dr. Ed Wells, Dr. Jonathan Gradie, Dr. Fred Taylor, Margaret Dermott, Sue Harris, Joy Veverka, and Nancy Adams without whose kind support and tolerance the completion of this thesis would never have been possible.

Finally, and most importantly, I'd like to acknowledge the unending help, encouragement, and love of my family - my daughter Tiffany and my wife Leslie.

This work supported by NASA Grant NGL-33-010-082 and NGL-33-010-220.

TABLE OF CONTENTS

LIST OF TABLES

LIST OF ILLUSTRATIONS

CHAPTER I: INTRODUCTION

Rationale

The question of climatic change on Mars

The discovery of channels and valleys on Mars during the Mariner 9 mission immediately posed an interesting and profound question: does the existence of a group of features that are generally similar to terrestrial river valleys and channels imply the possibility of open channel river flow on Mars, a process which could require a martian environment far different from the present one? Investigators have taken one of two general approaches to explain the martian "channels": (A) they assume that these features result from fluvial erosion and therefore postulate a martian paleo-environment in which such processes could occur, or (B) they hypothesize non-fluvial processes operative in the present martian climate which could produce a riverine morphology.

Before either hypothesis (A) or (B) can be evaluated, however, there are several outstanding and basic questions which must be answered in regard to martian "channels". They are: (1) What is the evidence to indicate that any surface or subsurface fluid flow occurred? (2) What is the evidence for a lithospheric versus an atmospheric source for any such fluid? (3) If the fluid is assumed to be water, what type of climatic change, if any, is required to permit the presence of flowing water on the surface or in the subsurface? If, for example, the morphologic evidence were very strong for widespread overland flow, then a uniformly distributed source of water, such as rainfall, would be attractive and would require gross climatic change. If the evidence were seen to be strong for mainly subsurface flow or even for sapping by sublimation of ice as a formative process, climatic constraints might be relaxed.

Of the three questions just posed, questions (1) and (2) can be addressed by geological analysis, while question (3) is more in the realm of atmospheric physicists and chemists, and is therefore beyond the scope of this dissertation. Although it has been often held in the post-Mariner 9 scientific literature that gross climatic change has occurred on Mars, a thorough and critical examination of the major part of the evidence, namely the morphology and distribution of the martian "channels", particularly the widely distributed "small channels", has been lacking. Answers to questions (1) and (2) posed above are critically important in assessing whether or not the "channels" represent evidence of climatic change on Mars. In an effort to begin to answer these two basic questions, the author (Pieri, 1976) conducted a study of the distribution of "small channels" on Mars based on

Mariner 9 data. This dissertation, with the inclusion of Viking Orbiter data, is an extension and expansion of that work. Its central thesis is that the distribution, interior morphology, network topology, and geologic setting of "martian channels" provide no compelling evidence for rainfall as a genetic agent. Rather, analysis of these important system properties implies valley formation early in martian history by the interaction of water from lithospheric sources both on the surface (i.e. runoff erosion) and in the subsurface (i.e. sapping).

Relevance of channel and valley classes

In assessing this question of gross climatic change, one must consider which class of channels or valleys would be most relevant. Many authors (Milton, 1973; Baker and Milton, 1974; Masursky, 1973; Sharp and Malin, 1975; Malin, 1976a, b) consider the large channels (i.e., outflow channels, primary and catastrophically modified, Sharp and Malin, 1975, Table 1) to be the result of catastrophic flooding events, analogous to the floods producing the channeled scablands of eastern Washington (Bretz, et al., 1956; Baker and Milton, 1974). Baker (1971) estimates a discharge in excess of 2×10^7 m^3/sec for the last Lake Missoula flood (13,000 to 18,000 B.P.), as compared with the maximum discharges recorded for rainfall-derived terrestrial floods of order 10^4 to 10^5 m^3/sec (UNESCO, 1976). The large martian channels and features within them are several orders of magnitude larger than the Scabland channels and so, by analogy, the volume of water required to create such martian channels far surpasses the ability of the atmosphere of either planet to provide the fluid quickly. The valley systems scattered throughout the cratered terrain, on the other hand, have dimensions which are similar to terrestrial river valleys. These features are not channels themselves, as pointed out by Sharp and Malin (1975), although they may contain channels. The criterion of required discharge is sufficient to rule out the large channels as having been conduits of coalescent flows directly derived from rainfall. This, of course, does not rule out the possibility that the catastrophic floods which may have carved the large channels were produced by the release of previously emplaced atmospherically derived fluids.

The cratered terrain valley systems are the most likely candidates of all the martian channels and valleys to have been produced analogously to terrestrial drainage basins. It is for this reason that a study was undertaken to determine the extent to which the martian valley systems resemble terrestrial river valley networks, and ultimately whether their existence implies climatic change on Mars.

Methodology of Research

Fundamental limits to remote analysis

Geologic or planetologic analysis of landforms using orbital images alone has definite limitations. A geologic analysis encompassing formative

process and history needs three components: (1) form, (2) internal structure, and (3) composition. The only well-defined parameter for martian landscapes, however, is form. Internal structure and composition are either unknowable at present for Mars or available only by inference. Essentially, the problem has three variables, two of which are free parameters. The task is to define a family of solutions for formative process and history that are plausible, given inferred boundary conditions and inferred values for the free parameters. This statement is true of any photogeologic study without ground observations and is particularly important for orbital studies of other planets.

Data base

The image data base used for this study consists of Mariner 9 synoptic (A-frame) and high resolution (B-frame) images with nominal line-pair resolution limits of 1km and 100m respectively, and Viking Orbiter images of varying scale and resolution. The highest nominal line-pair resolution limit for Viking Orbiter is about 40m for images taken at or near periapsis. The Viking Orbiter data that were used consisted of individual frames and mosaics with original resolution ranging from about 100m/pixel to about 1km/pixel, with the majority between 300 and 700m/pixel. The latitudinal range examined in detail extended from 65°S to 65°N, but polar regions were also studied. 240 valleys in the equatorial and sub-polar regions of Mars were studied and Table I contains tabulated data on these valleys used in the global analysis to be discussed in subsequent chapters.

Terminology

Past use of the term "channel"

The historic use of the word "channel" to describe markings of the martian surface originated with Italian astronomers, who used the word canale (translated without genetic connotation as "channel") to describe the linear features observed on Mars telescopically. Schiaparelli produced extensive maps of canali, although disavowing any speculation as to their origin. Later, Lowell advocated the existence of a dying martian civilization and translated canali into the highly connotative term, "canal". Largely as a result Lowell's popularization of the idea of life on Mars, the existence of a population of intelligent martians was accepted by many people until the early 1950's (see Martin, 1912; Hartmann and Raper, 1974; Mutch et al., 1976.)

Between 1965 and 1971 a series of reconaissance spacecraft were flown past Mars by the United States. Mariner 4, 6, and 7 sent back television images of Mars. Due to trajectory constraints, the spacecraft were able to observe only the southern hemisphere of Mars. Based on these pictures, investigators inferred a lunar-like cratered planet with little to no recent geologic activity. Murray et al. (1971), however, noted that the absence of

TABLE I

Network Morphology Parameters for 240 Martian Valley Systems

Mosaic or Frame #	(°) Latitude	(°) Longitude	Cross-section morphology	Wall morphology	Erosion state	System Type	Terrain
211-5207	-25	1	B/V	C	E	I	I
5207	-17	1	B	C	E	I	I
5534	-34	2	B	C	E	SV	S
5721	22	4	B	S	E	L	I
5207	-20	8	B	C	E	I	I
209A04-09	22	9	B	C	E	SV	C
5207	-25	10	B/V	S/C	E	I	I
407B73-100	20	10	B	S	E/F	SV	C
5473	-32	12	B/V	C	E	L	I
5564	25-29	13	V	S	F	L	P
5571	-22,	13	B	C	E	I	I
5603	16	13	B/V	C	E	SV	C
5763	-52	14	B	S	E	L	I
5769	-54	15	B	C	E	I	I
5571	-10	18	B	C	E	I	I
5473	-37	20	B	S/C	E	I	I
5428	-57	20	B	C	E	SV	S
639A67-72	-28	22	B	S	F	SV	C
5755	-25	22	B	C	E	I	I
5755	-25	25	B	C	E	I	I
5755	-18	26	B	S	E	L	I
5473	-35	30	B	S/C	E	I	I
5755	-25	30	B	C	E	L	I
380B11	-53	30	B	S	F	L	I
5755	-35	35	B/V	S	E	L	I
5428	-60	35	B	S/C	E	L	I
5540	-30	36	V	C/S	E	SV	C
5473	-28	37	B/V	S	F	L	I
669A51	30.5	40	B	S	E	L	P

(CONTINUED)

Mosaic or Frame #	(°) Latitude	(°) Longitude	Cross-section morphology	Wall morphology	Erosion state	System Type	Terrain
211-5768	-57	41	B	S	E/F	I	S
5141	-57	48	B/V	C	E	L	I
5586	5	50	B	S	E	I	P
5419	19	50	V	S	F	I	P/S
318A52	-24	50	B	C	E	L	P
5256	14	53	B	C	E	L	P/I
5371	26.5	54	V	S	F	L	P
5582	54	55	B	C	E	L	P
5419	20	57	B	C	F	L	P
5141	-56	58	B/V	C	E	L	I
5750	-30	60	V	S	F	L	I
5750	-30	60	V/B	S	E	SV	S
5141	-52	60	B/V	C	E	L	I
5239	10	60	B	S	E	L	P
667A24	31	60	B	C	E	L	I
5786	6.5	60.5	B	C	E	L	P
5471	-49	65	V	S/C	E	I	I
5141	-41	65	B	S	E	L	P/I
5253	-50	65-70	B	C	E	I	I
5736	-54	68	B	C	E	SV	S
667A18	31	66	B	S	F	L	I
5141	-47	72	B	C	E	I	I
5141	-53	73	B	C	E	SV	I
5382	26	73.5	B	S	E	L	P
5736	-45	75	B/V	S	E	I	I/S
5471	-49	76	B	S	F/E	SV	I
5471	-47	77	V	S	F/E	SV	I
5736	-45	77	B	C/S	E	I	I
5736	-49	77	B/V	C	E	I	I

(CONTINUED)

Mosaic or Frame #	(°) Latitude	(°) Longitude	Cross-section morphology	Wall morphology	Erosion state	System Type	Terrain
211-5762	-35	80	B	S	E/F	L	I/S
5253	-50	80-81	B	C	E	L	I
5253	-45	80	B/V	S	F/E	L	I
5141	-57	81	B	C	E	SV	I
5271F	0	82	B	C	E	L	P
5767	-47	89	B	C	E/F	I	I/S
5471	-45	90	V	S	F	SV	I
5471	-32	90	V	S	E	SV	S
5210	-35	90	B/V	C	E	SV	S
5253	-48	91	V	S	E	SV	S
5471	-41	92	V	S/C	E	I	I
5141	-54	92	B	C	E	SV	I
5471	-51	94	V	C	E	SV	S
5048	43	94	V	S	F	SV	C
5253	-51	94	V	C/S	E	SV	S
5253	-49	94	V	C	E	SV	S
5271E	-5	95	V/B	S	F	L	P
5141	-52	96	B	C	E	SV	I
5210	-35	100	B/V	C	E	SV	S
5253	-50	105	B	C/S	E	SV	S
5597	-47	108	B	C	E	SV	S
5656	39.5	109	B	S/C	E	I	P
5668	45	115	V	S	F	L	P
5471	-45	115	B/V	S	F	SV	S
5253	-50	115	B	C/S	E	SV	S
5210	-40	115	B/V	C	E	SV	S
5499	25	115	V	S	F	L	P
5734	44	116	V	S	F	L	V/P
5770	-31	120	B/V	S	F/E	SV	S
5253	-45	120	B	C	E	SV	S

(CONTINUED)

Mosaic or Frame #	(°) Latitude	(°) Longitude	Cross-section morphology	Wall morphology	Erosion state	System Type	Terrain
211-5785	12.5	129	B	S	F	SV	S
5785	12.5	129	B	S	F	L	P
5112	-40	130	B/V	C	E	SV	S
5253	-45	130	B	C	E	SV	S
5475	-40	130	B/V	C	E	I	I
5475	-40	130	B/V	C	E	I	I
5771	31	131	V	S	F	L	P
5598	39	134	B/V	S	F	L	S
5385	39	135	V/B	S	F	SV	C
5385	38	137	V	S	F	SV	S
5536	35	139	V	S	F	SV	C
5600	-25	140	B	S	F	SV	S
5778	-61	141	B	C/S	E	I	I
5609	-25	145-147	B	C	E	SV	S
5145	-15	148	B	C	E	SV	S
5790	-5	150	B	S	E	L	I/S
5145	-16	150	B	S	E	L	I/P
5548	-8	150	B	S	E	L	I/S
5738	-52	155	B	C	E	I	I
5738	-50	160	B	C	E	SV	S/I
5478	-20	160	B	C	E	I	I
5654	-40	168	B	C	E	SV	I/S
5475	-50	170	B	C	E	I	I
5320	-45	175	B	C	E	I	I
5213C	-15	180	B	C	E	I	I
5320	-50	180	B	C	E	I	I
5213C	-20	185	B	C	E	I	I
5474	-45	195	B/V	C	E	L	I
5766 and 5611	-25	200	B	C	E	I	I

(CONTINUED)

Mosaic or Frame #	(°) Latitude	(°) Longitude	Cross-section morphology	Wall morphology	Erosion state	System Type	Terrain
211-5760	-20	200	B	C	E	L	I
5760	-20	205	B	C	E	I	I
5760	-12	205	B	C	E	I	I
5760	-20	207	B	C	E	I	I
629A19	-45	214	B	C	E	SV	I
5664	33	218	B	S	F	L	P
5319	-47	217	B	C	E	I	I
5211	-50	220	B	C	E	I	I
5420	-35	220	B	C	E	I	I
5783	29	225	B	S	F	I	S
629A43	-10	225	B	C	E	SV	I
629A16	-33	226	B	C	E	SV	I
5783	30	228	B	S	F	I	I
5435	-25	229	B	C	E	SV	I
5579	0- -10	230	B	C	E	I	I
5508	42	230	B	C	E	L	P
5319	-64	230	B	C	E	I	I
629A41	-5	230	B	C	E	SV	I
5435	-12	231	B	C	E	L	I
5435	-12	231	B	C	E	SV	C
629A11	-29	223	B	C	E	SV	I
629A10	-23	234	B	C	E	SV	I
5435	-27	236	B	C	E	SV	I
629A08	-19	236	B	C	E	SV	I
5211	-60	238	B	C	E	I	S
629A07	-22	239	B	C	E	SV	I
5510	45	239	B	C	E	L	P
5754	30	240	B	S	E	L	I
5759	-62	240	B	C	E	I	I
5456	-50	240	B	C	E	SV	S
5455	1	241	B	S/C	E	L	I
620A04	-11	241	B	C	E	SV	I
629A05	-18	241	B	C	E	SV	I

(CONTINUED)

Mosaic or Frame #	(°) Latitude	(°) Longitude	Cross-section morphology	Wall morphology	Erosion state	System Type	Terrain
629A03	-15	242	B	C	E	SV	I
629A02	-8	242	B	C	E	SV	I
5456	-59	245	B/V	C	E	L	I
5319	-58	245	B	C	E	I	I
629A01	-10	245	B	C	E	SV	I
5771	-36	247.5	B	S	E	L	I
585B32	-38	249	B	C/S	E	L	I
5435	-5	249	B	S	F	L	P
5456	-50	251	B	S	E	L	P
5673	-43	252	B	S/C	E	L	I
5730	-20	252	B	S	F	L	P/V
5738	-38	255	B	C/S	E	S/V	S
5738	-44	265-260	B	C/S	E	L	I
5209	-57	260	B/V	S	E	SV	S
5209	-57	261	B/V	S	E	I	I
5456	-35	265	B	S	E	L	P
5738	-27	265	B/V	C/S	E	SV	S
5532	-24.5	271	B	C	E	I	I
5532	-24.5	271	B	C	E	SV	C
5579	-15-5	272	B	C	E	SV	I
5762	2	272	B	S	E	L	I/S
625A08	-19	274	B	C	E	I	I
625A10	-21	274	B	C	E	I	I
5410	28	275	V	S	F	SV	C
5532	-21	275	B	C	E	SV	C
5532	-22.5	277	B	C	E	I	I
5532	-20	278	B	C	E	L	I
625A02	-12	279	B	C	E	SV	I
625A02	-12	280	B	C	E	L	I/S

(CONTINUED)

Mosaic or Frame #	(°) Latitude	(°) Longitude	Cross-section morphology	Wall morphology	Erosion state	System Type	Terrain
211-5657	25	282	B	S/C	E	L	P
5427	21.5	286	B	S	E	L	I
5659	25	286	B	C	E	L	I
5601	-5	290	B	C	E	I	I
5209	-57	290	B	S	E	L	P
5532	-19	291	B	C	E	SV	C
5532	-19	291	B	C	E	I	I
5209	-22	291	B	C	E	I	I
5532	-17.5	293	B	C	E	I	C
5532	-17.5	293	B	C	E	SV	S
5532	-17.5	294	B	S/C	E	SV	C
5532	-17.25	295.5	B	C	E	L	I
5532	-16.5	297	B	C	E	I	I
5763	-15- -30	350-300	B	C	E	I	I
5784	-49	307	B	C/S	E	I	I
641A21	35	305	B	C	E	L	I
5604	9	312	B	C	E	I	I
5741	40	315	B	C	E	L	I
557B56	-45	315	B	C	E	SV	S
5773	-45	318	B/V	C	E	SV	C
5756	-60	320	B	C	E	I	I
5535							
and 5524	-35	323	B	S	F	SV	C
5524	-37	325	B/V	S	E	SV	C
5392	-10	325	B/V	C	E	SV	C
5789	25	325	B	S	F	L	I
5757	-27	325	B	C	E	I	I
5524	-47	330	B/V	S	E	SV	C
5661	40	330-342	B	S	F	SV	S

(CONTINUED)

Mosaic or Frame #	(°) Latitude	(°) Longitude	Cross-section morphology	Wall morphology	Erosion state	System Type	Terrain
211-5793	26	331	B	S	E	SV	C
5793	28	333	V	S	F	L	C/I
5757	-35	335	V	S/C	E	I	I
5392	-12	336	B	C	E	I	I
5535	-31	337	V	S	F	SV	S
5726	42	338	B	S	F	L	I
5793	28	339	V	S	F	L	C/I
5524	-45	340	B/V	S	E	SV	C
321A38	-5	340	B	C	E	I	I
321A40	-5	340	B	C	E	I	I
5793	27	340	B	C	E	L	I
263B44	12	341	B	C	E	L	I
283B42	12	341	B	C	E	L	I
5524	-30	342	B/V	S	E	SV	S
5564	-30	345	B	S	E	SV	S
5794	-28	347	V	S/C	E	L	I
669A25	-18	348	B	C	E	I	I
5603	16	352	B/V	C	E	SV	C
321A26	-5	355	B	C	E	I	I
5555	-30	355	B	S	E	SV	S
5564	-25	355	B	C	E	SV	I/S
5564	-12	357	B	C	E	SV	C
669A26	-2	358	B	C	E	I	I
5564	-14	359	B	C	E	SV	C
5791	17	359	B	C	E	SV	C

KEY FOR TABLE I

I. COLUMN HEADINGS

1. Mosaic Numbers - These are a series of seven digit numbers used to identify mosaics compiled from Viking Orbiter individual frames.

2. Latitude - The latitude in degrees represents the location of the central portion of a particular channel or valley system. It is accurate to within one degree.

3. Longitude - The longitude in degrees represents the location of the central portion of a particular channel or valley system and is accurate to within one degree.

4. Cross-section morphology - The morphology of the channel or valley cross-section is indicated here by either a B or V:

   a) B - box-shaped or U shaped cross section. Generally flat floored. Can have steep or shallow sloping walls. Walls may or may not be terraced or stepped.

   b) V - V-shaped cross-section. Not flat floored. Generally possess steep walls. Generally no terraces or steps.

5. Wall morphology - This refers to wall morphology and is either S or C:

   a) S - smooth morphology. May be gentle or steeply sloping. No inference here about presence or lack of talus cones. It is inferred here that the characteristic dimension of wall roughness elements is less than 50 meters.

   b) C - crenulated morphology. May be gentle or steeply sloping, however, gentle sloping, terraced or stepped morphology is common. Crenulations have a characteristic embayment dimension of greater than 100 meters.

6. Erosion state - This is a general qualitative impression of the erosion state of the feature and is either E or F:

   a) E - eroded. This implies an assumption that all features start in a pristine, smooth form and progress to a shallower, degraded, generally wider shape. Degradation is estimated by apparent differential erosion, rough valley or channel walls, obvious superposition by impacts, and general continuity or lack thereof in the valley network or channel pattern.

   b) F - fresh. Generally used when a pristine, uneroded feature is observed. Smooth walls and V-shaped interior valleys and channels generally fall into this category. The assumption of a pristine original morphology is implicit.

7. System Type - Uses I, L, or SV:

   a) L - longitudinal - as defined in text.

   b) I - integrated - as defined in text.

   c) SV - slope valleys - as defined in text.

8. Network Terrain - Describes the general terrain into which the valley or channel is emplaced - I, S, C, P, V:

   a) I - intercrater plains. Generally used for intercrater areas of moderately or heavily cratered terrain.

   b) S - scarp. Valley or channel embaying a plateau surface.

   c) C - crater rim. Valley or channel emplaced on the exterior or interior of a crater rim.

   d) P - plains. Valley or channel occurs on plains. Applied only to lightly cratered terrain.

   e) V - volcanic. Channels associated with obvious volcanic forms.

II. Combining Descriptive Categories

Many times identifying letters are combined (e.g. B, C/S, E, L, I) to indicate that both or several categories of description are appropriate under a single column heading. In principle, all valleys and channels are probably hybrid in this way, but only the most obvious cases are denoted here. The identifying letter which precedes the slash mark (/) has predominance. For instance, C/S means that a system has been observed which has generally crenulated walls, but also has a few smooth sections.

impact-saturated surfaces and the generally degraded appearance of many craters implied a redistribution of surface materials and perhaps a period of erosion.

In 1972, as a result of the Mariner 9 orbital reconaissance mission, many unexpected surface features were discovered on Mars. Some of these features, linear to sinuous depressions with global distribution, the largest with interior forms strongly suggestive of fluid erosion, were called "channels" as a general descriptive term (McCauley, et al., 1971; Masursky, 1973). It is unfortunate that these exciting features were immediately called "channels" both because of the association of the term with the martian canals of Lowell and because many, if not most, of the newly discovered martian "channels" do not show clear evidence of erosion by fluid as is implied in the traditional hydraulic connotation. In the usage of fluvial geomorphologists and hydraulic engineers, the term "channel" has a specific meaning. Terrestrial channels are generally considered to be stream beds, that is, features whose morphology is formed by the shear stress of the fluid now or formerly conducted through them. Such a genetic implication for the martian features is a point of strong contention for the so-called "large channels" (Baker, 1978; Cutts et al., 1978) and is probably unwarranted for another class of the features, the "small channels" treated here.

Other terms

Detailed analysis of Mariner 9 images (Milton, 1973; Sharp and Malin, 1975; Malin, 1975; Pieri, 1976) provided an impetus for a more appropriate terminology. As pointed out by Sharp and Malin (1975) the term channel is basically unsuitable as a general name for martian landforms. Although recognizing this problem they distinguished between "channel" and "channel-like form" on the basis of the likelihood of a particular feature having been formed by erosion (exogenic) or by internal (endogenic) processes (Sharp and Malin, 1975; p. 596). No further distinction was made in their terminology between features which exhibited clear evidence of fluid erosion and those for which fluid erosion was only inferred from overall planimetric network morphology. All were lumped together within the exogenic "channel" class.

Part of the nomenclature problem is that the martian "channels" are heterogeneous. Most likely the genetic processes are heterogeneous as well. The largest features (e.g. Kasei, Shalbatana, Ares, Mangala, Ma'adim) show what could be interpreted as channel bed-forms. An example of such a feature, a "stream-lined island" adjacent to a crater in Kasei Vallis, is shown in Figure 1. The downslope direction in Figure 1 is from left to right and the taper of the "island" is consistent with erosion by a flow in that direction. If so, resistant crater walls have protected the tapered island from erosion which has scoured a kilometer-deep "channel". Another section of Kasei Vallis is shown in Figure 2. The sinuous ridge and groove topography has been interpreted by Baker and Kochel (1978) as evidence of macro-turbulent flow analogous to scour grooves seen in the channeled scablands. Provided these interpretations are correct, the features could be called channels in the sense outlined above.

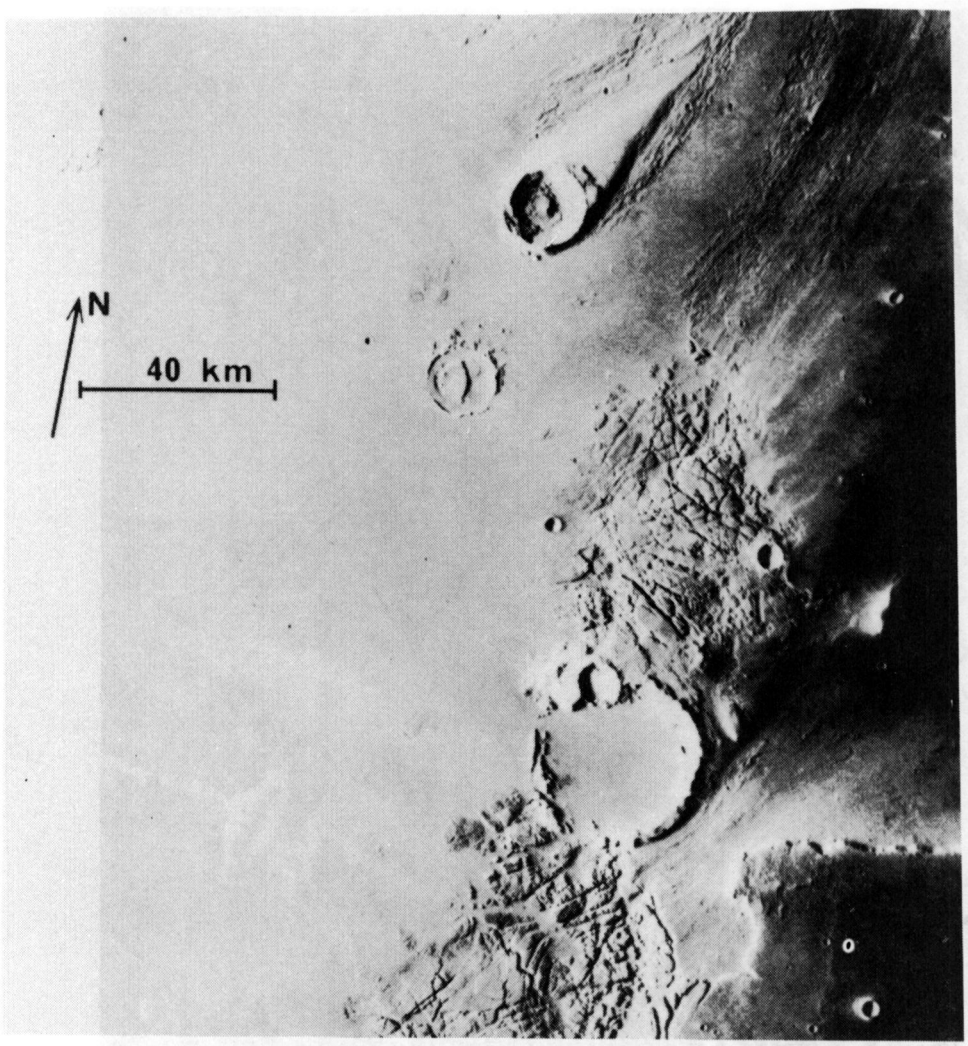

Figure 1.

Interior of Kasei Vallis. Note the large streamlined form adjacent to the large (10km diameter) impact crater and nearby parallel ridge and groove topography. The orientation of these features is consistent with downhill flow from the southwest and have been interpreted as morphological evidence of such by Baker and Kochel (1978).

Picture center: latitude 14.1°, longitude 75.5°
Resolution: 400 meters
Viking Orbiter Image: 519A01

Figure 2.

Northern section of Kasei Vallis. The main channel is in the lower half of the scene. Note the streamlined shapes of topographic projections and the parallel, sinuous grooves and ridges, consistent with erosion by flow from the west. Illumination is from the left, sun elevation above the horizon is 25°, and viewing angle is 13°.

Picture center: latitude 27.5°, longitude 69.3°
Resolution: 350 meters
Viking Orbiter Image: 519A29

Most of the remaining "channel" types show only ambiguous evidence of fluid erosion at best and are much smaller than the large channels (Figure 3). Fluid erosional or depositional morphology is not seen, possibly because: (1) the scale of such features is below the resolution limit of the orbiter cameras, (2) the features have been substantially modified by other processes such that they are no longer identifiable as resulting from fluid erosion or deposition, or (3) the features are not and were never there. These features were first called "fine channels" by McCauley et al. (1972) and have since been called "small channels" (e.g. Pieri, 1976). Soderblom et al. (1974) refer to these features as "filamental channels". The term "dendritic channels" (Milton, 1973) has been equated with "small channels" although most of these features have neither a purely dendritic planimetric configuration, nor are they obviously channels.

The term "furrow" used by Mutch et al. (1976) was generally applied to small widely scattered "channel" features in cratered terrain. However, the terrestrial concept of a small straight ditch with rims formed by excavated sediment is distracting and makes the term inappropriate for the martian depressions.

The "small channels" have been included in the channel class called "runoff channels" by Sharp and Malin (1975), in a subset of this class they termed "slope gullies". Although Sharp's and Malin's categorization identified and separated the major types of martian "channels", its terminology consisted of names with considerable genetic implications. The terms "fine channel", "filamental channel", "dendritic channel", "furrow", "runoff channel" and "small channel" have been used interchangeably in the literature and interchangeably even within a single paper. An alternative, precise, less genetic and more consistent terminology would be useful.

Use of the terms channel and valley in this paper

In an attempt to bring the terminology for these features more in line with geomorphologic useage, terms are used here in a way which it is hoped will help clarify the semantics. The term channel will be used to denote the class of martian surface features that exhibit forms analogous to those observed in terrestrial river channels, e.g. braiding, deposition or absence of erosion behind obstacles, terraces features, generally acute tributary entrance angles, and accordance at tributary junctions. Features observed on Mars that fall into this class are generally the largest of the so-called "martian channels" (e.g. Kasei, Tiu, Mangala, Ma'adim and Shalbatana). Many authors (Milton, 1973; Baker and Milton, 1974; Sharp and Malin, 1975) have proposed that these channels result from catastrophic floods of water and that channel morphology results directly from the application of fluid tractive force. Arguments have arisen as to whether water is necessarily the eroding fluid (e.g. Cutts et al., 1978), with air and lava the most often mentioned alternatives. These channels are not at the bottoms of valleys as stream channels are on the earth, but are usually incised directly into cratered plains.

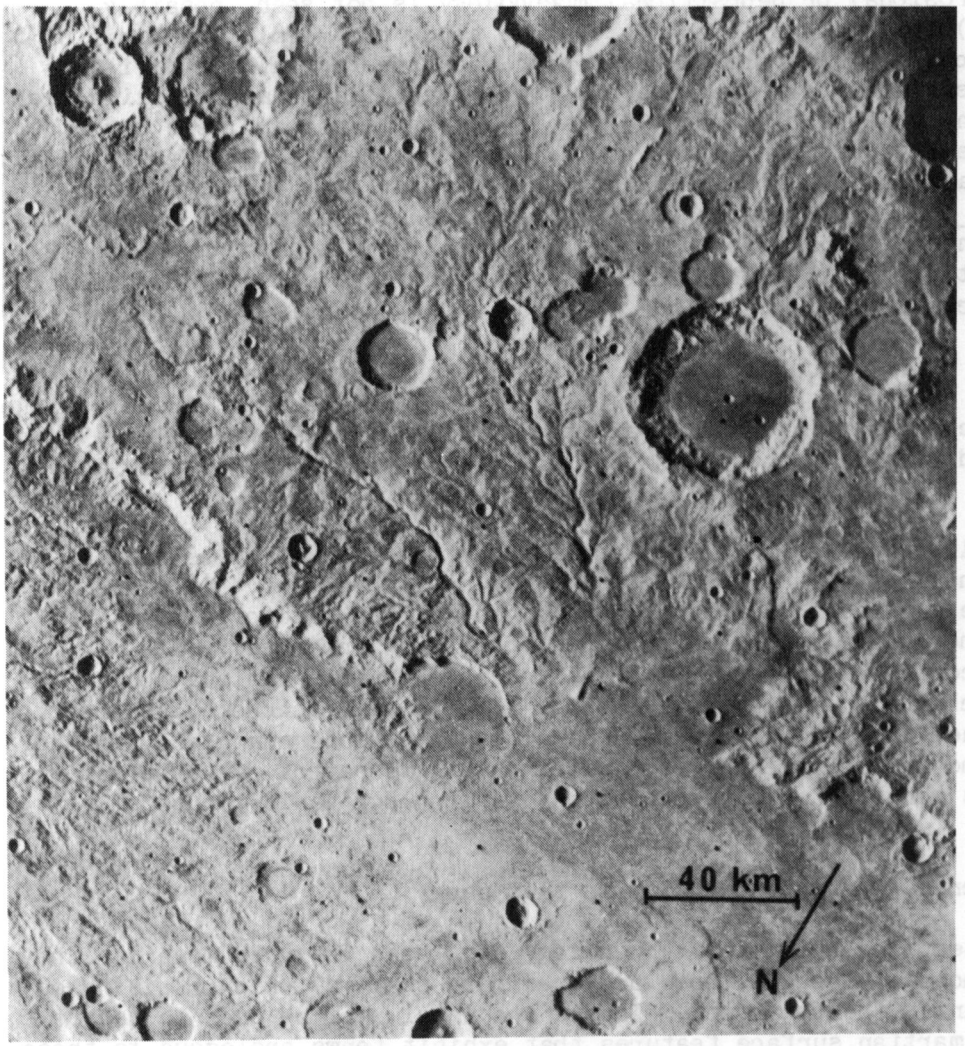

Figure 3.

Group of valleys in the Iapygia region. These valleys are typical of valley systems in heavily cratered terrain on Mars. Some reaches are deep as 250 meters. Note the superposition of impact craters on the valleys. A high resolution view of this area is shown in Figure 6. Sun elevation is 25.5°, illumination is from the left, and the viewing angle is 26°.

Picture center: latitude -11.41°, longitude 278.21°
Resolution: 500 meters
Viking Orbiter Image: 102A15

The term valley will be used here to denote the class of martian features previously referred to in the literature as "small channels" (Sharp and Malin, 1975; Pieri, 1976). These are the linear or sinuous branching depressions reminiscent in pattern of terrestrial river valley networks. They are generally 1-10km in width, with systems seldom exceeding 200km in length. They are ubiquitous on the cratered terrain of Mars (Pieri, 1976). It is uncertain whether these small martian valleys ever contained flowing water and therefore whether true river channels were ever cut into the valley floors. The observation of very small channels within martian valleys would be important. All other linear or sinuous depressions not falling into the valley or channel categories are called troughs.

Overview

The remaining chapters of this dissertation cover a broad range of topics. Chapter II presents a comprehensive classification scheme for martian valley systems and discusses their global distribution and its significance. Chapter III discusses a method of dating valley systems by crater counts from which a likely minimum age for valley networks is deduced. Chapter IV presents a new model for the systematics of junction angles in drainage networks and applies this model to both terrestrial and martian valley networks. Chapter V discusses the physics of stream flow under martian gravity and low atmospheric pressure. Chapter IV summarizes and synthesizes the work presented here and concludes with hypotheses of valley system formational processes and history.

CHAPTER II: CLASSIFICATION AND DISTRIBUTION OF VALLEY SYSTEMS ON MARS

Pattern Classification

Previous work

Mariner 9 imaging team studies (McCauley et al., 1972; Milton, 1973) divided the martian "channels" into two general groups on the basis of size - "large channels" and small channels". The "large channels" in this case were the huge (e.g. 50km wide, 2km deep, 1000km long) features debouching into Chryse Planitia, and the slightly small Ma'adim and Mangala Vallis debouching into Elysium Planitia. The widely distributed valley networks in heavily cratered terrain were generally referred to as the "small channels". Masursky (1973) introduced a classification scheme with four categories: (1) broad and sinuous, (2) narrow with braided floors and tributaries, (3) small and closely spaced, and (4) those associated with volcanic centers. Pieri (1976) devised a similar four category working classification system consisting of (1) large channels, (2) intermediate channels, (3) small channels and (4) anomalous channels. This system was based on differentiation by size and morphology. A far more comprehensive system, which recognized eleven separate "channel" types, was introduced by Sharp and Malin (1975) (see Chapter I).

All of these classification schemes were useful to the extent that they served to emphasize the heterogeneous morphology and distribution of martian "channels". Nevertheless, none of the classification systems was completely satisfactory because none differentiated between "channels" which show good evidence in their interior morphology of flow erosion and "valleys" which do not.

New Work

The focus of this dissertation is on valley systems. There are several reasons for this choice: First, they are the only class of features on Mars which bear resemblance to terrestrial stream valley networks in scale or morphology. Consequently these features are often cited as evidence for past "climatic change" on Mars (Sagan et al., 1973), since liquid water is not stable in the present surface environment.[1] Second, the valley

---

[1]Further, Wallace and Sagan (1977) raise the possibility of stable frozen-over water rivers under present conditions on Mars.

systems have not been adaquately studied. Only one published paper (Pieri, 1976) deals with the valley systems as a separate topic, yet they are an important key to understanding the evolution of the martian surface. 240 separate valley networks were catalogued in this study from Viking Orbiter data (Chapter I; Table I) with an expanded non-genetic classification scheme.

In classifying valley network planimetric patterns, an obvious approach would have been to use the classification system already in use for terrestrial drainage networks. In looking at martian networks, however, it becomes clear that true terrestrial patterns are rare. For example, dendritic drainage patterns are characterized on Earth by irregular branching of stream valleys in many directions, a pattern that does not occur on Mars. Such a network develops by random headward erosion on rocks of uniform resistance which lack structural controls (Easterbrook, 1969). On Mars, patterns tend to be generally elongated, often with long first order tributaries and little dissection of inter-valley plateau surfaces within the networks. Drainage basins are indiscernible and small scale dissection by tributary valleys is absent. Martian networks generally appear to be very sparse and angles are generally very low. A modified terrestrial network classification scheme is needed to reflect the uniquely martian network patterns.

Patterns of Martian Networks

Nine terms are used here to describe the planimetric character of martian valley networks. They are: digitate, stem, parallel, rectilinear, radial centrifugal, radial centripetal (interior or exterior) (Figure 4) and fragmented[1].

Digitate

"Digitate" refers to a "handlike" or "fingerlike" quality that many martian networks exhibit. In such systems, particularly in the well-developed networks in Margaritifer Sinus, major trunk segments join at or near the mouth of the systems, much as the fingers join the palm of the hand. Trunk tributaries are generally sparse and inter-valley dissection is absent. In particular, a digitate pattern is distinguished from a dendritic one in which intermediate trunk segments intersect far up-network and form a parallel pattern which is elongate.[2] Digitate networks often appear

---

[1]The term "fragmented" can modify any other term such as a "fragmented digitate" pattern.

[2]Parallel and digitate networks are end members of a continuum of patterns. As a crude analogy, consider a folding oriental fan. The closed fan position corresponds to a parallel network while a digitate net corresponds to the fan in an open position.

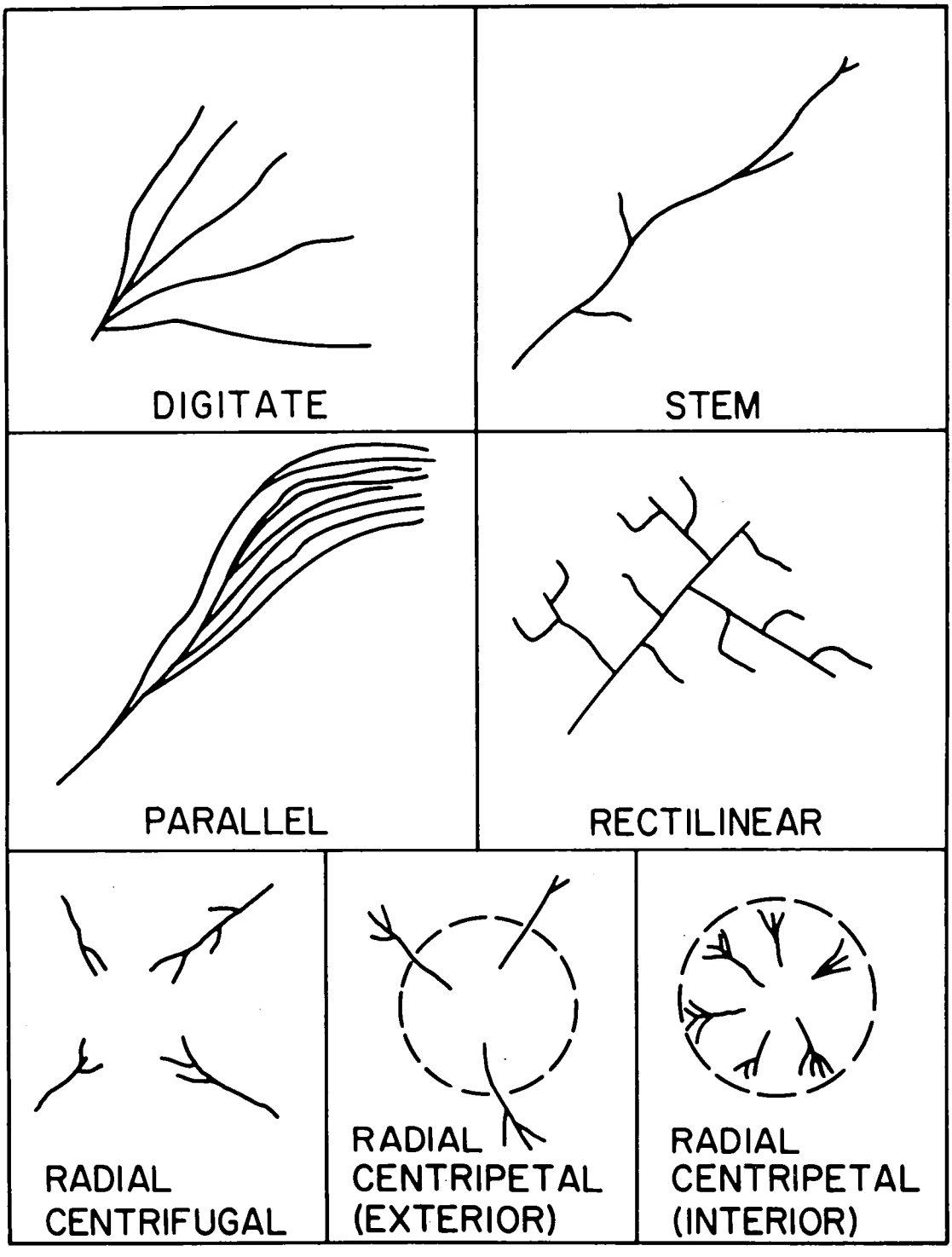

Figure 4.

Sketches of valley planimetric patterns observed on Mars.

degraded with rough and dissected walls. They have U-shaped cross-sections and display the amphitheater valley heads common to all valley types (Figure 5a and b, 6). Digitate networks comprise about 50% of all networks surveyed (Table I). A good example of a digitate valley network occurs in Margaritifer Sinus (Figure 7). This integrated valley network, several hundred kilometers in length, coalesces downhill and connects ridged intercrater plains with a 200km depression at its mouth. It generally increases in depth down-network, and exhibits amphitheater terminations. Inter-valley areas appear undissected; however, some valley segments have depressions 100 meters deep at their up-network terminations. These valleys have both U and V cross-sections with both smooth and rough walls. Most reaches are curvilinear, however, there are some nearly straight sections. Part of the digitate network shown in Figure 7 appears to be oriented in a radial centrifugal pattern around a 50km flat-floored crater. Even these densely packed valleys do not show competition for undissected intervalley plateau surfaces. Note that all major network branches coalesce near the mouth of the system.

The example of a digitate valley network shown in Figure 5a is taken from the Nirgal Vallis Complex. These valleys are several tens of kilometers long and about 500 meters deep. Valley walls are rough and valley floors appear flat and smooth at 20 meters resolution. Amphitheater terminations are visible, the surrounding terrain appears undissected at this resolution with abundant lobate scarps and ridges. The general pattern is digitate with sparse dissection of inter-valley divides. Thus significant drainage basin development is lacking.

Parallel

"Parallel" is employed in the traditional sense; that is, to describe the pattern of a valley with major parallel tributaries. This term differs from "digitate" in that (1) major tributaries coalesce more frequently up-network, and (2) the network plan outline is narrower in the direction transverse to the main coalescence direction of the network. A parallel drainage pattern suggests an areally restricted headward source area, very strong structural control, or immature drainage on strongly undirectional, flat slopes. About 16% of all networks examined fall into this class (Table I). Several examples of parallel networks are presented here. A striking valley system described in the Viking Orbiter team reports (Carr et at., 1977; Masursky et al., 1977) occurs on an isolated block of heavily dissected, cratered, and faulted material in Thaumasia (Figure 8).

Although the planimetric pattern exhibited in Figure 8 is referred to as "dendritic" (Masursky et al., 1977, p. 4030, Figure 9c), examination reveals that most inter-junction segments or links are parallel or nearly parallel. Evidence of inter-valley drainage competition is non-existent as evidenced by the lack of small tributaries with entrance angles, near 90° (see Chapter IV). Such drainage patterns imply (1) an immaturity of pattern development, (2) that inter-valley gradients are lower than down-network gradients, and (3) little additional down-valley contribution of water to

initiate a more mature dendritic pattern development. Parallel drainage patterns in the absence of structural control indicate a confined fluid source region and a planar, although not necessarily low gradient, pre-network topography.

A group of about 10 distinct parallel and digitate valleys occur in the Thaumasia region about -47° latitude, 75° longitude (Figure 9). By shadow measurements they are an estimated 800 meters in depth, up to 4km in width and about 180km long. The valleys are parallel, highly crenulated, with amphitheater terminations. In many cases there is a distinct widening distal to the mouth up to and including the amphitheater. Valley system orientation is generally E-W although the network curves to the south as it coalesces, consistent with the regional downhill direction (the region gradient is about 0.2%) (Christensen, 1975).

Rectilinear

"Rectilinear" is also used in the traditional terrestrial context. Rectilinear networks, comprising 2% of all valley networks examined (Table I), have straight segments between junctions that appear to be influenced by strong tectonically imposed fracture trends. They exhibit U-shaped or flat-bottomed valley cross-sections with steep walls and display the best amphitheater terminations. Often they occur as part of or parallel to graben or trough systems and this association combined with the angular pattern suggests structural control.

A matrix of several rectilinear networks is visible in the neighborhood of -35° latitude, 25° longitude (Figure 10). These networks have straight valley segments with numerous right angle tributary intersections and right angle turns in trunk orientation. They are associated with the east-west trending grabens prominent in Margaritifer Sinus. These valleys debouch into the grabens and trend north-south, entering the troughs at nearly right angles. The grabens are closed at both ends. The valleys are of uniform width with no systematic widening toward the valley mouths. They are flat-floored with smooth appearing walls. The consistently rectilinear patterns imply strong control of valley development and orientation by local structure.

Stem

The term "stem" is used for networks which are greatly elongated along a longitudinal axis, often with little tributary valley development. They comprise about 30% of the networks surveyed here (Table I). Stem valleys often connect headward with digitate systems, the stem-digitate pattern being common in the Margaritifer Sinus region. Several prominent 1000km long stem valleys occur in the Margaritifer Sinus area (Figure 11). These valleys are relatively narrow (less than 5km across) and are less than 200 meters deep. They are sinuous and vary in interior morphology from V-shaped to U-shaped. They have few major tributaries and show no systematic widening down-network. Sections of these valleys show an interior channel

Figure 5a.

Section of a distal reach of the Nirgal Vallis system. Note the cuspate, amphitheater terminations and the lack of any associated drainage basin development on surrounding plains. Many tributaries have widths and cross-sections of size comparable to those of the main valleys. Note also the increase in width when approaching the valley terminations. These valleys are about 800 meters deep with flat floors. Illumination is from the bottom of the picture, sun elevation is 30°, and viewing angle is 34°.

Picture center: latitude -27.5°, longitude 47.0°
Resolution: 125 meters
Viking Orbiter Image: 466A69

Figure 5b

Digitate tributary network in Nirgal Vallis system. This small tributary system in the center of the picture shows amphitheater terminations and a distinctly digitate planimetric pattern. Note here also that tributaries widen distally from the mouth of the network. Sun elevation is 31°, illumination is from the left, and viewing angle is 6°.

Picture center: latitude -27.1°, longitude 45.31°
Resolution: 130 meters
Viking Orbiter Image: 466A52

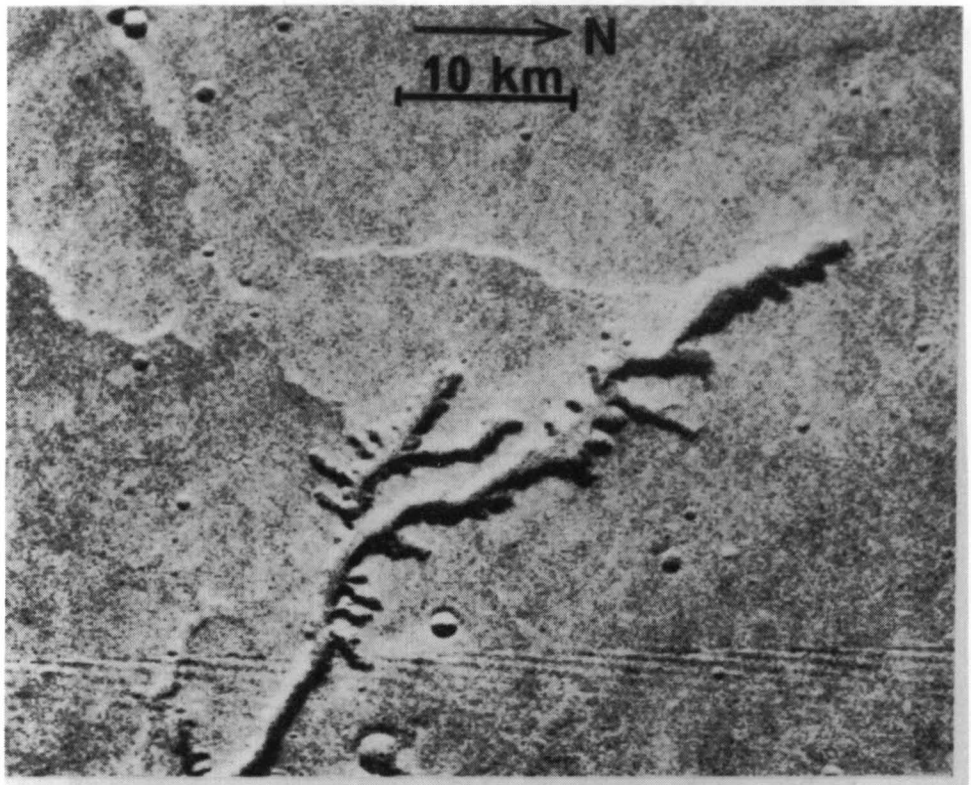
N
10 km

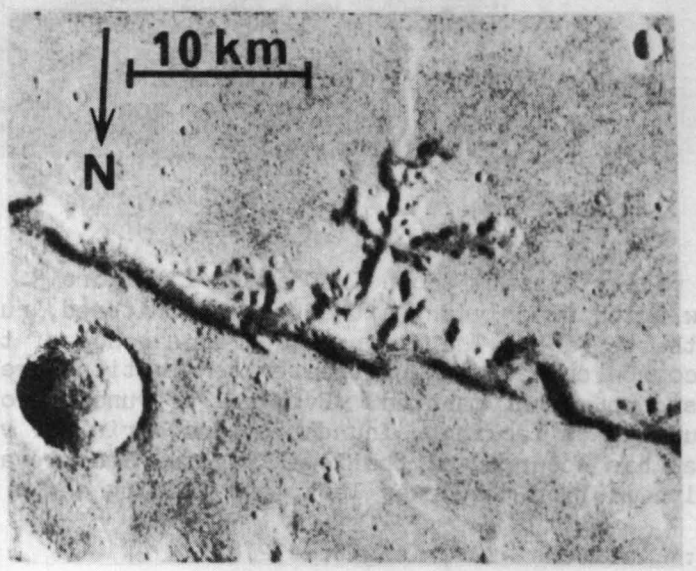
10 km
N

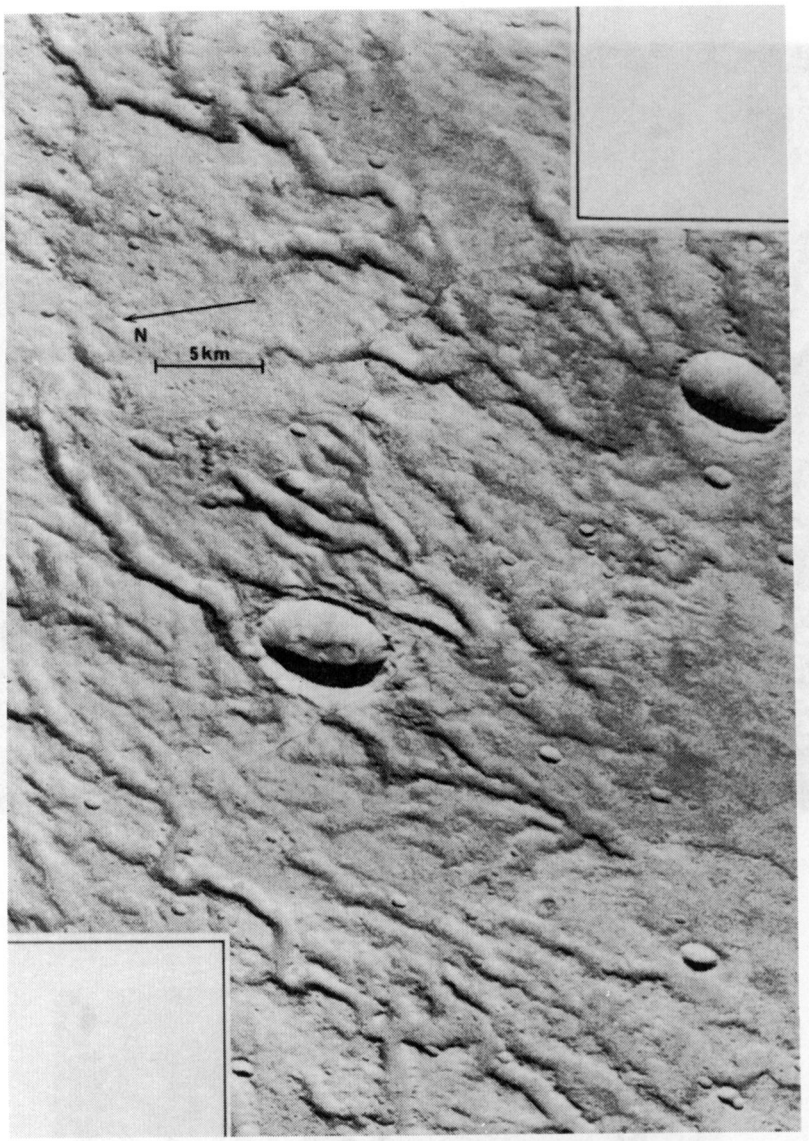

Figure 6.

Closeup of valley systems shown in Chapter I, Figure 3. A high resolution view which clearly shows the heavily cratered, rugged and eroded appearance of the terrain. The disorganized appearance of the valleys at this scale is common on Mars. Amphitheater terminations are present, valley interiors are smooth, as if mantled. Evidence of runoff erosion on inter-valley surface is lacking. Inundation and burial of valleys by plains forming material has occurred at the lower right. Sun elevation angle is 28°, illumination is from the lower left, and viewing angle is 50°.

Picture center: latitude -10°, longitude 278°
Resolution: 48 meters
Viking Orbiter Images: 754A16, 17, 18, and 19

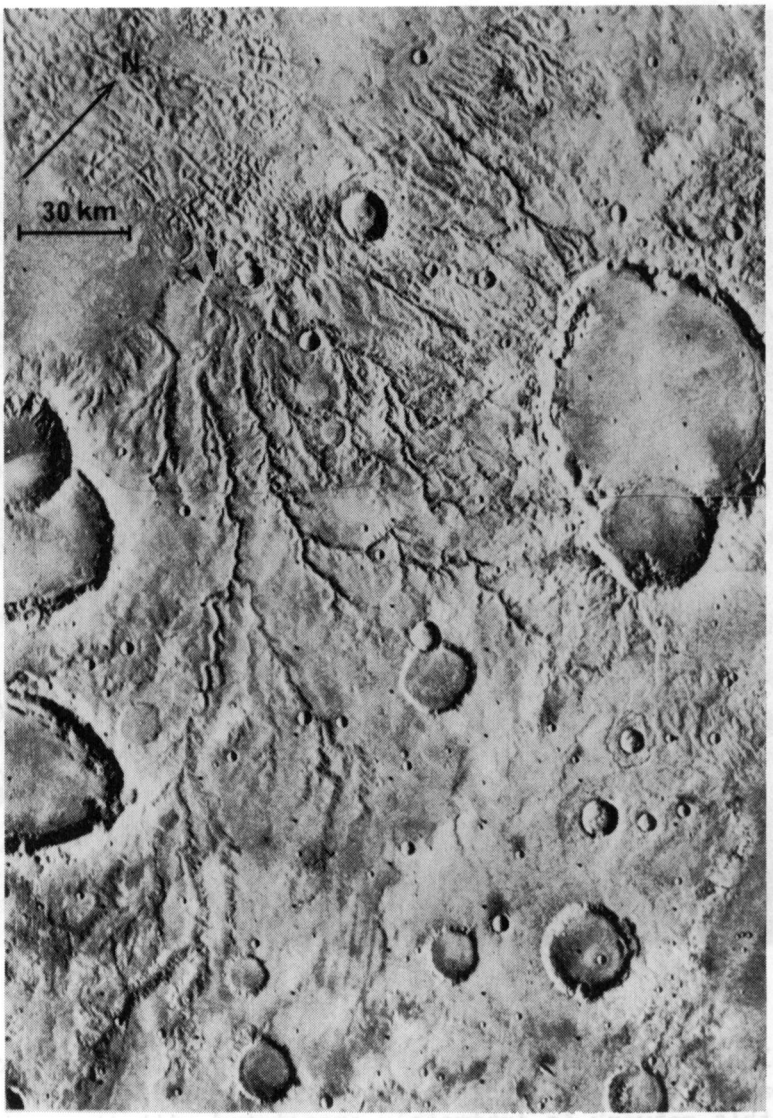

Figure 7.

Digitate network system in Margaritifer Sinus. Note the junction of three major trunk valleys (arrows). Long parallel inter-valley septae are visible. Amphitheater terminations to tributaries are common. Also note the prevalence of stubby tributaries parallel to main valleys. Evidence of dissection and drainage basin development in inter-valley area is lacking. Sun elevation is 35°, illumination is from the right, and viewing angle is 10°.

Picture center: latitude -25°, longitude 26°
Resolution: 400 meters
Viking Orbiter Images: 084A46, 47, 48

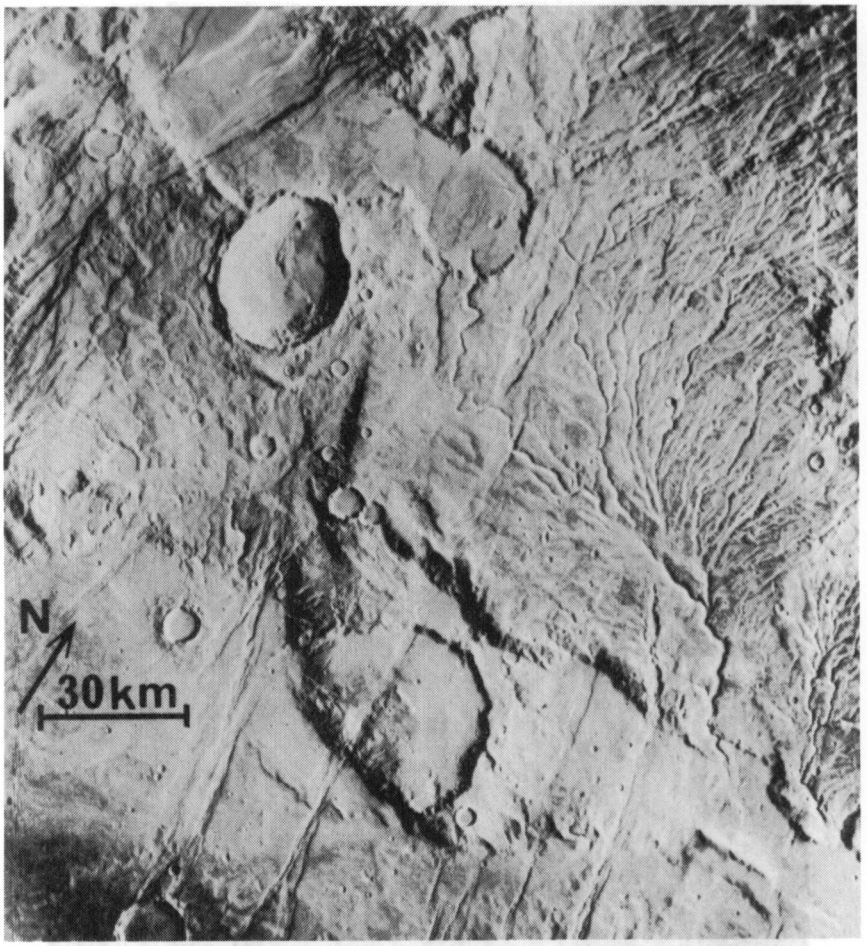

Figure 8.

Parallel network near Claritas Fossae. This network is expressed in a block of heavily fractured ancient heavily cratered terrain. The upper reaches of this network is intimately associated with the northeast and east-northeast trending fractures and appears to be truncated by them in several places. The network clearly post-dates the east-west trending scarp at the bottom of the picture. Note the long parallel valley sections and the strong coalescence near the mouth, similar to digitate systems. The strongly parallel arrangement of tributaries, lack of evidence of capture across inter-valley divides, and absence of deflection of small tributaries into larger ones suggest formation other than by rainfall, although this system is often cited as evidence of pluvial erosion (Masursky et al., 1977). Sun elevation is 35°, illumination is from the right, and the viewing angle is 13.5°.

Picture center: latitude -43.8°, longitude 93.5°
Resolution: 350 meters
Viking Orbiter Image: 532A16

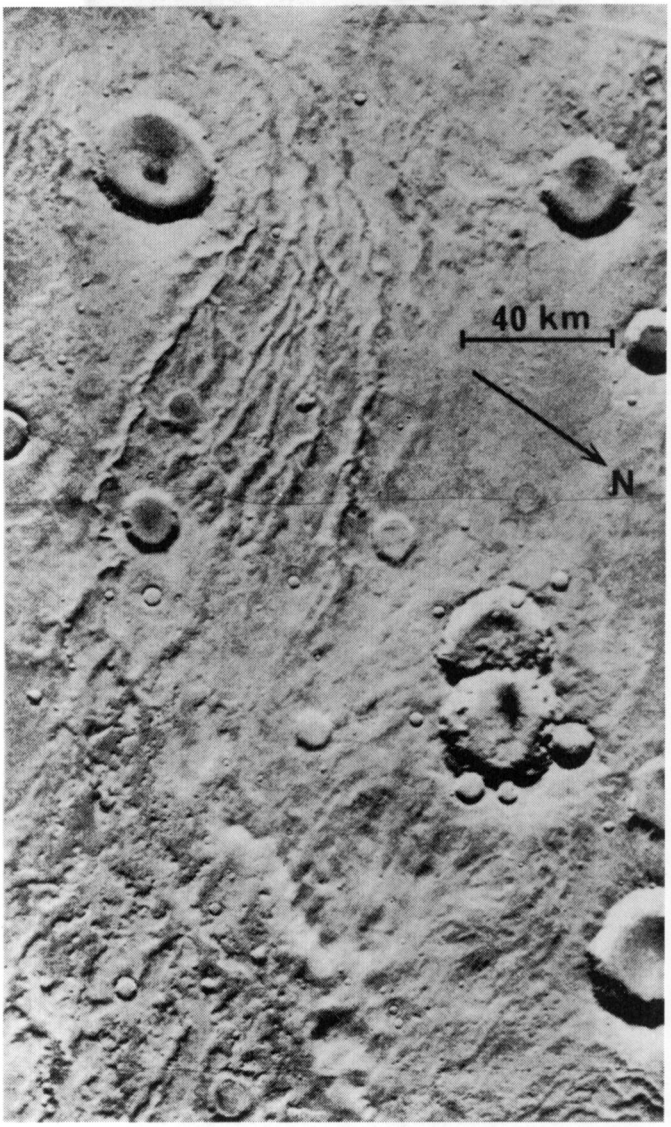

Figure 9.

Parallel and digitate valley system in Thaumasia. Again, amphitheater terminations and widening distal to the valley mouth is observed. Many parallel networks are observed in this area as part of a centrifugal assemblage of valley systems radial to the chaotic terrain in the lower left. Notice the prominent valley which appears to originate in the chaotic terrain. Sun elevation is 24°, illumination is from the bottom of the picture, and the viewing angle is 14°.

Picture center: latitude -47°, longitude 73°
Resolution: 300 meters
Viking Orbiter Images: 535A23 and 25

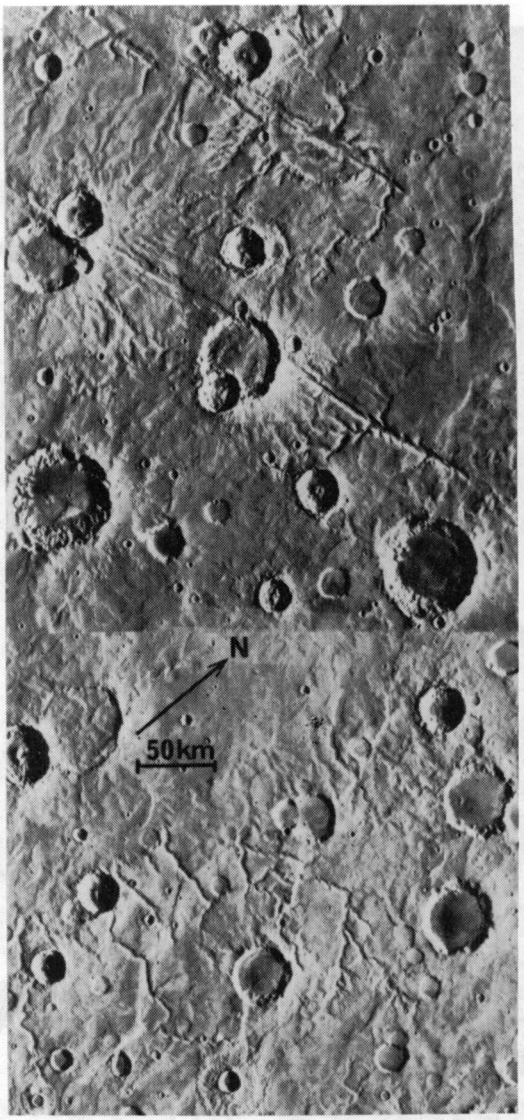

Figure 10.

Rectilinear valleys in Margaritifer Sinus. Several discrete systems are visible in this view. Rectilinear valleys at the top of the illustration are associated with large east-west trending troughs. The regional slope is downhill toward the upper right corner of the picture. Valley development appears more extensive on the uphill side of the troughs. Another rectilinear network appears in the lower portion of the figure. Numerous straight segments are visible. The westernmost part of this network appears to have been buried by smooth ridged plains material. Sun elevation is 10^{o}, illumination is from the right, and the viewing angle is 5.4^{o}.

Picture center: latitude -32.1^{o}, longitude 21.5^{o}
Resolution: 400 meters
Viking Orbiter Images: 084A05, 06, 07, 36, 37, 38

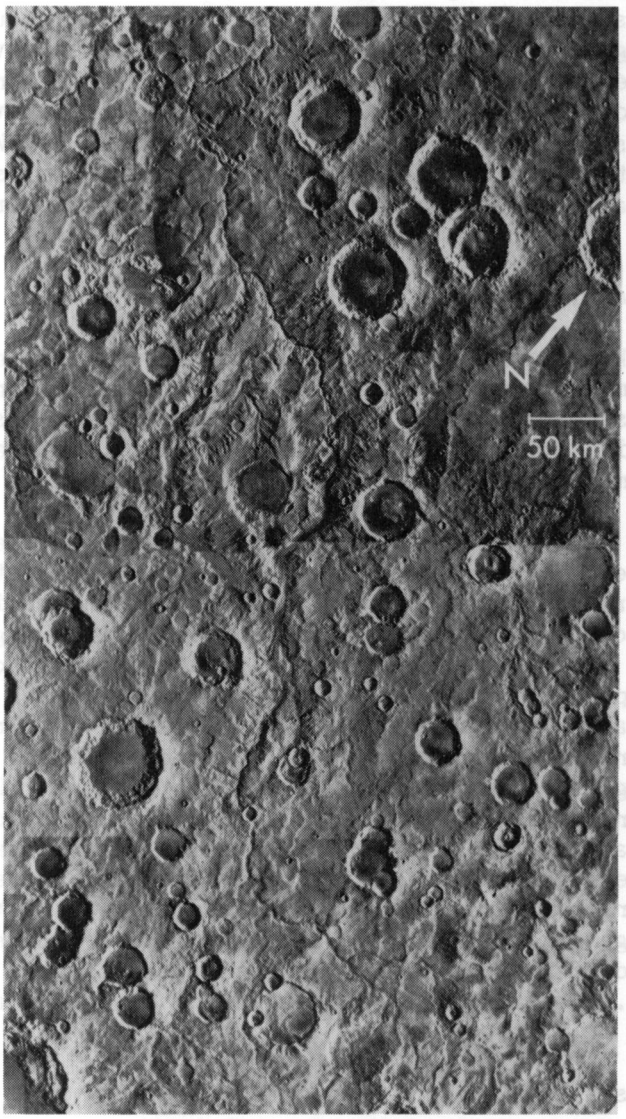

Figure 11.

Stem valley is Margaritifer Sinus. This valley is part of a longitudinal system in heavily cratered terrain. The regional slope is downhill toward the top of the picture. A rudimentary digitate pattern occurs in the headward reaches at the bottom of the mosaic. Very few tributaries join the main valley down-network. Valley wall morphology varies from smooth to rugged. An older filled valley, superimposed by numerous large craters appears to the left of the more deeply expressed continuous stem valley. Sun elevation is 25°, illumination is from the right, and the viewing angle is 64°.

Picture center: latitude -28°, longitude 14°
Resolution: 460 meters
Viking Orbiter Images: 84A09, 10, 11, 12, 13, 40, 41, 42, 43, 45

present on valley floors (Figure 12). Two prominent stem valleys in Margaritifer Sinus have mouths near chaotic terrain at about -15° latitude, 20° longitude and extend southward into more heavily cratered terrain. They die out headward in ridged intercrater plains to the south at about -30° latitude, 30° longitude. These linear-sinuous valleys cut across the major structural grain of the area, namely a WNW-ESE graben-trough system parallel to Nirgal Vallis. The coalescence direction of network tributaries conforms with that expected for downhill flow.

Radial valley assemblages

Radial network assemblages are common on Mars and are most often associated with impact craters or basins. The radial arrangements of valleys without association with obvious structures has also been noted, but suggests that radial configurations can also result from valley formation on the rims of old impact basins too subdued to be visible.

There are two major types of radial assemblages and the traditional terminology is used: (1) "centrifugal", and (2) "centripetal". A centrifugal pattern has acute junction angles pointing radially outward from the center and a centripetal pattern has acute junction angles pointing radially inward. Two types of centripetal patterns exist on Mars; interior and exterior. Typically interior and exterior centripetal networks are associated with large impact basins (Figure 13 and 14). Interior centripetal networks are emplaced on the interior walls of basins and have acute junction angles pointing toward the basin centers. Exterior centripetal networks traverse basin walls, penetrating from the outside. Some assemblages around basins are both interior centripetal, and centrifugal. Older, larger basins (e.g. Schiaparelli) often exhibit interior and exterior centripetal network assemblages. Some moderate-sized craters (e.g. Margaritifer Sinus, 40-80km in diameter) have radial valley assemblages around them which are exclusively centrifugal, as does Huygens Basin (Figure 15). Centrifugal assemblages are also seen around several broad domal areas in Thaumasia.

Fragmented valleys

Finally, "fragmented" is used for valley systems which appear to have been disrupted by subsequent erosion or deposition. Fragmented systems occur commonly in heavily cratered terrain, and not surprisingly, since many valley systems predate large impacts. Impact ejecta and other intercrater materials (e.g. lava, sediment) have partially buried many valleys and may have completely buried others. Numerous valley networks are at least partially fragmented. Unless a fragmented valley system has a clear mouth or many tributaries, it would be relegated to the trough category. Conversely, a well-oriented system with moderate tributary development ending abruptly in a closed depression would be considered to have been fragmented by impact or burial.

The Uzboi-Holden-Landon Valles system is an example of a fragmented system (Figure 16). Uzboi Vallis is a north-south trending feature, to

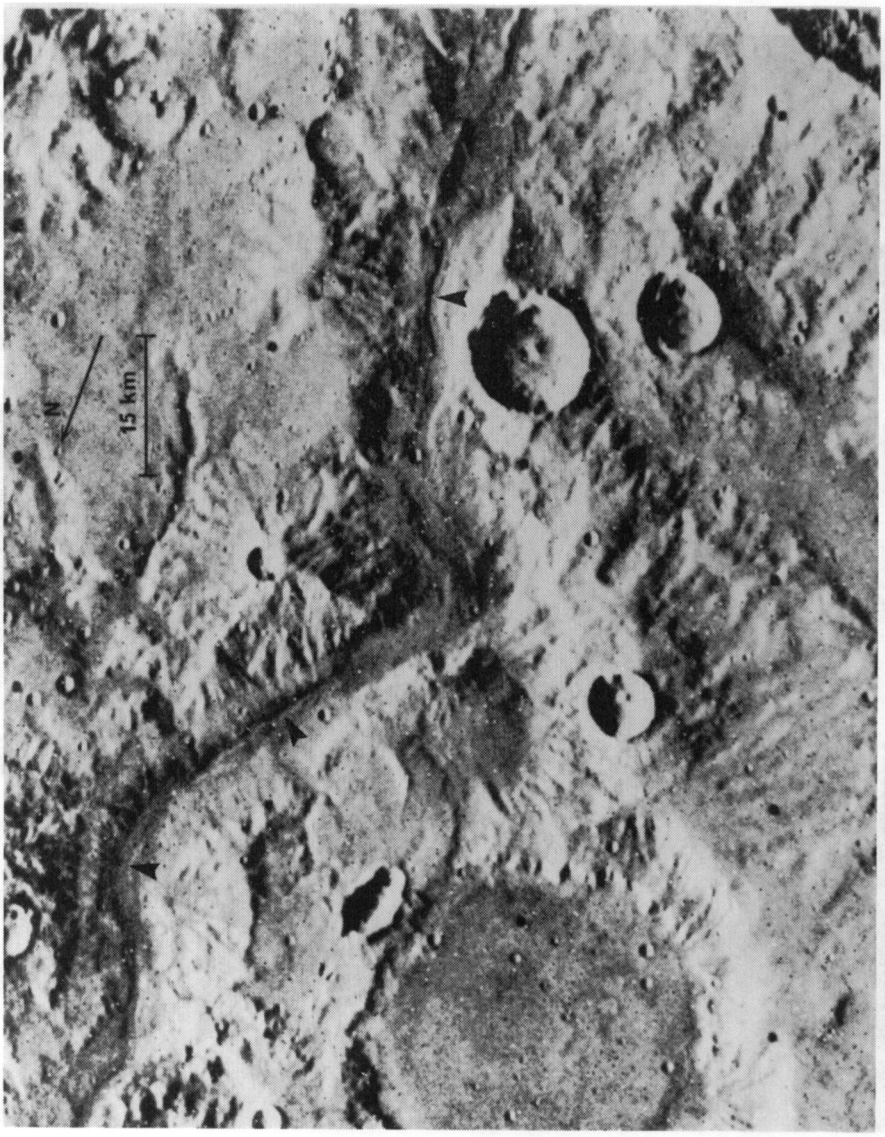

Figure 12.

Closeup of interior channel. This blowup shows a 125km long section of the stem valley in Figure 11. Visible sections of the interior channel are indicated by arrows. There are in general very few examples of interior channels with martian valleys. No streamlined erosional forms are visible. Sections of the surrounding terrain here appear dissected. Smooth material in which the valley is entrenched has embayed more rugged terrain generally in this area as evidenced both here and in Figure 11 by partially buried craters. Sun elevation is 25°, illumination is from the top and the viewing angle is 6.4°.

Picture center: latitude -30.4°, longitude 13.4°
Resolution: 460 meters
Viking Orbiter Image: 084A10

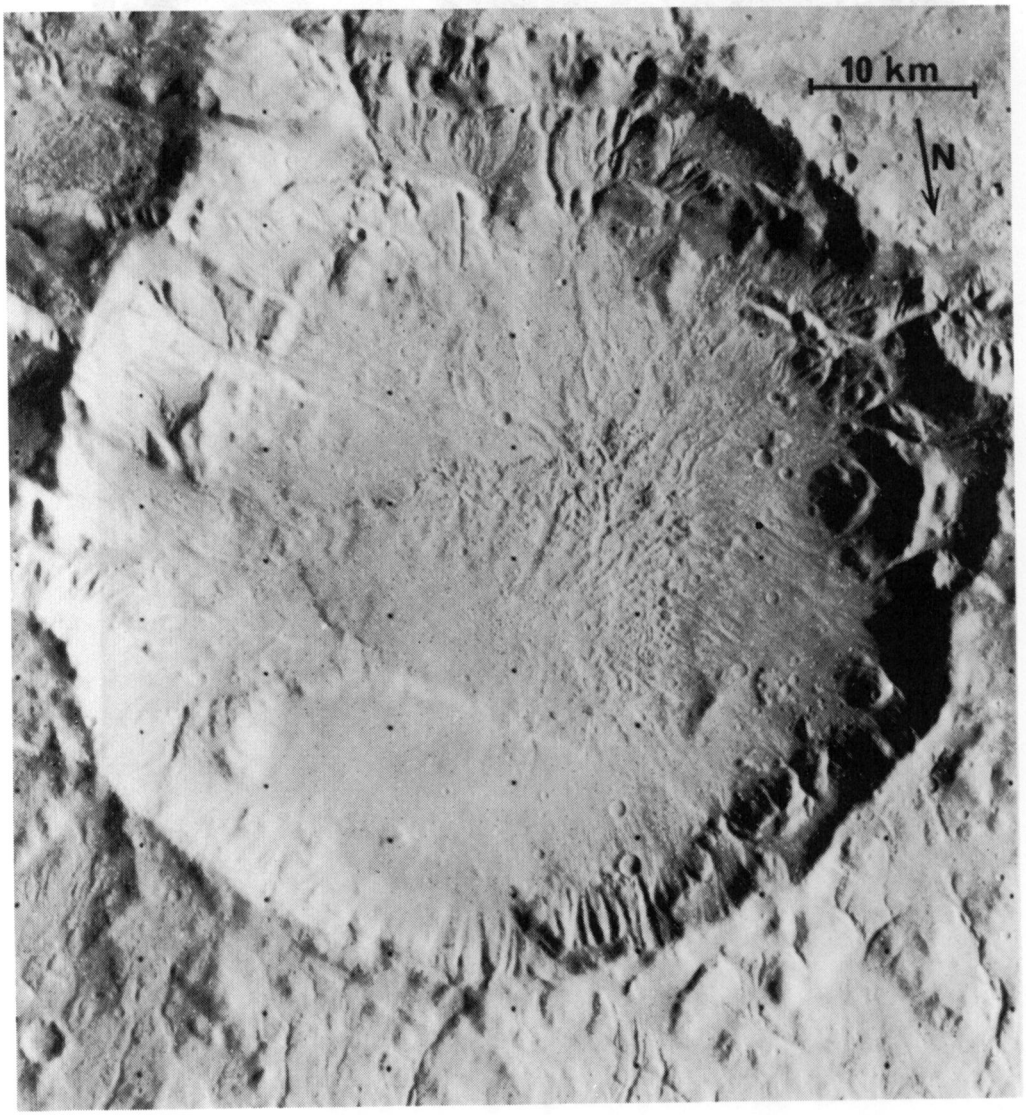

Figure 13.

Interior centripetal networks in large crater. Small coalescent parallel and digitate networks appear on the interior wall of the crater at the top of the picture. Wall slopes are on the order of 10°. Note the apparent anastomosing pattern visible in some valleys. Similar features appear in lunar craters suggesting that downslope mass movement (e.g. avalanching) without fluid flow may be important in their formation. Sun elevation is 26°, illumination is from the right, and viewing angle is 10°.

Picture center: latitude 39.3°, longitude 135.3°
Resolution: 110 meters
Viking Orbiter Image: 129A39

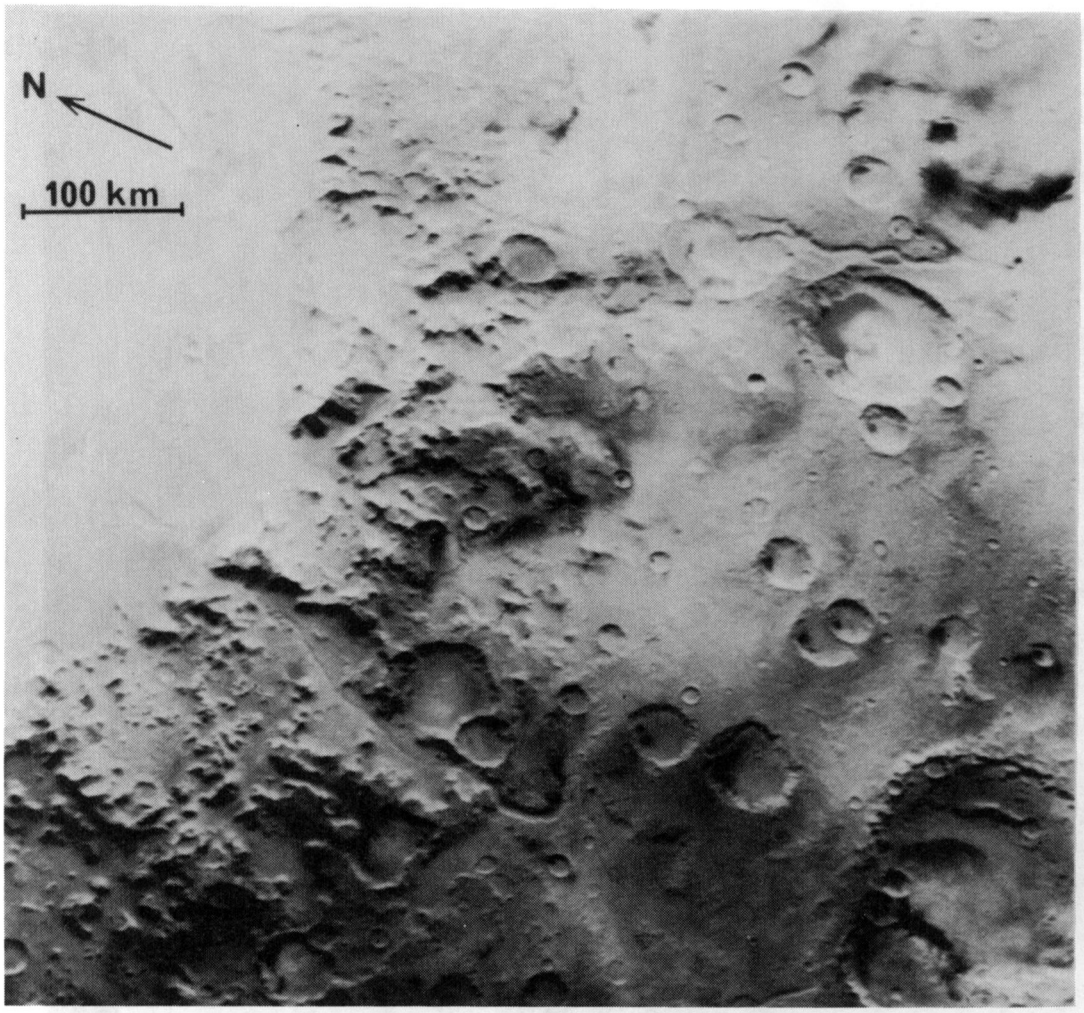

Figure 14.

Exterior centripetal valleys in Argyre. There are five stem valleys which penetrate the ring mountains which surround Argyre Basin, two of which are shown here. There is little to no tributary development visible. The upper valley has breached several large craters. Sun elevation is 25°, illumination is from the top of the picture, and the viewing angle is 31°.

Picture center: latitude -60°, longitude 41°
Resolution: 130 meters
Viking Orbiter Image: 407B21

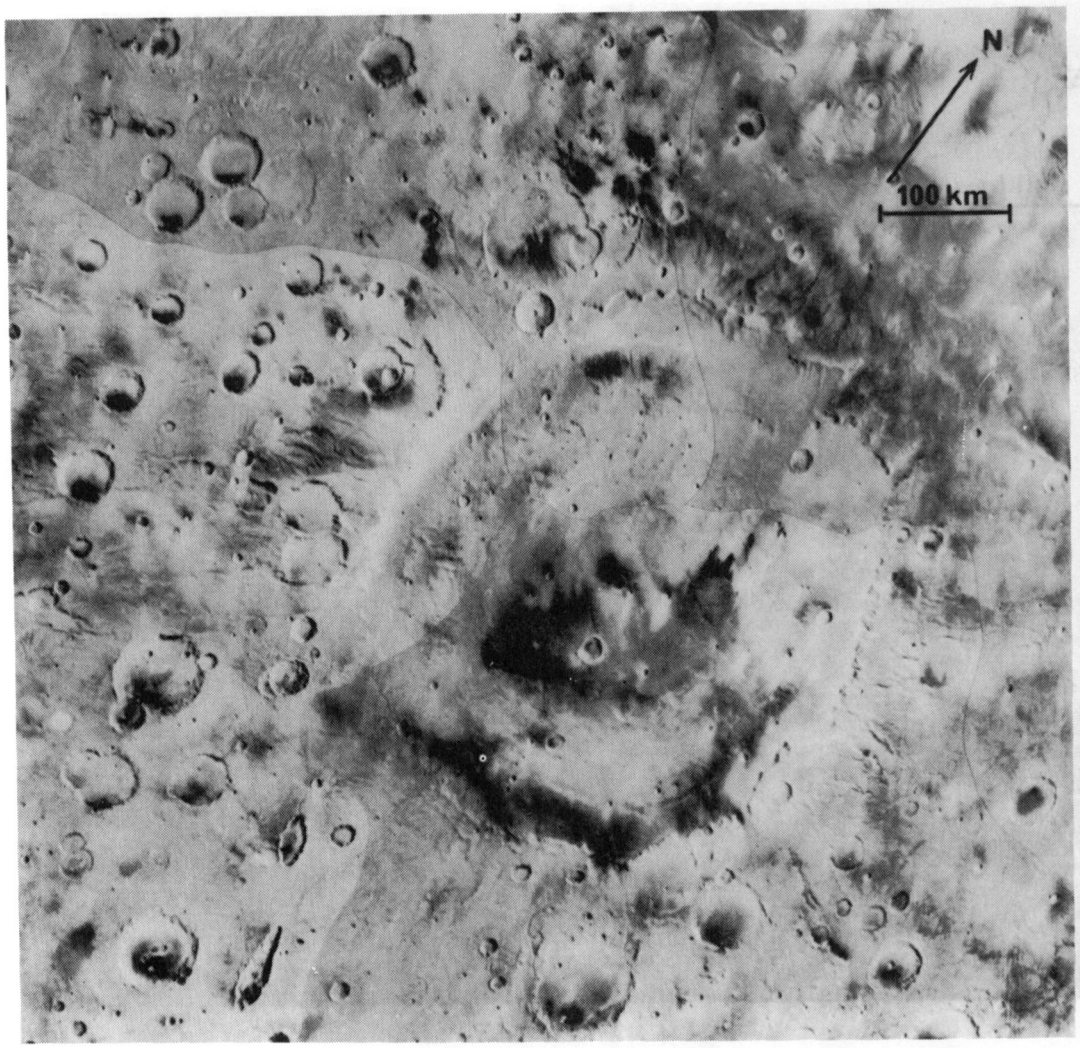

Figure 15.

Centrifugal network assemblage around Huygens Basin. Valleys coalesce away from the basin rim in all directions and are mainly digitate, although a Mariner 9 B-frame reveals at least one longitudinal system (Pieri, 1976). The regional slope is about 0.1° toward the bottom of the picture. Sun elevation is 55°, illumination is from the right, and the viewing angle is 13.5°.

Picture center: latitude -7° longitude 310°
Resolution: 350 meters
Viking Orbiter Images: 623A74, 75, 76, 77

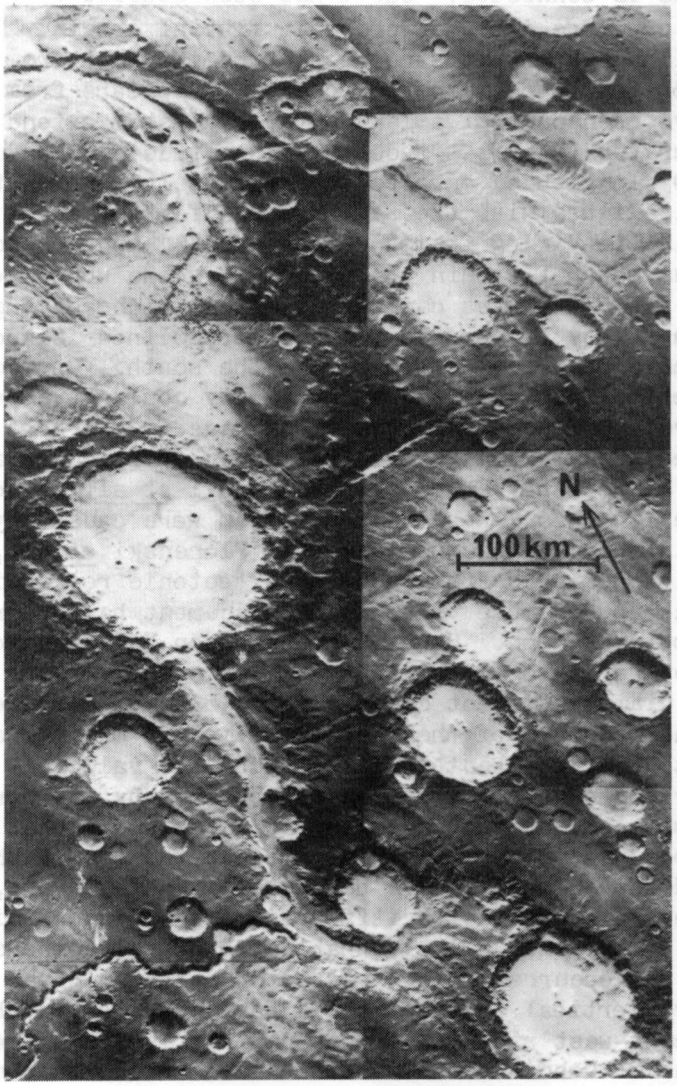

Figure 16.

Fragmented longitudinal valley north of Argyre. Uzboi-Holden-Landon Vallis spans this mosaic from lower right to upper left. Nirgal Vallis enters the west in the lower left portion of the picture. The shapes of streamlined mesas at upper left suggest flow from the south which is consistent with regional topography. Obliteration of the valley by prominent superimposed impact craters and by plains formation has occurred. Sun elevation is 27°, illumination is from the upper right, and the viewing angle is 34°.

Picture center: latitude -25°, longitude 30°
Resolution: 450 meters
Viking Orbiter Images: 611A21, 22, 23, 24, and 25

which Nirgal Vallis is connected. Uzboi has been studied by Florenski et al. (1975) who conclude it is of probable fluvial origin. They describe it as about 800km long, somewhat sinuous ranging in width from 25km to 30km in the northern portion to 80km in the south. It appears from Viking data that Uzboi may have been part of a larger valley system extending from the vicinity of Hale crater (-35° latitude, 30° longitude) to Landon Vallis (-22° latitude, 29° longitude) oriented approximately northeast-southwest and well aligned with the regional gradient of about 200 feet/mile. Uzboi Vallis (in Viking frames 466A69 and 70) appears to have a faint talweg-like sinuous channel within the valley. In the upper section, Holden Vallis, no valley floor features can be discerned which are suggestive of fluid flow erosion. They are however, large streamlined islands which presumably could have been cut by flows from the south. One could speculate that a large connected Uzboi-Holden-Landon Valley could have been used as an outlet through Nereidum Montes for ponded drainage from Argyre Basin, the most southern reach of Hale Vallis terminating in chaotic terrain on the northern Nereidum Montes-Argyre border. Florenski et al., hypothesize that the discontinuities in this linear valley system were caused by "transverse tectonic rifts." Although it is unclear what Florenski et al., meant by this phrase, tension has been the predominate tectonic regime in this area. It is unlikely that appreciable vertical displacement has occurred in this area for the following reason. Uzboi-Holden-Landon Vallis is oriented perpendicularly to the regional gradient (Christensen, 1976). There are at least three 100km diameter impact craters which are superimposed along its 1000km length. The presence of these craters imply a minimum age for the valley of at least 3.5b.y. (Chapter III). Since the valley is still oriented correctly for downhill flow, as ascertained by the directionality of streamlined obstacles in Landon Vallis, it is unlikely that major readjustment has occurred since that time. Since the topographic depression into which Uzboi-Holden-Landon Vallis debouches is a major one, upon which many smaller valleys all over Margaritifer Sinus and Sinus Meridiani appear to be consequent, it is also unlikely that coincidental compensating regional movement has occurred which has restored the original orientation. Only minor relative vertical movement could have occurred, perhaps related to the pervasive east-west structural pattern. It is more likely that the erasure of sections of Uzboi-Holden-Landon Vallis is due to the burial by ubiquitous lavas and impact ejecta rather than down-faulting.

Categorization Scheme for a Global Survey

For purposes of a global survey, it is not necessary or convenient to work with eight classes of valley networks that can be arranged in at least 20 different network system combinations (e.g. an exterior centripetal stem-digitate valley network). A more generalized scheme that capitalizes on the tendency for certain combinations to reoccur frequently consists of three broad system categories: (1) integrated, (2) longitudinal, and (3) slope valleys.

Integrated valley systems

About 70% of all martian valley networks surveyed are either digitate or parallel. 42% of the total are integrated valley systems, but 99% of all integrated valley systems are either digitate or parallel. The remaining 1% fall into the rectilinear class. Integrated network systems are well-organized, are relatively compact or "dense", are not excessively elongate, and are found generally in intercrater plains. It is this system type which has been referred to as "dendritic" in the literature. Integrated network systems are aligned with and coalesce down regional slopes.

Longitudinal valley systems

Longitudinal systems are typically composed, in part, of valleys of the stem type, with poor tributary development. Often, poorly developed digitate or parallel networks occur at the head of a long stem network and these together comprise a longitudinal valley system. Occasionally, a longitudinal system will be fragmented due to transection by later landforms. A few longitudinal valley systems traverse basin rims, coalescing toward basin interiors. These comprise of exterior centripetal stem networks and often display small digitate networks at their heads.

Longitudinal network systems extend over great distances (often $\geq$ 500km) in one direction and are analogous to allochthonous rivers on the earth (e.g. the Nile), with few discernable down-network tributary valleys. The most headward reaches may bifurcate into a more integrated network. Longitudinal systems may extend through terrain of varying morphology and through several geologic units. The term longitudinal refers to the gross elongation along trend, but does not necessarily imply the absence of sinuosity. Some reaches of these longitudinal systems may be quite sinuous.

Slope-valley systems

The term slope-valley system is used to describe valley networks development on steep slopes such as crater rims, scarps, basin rims, or canyon walls. These are wide, poorly integrated valleys usually less than 30km long. When such valleys occur on inward facing slopes of crater rims they are termed interior centripetal. Often when arranged in a centrifugal pattern on exterior rims of craters, valleys appear as small digitate networks with amphitheater terminations, rough walls, and flat floors.

In the preceding sections a hierarchical scheme for classifying and categorizing martian valleys has been established. The fundamental unit is the valley network (e.g. digitate, stem, rectilinear, or parallel). Valley networks are then classified by the way they combine into network systems (e.g. longitudinal, slope valleys, or integrated). Assemblages of network systems are classified by their overall orientation (e.g. radial). Thus one could have a group of radial longitudinal valley systems comprised of stem

and digitate networks. Likewise, other patterns common on Mars are assemblages of interior centripetal radial systems of slope valleys comprised of digitate and parallel valley networks. In each case the assemblage of systems, the system type, and the network type comprising the system has been identified.

System categories

From Table II it is clear that most martian valley networks are of the digitate and parallel type (78%), comprising 99% of the integrated system category. Integrated and slope valley systems taken together comprise the group of features loosely called the "dendritic" channels or "small channels" mentioned previously and account for about 64% of all network systems. The remaining 37% is comprised of longitudinal systems, 79% of which are stem valleys, 20% of which are stem networks juxtaposed to digitate, parallel, or rectilinear networks.

TABLE II

Percentages of valleys in class and category

Network Class	% of total valleys surveyed in class	% of specified valley system category which contains a specified network class		
		Integrated	Longitudinal	Slope Valley
Digitate	52	50	6*	43
Parallel	16	10	22*	68
Stem	29	0	98	2
Rectilinear	2	20	50*	20

Valley System Category	% of total valleys surveyed in system category	% of specified network class occurring in specified system category			
		Digitate	Parallel	Stem	Rectilinear
Integrated	28	93	6	0	1
Longitudinal	37	8*	9*	79	3*
Slope Valleys	36	63	30	2	5

*stem-digitate, stem-parallel, or stem-rectilinear combinations

Distribution of Valley and Channel Systems

The global distribution of valley and channel systems on Mars has been the subject of interest and discussion since the acquisition of Mariner 9 data. Many papers based on analysis of these data (McCauley et al., 1972; Sagan et al., 1973) observed that "small channels" occurred in restricted latitudinal bands near the equator. However, Pieri (1976) argued that this valley distribution was not the original distribution, but that the equatorial concentration both the result of valley filling by mantling (e.g. eolian or volcanic) in bright areas, and of incomplete imaging coverage away from the equator.

In this section the distribution of valley and channel systems will be re-examined in light of the high resolution images acquired by the Viking Orbiter spacecraft and a generalized categorization scheme for valley networks just described. This evaluation is based on the 240 valleys and channels that were catalogued on the basis of position and morphology. The general coalescence direction of each network system was also noted.

Latitudinal correlations

Figure 17, 18, 19a,b show a histogram of the areal frequency and generalized maps of their areal distribution for the valleys categorized and listed in Table I. The ordinate is the number of valley or channel systems per $10^6 km^2$ within each 10^o latitude band, with the exception of the 5^o band between 60^o and 65^o N and S. The areal density for each latitude range is plotted at mid-bin. In this survey, a valley system was counted within a latitude band if any part of it overlapped into the band. In the case of high density areas where many systems were visible and only the general extent of the dissected area was mapped, the magnitude was scaled to the area dissected. This may have resulted in an underestimation of the number of systems within the -20^o to 0^o latitude bands and values in this range could be as much as 25 to 35% higher than plotted.

Over 75 percent of the mapped valley systems are south of the equator. This dichotomy was partially recognized from Mariner 9 data, although the near coincidence of the high density band with the equator was distracting. Pieri (1976) made the statement that "small channels" would be found to be distributed throughout the cratered terrain on Mars when the superior Viking imaging became available, and indeed that is the case, at least in the southern hemisphere. Integrated and slope valley systems--the "small channels" or "dendritic valley networks"--are indeed the most numerous type of valley or channel (74%, Table II) and show a broad peak across nearly all the sub-equatorial latitudes. Their detection is apparently only limited by the increasingly thick mantling on the order of several hundred meters at -55^o latitude, which increases in thickness southward (Soderblom, et al., 1974). Some valleys in the far southern latitudes are seen on broad dark high areas exhibiting a higher albedo than the surrounding terrain. Dust or, more likely, frost or freezing fog has inundated these features, enhancing their visibility under certain lighting conditions. Other

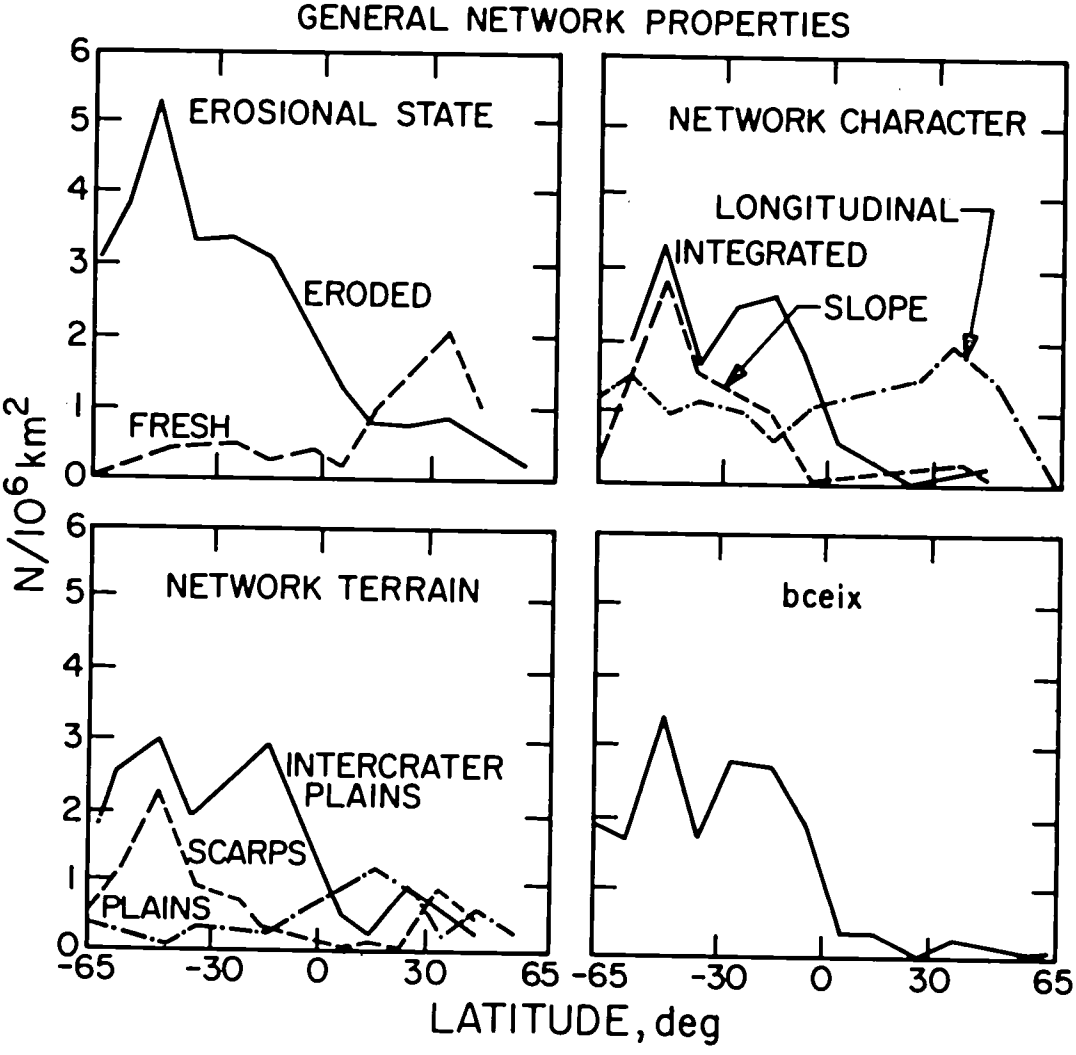

Figure 17.

General network properties of martian valleys as a function of latitude. The overall erosional state of valley systems was classified as either eroded (e.g., Figure 16) or fresh (e.g., Figure 8). Eroded-looking valleys follow the latitudinal fresh-looking valleys follow the longitudinal distribution. From both the network character and the network terrain (i.e. type of terrain in which the network occurs) it is clear that integrated and slope valley systems preferentially occur on intercrater plains and on scarps. Longitudinal valleys occur equally often on all terrains. The graph labeled "bceix" represents the distribution with latitude of box-shaped, crenulated, eroded, integrated networks on all terrains. The bceix distribution is clearly correlated with the distribution of intercrater plains.

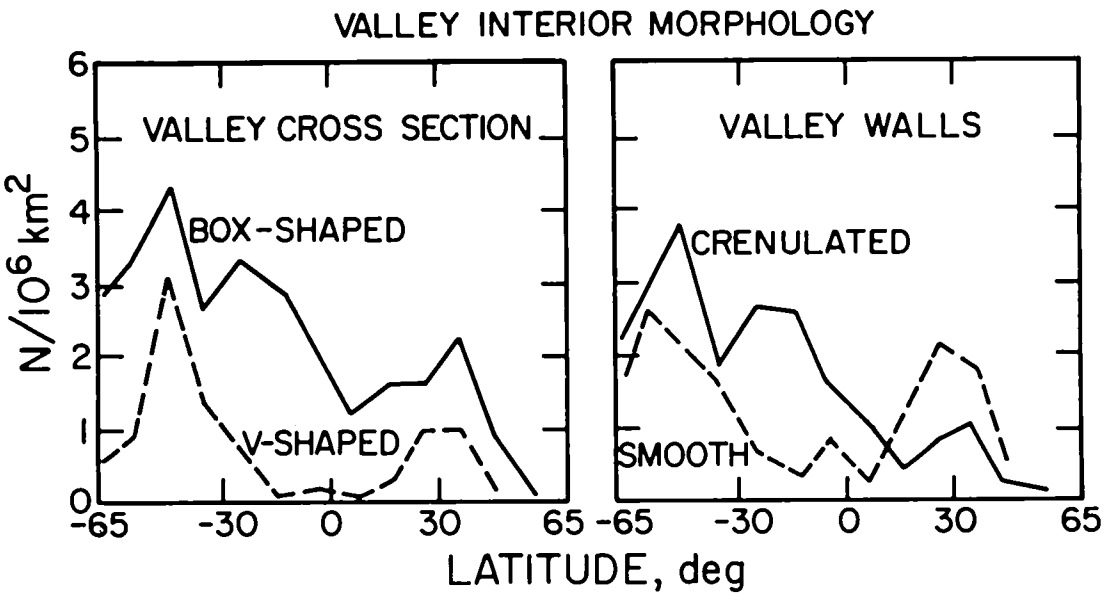

Figure 18.

Distribution of valley interior morphology with latitude. Two types of cross sections were delineated, "box or U-shaped" (e.g. rectilinear valleys, Figure 10) or "V-shaped" (e.g. valleys in Figure 8). Valley walls were categorized as either "crenulated" (e.g., headward reaches at lower left in Figure 7) or "smooth" (e.g., rectilinear network in lower half of Figure 10). The latitudinal distribution of box-shaped and crenulated valleys follows that of integrated and slope valley systems shown in Figure 17. V-shaped and smooth valleys follow more closely that of longitudinal valleys.

southern valleys, particularly those just east of Argyre, are heavily mantled and are visible only at relatively high resolution ($\leq$300 meters) and under favorable lighting ($\leq 20^{o}$ sun elevation). A large contribution to the histogram at about -40^{o} latitude is made by valley systems which are generally small, short, and occur on isolated massifs, and were generally invisible or barely visible on Mariner 9 pictures. They do not appear to be mantled or draped with sediment, although in many cases they disappear into the surrounding plains material, apparently inundated and buried by younger lavas.

Valleys or channels that do occur north of the equator appear to be predominately smooth-walled, fresh-appearing, rectilinear and incised into plains material. They posses either U-or V-shaped cross-sections. Many of these valleys are associated with the fretting process which apparently has formed the northern erosional border between the heavily cratered terrain

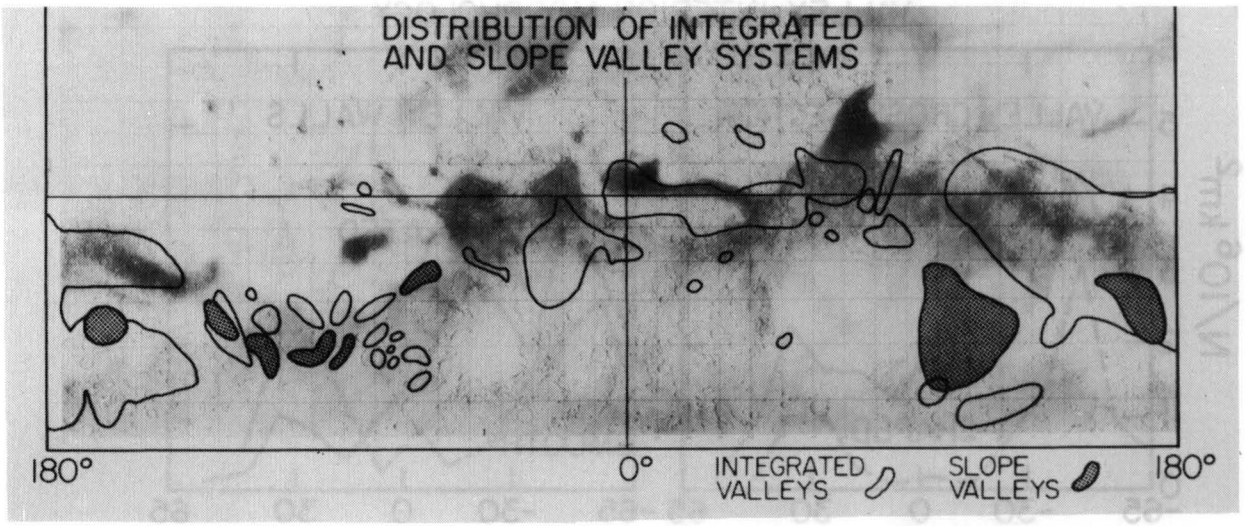

Figure 19a.

Distribution of integrated and slope valleys. The distribution of these features is indicated on a shaded relief map of Mars with classical albedo features shown.

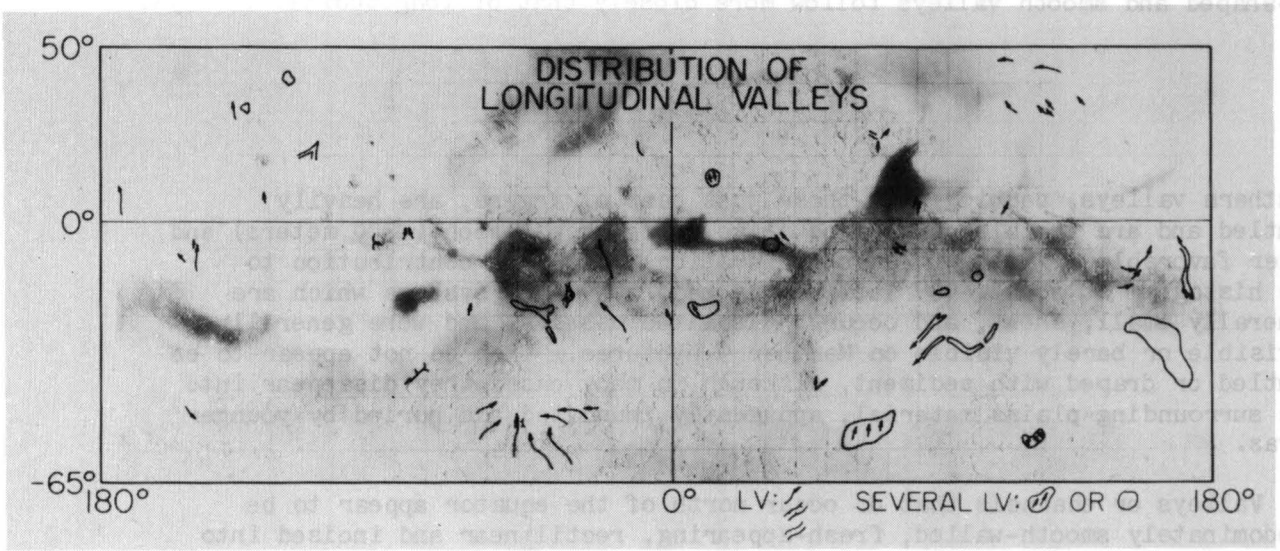

Figure 19b.

Distribution of longitudinal valleys.

and the northern plains units (Sharp, 1973). Another large contribution to the histogram at 15° north latitude is derived from the outflow channels north of Vallis Marineris associated with Lunae Planum and Chryse Planitia. Integrated network systems, however, which do not occur north of the equator are located west of Syrtis Major and were noticed from Mariner 9 data. A few isolated networks also appear at 13° latitude, 340° longitude. These networks are mantled, degraded and fragmented. North of 20° latitude, inundation and burial by younger ridged lava plains have erased these features. In the far north, about 40° latitude, isolated longitudinal stem valleys occur. They are eroded, are perhaps exhumed, and do not possess any appreciable tributary systems. Longitudinal valleys show no latitudinal dependence, nor do craters which have slope valleys on their rims.

Correspondence to classical albedo features

Pieri (1976) demonstrated that almost all small valley systems are confined to dark, low albedo regions between 15°N and 30°S latitudes, centered at about 20°S latitude. This was the first time that the classical albedo features of Mars had been well-correlated on a global scale with the occurrence of a geologic feature.

There are a few anomalies in this global correlation. Two anomalous regions, Hesperia Planum and Syrtis Major Planitia, are low albedo cratered plains units markedly devoid of small channels. All martian plains units of both low and high albedo show very few valleys. High northern and southern latitudes are usually also devoid of valleys. Hence, a second condition must be added to the stated global correlation of high small-channel density and low albedo; valleys are predominately seen in regions of both low albedo and high density of large ($\leq$20km in diameter) craters. This double correlation implies that valley systems are most numerous in cratered uplands of low albedo (Pieri, 1976) (i.e., valleys are old and dark).

Other correlations

It has been pointed out by Soderblom et al., (1974) that several other phenomena correlate with the zone of high valley density. The region of highest small-crater (0.6-1.2km in diameter) density (from Mariner 9 B-frames) is coincident with the equatorial band of high valley network density. They conclude that the small craters are easily obscured due to complete and partial burial by surface dust and debris mantling, and it seems probable that valleys are likewise affected, probably to a greater degree. The decrease in spatial density of small craters and valleys with increasing latitude and the filling of crater interiors with bright material (Soderblom et al., 1973; Woronow and King, 1972; Sagan et al., 1973) indicates that burial is at least one mechanism which could account for the erasure of valley networks in these same regions.

Overview of equatorial valleys

Several interesting points emerge from the mapping of valleys in the equatorial region. Valley systems have extremely high densities in the Sinus Sabaeus-Meridiani Sinus area. They are oriented radially outward to almost all craters larger than about 10km and radially inward to old degraded basins some of which have only scattered poorly defined remnants of their original rims. Schiaparelli Basin has many exterior centripetal valley systems. The albedo boundary between Sinus Sabaeus and Deucalionis Regio also serves to make the limit of obvious valleys, although subsequent Viking mapping does indicate the presence of several valley systems in the higher albedo Deucalionis Regio area. East toward Huygens Basin, the valley density remains high. Huygens has numerous interior centripetal and centrifugal valleys. The Iapygia area has many well-developed integrated valley systems, some occurring on a remnant outer ring of Isidis Basin.

In general the coherence of the integrated valley networks data decreases from Sinus Sabaeus to Iapygia. Either the erosion state is more advanced in the intercrater plains lava or sediment cover is less complete in the eastern systems of this zone than near Schiaparelli. The abrupt decrease in valley density north of Sinus Sabaeus may be due to an eolian debris cover in the adjacent northern high albedo cratered terrain and increased infilling of intercrater plains to the south of Sinus Sabaeus. Valley systems are moderately well-integrated, ubiquitous in dark, heavily cratered areas, present on the rims of large craters, and obscured in many areas by younger deposits of varying origin.

Comparison of Mariner and Viking data

The bulk of valleys observed are concentrated in a roughly subequatorial zone which correlates well with the position of the classical dark albedo features. Mariner 9 data hold up best relative to Viking at near-equatorial latitudes, particularly between 0^{o} and -20^{o} latitudes. Here, the Mariner 9 data compare quite well with Viking imaging at comparable scale. Viking imaging, in this zone, is in general more oblique. Valleys are well-incised in these dark equatorial areas and therefore have good shadowing even at the generally higher Mariner 9 solar elevations.

Viking coverage at viewing ranges of less than 1000km (about 40 meters resolution) is sporadic but wide-ranging. Many of the typical landforms are not seen at such high resolution at the 100m resolution level common to Mariner 9 B-frames, and particularly not at the 1km A-frame resolution. Consequently, many intricate networks are visible in Viking coverage which were totally or nearly invisible on Mariner 9 pictures. This is not usually significant in terms of establishing the global distribution of major system positions since most major systems have at least trunk segments visible on Mariner 9 images along with the finely textured portions visible from Viking. In the Thaumasia-Argyre region, however, such an increase in resolution is significant because many of the valleys observed there are relatively small (100-500m wide), short, and emplaced on isolated massifs.

Mariner 9 had generally higher lighting angles (60° to 80° versus 10° to 40° for Viking Orbiter). This factor, coupled with the increase in resolution, accounts for the major differences between Mariner 9 and Viking distribution maps. This is particularly true in mantled areas, such as for the valley systems west of Syrtis Major (10° latitude, 310° longitude) and for valleys between -35° latitude and -65° latitude for all longitudes. The major new Viking addition to the valley distribution map is the extension of the major zone of integrated and slope valley systems to the zone between -55° and -65° latitude.

Conclusions Based on the Distribution of Valleys and Channels

Implications for process

The distribution of valley and channel networks may yield clues to the processes and conditions of their formation. In particular it is extremely significant that no major integrated or slope valley systems occur outside of the heavily cratered terrain. Plains show few valleys or channels. A major exception, of course, is Chryse Planitia and Lunae Planum where major outflow channels occur. It appears, however, that even in the Chryse region many younger deposits have inundated the large channels and also that channel incidence decreases markedly in the plains units to the north of Chryse. All major integrated and slope valley systems occur in heavily cratered, low albedo terrain and both integrated and slope valleys are ubiquitous in these areas, except where valleys have been filled by inter-crater deposits such as lava, ejecta blankets, or eolian debris. Valley networks exist around nearly every major basin and the coalescence directions of all major valley systems conform to that expected for downhill flow, including slope valleys on the interior and exterior of crater rims. These facts argue for a formative process which was global and able to produce sinuous, riverine, branching erosional patterns which, because they conform to the coarse regional topography, are suggestive of erosion by downhill movement of a fluid. Evidence from this global survey shows that such a process was active nearly everywhere in the heavily cratered terrain and relatively inactive on most plains, even though gradients are much the same in both.

Implications for age

The predominant occurrence of integrated and slope valley systems in the heavily cratered terrains and the remarkable lack of them in both low and high albedo plains, despite, in many cases, similar gradients argues for a relatively ancient period of valley formation predating most plains formation. The close association of degraded craters and dissected scarps with valley occurrences in the old heavily cratered terrain and the lack of any dissection visible on ridges or on lobate ejecta blankets superimposed on plains argues for wide spread erosion processes in the old heavily cratered terrain and only extremely localized occurrences of channels (e.g. Kasei or Chryse channel) in the younger plains. In addition, younger low albedo lava plains such as Hesperia Planum and Syrtis Major Planitia

inundate the mouths of valleys proximal to these plains units, implying that the integrated valley systems occupy the lower stratigraphic position. Longitudinal valley systems and large channels, on the other hand, show little dependence on terrain type or latitude. Such a distribution could reflect the fact that the longitudinal systems and large channels are in general younger than the integrated valley systems.

CHAPTER III: AGES OF VALLEY SYSTEMS

Previous Studies of Channel and Valley System Ages

A fundamental part of the discussion of the evolution of planetary surfaces is discovering when geologic features were formed. Since the discovery of the martian channels and valley networks, several studies using crater size-frequency distributions have dealt specifically with the question of the timing and duration of channel and valley formation (Hartmann, 1974; Pieri, 1976; Malin, 1976a, b; Masursky, et al., 1977).

Hartmann, using Mariner 9 data, employed two separate crater count dating techniques: (1) estimating the likelihood of the occurrence of a single impact upon a specific reach of Mangala Vallis, and (2) using a sample of 31 craters within "channels" to plot their size-frequency distribution. He concluded that exposure ages exceeded one billion years based on his model for cratering rates at Mars (Hartmann, 1973). Malin (1976a) has noted several deficiencies in Hartmann's analysis, namely (1) his reliance on the probability of occurrence of one 2.5km crater on Mangala Vallis, (2) the fact that at least two of the five "channels" included in Hartmann's analysis are structural troughs which show no morphology potentially attributable to flow erosion, and (3) the small number of craters (31) used to establish a size-frequency distribution for the other "channels" included in the study. Further, Hartmann (p. 3953, paragraph 5) has excluded from his study the valley networks which are the main topic of this work.

Malin's study, using a coherent classification scheme (Sharp and Malin, 1975; Malin, 1976a, b) also relied on Mariner 9 data and was explicit in terms of valley and channel classes studied. Malin studied the size-frequency distribution of about 80 craters ranging in size from 0.25 to 16km in diameter, superimposed on five of the 20 or so major "runoff" and "outflow" channels on Mars (Malin, 1976a, p. 55a). He concluded that most of the channels had exposure ages on the order of billions of years. As with Hartmann, the statistical confidence of Malin's work was limited by the paucity of counted craters.

Masursky et al., (1977) listed crater counts on 7 valley and channel interiors, 8 crater counts on immediately adjacent surfaces, several miscellaneous counts on volcanic features, and a calibration count of craters near the Viking I landing site. They concluded that the channel and valley forming process spanned all of martian geologic history, because some valley and channel interiors exhibited no craters whatsoever and others had crater densities as high as they observed on Mars. Masursky et al., (1977)

deal primarily with intermediate to large valley and channel systems and only briefly mention one "dendritic" valley system in Thaumasia, a "dendritic" valley or channel system of dubious origin in the Alba region, and the "dendritic" Vedra Vallis system.

The effort of Masursky et al., represents the largest set of crater statistics yet compiled for the purpose of determining channel and valley ages. Several assertions in this interesting paper, however, need to be considered carefully with regard to the ages of valley systems. They assert in their conclusion that "channel" formation has spanned all of decipherable martian history (p. 4037, paragraph 3). In particular they cite the "younger ages determined for some channel networks" suggest that warm periods, possibly cyclic, intermediate in martian history, as proposed by Sagan et al., (1973), Hartmann (1973), Ward (1973, 1974), and Jones (1974), could have allowed liquid water to exist for periods of time long enough to cut the observed "channels". An examination of their data (p. 4035, Figure 13a) reveals that none of their counts were of craters superimposed on integrated valley systems. Therefore, they have not attempted to date the features likely to be the result of erosion during the hypothetical climatic modification, by arguments presented here in Chapter I. This omission was made because, as they state, high resolution Viking pictures of valley networks were not available to them at the time of their writing (Masursky et al., 1977, p. 4037). All of the features for which they present data are either large channels or poorly integrated valley systems of the longitudinal type. Large channels have been interpreted by many authors as being the result of catastrophic floods (Baker and Milton, 1974; Sharp and Malin, 1975). As pointed out here in Chapter I it is unlikely that these features were formed directly by atmospherically precipitated water. Further, catastrophic flooding does not require a higher atmospheric pressure in order to erode effectively (Sagan and Wallace, 1977; Baker, 1978). The longitudinal valleys which they cite as examples of very young "channels" (Hrad Vallis and N.E. Hellas "channel" p. 4035, Figure 13a) have undergone extensive modification. Hrad Vallis has been exhumed (Mutch et al., 1977) and the N.E. Hellas longitudinal valley has experienced extensive mass wasting of wall material and progressive infilling of its floor (Malin, 1978). An example of such wall degradation is displayed in Figure 20. In both cases, the meaning of crater densities measured on valley and channel floors is unclear, but at best represents an interval of time in the first case since exhumation, and in the second case, since burial.

In addition, Masursky et al. (p. 4020, Figure 2a) cite Vedra Vallis and a nearby system as examples of "dendritic" channel systems, and assert that rainfall is necessary to form this type of "channel" system. While an extensive discussion of rainfall as a formative agent is not within the scope of this chapter on valley ages, the young age (p. 4035, Figure 13a) attributed to this feature and its characterization as a "dendritic channel" requires comment. First Vedra Vallis does not display a dendritic planimetric pattern. Rather, it is a strongly oriented parallel pattern. Secondly, there is no dissection whatsoever of inter-valley divides and no hint of coalescent flows having drained directly from valley walls as would be expected for a pluvially supplied network. Further, there are

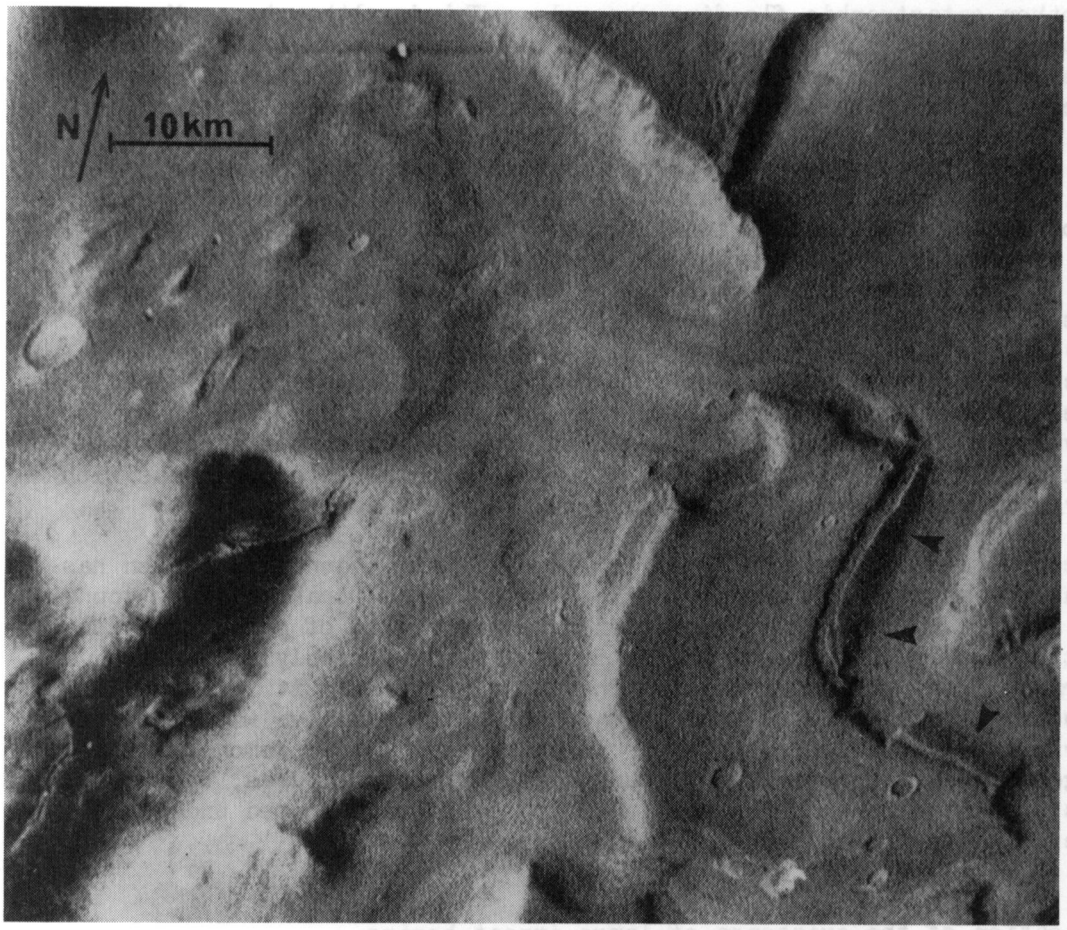

Figure 20.

Example of wall degradation. Note how the block marked by the arrow has moved down and away from the plateau surface along the perimeter of the valley at lower right. Such collapse, by undermining less competent substrata results in valley widening and resurfacing, complicating the interpretation of impact crater statistics with regard to determining valley "age". Sun elevation is 38°, illumination is from the left, and viewing angle is 41°.

Picture center: latitude 36.3°, longitude 345°
Resolution: 100 meters
Mariner 9 Image: DAS 10650904

anastomosing patterns in the upper reaches of Vedra Vallis, similar to those seen in other catastrophic flooding channels. Third, although, as Masursky et al. point out (p. 4020, Figure 2a), the headward reaches of Vedra Vallis do not terminate in box canyons, they do end in a relatively smooth featureless plain, which appear to have buried these reaches, with no evidence of erosion. The Vedra Vallis systems, rather than being clear evidence of rainfall, appears to be the result of catastrophic water flooding, or perhaps formed by lava drainage. Also, it appears that several craters of diameters between 5 and 10 km overlie valleys in the Vedra complex, suggesting that Vedra Vallis is at least as, or more, densely cratered at those sizes as the Viking I landing site. The small counting area presented in the Masursky et al. data for the Vedra valley complex (400 km^2) is, as they admit, statistically insignificant. Therefore, on the basis of the preceding arguments, the Vedra Vallis system is by itself not compelling evidence of a relatively recent period of rainfall. Nor is it likely to be any younger than Lunae Planum plains which are about as old as the Viking I site. This makes Vedra Vallis roughly contemporaneous with other large channel systems, as reported by Malin (1976a, b).

The contention of Masursky et al. that valley and channel formation has spanned all of martian history is interesting but questionable. Very young relative ages (e.g., N.E. Hellas channel) are the result of post-formational modification and resurfacing of valley interiors and possibly exhumation (e.g., Hrad Vallis) which complicates the issue. Further, it is shown in this chapter that the time of formation of integrated valleys was restricted to an early epoch. These features for which Masursky et al demonstrate a wide range of ages, including very young ages, are the features, by arguments presented here, which are least likely to have formed under the influence of any hypothetical climatic change.

The implication of the existence of large impact basins

The vast predominance of integrated and slope valley systems in heavily cratered terrain is one of the most fundamental aspects of the distribution of martian valley systems (Chapter II). However, another fundamental observation that is relevant both to the age of the valley systems and to deciding among candidate processes is the retention of impact craters larger than 50km in diameter which exist in various states of preservation. The fact that they are visible at all immediately constrains hypothetical epochs of rainfall.

On earth, uplift continually counteracts the effects of erosion. Major mountain chains would be eroded to low hills within several times 10^7 years were it not for tectonic renewal of relief (Carson & Kirkby, 1972). The absence of evidence of such erosion and uplift of Mars is consistent with the lack of a comparable cycle. If (as a hypothetical upper limit to erosion rates) a terrestrial-like pluvial environment once existed on Mars, erosional intensity would not be mitigated by any gravitational scaling effects, nor it is likely that the gross surface rock composition and competency differs significantly from those of terrestrial or lunar rocks.

Thus, the most reasonable interpretation is that martian surface features have not been subjected to terrestrial-type erosional environments. The existence and preservation of large impact craters suggests that any hypothetical rainfall epoch must have either predated their formation or have been an episode of such short duration (or several transient episodes with a small cumulative duration) that only modest amounts of erosion occurred. Simply, there is no morphologic evidence of earthlike rainfall on Mars for at least the last 3.5b.y.

Dating by Crater Counts

Problems associated with the method

There has been a long and confusing debate concerning the use of size-frequency distribution of impact craters to date planetary surfaces in an absolute sense. The interested reader is referred to a series of papers by Hartmann (1973), Chapman (1974), Soderblom et al. (1974), Jones (1974), Neukum and Wise (1977), and Woronow (1976) which debate the issue. Controversy centers around the crater production function, a convolution of the availability of impacting bodies and the rate and mode of impact crater distribution. The size-frequency distribution of bodies available to impact a surface, combined with the dependence of crater morphology on time, size, and erosional/depositional regime, should together determine the number of craters visible on a surface of a given age. In reality, the history of the size-frequency distribution of impacting bodies is an estimate based on collision models for asteroids and other objects. Further, the erosional/depositional history of Mars is highly uncertain, based on crater morphology and on changes of the slope in plots of measured crater size-frequency distributions (Woronow, 1975). Soderblom et al. (1974) proposed that Mars had an impacting-body flux history similar to that of the moon. This assertion was based on the fact that the ratio of densities of 4-10km diameter craters on the smooth plains are roughly equivalent on the moon and Mars. On the moon, radiometric dating of samples returned by the Apollo missions revealed that the lunar highland-plains dichotomy in crater density resulted from a rapid fall-off in the rate of impacts, rather than from a discontinuity in the ages of the two surfaces. Soderblom et al. (1974) inferred that the highland-plains dichotomy on Mars was due to a simultaneous solar system-wide dropoff in the impact crater production rate.

Soderblom et al. (1974) also proposed that 4-10km was an appropriate range of crater diameter for the investigation of non-eolian resurfacing processes on Mars. They demonstrated that craters smaller than 4km were obscured by debris mantles, probably of eolian origin, and argued that craters larger than 10km would persist for long periods of time independent of resurfacing process, such as lava extrusion or fluvial activity. While crater retention time probably varies planetwide, a large data base of crater statistics has been compiled in the 4-10km size range for use in intercomparison of various areas. The model proposed by Soderblom et al. (1974) for density of 4-10km impact craters as a function of age (Figure 21) is used here as a convenient way of assigning absolute ages, for reference purposes, to crater size-frequency distributions.

There are a number of technical difficulties in applying crater counting techniques. Among these are: (1) obtaining a large enough sample in a particular crater diameter size bin to insure statistical significance, (2) choosing crater diameters such that erosional or depositional modification of populations is portrayed, (3) specifying and identifying the crater morphology type under consideration, and (4) picking a convenient and consistent graphical format for the distribution.

Basic geological assumptions in utilizing the technique are also numerous. These include: (1) competition between geologically significant but areally restricted surface units and the need for a statistical significant sampling of craters, (2) assuming uniform lithology beneath surface under consideration and therefore, by implication, an areally uniform morphology response to the input of energy during the impact (i.e., given a quantum of impact energy, all craters will look the same), (3) assuming, if one is delineating craters by morphological class, that all class size ranges degrade similarly in time, (4) assuming random distribution of impacting objects, and (5) identification elimination from counts of endogenic craters (e.g., collapse pits, calderas).

Both cumulative and incremental plots on log-log axes are used in the literature to portray crater size-frequency distributions. Cumulative plots are useful in that the technique is well known and plots are easily constructed. Further, the integral of the size-frequency distribution function, $\int F(D)dD$, is better determined as every diameter than is the differential function, F(D) (Woronow, et al., 1978). The main drawback of using cumulative plots is obvious, namely that the integral of the distribution function propagates information toward lower diameters. Thus, the distribution function curve shape and amplitude depend on data from lower diameters.

The relative size-frequency plot (Woronow, et al., 1978) has a number of advantages. First, the frequency value at any diameter is independent of other data at higher diameters. Second, by plotting F(D) relative to a D^{-3} function, small variations in slope and density are accentuated as compared to steeply sloping unreferenced incremental plots. The main drawback is that relative incremental plots are somewhat more difficult to construct, and error bars are generally larger than in cumulative counts. The larger error bars, however, reflect real variability in the data, which is masked by log-log cumulative plots. Following the recommendations of the Crater Analysis Working Group (Woronow et al., 1978) crater size-frequency data are presented here in both the cumulative and relative incremental formats (see Appendix I). Figure 22 shows isochrons from Soderblom et al. (1974) data plotted in relative incremental format.

Size frequency distribution of impact craters on five valley networks

On the basis of Mariner 9 data, Pieri (1976, p. 48-49) observed that martian "small channels" exhibit a crater size-frequency distribution curve which is very similar to that of the cratered upland terrain. This conclusion was based on crater size-frequency distributions of about 60

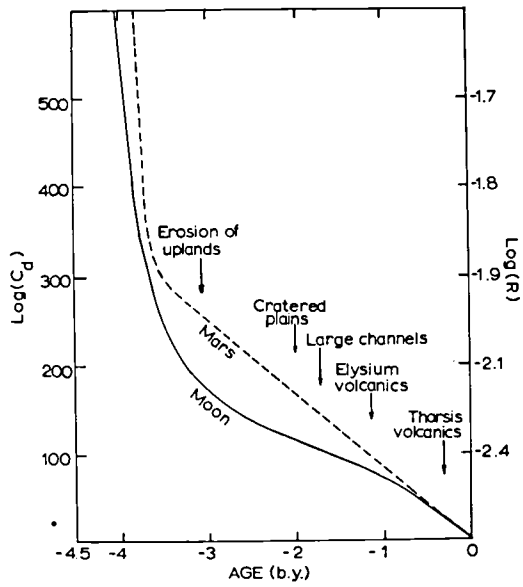

Figure 21.

Soderblom et al. (1974) model for impact-body flux history on Mars. Cd is the cumulative number of craters with diameters between 4 and 10km. R is the ratio of the incremental number of craters in a given diameter bin as defined in the text. Age is in billions of years before the present. The lunar curve is substantiated by radiometric ages, while the martian curve is theoretically derived.

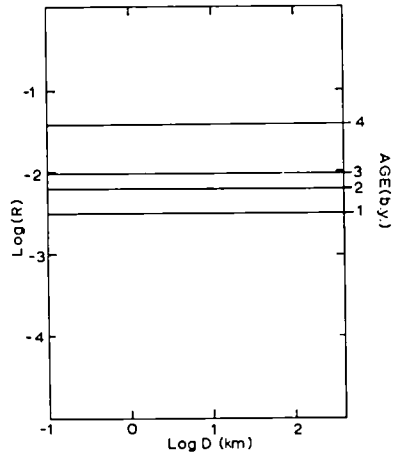

Figure 22.

Log(R) versus log D(km) with absolute ages. Model from Soderblom et al. (1974).

craters superimposed on valley interiors obtained from 4 narrow-angle Mariner 9 pictures (Figure 23).

New crater size-frequency data are presented here (Figures 24-33) for five valley networks in cratered terrain gathered using high resolution Viking images. Craters superimposed on valley interiors and walls were counted and their densities were compared to crater areal densities measured on surrounding terrain. A total of 702 craters were counted, 524 on surrounding terrain and 178 superimposed on valleys.

Valleys were selected from diverse areas of intercrater plains in heavily cratered upland terrain. Four of the networks are part of integrated systems as in the terminology of Chapter II, while the remaining one is a degraded stem valley which is part of a larger longitudinal system in Margaritifer Sinus. These valleys comprise a representative sample of networks found in heavily cratered terrain.

Crater size-frequency distributions plotted in relative incremental format are displayed for individual valleys and summary plots for all five systems taken together are shown in Figures 32 and 33.

Several observations can be made from these data.

First, all individual counts of craters superimposed on valleys show plateaus in log (R) values between -2.2 and -1.6, with the averaged plot displaying a prominent log (R) plateau at about -1.85. This corresponds to an absolute age of about 3.7 billion years before present, using the Soderblom flux model. This log (R) plateau means that craters between about 1.5 and 6.5km in diameter have remained intact (i.e. unburied and uneroded) in these valleys for about 3.7 billion years. Therefore, any erosional or depositional processes within the valley were incapable of obliterating craters in this size range since about that time.

Next, the curve representing the distribution of craters on surrounding terrain requires comment. The overall slope of the surrounding terrain distribution would obviously be less than -3 on an unreferenced log-log incremental plot, and therefore less than -2 on a log-log cumulative plot. If it is assumed that the original extra-planetary incremental impacting body distribution produced a -3 dependency of impact frequency on resulting crater diameter (Soderblom et al., 1974), then it is clear that the crater population visible in the cratered terrain surrounding the valleys has been significantly depleted in craters below 32k in diameter. This is common in heavily cratered terrains on Mars (Masursky et al., 1977; Malin, 1976; Woronow, 1975; Chapman and Jones, 1977). The gradual fall off in the slope of the curve for surrounding terrain, visible in Figures 32 and 33, is probably due to progressive depletion of visible craters over time due to erosion and deposition.

Four slope inflections are observed by eye along this curve, and can be seen clearly in both Figures 32 and 33. The first inflection occurs at log

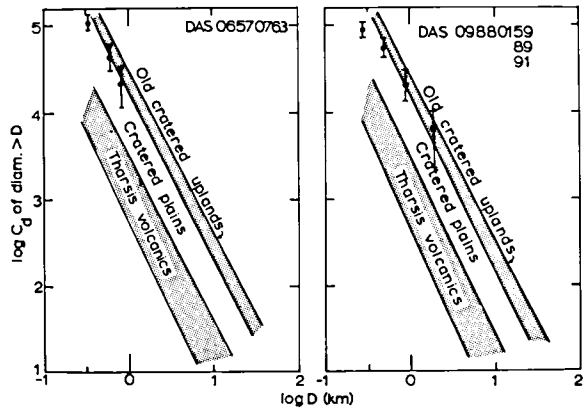

Figure 23.

Cumulative crater distribution from Mariner 9 B-frames. Cumulative crater distribution for 62 craters on two martian valleys in heavily cratered terrain. These counts were made on the 4 Mariner 9 B-frames indicated and are included here for the sake of completeness.

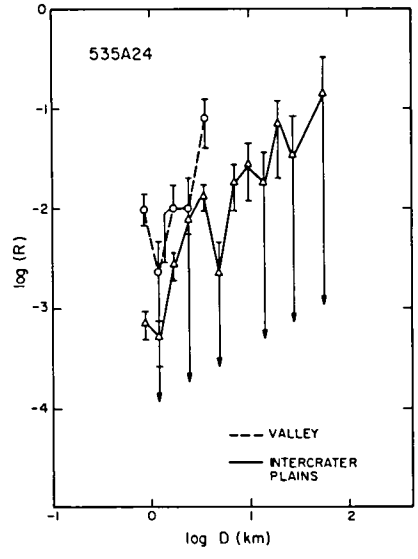

Figure 24.

Referenced incremental crater size-frequency distribution for valley in Figure 25. Data points with extended arrows indicate only one crater per diameter bin.

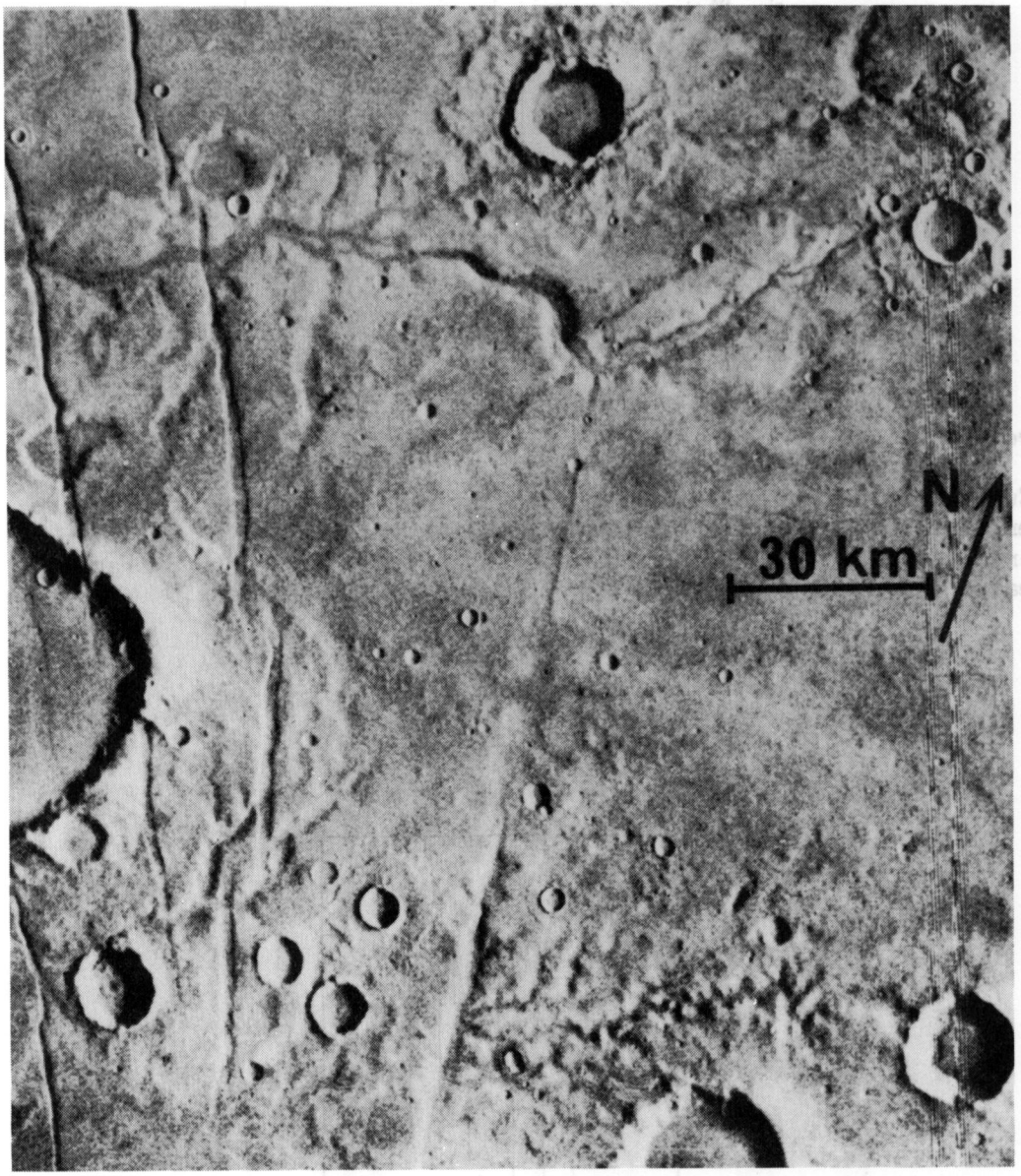

Figure 25.

Valley expressed in remnant of heavily cratered terrain in Thaumasia. Valleys here have been inundated by smooth material, superimposed by impact craters with extensive ejecta blankets and cut by transverse graben. Sun elevation angle is 23°, illumination is from the right and viewing angle is 10.2°.

Picture center: latitude -46°, longitude 78°
Resolution: 300 meters
Viking Orbiter Image: 535A24

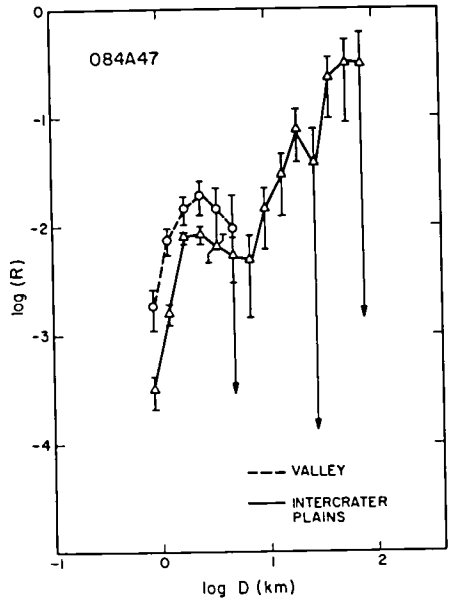

Figure 26.

Referenced incremental crater size-frequency distribution for valley system in Figure 7.

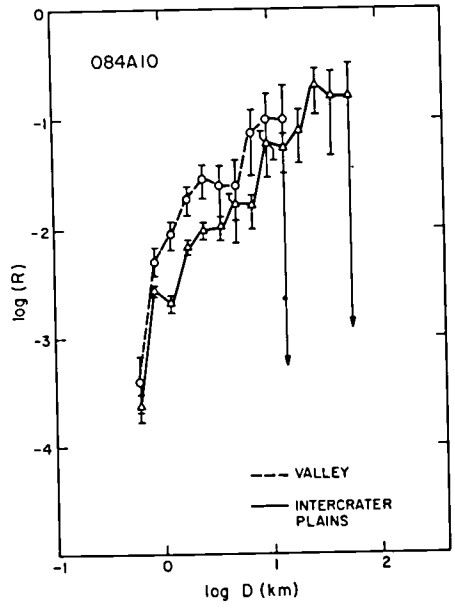

Figure 27.

Referenced incremental crater size-frequency distribution for valley system in Figure 28.

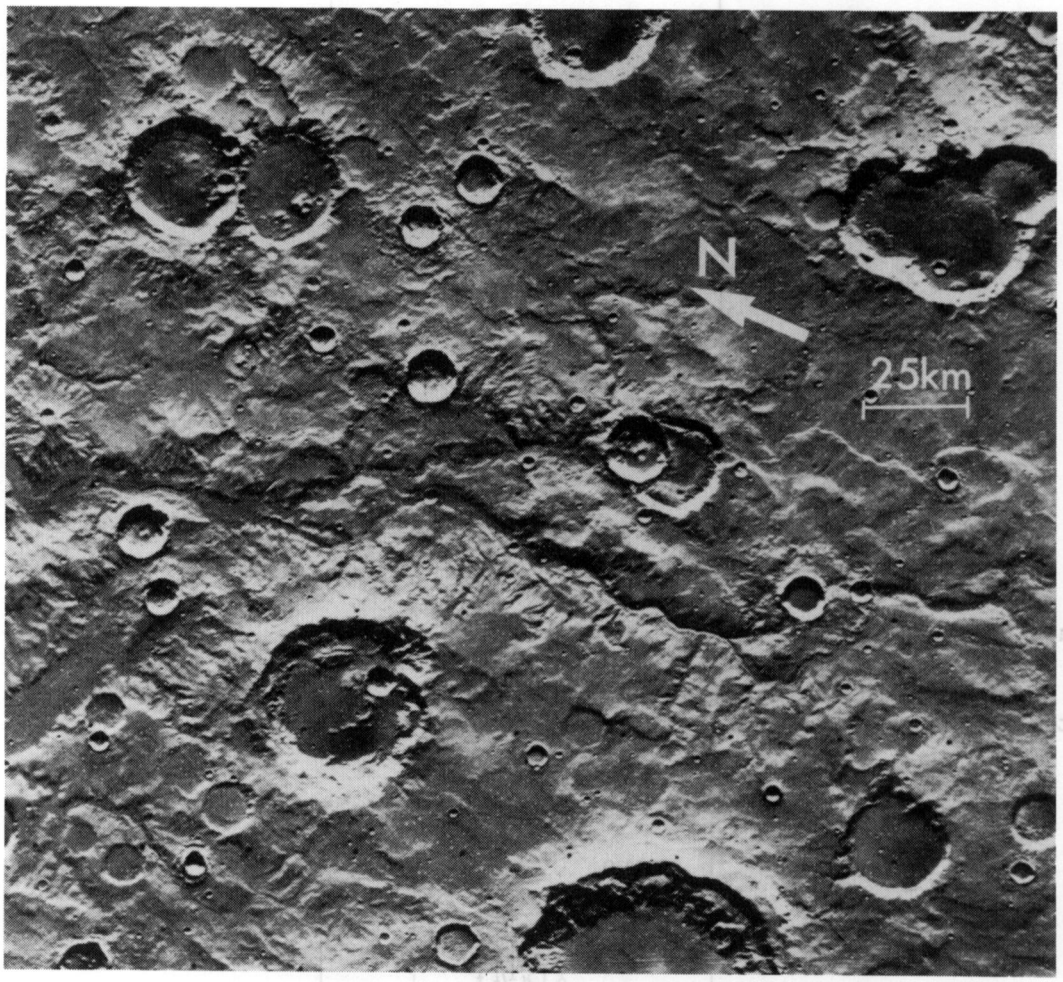

Figure 28.

Section of longitudinal valley system and surrounding terrain for data shown in Figure 27. This is a section of the valley shown in Figure 11. Sun elevation is 25°, illumination is from the top of the picture, and viewing angle is 6°.

Picture center: latitude -30.4°, longitude 13.7°
Resolution: 460 meters
Viking Orbiter Image: 084A10

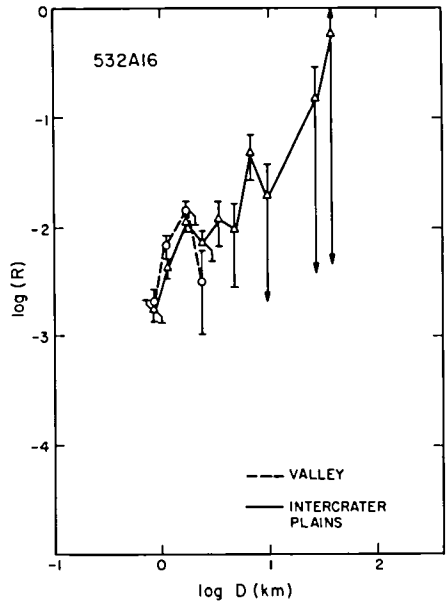

Figure 29.

Referenced incremental crater size-frequency distribution for valley system in Figure 8.

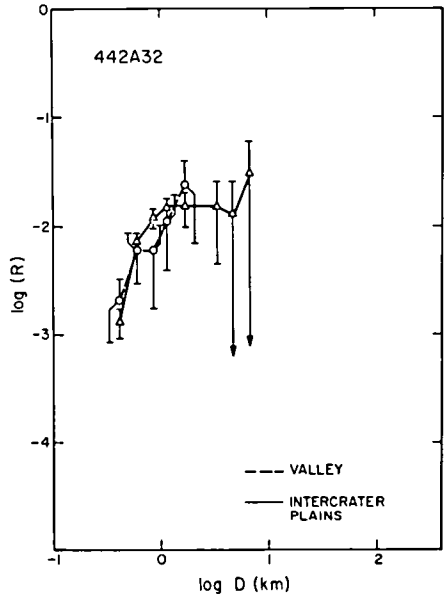

Figure 30.

Referenced incremental crater size-frequency distribution for valley system in Figure 31.

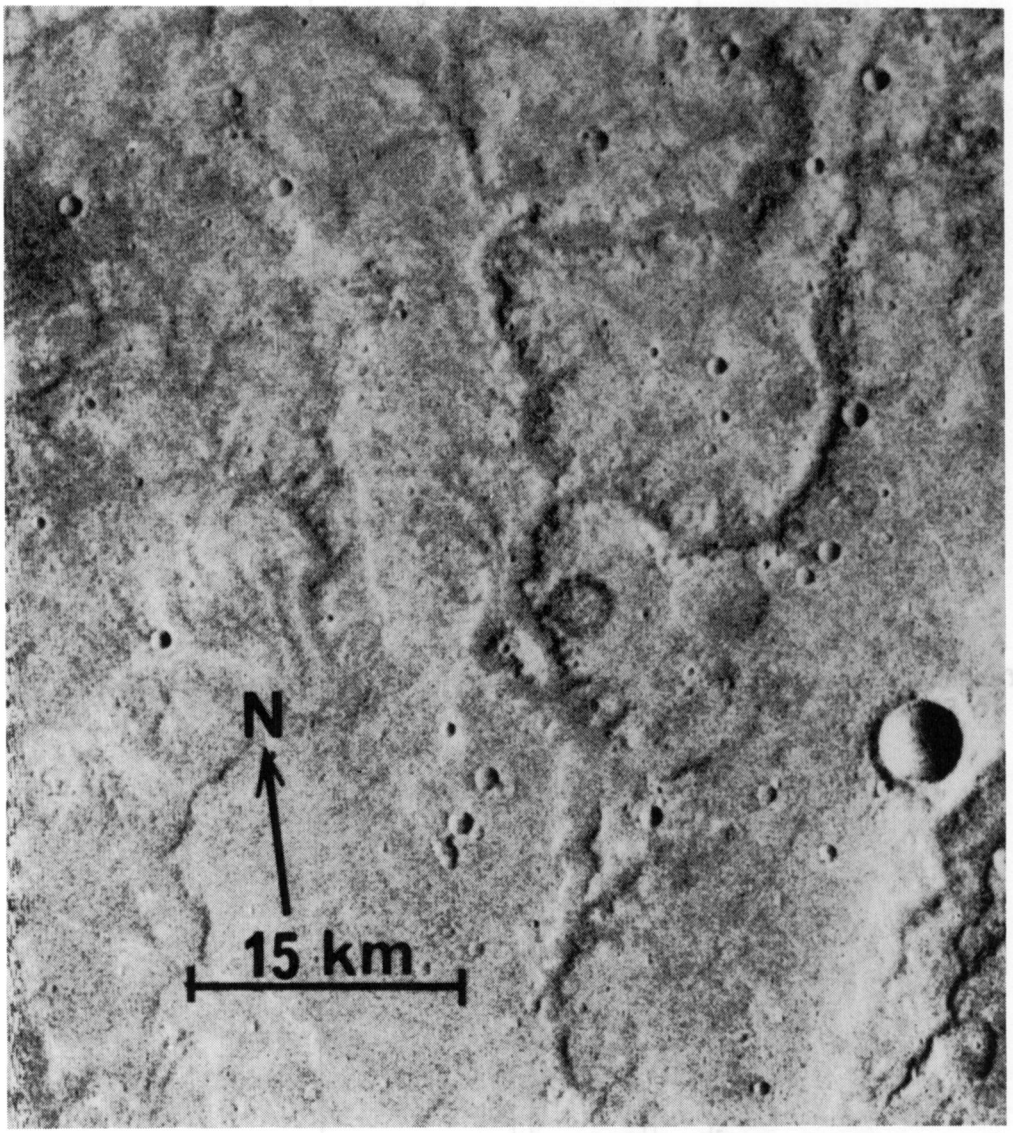

Figure 31.

Valley system for data in Figure 30. This is an eroded valley in Iapygia. Crater densities appear equal on both valley interior and surrounding terrain. There is no indication of more recent burial by smooth material in this immediate area. Sun elevation is 33°, illumination is from the right and the viewing angle is 11°.

Picture center: latitude 21.8°, longitude 272.2°
Resolution: 125 meters
Viking Orbiter Image: 442A32

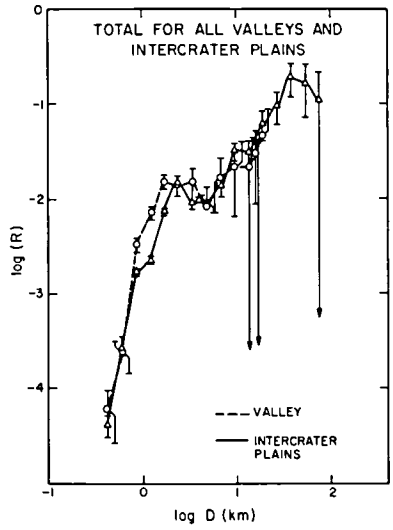

Figure 32.

Referenced incremental crater distribution for all craters superimposed on valleys and on surrounding terrain. These data include a total of 702 craters.

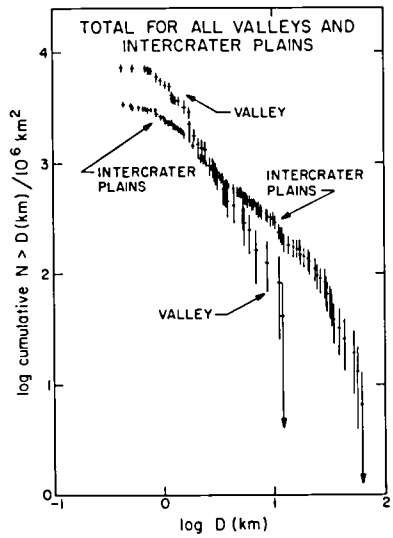

Figure 33.

Cumulative distribution of all craters on valleys and surrounding terrain. Cumulative number of craters per million km^2 greater than a given diameter versus diameter. This is the same data set used for Figure 32 plotted in cumulative format.

(R) equals -0.72, where curves turn down at the 32 to 45.25km diameter range. Log (R) = -0.72 probably represents the original size-frequency distribution present in this size range at the time of formation of the highland terrain. The lower log (R) values in the 45.25km to 90.51km range are the result of the count area (152,936km^2) being too small (by over 50%) to have enough craters at larger sizes to yield a log (R) value of -0.72 for an integral number of craters. For log (R) equal to -0.72, this density decrease becomes pronounced when individual craters take up more than about 4% of the area over which the count is done.

The second inflection point occurs at log (R) = -1.5 for craters between 8 and 16km in diameter. This plateau includes about 5% of all the craters counted on terrain adjacent to valley systems. Log (R) = 1.5 corresponds to 3.9 b.y. before present using the Soderblom model. The plateau here indicates that craters below the lower plateau diameter threshold, 8km have been depleted, but for craters between 8 and 16km the size frequency distribution recorded 3.9 billion years ago has been preserved.

A major plateau occurs at about log (R) = -2.05. This plateau also shows up in counts of all fresh bowl-shaped craters and craters with intact ejecta in these same areas. It corresponds to an absolute age of about 2.9 billion years and shows that a D^{-3} crater population has been preserved for craters between 1.4 and 5.66km in diameter since that time. Finally, the decrease in log (R) below about 1km is primarily the result of loss of resolution in some of the pictures and represents craters 0.5mm and smaller in actual size on Viking pictures.

Discussion and conclusions

The peak in log (R) surrounding terrain at 40km in diameter shows that craters surviving from the early intense bombardment phase have been counted. Erosion and deposition has since depleted the surface of all small diameter craters. That volcanic extrusion is an effective agent for crater obliteration has been amply demonstrated on earth (e.g. Hawaii) and in recent Voyager I pictures of the Gallilean satellite, Io, where no recognizable impact craters can be seen and currently active volcanoes have been detected. The retention of a plateau at 3.9 billion years may indicate a resurfacing of intercrater plains and complete obliteration of all craters smaller than about 13km in diameter at that time, or may indicate a cessation of erosion processes. One case is indistinguishable from the other on the basis of crater counts alone.

Crater distribution on valley walls and floors is statistically indistinguishable from the surrounding terrain counts for craters between 4.8km and 19km in diameter. Although the valley crater distribution appears to be climbing toward higher log (R) values in this range, this trend is not statistically relevant for craters on valley networks because of the large error bars. The last three points on the valley curve represent only 4 craters. It is therefore impossible to say whether the craters on valleys at diameters between 8 and 23km are slightly older than those between 1.5

and 6.5km in diameter. It is permissible to conclude only that obliterative activity ceased removing craters larger than about a kilometer and a half in diameter within valleys about 3.7 billion years ago. Further, craters larger than about 3km in diameter are substantially the same age in both the valleys and on the surrounding terrain. Therefore, since valleys obviously cannot be older than the adjacent surfaces, all that can be said is that valley formation occurred too soon after the formation of the intercrater plains to be resolved by these counts, but has ceased by about 3.7 billion years.

For crater diameters between about 1.25km and about 3.5km, the log (R) values for craters on valleys and craters on adjacent terrain diverge. The distributions appear to imply that the surfaces adjacent to valleys have a lower crater density and therefore a lower exposure age than the valley interiors, which is unlikely, unless the craters on the valley floors are exhumed. Although this is possible (and probable for Hrad Vallis) it is unlikely for the valleys included here since these craters, without exception, show no evidence for exhumation such as dissected ejecta blankets or filled interiors. Many have intact ejecta blankets, and no pedestal craters are visible. Rather, intercrater plains show numerous examples of lava extrusion occurring after valley formation. Figure 34 shows ridged material burying several valleys. This is commonly observed. Therefore the lower crater densities on surrounding terrain results from the inclusion of younger, less-cratered intercrater plains into the areas adjacent to valleys over which the counts were made.

Valleys, therefore, in some areas of Mars are seen only where older terrain remains uncovered by more recently formed overlying intercrater plains. Of the five networks included in this study only two (Figures 29 and 30) do not display this relationship. In these two figures, valley interior and the adjacent terrain display comparable crater densities. These valleys are probably somewhat older than the other three networks shown. The valley in Figure 30 occurs in one of the oldest areas on Mars and has experienced little resurfacing since the formation of the valley networks. The valley itself appears more degraded and eroded than the other valleys shown, although degrees of degradation of valley walls is not necessarily an indication of relative age (Masursky et al., 1977). Margaritifer Sinus valleys appear less degraded and smooth or ridged intercrater plains are more prevalent. These observations are consistent with the earlier conclusion by the author (Pieri, 1976) based on Mariner 9 data, that the present global distribution of valley systems has been modified from an early distribution. Areas of lower albedo in heavily cratered terrain have a high area density of valley networks, valleys appear more degraded and smooth intercrater plains occur less frequently, such as in Meridiani Sinus, Sinus Sabaeus, Iapygia, and Hesperia. In regions such as Noachis which have a higher albedo and consist of mantled heavily cratered terrain (Scott and Carr, 1977; Potter, 1976), valley density is low in intercrater plains and there the old dissected cratered terrain has been buried by a higher albedo mantled probably of volcanic and eolian origin (Potter, 1976; Soderblom et al., 1974).

Figure 34.

Headward reaches of valley network obliterated by ridged intercrater plains. In this picture, the upper section of the longitudinal network shown in Figure 11 is transected by ridges and is obliterated by material forming intercrater plains. Transections are indicated by arrows.

Summarizing: (1) small valley systems are younger than the oldest heavily cratered terrain (by simple superposition), but are older than smooth intercrater plains, all northern plains, and interior mare-like plains (e.g., Hesperia Planum, Syria Planitia), (2) the existence of large impact craters 50km in diameter argue for any hypothetical epoch of rainfall to predate their formation, and (3) crater size-frequency distributions indicate a minimum exposure age for the valley systems surveyed of at least 3.5 billion years using the Soderblom flux model.

TABLE III

Crater size-frequency data for valley networks and surrounding terrain

1) Martian cratered highlands, terrain adjacent to valleys

Picture number	084A40	532A16	442A32	084A47	535A24	ALL
			Area (km^2)			
Diameter Bin (km)	5.21×10^4	1.39×10^4	4.40×10^4	5.38×10^4	2.87×10^4	1.53×10^4
0.35 - 0.50			12			12
0.50 - 0.71	11		31			42
0.71 - 1.00	62	10	25	3	2	102
1.00 - 1.41	18	9	16	11	3	57
1.41 - 2.00	36	15	8	46	8	113
2.00 - 2.83	25	8	0	23	13	69
2.83 - 4.00	14	5	2	9	8	38
4.00 - 5.66	13	2	0	4	1	20
5.66 - 8.00	4	5	1	2	4	16
8.00 - 11.31	12	1		3	3	19
11.31 - 16.00	5	0		3	1	9
16.00 - 22.63	4	0		4	1	9
22.63 - 32.00	5	1		1		7
32.00 - 45.25	2	2		3		7
45.25 - 64.00	1	0		1		1

TABLE III (CONTINUED)

2) Craters superimposed on valleys

Picture number	084A40	532A16	442A32	084A47	535A24	ALL
			Area (km^2)			
Diameter Bin (km)	5.21×10^4	1.39×10^4	4.40×10^4	5.38×10^4	2.87×10^4	1.53×10^5
0.35 - 0.50			3			3
0.50 - 0.71	2		4			6
0.71 - 1.00	13	9	2	6	8	38
1.00 - 1.41	12	16	2	13	1	44
1.41 - 2.00	12	16	2	12	2	44
2.00 - 2.83	9	2	0	8	1	20
2.83 - 4.00	4		0	3	4	11
4.00 - 5.66	2		1	1	0	4
5.66 - 8.00	3				0	3
8.00 - 11.31	2				0	2
11.31 - 16.00	1				0	1
16.00 - 22.63					1	1

CHAPTER IV: JUNCTION ANGLES IN DRAINAGE NETWORKS

Introduction

Downhill coalescent flow

One of the main pieces of quantitative data available for martian valley networks is their planimetric pattern. In contrast, topographic data are obtainable only at contour intervals of 1km (Christensen, 1976) good enough to determine regional slopes, but too coarse, for example, to allow the construction of detailed longitudinal profiles of valley networks. It therefore is logical to ask what the planimetric pattern of any drainage network, martian or terrestrial, can indicate about processes involved in forming that feature.

The most basic question is whether or not the network pattern implies erosion by downhill surface flow. A fluid flowing downhill will attempt to expend its potential energy as efficiently as possible and therefore will take the shortest downhill path. In the absence of interference, a coalescent network with acute angles of junction closing in the downhill direction results. All terrestrial river networks attempt to achieve this condition. Departures from it are perceived as anomalies (e.g. "barbed drainage") and are used to detect such conditions as tectonic reversal of slope and stream capture. Likewise, all martian valley systems except where they have been partially obliterated by impact, burial, or erosion, tend to coalesce down regional slopes (delineated at the 1km contour interval) and downhill fluid flow is therefore inferred.

Pattern character

Another basic question involves pattern character. What does the type of pattern (e.g. dendritic, parallel, digitate) say about how the eroding fluid is introduced into the network?

There are three ways in which a drainage network can be formed and enlarged. (Leopold et al. 1964, p. 429): (1) surface runoff, (2) subsurface seepage, and (3) headward erosion of scarps or headcuts. All three modes of network extension can occur as a result of the introduction of a fluid on a land surface by atmospheric precipitation.

Precipitation from the atmosphere is capable of providing a spatially uniform (though not necessarily temporally uniform) source of fluid, in the sense that all slopes exposed to the atmosphere have the potential to supply

fluid to a drainage network. A wide range of drainage network patterns is associated with this mode of fluid erosion on the earth, most notably dendritic. Other drainage patterns either will evolve toward a dendritic pattern (e.g., parallel), are the result of lithologic and structural controls preventing the formation of a dendritic pattern (e.g. rectilinear, angular, trellis), or are an assemblage of individual networks (e.g. the various radial patterns). Dendritic, meaning "treelike" or "arborescent", describes a drainage pattern characterized by irregular branching of tributaries in many directions usually joining the mainstream at acute angles (Easterbrook, 1969, p. 425). Trees branch the way they do in order to maximize the light-gathering efficiency of their leaves. Pulmonary blood vessels branch in a similar way to maximize the surface area available for gas exchange with blood. Both are three-dimensional patterns which achieve maximum efficiency at filling space. Likewise, the ideal dendritic pattern maximizes efficiency of transport by allowing water to flow down the most direct downhill path, draining all exposed slopes. This is consistent with the hypothesis of Leopold and Langbein (1962, p. 413) that the most probable state for a river system is one which minimizes total work and maximizes entropy. The discovery of martian valley networks with well developed dendritic patterns would imply a spatially uniform distribution of fluid on all available slopes and thus would support a hypothesis of valley formation by rainfall runoff.

Studies of mature dendritic networks have shown that longitudinal slopes decrease exponentially down-stream (Hack, 1957; Schumm, 1978). Similar longitudinal profiles for martian valley networks, if they could be measured, could imply in the extreme, that martian valley flows had achieved the sort of steady-state equilibrium of hydraulic variables implied by the smoothly exponentially decreasing longitudinal profiles of mature terrestrial streams.

Martian valley systems have often been referred to as being "dendritic" (Milton, 1973; Sharp and Malin, 1975; Malin, 1976; Sagan et al., 1973; Pieri, 1976; Chapman and Jones, 1978). Often the term dendritic is coupled with speculation about erosion of valley networks by rainfall runoff and of necessary climatic change. As has been already pointed out in Chapter II on the basis of work presented here, martian networks have little qualitative resemblance to terrestrial dendritic drainage networks. A more quantitative comparison between well-developed terrestrial drainage networks and martian valley systems is desirable. In particular, it is useful, since martian topography is only poorly known, to understand what the structure of patterns can imply about rate of decrease of slope down-network. The systematics of tributary junction angles within a network, though previously little studied, are helpful in this context.

Tributary junction angles are related to topography, erosional competence, and stream history. An analysis of junction angles can better characterize a network and provide insight into the mechanics of the valley forming process and the erosional history of watersheds.

There are two particularly important aspects to the study of network junction angles. One is the relation of the tributary junction angle to the ratio of the tributary and trunk gradients.[1] Horton (1932) quantitatively considered the relation between stream junction angles and his formulation is discussed in the following section. The Horton relationship is important because it predicts an entrance angle of minimum work. The second aspect is the overall relationship of tributary junction angle to position of the junction in the network. New work presented here is an extension and physical rationalization of previous empirical studies. It demonstrates that there exists a well-defined, scale-invariant, distribution of tributary junction angles, indicative of the degree to which a drainage system has achieved an exponentially decreasing longitudinal profile. The progressive increase of junction angle down-network is demonstrated for selected dendritic terrestrial drainage networks with main-stream lengths that vary over two orders of magnitude.

Application to martian valleys

The systematics of tributary junction angles for several martian valley networks have been analyzed. In the analysis it is assumed that martian valleys can be treated similarly to terrestrial valley networks in the manner of Lubowe (1964). Were a pluvial period to have existed on Mars, the form of tributary junction angle systematics should be identical to that exhibited by a terrestrial river formed on martian topography in the absence of other erosional processes. Tributary entrance angles are dependent only on relative slopes and are independent on the magnitude of gravitational force. Observed martian tributary junction angles however, are significantly lower than those measured for terrestrial valley networks. Further, martian data are more variable by a factor of three than data from terrestrial networks. The weak dependence of junction angles on position within the network and the high variability of junction angles suggest that martian valley networks are immature. Such networks could develop as a result of erosion by runoff episodes of short duration on undirectional slopes, or by processes not involving runoff, such as basal sapping (Leopold et al., 1964, p. 429). The observed rarity of inter-valley divides, the necessarily restricted source regions implied by the consistently observed parallel drainage, and the characteristic amphitheater terminations of the smallest tributaries, all militate strongly against rainfall as the predominant source of the eroding fluid for the vast majority of martian valley systems.

---

[1]The "tributary junction angle" is defined here as in Figure 35. A "tributary" is defined here as a stream which contributes its lesser discharge to a "trunk" stream of greater discharge at the junction of the two.

Previous Work

The Horton Law and its verification

Stream junction angles were first studied quantitatively by Horton (1932, 1945). He proposed for a tributary intersecting a main stream:

$$\cos Z = \frac{S_g}{S_c} \quad \text{(Horton, 1932)} \qquad (1)$$

where Z is the angle projected onto a horizontal plane between a straight mainstream and the joining tributary, S_g is the gradient (slope tangent) of the mainstream and S_c is the gradient of the joining tributary (Figure 35). Horton's law is strictly geometrical and is precisely true only for the situation depicted in Figure 35. Field studies (Schumm, 1956; Lubowe, 1964; Howard, 1971) have demonstrated the empirical validity of the Horton law: the junction angle between two streams, in the absence of geologic controls, is related to the relative gradients of the intersecting streams.

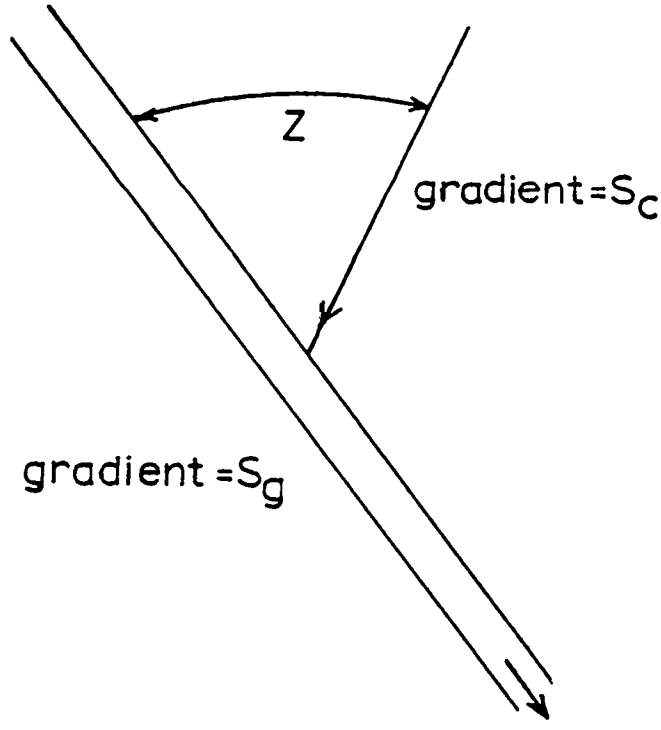

Figure 35.

Horton tributary and mainstream diagram. Diagram of tributary and mainstream intersection as defined by Horton (1945).

The Howard modification

Howard (1971) showed that the concept of tributary and mainstream was inaccurate in the context of junction angle analysis. Both the upstream segment of the "mainstream" and upstream joining "tributary" usually make an angle larger than zero with the down-stream segment of below the junction (Figure 36).

The Howard modification of the Horton cosine law (Howard, 1971) assumes that the simpler Horton Law is followed independently by both incoming arms at a stream junction, resulting in two equations analogous to equation (1):

$$\cos \theta_1 = \frac{S_3}{S_1} \qquad (2)$$

$$\cos \theta_2 = \frac{S_3}{S_2} \qquad (3)$$

where the variables are defined as in Figure 36. Howard demonstrates that the predictive ability of this modification is statistically superior to that of the original Horton formula, using badland rill systems as an example. The Howard Law predicts junction angles more realistically than the Horton Law because it takes into account the possibility of intersecting streams of nearly equal discharge.

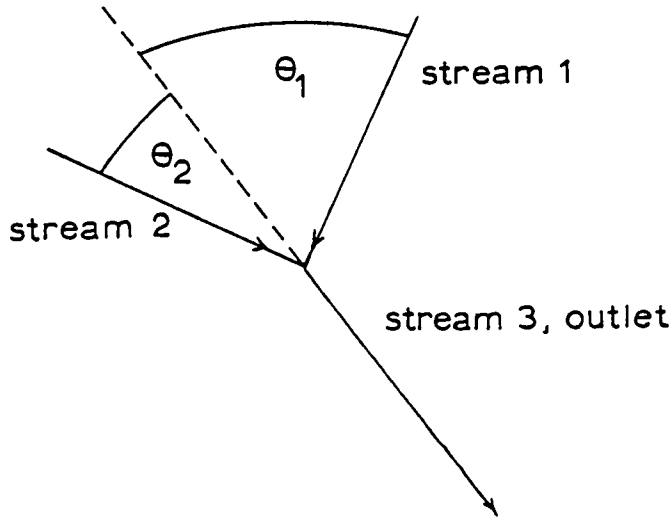

Figure 36.

Howard diagram. Diagram of Howard's modification of Horton's original geometry (Howard, 1971).

A Model for Junction Angle Systematics for Drainage Basins

Rationale

Knowledge of topography enables the delineation of divides and the longitudinal profiles of streams. The coarse resolution of martian topographic data is inappropriate for the study of basin divides and longitudinal profiles. Hence, the main quantitative data available for martian valley systems are their planimetric network patterns.

Topographic maps of Mars currently available show that all major valley networks coalesce downhill on regional slopes (Chapter II). This important piece of information alone suggests that the martian networks are the result of erosion by downhill flow. Without detailed topographic data, however, it is impossible to discern whether surface drainage basins and divides exist for individual networks. It seems logical, however that if the Horton style laws for junctions are correct, information about the relative slopes of intersecting tributaries can be extracted from the network patterns. From this, two important questions can be investigated: (1) Do the martian valley systems exhibit a decrease in slope down-network, and (2) If so what is the rate of decrease? Exponentially decreasing relative slope would imply an equilibrium between the forces resisting erosion within the channel and the force available to do the work of erosion. Lower slopes are intuitively expected downstream (Hack, 1957, p. 90). Lubowe made a systematic study of junction angles as a function of Strahler order for dendritic drainage networks. Stream junction angles in her study areas showed a statistically significant increase as the order of the receiving stream increased with respect to the tributary and a good correspondence was observed between measured junction angles and the angles predicted by the Horton equation. (Lobowe, 1964, p. 339). The main result of this empirical study was that a systematic organization of junction angles in mature dendritic networks was observed. The Lubowe study is empirical, however, a quantitative model for the distribution of network junction angles would give a physical basis for understanding the empirical results.

The model

At this point, a digression is required for the definition of terms that will be frequently used in the discussion following. An idealized stream network is composed of links. Links are of two kinds: exterior and interior. An exterior link only joins another link at its downstream end. Its upstream end is defined as a source. Interior links connect junctions. There is only one outlet link for a network. It connects with a junction on its upstream side only. Exterior links are assigned a magnitude (m) of 1. Link magnitudes add arithmetically at junctions. For example, if a link of magnitude m_1 joins a link of magnitude m_2, resulting outlet link for the junction will have magnitude $m_1 + m_2$. Networks of equal magnitude have equal numbers of links, junctions, sources, and first order Strahler streams and are therefore of comparable topological complexity (Shreve, 1967).

Figure 37 compares methods of stream ordering by Strahler and Shreve. Notice that for the case shown, a network of Strahler order 3 has a Shreve magnitude of 5. An important physical approximation that can be made when using Shreve magnitude is that each link contributes a unit magnitude of discharge, if one assumes uniform distribution of rain over the entire network. Alternatively, one could assume that only source links (exterior links) contribute water. Then the ratio of discharges between two networks would be equal to the ratio of their outlet link magnitudes.

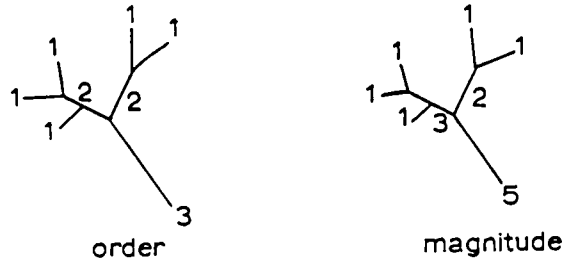

Figure 37.

Network order versus network magnitude.

Although Lubowe used Strahler stream orders to delineate between streams of different sizes within the network the concept of magnitude (m) in the form introduced by Shreve (1976) is more appropriate for use here for several reasons: (1) Strahler orders in a stream network change only when two streams of equal order join, but physical properties (e.g. discharge, width) change at all junctions, (2) Strahler's rule for combining streams is not associative; symbolically order 2+ (order 1 + order 1) = order 3, but (order 2 + order 1) + order 1 = order 2 (Smart, 1972, p. 308), and (3) it is implicitly assumed that unit magnitude is equivalent to unit discharge within a network. Although not always necessarily true this assumption is particularly convenient, and is on the average valid.

Several convenient theorems arise from ordering networks by magnitude:

(1) the magnitude (M) of the network outlet is equal to the total number of source links,

(2) the total number of links in a network is equal to 2M-1;

(3) the total number of junctions in a network is equal to M-1. What follows in the next few paragraphs is a derivation of slope as a function of link magnitude adapted from Flint (1974).

Shreve has demonstrated that area of a drainage basin is related to the magnitude of the drainage network by

$$A = kl^2 (2m-1) \qquad (4)$$

where A is the total area, l is the average link length, and k is dimensionless coefficient equal to one.[1]

A power law relation between discharge and area drained has long been established empirically (Leopold and Miller, 1956; p. 23; Wolman, 1955, p. 34; Flint, 1974, p. 969):

$$Q = aA^x \tag{5}$$

where a is proportional to runoff from a unit area of drainage basin, A is the total area, Q is the total discharge, and x is a coefficient equal to 1.0 for mean annual discharge and between 0.70 and 0.75 for bankfull discharges (Flint, 1974, p. 969; Leopold et al., 1964, p. 251). Substituting for A in (4) yields

$$Q = a\left[kl^2(2m-1)\right]^x \quad \text{(Flint, 1974, p. 970)} \tag{6}$$

The power law relation between slope and discharge has also been well-established (Leopold and Miller, 1956; Wolman, 1955):

$$S = tQ^z \tag{7}$$

where S is the stream gradient, and z is a negative exponent. The coefficient t is the stream gradient for unit discharge (Flint, 1974, p. 969). Substituting (6) into (7) yields

$$S = t\left[a\left[kl^2\,(2m-1)\right]^x\right]^z \quad \text{(Flint, 1974, p. 969)} \tag{8}$$

As Flint points out, this relationship provides a connection between "topologic or planar parameters of the fluvial system with its vertical dimension" (Flint, 1974, p. 970). Flint tested this relation for 11 basins of magnitude 52 to 108 on the Appalachian Plateau. All were well dissected and dendritic in pattern. His linear regression coefficients for the logarithm of link slope versus logarithm of basin magnitude are all higher than -0.80, with the linear regression exponent xz ranging from -0.37 to -0.837. Other theoretical and empirical studies imply an average value of -0.6 for z, with which, if x is assumed to be equal to 1.0, his values seem to be consistent. Combining constants, a simpler expression

$$S = k'(2m-1)^{\alpha} \tag{9}$$

can be written.

A formula relating junction angle to link magnitude (and therefore to position within the network) can be derived using the modified Horton cosine law:

---

[1]The constant k is the ratio of the area drained by an individual link to the link length squared. That ratio was reported by Shreve (1967, p. 185) to be about unity.

$$\cos \theta_m = \frac{S_{m+m'}}{S_m} \tag{10}$$

$$\cos \theta_m = \frac{k_{m+m'} [2(m+m') - 1]^{\alpha}}{k_m [2m-1]^{\alpha}} \tag{11}$$

Here θ_m is the tributary junction angle of the tributary of magnitude m, relative to the junction outlet direction, m and m' are the Shreve magnitudes of incoming tributaries to the junction, and k_m and $k_{m'}$ are the combined constants from (8) for their respective tributaries. $S_{m+m'}$ is the gradient of the outlet and S_m is the gradient of the tributary with magnitude m. The analogous expression for $\theta_{m'}$, is

$$\cos \theta_{m'} = \frac{k_{m+m'} [2(m+m')-1]^{\alpha}}{k_{m'} [2m'-1]^{\alpha}} \tag{12}$$

Assuming that all constants in m and m' are equal from one side of the junction to the other, (11) and (12) reduce to:

$$\cos \theta_m = \left(1+ \frac{m'}{m-1/2}\right)^{\alpha} \tag{13}$$

and

$$\cos \theta_{m'} = \left(1+ \frac{m}{m'-1/2}\right)^{\alpha} \tag{14}$$

These basic equations relate junction angle to link magnitude for uniform drainage density, and are derived from simple, physically and geometrically reasonable assumptions. For $m<m'$ as $(m-m')$ increases, θ_m should tend toward 90° and $\theta_{m'}$ should tend toward zero. This is equivalent to the statement that first magnitude streams should enter major trunk streams at nearly right angles. It also provides a physical justification for Lubowe's empirical observations. A graphical representation of these equations is shown in Figure 38.

Application to Real Networks

Introduction - technique

Junction angles were measured for 17 terrestrial and 5 martian networks. Networks range in outlet magnitude (M) from 20 to 200. Each network has by definition M-1 junctions and both right and left junction angles (Figure 36) were measured, therefore 2 (M-1) angles were measured for each network.

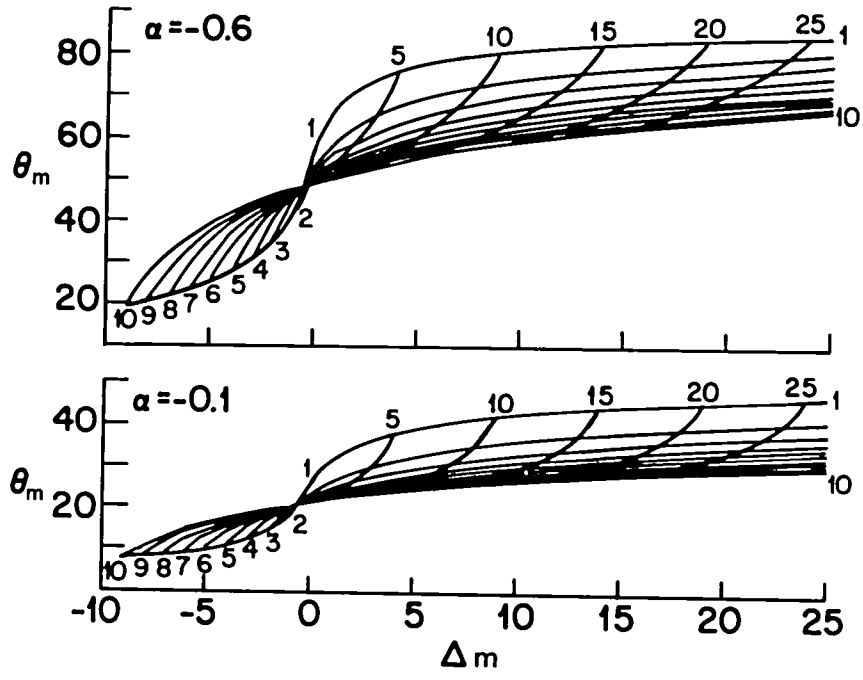

Figure 38.

Model for the junction angles for magnitudes from 1 to 25. Junction angles of tributaries and recipient streams are calculated for two values of alpha. The ordinate represents the angle of intersection as defined in Figure 36. The abscissa is the difference in link magnitude between the two intersecting streams (e.g. a magnitude 1 link intersecting a magnitude 5 link yields a $\Delta m = 4$). For positive Δm each line with convex curvature upward represents the junction angles for a given magnitude m link intersecting progressively higher magnitude recipient links (i.e. Δm increases). The value of m for each line is listed in a column at the right of the curves. For negative Δm, θ_m is plotted for progressively decreasing m' (recipient link magnitude). Positive θ_m values in the positive field of Δm are the angles that smaller tributaries make with larger recipients, angles which are increasing asymptotically to 90°. θ_m values in the negative field of Δm are the angles that larger "tributaries" (m = 2 through m = 10) make with progressively smaller "recipients", angles which are decreasing to zero, since the very small "recipients" (e.g. $\Delta m = -9$) have progressively less effect on the very large "tributary". The numbers which follow the upper convex curve across the field refer to constant recipient magnitude. For instance, for a tributary of magnitude on (m = 1) and $\Delta m = 4$, the recipient magnitude (m') must be equal to 5, as can be seen on the upper curve. For a tributary of magnitude two (m = 2), $\Delta m = 3$ for a recipient of magnitude 5. Hence the concave upward lines are lines of constant recipient magnitude, corresponding to the numbers across the top of the curve. Curves for two values of alpha, -0.1 and -0.6, are shown.

Terrestrial systems were measured from a variety of sources at a variety of scales. Satellite (LANDSAT) pictures, high and low altitude photography and topographic maps were used. Martian systems were mapped from Viking Orbiter pictures. Maps of the valley center were drawn and the junction angles measured.

Links are often approximated by straight connecting lines between junctions. However, for real measurements, gross errors would be introduced by ignoring curvature in valley segments. Lubowe notes (p. 331) that using the average flow directions of the entire stream segment shows consistently lower mean values and greater dispersion. She adopts the following method for junction angle measurement: "the junction angle is defined as the angle projected to the horizontal, between average flow directions, determined by the end of stream segments extending from the junction point to an upstream point at a distance equal to 0.2 the average length of second-order streams". Although she adopted this method for its simplicity and standardization, this technique also introduces scatter and a systematically lower junction angle. The entrance angle of a tributary into a trunk stream is determined by the tributary gradient adjacent to the trunk, because any differential in the rate of downcutting in the trunk is felt by the tributary immediately only at the junction. In measuring a junction angle, the direction of the smallest discernable link segment[1] upstream from the junction was used. This is equivalent to measuring the link direction one-quarter to one-third of a link length away from the junction. This procedure is designed to measure the section of the link which is most likely to be in compliance with the cosine relationship.

Terrestrial network measurements

A number of terrestrial networks were analyzed to check the validity of the model equations. Junction angles were measured for a range of dendritic networks, (See Table IV), varying in relief, substrate character, and in basin length. The following observations were made: (1) a rapid increase of junction angle between low magnitude tributaries and higher magnitude recipient valleys was observed as one proceeds toward the network outlet (i.e. junction angle increases as the magnitude contrast of joining tributaries increases); (2) junction angles are usually greater than 50^{o} for low magnitude tributaries ($m \leq 3$) joining high magnitude recipient valleys ($m \geq 10$). Plots of junction angles for first magnitude tributaries joining higher magnitude valley links are shown in Figures 39-48. Model curves are consistent with the field data.

---

[1]Link segment is defined here as the smallest linear portion of the link. Obviously for a curved channel, such a definition defines a link segment to be infinitesimally small. Practically a limit is reached at the limit of measurement which is, in this case, about 1mm on a map or photograph.

TABLE IV

Dendritic networks analyzed for Junction Angle Data

Name	Location	Underlying Rocks	Relief	Basin length	Data Source
Moenkopi Wash	Black Mesa, Ariz.	Mesozoic Shales & Sandstones	Moderate	80km	1:250,000 USGS topo
Perth Amboy	Perth Amboy, N.J.	Landfill	Low	0.1km	1:240 Strahler & Coates, 1948
Bell Watersheds	San Gabriel Mountains, Calif.	Crystalline metamorphics	High	1km	1:4800 topo (Lubowe, 1964 map)
Monterey	Lexington Plain, Ken. (interior low plateau)	Horizontal shale & limestone	Low	2km	1:24,000 USGS topo (Lubowe, 1964 map)
Yellow-stone	Yellow-stone National Park, Wyo.	Crystalline metamorphics	High	50km	1:24,000 Mapped from LANDSAT
Colorado State	R.E.F. Colorado S.U.	Fill	Low	0.01km	Parker, 1977 map
Gillis Falls	South Branch Patapsco R. Carroll City, Md.	Wissahikon Schist (phyllite/ quartz)	Moderate	19.1km	Hack, 1957 1:9300 map
	Central Plains, Midwest U.S.		Low	200km	1:1,000,000 Mapped from LANDSAT

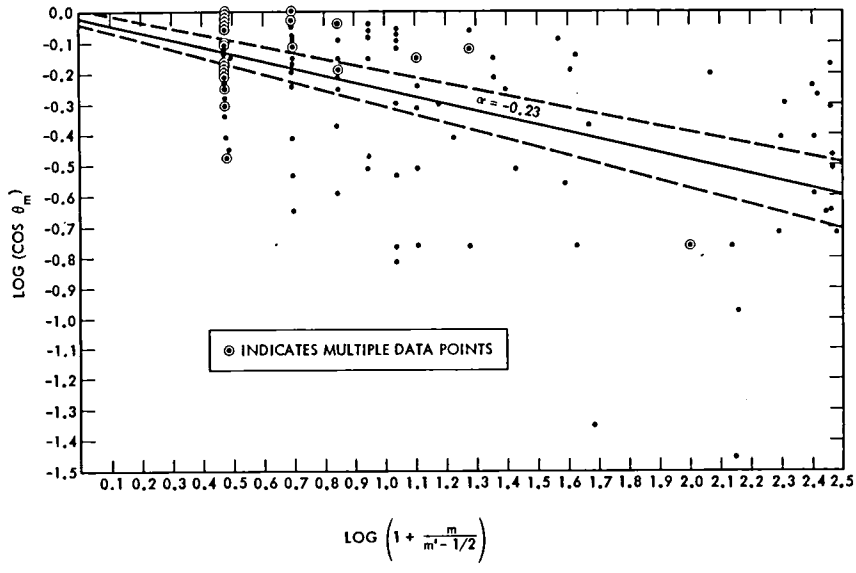

Figure 39a

Linearized parameters for Moenkopi Wash. Shown here is a plot of the indicated parameters for m = 1 and m' ranging from 1 to 150. The parameter α is the slope of the least squares line fitted to the scatter. The dotted lines represent a 1σ standard deviation in the slope of α (Table V).

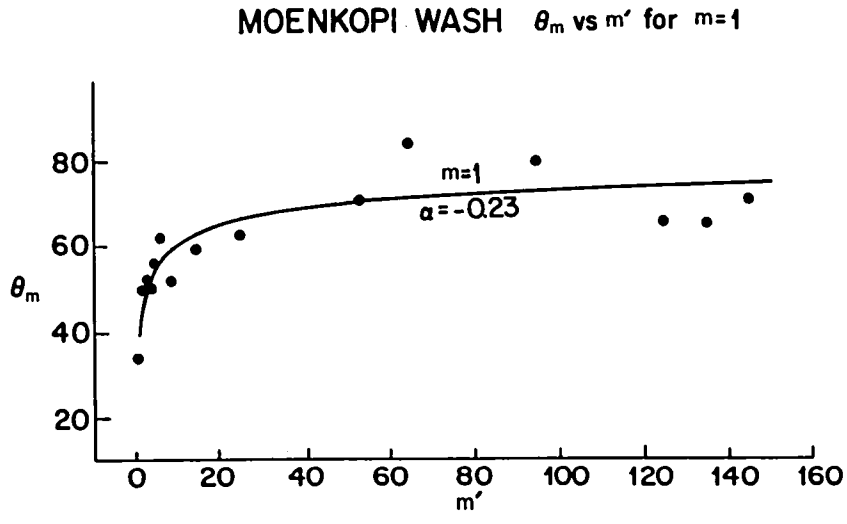

Figure 39b

Junction angle data from Moenkopi Wash, m = 1. Plot of θ_m versus m' from m = 1. Data from U.S.G.S. Marble Canyon, Arizona quadrangle, 1:250,000 map. Black circles in this and the remaining junction angle plots represent mean junction angles for a given recipient link magnitude

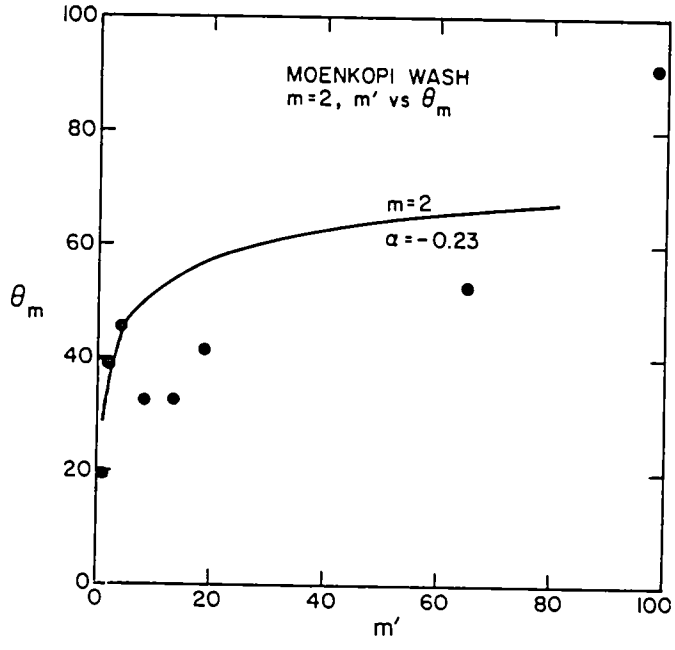

Figure 40.

Moenkopi Wash data, m = 2.

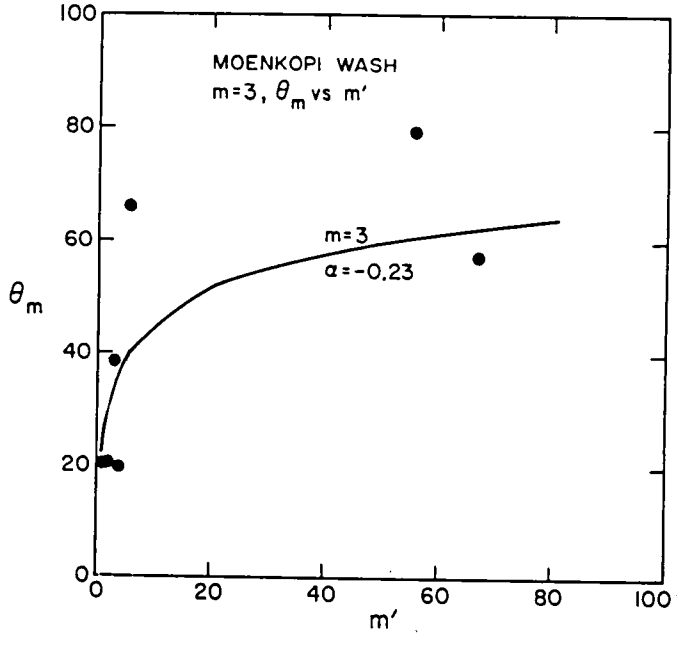

Figure 41.

Moenkopi Wash data, m = 3.

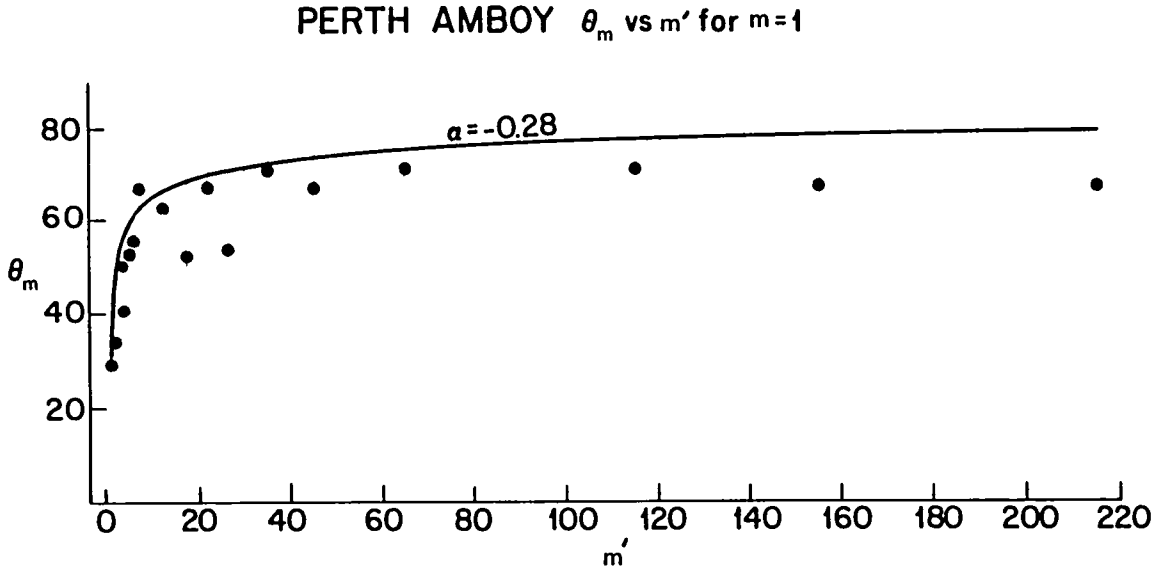

Figure 42.

Junction angle data for Perth Amboy m = 1. Data from map by Strahler and Coates, 1948, reproduced in Schumm (1958), at 1:240 scale.

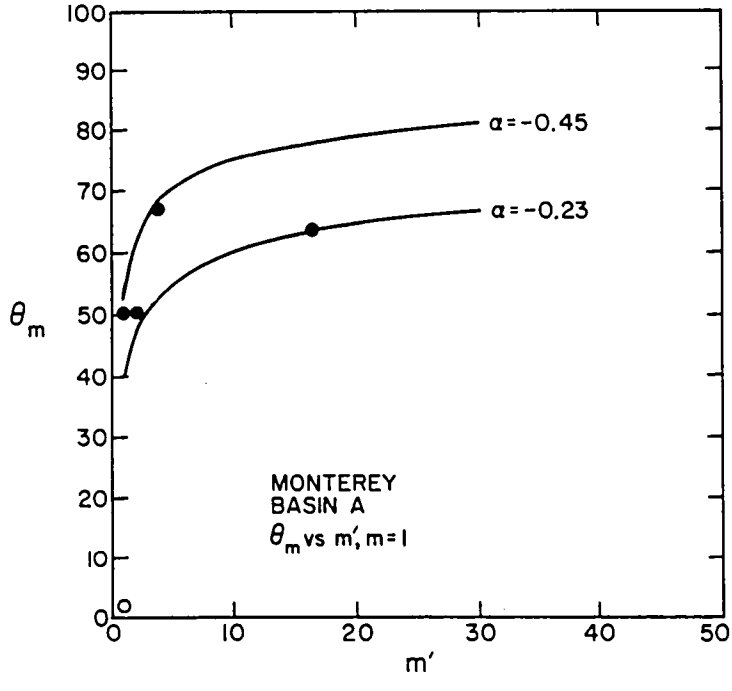

Figure 43.

Junction angle data for Monterey quadrange, m = 1. Data from Lubowe (1964). Map scale 1:28,800.

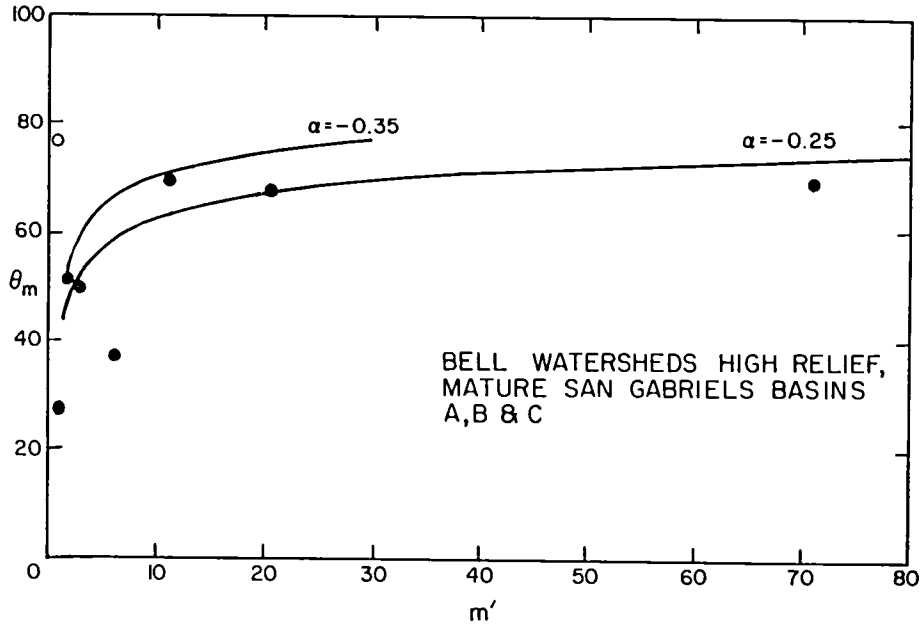

Figure 44a.

Junction angle data for Bell Canyon m = 1. Data from Lubowe (1964). Map scale 1:12,000.

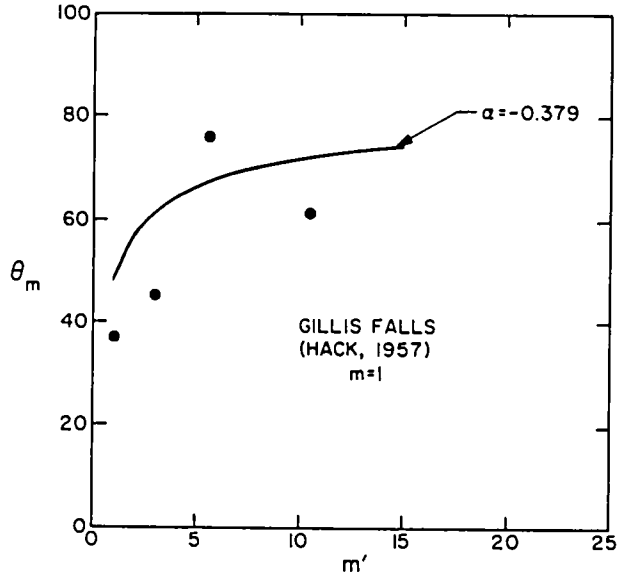

Figure 44b.

Junction angle data for Gillis Falls, m = 1. Data for the Gillis Falls, Maryland network (Hack, 1957).

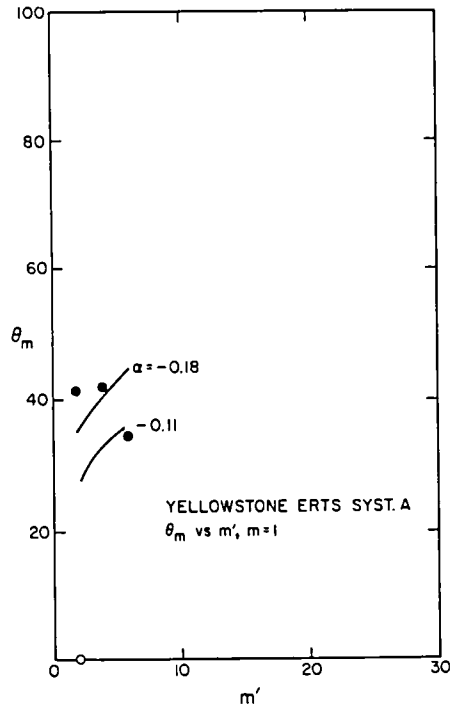

Figure 45.

Junction angle data for Yellowstone, network A, m = 1. Data for a drainage network (see Figure 46) in Yellowstone National Park observed on LANDSAT image 1123-17414. Map scale 1:1,000,000.

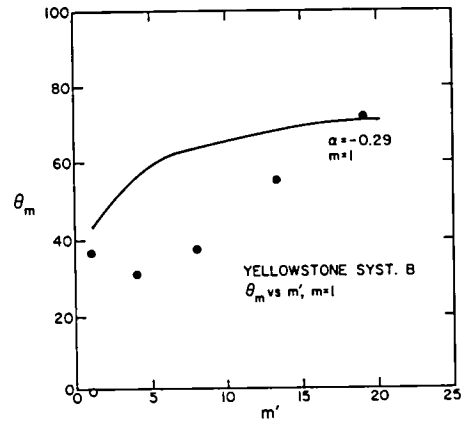

Figure 46.

Data for Yellowstone, network B, m = 1. Junction angle data for drainage network (see Figure 45) in Yellowstone National Park mapped from LANDSAT image 1123-17414. Map scale 1:1,000,000.

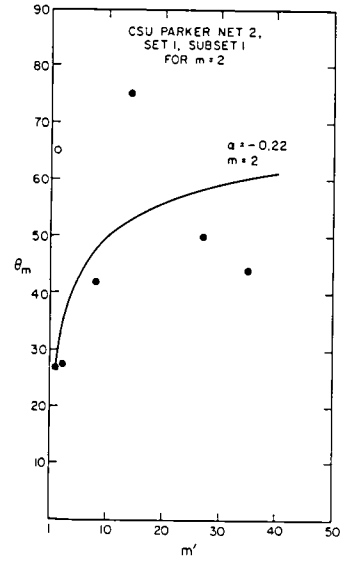

Figure 47.

Junction angle data for CSU network, m = 1. Data from drainage networks in the Colorado State University Rainfall Erosion Facility. The network was mapped at 1:120 scale. These dendritic networks were produced artificially by R. Parker, for his experimental study of the evolution of drainage basins (Parker, 1977). Data available through the courtesy of Professor S. Schumm.

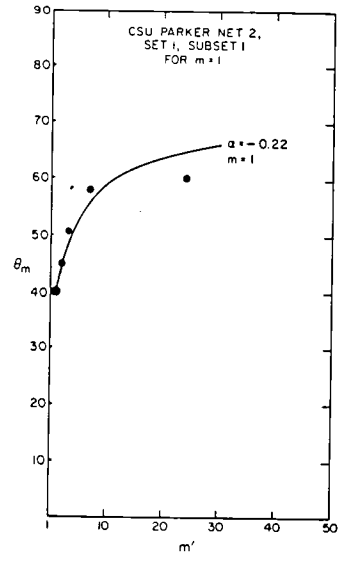

Figure 48.

CSU network, m = 2. Junction angle data for the network described in Figure 47.

The rapid increases in angle for magnitude 1 tributaries joining higher magnitude links are characteristic of all the networks analyzed. This tendency appears to operate at all scales since the Perth Amboy network exhibits a junction angle distribution in form to that of Moenkopi Wash even though their mainstream lengths are different by nearly three orders of magnitude.

The values of α seen in θ_m vs m' were determined by linearizing equations (13) and (14), plotting the log ($\cos \theta_m$) versus $\log \frac{1 + \frac{m}{m' - 1/2}}{}$ and fitting a straight line by least squares to these points (Figure 39a). The slope of that line is α. In the mathematical development of this model α is a dimensionless free parameter and is equal to the rate of decrease of slope with increase in link magnitude divided by the rate of increase in a drainage area with increase in link magnitude, times minus one (Flint, 1974). Another interpretation of α can be gained by looking at equation (9). If equation (4) is substituted back into equation (9), the following relationship is obtained:

$$S = t\, a^z\, A^{xz} \tag{15}$$

$$= t\, a^z\, A^{\alpha} \tag{16}$$

$$S = t'\, A^{\alpha} \tag{17}$$

And,

$$\log S = \alpha \log A + t'. \tag{18}$$

Basin slopes and drainage have been measured for many systems. For a given drainage basin it is useful to compute α independently of the junction angle method directly from the values of slope and drainage area. If the network is near equilibrium, that is if the longitudinal profile is smoothly varying, the value for α measured by both methods should be identical. For networks where this has been done, there is good agreement (Table V). By examining junction angle systematics in well developed drainage networks, information can be obtained about the longitudinal profile in the basin. For instance, ephemeral streams have very flat longitudinal profiles (Leopold and Miller, 1956). This is probably the result of an increase in sediment concentration downstream, requiring a higher velocity than characterizes normal rivers (Leopold and Miller, 1956, p. 28), and therefore slope decreases less rapidly downstream in these systems. Values of α calculated here for ephemeral streams reflect this trend ranging from -0.1 to -0.3, being the lower measured. Junction angle systematics also clearly reflect this trend, with generally much lower absolute values for junction angles for ephemeral streams relative to perennial rivers, and a slower increase of tributary junction angle with increasing recipient link magnitude. Again, this is expected since α calculated from the slope of the drainage basin area versus stream gradient curve and α calculated from the rate of increase of junction angle downstream have been shown (Table V) to be close.

Martian valley networks

Junction angles were measured for three martian valley networks listed in Table VI. Angles were measured from maps of valley centerlines produced using Viking Orbiter pictures. Figures 49 and 50 show plots of the junction angles of first-magnitude tributaries with increasingly higher magnitude recipient valleys. There is almost no correlation between junction angle and position of the junction within martian valley networks. The systematic and sharp increase in mean junction angle as seen in terrestrial networks is lacking, and mean junction angles are never over 40^{o}. The scatter of data points for the martian valleys is roughly a factor of three higher than for the terrestrial networks analyzed.

Discussion

The systematic increase of tributary junction angle with increase of recipient magnitude for tributaries of a given magnitude is a fundamental property of mature terrestrial drainage networks. That tendency was recognized empirically by Lubowe (1964) utilizing Strahler network ordering. The junction angle systematics were predicted here independently using simple geometrical and physical assumptions and these predictions are confirmed by analysis of real networks.

Mature terrestrial drainage networks have link slopes which are adjusted so as to be able to transport available load. The flow efficiency gained by the progressive decrease downstream of skin friction (decrease in the ratio of the wetted perimeter to cross-sectional area) and the progressive decrease downstream of sediment size (Hack, 1957) allow major downstream trunks to possess very shallow gradients. Junctions of high magnitude contrast exhibit relatively high tributary junction angles since the low magnitude tributary is flowing on slopes which have adjusted to a baselevel determined by the high magnitude (low slope) link. Therefore the systematic tendency of low magnitude links to enter high magnitude links at high angles is evidence of downhill flow on the valley sides toward the high magnitude link. Where exterior links join high magnitude interior links within basins, (i.e. flowing away from interior divides) sources of fluid over interior parts of the networks must exist. Such an arrangement also implies inter-valley competition for undissected terrain within the basin. A network which fills space efficiently, services all available source areas, and expends a minimum of energy in eroding to baselevel then ideally results.

Martian valley networks exhibit nearly none of the traits of terrestrial networks, except for bifurcation. The quality of bifurcation, alone, is not sufficient to demonstrate the existence of a drainage network supplied by an isotropic source (rainfall) as many authors have suggested (Masursky, et al., 1973; Milton, 1973; Sagan et al., 1973; Pieri, 1976). In particular, the near randomness of the junction angle development for martian valley networks implies lack of development of a topography adjusted to surface runoff erosion. Further, the generally parallel configurations of the networks with no visible development of drainage basins between truck valleys implies a restricted source area.

TABLE V

Comparison of α values derived from junction angle and slope-area measurements

Network	Location	Data Source	α by junction angle	α by slope-area
Gillis Falls	Maryland	Hack, 1957	-0.379 ± 0.07	-0.35 ± 0.05
Perth Amboy	New Jersey	Schumm, 1956	-0.277 ± 0.03	-0.28 ± 0.05
Arroyo Caliente	New Mexico	Leopold and Miller, 1956	-0.369 ± 0.06	-0.30 ± 0.05
Moenkopi Wash	Arizona	USGS Topo Map	-0.226 ± 0.02	-0.29 ± 0.06

TABLE VI

Martian networks analyzed for junction angle systematics

Name	Location	Terrain type	Relief	Length network	Data source
Margaritifer Sinus II, 1	lat. -25° long. 26°	Intercrater Plains	Low	200km	Viking Orbiter Images - 084A46 47, and 48
Margaritifer Sinus II, 2	lat. -25° long. 26°	Intercrater Plains	Low	100km	Viking Orbiter Images - 084A46 47, and 48
Thaumasia (Claritas) Fossae)	lat. -43.8° long. 93.5°	Isolated Block of ancient cratered terrain	?	190km	Viking Orbiter Image - 532A16

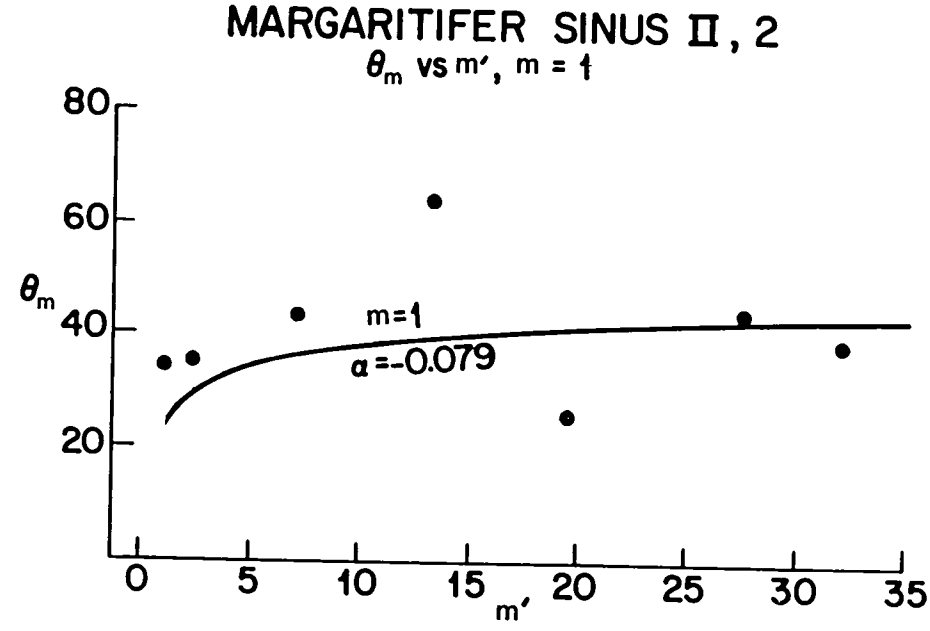

Figure 49.

Junction angle data for martian network shown in Figure 7, m = 1.

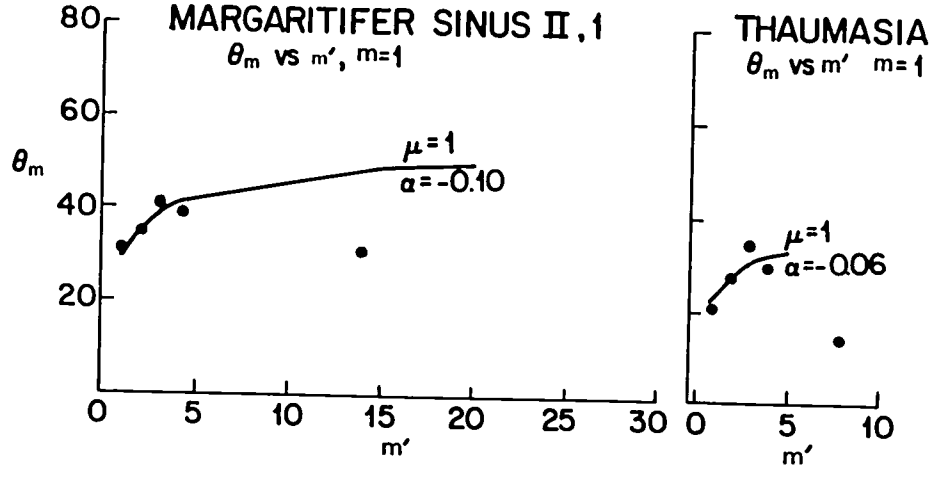

Figure 50.

Data for martian networks shown in Figure 7 (Margaritifer Sinus II) and in Figure 8 (Thaumasia), both for m = 1.

Parallelism alone cannot rule out rainfall as a source of fluid. Other factors must be considered. In martian valley systems the presence of deep first magnitude tributaries down-network with cross-sectional areas comparable to those of the recipient trunk valleys implies a gross disequilibrium. Additionally, these tributaries enter at low angles apparently consequent on the low regional slopes, and do not display any evidence of control by valley wall topography at the junction, where well-adjusted streams would show an effect. Thus, there is no hint of a drainage pattern that developed by coalescing runoff. Alternative mechanisms such as subsurface seepage and basal sapping can produce branched networks (Leopold et al., 1964, p. 429). Martian network planimetric patterns and valley morphology suggest that these processes may have been active in martian valley formation.

CHAPTER V: PHYSICS OF RIVER FLOW ON MARS

Equations of River Flow

Introduction

The morphology of many features on Mars suggests erosion by flowing water or other fluids. Liquid-water rivers could have existed on Mars because: (1) water is extremely abundant in the solar system, (2) modest pressure increases (~ 100mb) allowed by some martian climatic change models (Sagan et al., 1973; Ward, 1973; Toon et al., 1977) bring the liquid phase into a stability field at ambient or warmer temperatures (Malin, 1974, p. 3892), (3) features indicative of erosion by a channelized fluid are visible in imaging, and (4) features which are likely indicators of permafrost, and hence surface water, have been reported frequently (Soderblom and Wenner, 1978; Carr and Schaber, 1977), and are characteristic of much of the planet. For these reasons, the gravity dependence of some simple relations used for describing the characteristics of terrestrial river flow and sediment transport are examined in this chapter. The simple equations used successfully to describe river flow at terrestrial scale predict no major changes in river regimes due solely to the lower martian gravity. Flows under ambient martian pressures, however (1-10mb) should experience cavitation, boiling, and, if deep enough, macro-turbulence. Tranquil (Froude number ≤ 1) flows (turbulent or laminar) may be protected by an ice layer as predicted by Wallace and Sagan (1977), although the ability to erode under such conditions is questionable.

Settling velocity

Consider first the case of simple settling of spherical particles into quiet water.

Basset (1910) using Newton's second law of motion presents a solution for the problem of the descent of a sphere in a viscous liquid. He uses a lengthy series of integrations, to obtain the settling velocity, v_s, (Basset, 1910, p. 373; Graf, 1971, p. 31) for a sperical particle in a fluid moving with variable velocity v:

$$\frac{4\pi a^3}{3}\rho_s\dot{v}_s = \frac{4\pi a^3}{3}\rho_s\dot{v} - \frac{2\pi a^3}{3}\rho\,(\dot{v}_s - \dot{v})$$

$$- 6\pi a\mu\left[(v_s - v) + \frac{a}{\sqrt{\pi\nu}}\int_o^t dt_1\,\frac{\dot{v}_s(t_1) - \dot{v}(t_1)}{\sqrt{t - t_1}}\right.$$

$$\left. + \frac{4\pi a^3}{3}(\rho_s - \rho)\,g\right] \qquad (1)$$

Assuming a steady state motion for the particle, equation (1) reduces to

$$v_s - v = \frac{2}{9}a^2 g\,\frac{(\rho_s - \rho)}{\mu} \qquad (2)$$

Equation (2) is applicable only under low Reynold's number conditions ($R_e \lesssim 2$), i.e. Stokes resistance range.

An equivalent approach is presented by Dryden et al. (1956; p. 300), who, using the Navier-Stokes equation, derive the well-known Stokes result, equation (2). Their formulation yields equation (2) in the limit, for a small rigid sphere falling through a viscous media under the influence of gravity.

It is clear that the settling velocity is directly proportional to the first power of gravity. Equation (2) predicts that under laminar, slack water conditions, the resistance to the falling particle will be viscous and linear. The third term in equation (1),

$$6\pi\mu a\,v_s = r_L \qquad (3)$$

is the Stokes formula for drag with r_L, the resisting force of the fluid on the moving particle. Equation (3) is equally true for a stationary obstacle in a moving fluid. The low Reynolds number condition would apply to fine dust particles settling in quiet water.

Turbulent settling is, of course, the other possibility. Here, the steady state solution to equation (1) must be modified to reflect quadratic resistance to flow:

$$R_t = C_D\,a^2\pi\,\rho\,\frac{(v_s - v)^2}{2} \qquad (4)$$

Substituting equation (4) for the Stoke's resistance term in equation (1), equation (2) reduces to

$$v_s - v = \sqrt{\frac{8}{3}\,\frac{(\rho_s - \rho)}{\rho}\,g}\,\sqrt{\frac{1}{C_D}} \qquad (5)$$

for still water. Equation (5) should apply to turbulent flows at high Reynolds numbers. C_D is the steady-state drag coefficient. Although for Re $\lesssim$ 100 the drag constant, C_D, appears to be a function of the particle Reynolds number, at Re $\gtrsim$ 100 it can be roughly assumed to be constant (Graf, 1971, p. 52). Therefore, equation (5) predicts that for large particle Reynolds numbers, (for example, of gravel setting in water) the terminal settling velocity is dependent on $\sqrt{g}$.

Flow velocities downhill

Leopold et al. (1964, p. 57) provide a simple rationalization of the well-known Chezy flow equation for uniform flow. For unaccelerated downhill channel flow

$$F_d = \rho g d L \omega \sin \beta \tag{6}$$

Where F_d is the downhill force of the water due to its own weight. The resisting stress, τ, can be found from

$$F_r = \tau \ (2d + \omega) \ L \tag{7}$$

Because the flow is assumed to be unaccelerated,

$$F_d = F_r \tag{8}$$

so that

$$\tau = \rho g R S, \tag{9}$$

if R is defined in the usual way as the hydraulic radius and S is the slope of the energy grade line using the small angle approximation. Where flow is uniform, the water surface slope and the energy gradeline are parallel. Remembering for turbulent flow, that the shear stress on the boundary is proportional to the square of the mean flow velocity,

$$\tau_t = k \bar{v}^2 \tag{10}$$

where k is the constant of proportionality.

Then,

$$\tau_t = k \bar{v}^2 = \rho g R S \tag{11}$$

and therefore

$$\bar{v} = \sqrt{\frac{1}{k} g \rho R S} \ . \tag{12}$$

$(1/k \ g\rho)$ is called C, the Chezy coefficient and the familiar Chezy equation results:

$$\overline{v} = C\sqrt{RS} \quad . \tag{13}$$

It is obvious that C contains a $\sqrt{g}$ gravity dependence and this fact has been pointed out previously (Pieri, 1974, 1978; Nummedal, 1977). A river moved instantaneously from the earth to Mars would have its mean flow velocity decreased to 0.62 of its terrestrial value due to the lower gravity, since $\sqrt{g}$ earth/ $\sqrt{g}$ Mars = 0.62.

The shear stress within the laminar boundary layer, τ_L, is simply

$$\tau_L = k\overline{v} \tag{14}$$

which would imply

$$\tau_L \alpha \sqrt{g} \quad . \tag{15}$$

Critical shear stress

It is of interest to examine the critical shear stress necessary to initiate grain movement in terrestrial rivers and to calculate that quantity for identical hypothetical martian rivers. If, for instance, grain movement occurred at relatively lower values of critical stress on Mars than on the earth, lower gradients for a given sediment size and hydraulic radius might result. As will be shown below, this is not the case.

[1]If W_c is the energy required to move a particle on a stream bed, then

$$W_c \alpha (\rho_s - \rho)\, gd^4 \tag{16}$$

Since local mean velocities over a hydrodynamically rough bed are proportional to the shear velocity, the energy imparted to a particle of diameter d from the turbulent flow is

$$W_s \alpha \rho d^3\, u_*^2 \tag{17}$$

with $u_* = \sqrt{\tau/\rho}$, the shear velocity, where τ is the bed shear stress. If sediment is to move on the bed, W_s/W_c should exceed a critical value.

$$\frac{W_s}{W_c} = \frac{\rho d^3\, u_*^2}{(\rho_s - \rho)\, gd^4} = \frac{\tau}{(\rho_s - \rho)\, gd} \tag{18}$$

---

[1]Eqns. 16, 17, 18 are from Nummedal, 1977.

That is, the force necessary to initiate motion (F_c) should exceed some fraction of the submerged particle weight, since

$$\tau \alpha \frac{F_c}{d^2} . \tag{19}$$

For fully turbulent flows, the value of (18) remains constant, (Graf, 1971, p. 97), but Shields (see Graf, 1971) demonstrated that for laminar and transition flow,

$$\theta_o = \frac{\tau}{(\rho_s - \rho)\, gd} = f\left(\frac{u_* d}{\nu}\right) = f(Re_*) \tag{20}$$

where θ_o is called the dimensionless critical shear stress and Re_* is called the shear Reynolds number, (Graf, 1971, p. 95). The Shields curve is reproduced in Figure 51 from Graf's book, p. 96.

The Shields curve in Figure 51 can be readily applied to flows in 0.38 g. The functional dependence of the dimensionless critical shear (θ_o) stress on Re_* has been demonstrated over a range of particle densities and fluid densities (Sagan and Bagnold, 1975). It is reasonable to expect that it will be gravity invariant, particularly since the effect of gravity is explicit in both θ_o and Re_*, since $u_* = \sqrt{gRS}$. It is therefore possible to construct a plot showing the ratio of martian bed shear stress to terrestrial bed shear stress as a function of Re_* for terrestrial river under martian gravity. If, for example, the ratio of critical stress for earth and Mars differs from the ratio of available stress at the bed due to flow, then a gravity scaling effect would be proved and one could conclude that a terrestrial river would look different if it evolved under 0.38 g.

Figure 52 is such a plot showing the earth-Mars ratio of critical bed shear stress as a function of shear Reynold's number of a terrestrial river for arbitrary particle sizes and sediment density. For a laminar flow regime ($Re_* \leq 2$), the critical shear stress ratio, ϕ_c, equals about 0.62-0.63, for transitional flows ϕ_c is variable between 0.62 and 0.38, and for full turbulent flow ($Re_* \gtrsim 450$) $\phi_c = 0.38$. The procedure in obtaining ϕ_c was to calculate the terrestrial dimensionless shear stress, θ_o, using equation (20), to obtain values for the right side of (20) from the Shields diagram for a given Re_* A shear Reynolds number for martian conditions was obtained from the relation

$$0.62\ Re_{*_\oplus} = Re_{*_\sigma} \tag{21}$$

(using $Re_* = d\ \sqrt{gRS/\nu}$) assuming the same hydraulic radius, channel slope and grain size. A martian value of θ_o was then ascertained from the Shields graph for Re_{*_σ} . Finally,

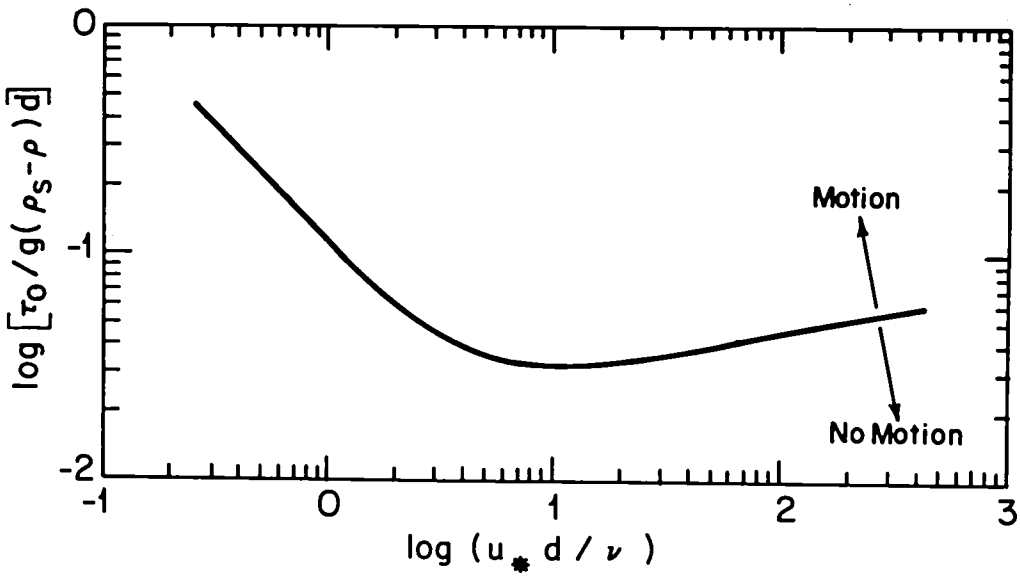

Figure 51.

Shields diagram (adapted from Graf, 1971). The abscissa is the shear Reynolds number and the ordinate is the ratio of tractive to inertial forces on a grain.

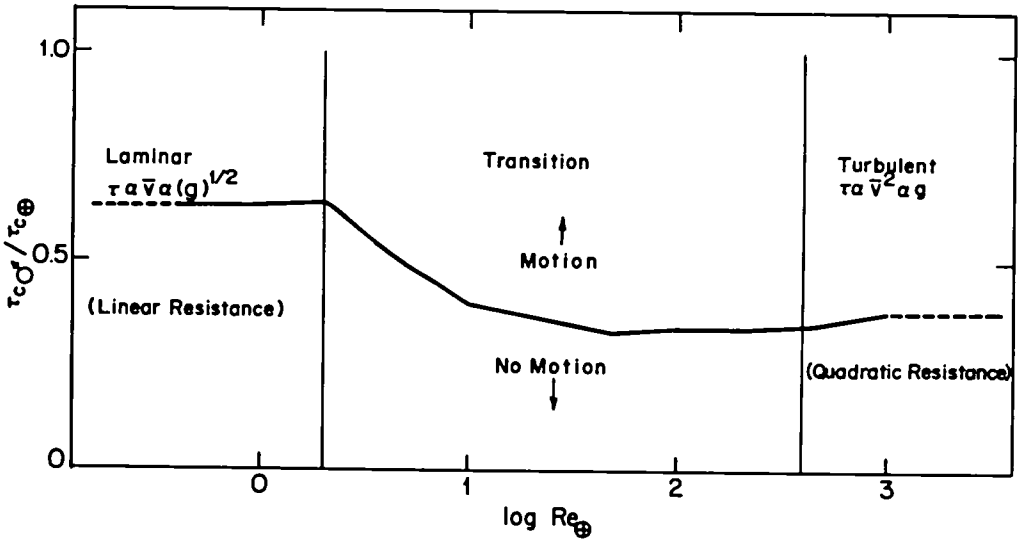

Figure 52.

Plot of Re_* versus tractive stress ratio. Shear Reynolds number for a terrestrial river (abscissa) versus the ratio of critical tractive shear stress exerted at Mars and at the earth by a flow with that terrestrial Reynolds number.

$$\phi_c = \frac{\theta_{o_{\sigma'}}}{\theta_{o_\oplus}} = \frac{\tau_{c_{\sigma'}}}{\tau_{c_\oplus}} = \frac{f\left(Re_{*_{\sigma'}}\right)}{f\left(Re_{*_\oplus}\right)} \cdot \frac{g_{\sigma'}}{g_\oplus} . \qquad (22)$$

We already know that the bed stress ratio, ϕ_t, for turbulent flow for a given slope and hydraulic radius

$$\phi_t = \frac{\tau_{t_{\sigma'}}}{\tau_{t_\oplus}} = \frac{\bar{v}^2_{\sigma'}}{\bar{v}^2_\oplus} = \frac{g_{\sigma'}}{g_\oplus} = 0.38 \qquad (23)$$

This is exactly what the Shields relation predicts for the critical bed stress scaling in the turbulent range (figure 51). Further, the laminar flow stress ratio, ϕ_L, is

$$\phi_L = \frac{\tau_{L_{\sigma'}}}{\tau_{L_\oplus}} = \frac{\bar{v}_{\sigma'}}{\bar{v}_\oplus} = \frac{\sqrt{g}_{\sigma'}}{\sqrt{g}_\oplus} = 0.62 . \qquad (24)$$

Again, the Shields relation predicts this value for ϕ_c in the laminar ($Re_* \lesssim 2$) range.

It is clear from equations (23) and (24) that

$$\frac{\tau_{L_{\sigma'}}}{\bar{v}_{\sigma'}} = \frac{\tau_{L_\oplus}}{\bar{v}_\oplus} \quad \text{and} \quad \frac{\tau_{t_{\sigma'}}}{\bar{v}^2_{\sigma'}} = \frac{\tau_{t_\oplus}}{\bar{v}^2_\oplus} \qquad (25)$$

Equation (25) states that the available bed shear stress per unit velocity is gravity invariant. Therefore the critical stress ratio must also be gravity invariant. That is, if a river at terrestrial gravity with a particular slope and hydraulic radius is initiating grain movement in a particular size range under either turbulent or laminar flow conditions, grain movement would continue, as is, even if both the flow velocity and critical shear stress are reduced by a switch to a lower gravity.

Power to transport bedload and suspended load versus available power

For the movement of particles in a fluid Leopold et al. (1964, p. 176) define a dynamic transport rate, I, in terms of immersed weight ($[\rho_s - \rho]/\rho_s$, where ρ_s is the particle density), Mg, times the particle velocity, v_s (force times velocity):

$$I = \left(\frac{\rho_s - \rho}{\rho_s}\right) Mg\ V \qquad (26)$$

I has the dimensions of power (rate of doing work). The movement of bedload mass, M_b, at transport rate I_b is accomplished at the rate of work, Ω_b, defined by

$$\Omega_b = I_b\ (\cos\beta \tan\alpha \pm \sin\beta) \qquad (27)$$

where the sign of sin β depends on the bed slope (Leopold, et al. 1964, p. 176), where

$$I_b = \left(\frac{\rho_s - \rho}{\rho_s}\right) M_b g v_s \qquad (28)$$

where the bedload velocity is assumed to be equal to the average velocity of water in the channel. The gravity dependence of Ω_b is,

$$Z_b = \frac{\Omega_{b_\sigma}}{\Omega_{b_\oplus}} \propto \left(\frac{g_\sigma}{g_\oplus}\right)^{3/2} = 0.23 \qquad (29)$$

For suspended load, the power is expended by the fluid maintaining an upward flux of momentum in order to suspend the particles. Therefore the power, Ω_s, necessary to maintain suspended load is

$$\Omega_s = \left(\frac{\rho_s - \rho}{\rho_s}\right) M_s g\ (v_s \pm v\ \sin\beta)\ , \qquad (30)$$

where

$$\left(\frac{\rho_s - \rho}{\rho_s}\right) M_s g$$

is the force exerted by the particles on the fluid, and $(v_s \pm v \sin\beta)$ is the settling velocity aided or hindered by the vertical downslope component of the flow velocity, v. Further,

$$\Omega_s = \left(\frac{\rho_s - \rho}{\rho_s}\right) M_s g v_s \pm \left(\frac{\rho_s - \rho}{\rho_s}\right) M_s g v\ \sin\beta \qquad (31)$$

or

$$\Omega_s = A \pm B\ . \qquad (32)$$

The gravity dependence of v_s is determined by the particle Reynolds number

$$R_e = \frac{2d\ (v_s - v)}{\nu} \tag{33}$$

where $(v_s - v)$ is the vertical velocity of the particle minus the vertical velocity component of the fluid. If a particle of diameter d is small and $v_s - v$ is small, as expected for very small particles, then R_{e_p} is small (≤ 2) and Stokes resistance applies. Therefore

$$A \propto g^2 \text{ , and} \tag{34}$$

$$B \propto g^{3/2} \text{ .} \tag{35}$$

For a slope, s, typical of channel flow, B vanishes. Therefore the gravity dependence of Ω_s can be expressed as

$$Z_s = \frac{\Omega_{s_{\sigma^*}}}{\Omega_{s_\oplus}} \propto \left(\frac{g_{\sigma^*}}{g_\oplus}\right)^2 = 0.14 \tag{36}$$

The available power, Ω_a, for a stream of flowing water (force times velocity) is

$$\Omega_a = \rho g A V s \tag{37}$$

which is the rate of loss of potential energy. If V is taken as the average flow velocity, then

$$Z_a = \frac{\Omega_{a_{\sigma^*}}}{\Omega_{a_\oplus}} \propto \left(\frac{g_{\sigma^*}}{g_\oplus}\right)^{3/2} = 0.23 \tag{38}$$

Finally,

$$\frac{Z_b}{Z_a} = 1 \tag{39}$$

But

$$\frac{Z_s}{Z_a} \propto \left(\frac{g_{\sigma^*}}{g_\oplus}\right)^{1/2} = 0.62 \tag{40}$$

Equation (39) says that the ratio of available power to the power necessary to transport bedload is equal on earth and Mars. Equation (40), however, implies that for settling under Stokes conditions that is, for suspended load at small particle Reynolds numbers, martian streams requires a smaller fraction of the power available. This presumably would make them more efficient at carrying the suspended load fraction of the total load, and perhaps more erosive with regard to fine grained material although the minimum tractive velocity is unchanged. For the largest size fraction of the suspended load, the low-gravity effect would diminish until the bedload size range is reached in which the effect would be negligible.

A comment on flow regimes in martian rivers

Figure 53 is a plot of Reynolds number versus channel width for a range of discharges with the occurrence range of terrestrial rivers indicated. The Reynolds numbers were calculated here in the following manner. The Reynolds number is

$$Re = \frac{\bar{v}\, D}{\nu} \qquad (41a)$$

where $\bar{v}$ is the average velocity of flow ν is the kinematic viscosity, and D is the flow depth. $\bar{v}$, however, equals the discharge divided by the

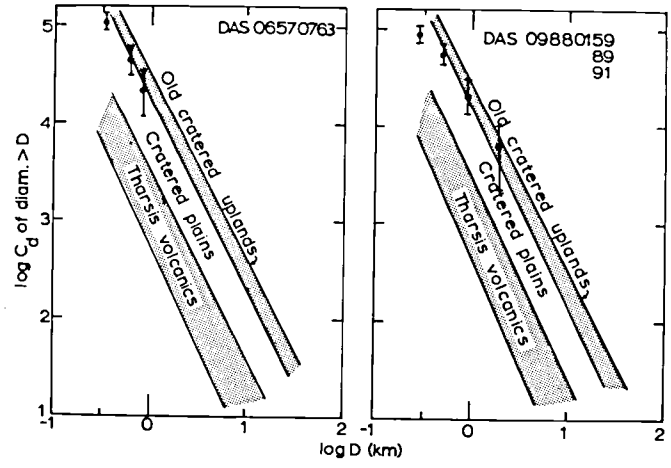

Figure 53.

Plot of Reynolds number versus channel width for terrestrial rivers. Data from Leopold et al. (1964, p. 242).

cross-sectional area, Q/A, and remembering that the cross-sectional area equals the width times the depth implies that

$$Re = \frac{Q}{W\nu} . \qquad (41b)$$

For open channel flow in rivers, Re $\leq$ 500 implies a laminar flow, Re $\geq$ 2000 implies fully turbulent flow (Gregory and Walling, 1973), but the characteristic length used by them in equation (a) is the hydraulic radius R_h, which is equal to the cross-sectional area divided by the wetted perimeter,

$$\frac{w\ D}{2D + w} . \qquad (41c)$$

For channels where w is much greater than D, that is most river channels, R_h about equals D and therefore equation (41a and 41b) are generally valid. Leopold et al. (1964) give data for 9 terrestrial rivers, including the Mississippi and the Amazon, from which a zone on the Re vs channel width diagram was plotted. A width range is also indicated for martian channels and valleys. Although, as mentioned, for a given hydraulic radius and slope, a martian channel will have a lower Re and Q, for channels wider than 100 meters and discharges greater than about a half a meter per second, martian flows should have an average Re in the turbulent range.

Cavitation in Terrestrial and Martian Streams

Introduction

Cavitation is the phenomenon of bubble formation and nearly instantaneous collapse associated with extreme erosive damage by a flowing fluid on obstacles in the flow. Cavitation damage has been seen, for example, on ship's propellers, turbines, and dam spillways (Knapp, et al., 1970, Chap. 1). Bubbles occur in a liquid when it is heated under constant pressure or when the fluid pressure is reduced statically or dynamically. Bubbles may grow slowly if dissolved gas diffuses into them or if the expansion is caused by increased gas volume due to heating or a reduction of pressure. The bubbles growth will be "explosive" if it is mainly by vaporization into a cavity, and its instantaneous collapse will be equally "explosive". Bubble growth is termed boiling if it is caused by temperature increase, and cavitation if it is caused by dynamic pressure reduction at constant temperature (Knapp et al., 1970, p. 1).

On the earth, cavitation under natural conditions is an interesting, but relatively rare phenomena. Cavitation has been suggested as a mechanism for pothole initiation in glacial meltwater streams by Barnes (1956), and by Embleton and King (1968 p. 148). Baker (1973) has suggested cavitation as an active erosion mechanism during the Lake Missoula floods in the channeled scablands of eastern Washington. The reason that cavitation is so rare in the natural terrestrial setting is that to attain the high velocities and in

turn, the reduction in pressure to initiate cavitation, requires either relatively steep slopes for shallow flows (Barnes, 1956, p. 500) or enormous discharge (Baker, 1973, p. 133).

It has been suggested previously that cavitation would be an active erosion process on Mars for catastrophic flooding under the present low pressure atmospheric conditions (Pieri, 1974; Baker, 1978). The following section will present (1) a detailed calculation of the critical cavitation velocity on Mars as a function of flow depth, assuming a simple model, and (2) a calculation of the bubble collapse pressure as a function of depth for stream flow on earth and Mars. For flows in the present martian environment cavitation will occur. However, its intensity will be several orders of magnitude smaller than in the terrestrial case for a given flow velocity.

Critical cavitation velocity

Barnes (1956, p. 499) shows an approximate method to calculate the critical cavitation velocity, the velocity which must be exceeded in order to initiate cavitation. Neglecting energy dissipation due to turbulence or bottom friction, the Bernoulli equation reads:

$$\frac{v_1^2}{2g} + \frac{p_1}{\rho g} + z_1 = \frac{v_2^2}{2g} + \frac{p_2}{\rho g} + z_2 \qquad (42)$$

where v_1 = mean stream velocity,
p_1 = atmospheric pressure = 10^6 dynes/cm^2
z_1 = stream depth
v_2 = velocity at the cavitation point (channel bottom = $2v_1$
P_2 = vapor pressure = 3.6×10^5 dynes/cm^2 for water at 25°C
z_2 = 0,

all in cgs units.

The assumption of $\bar{v} = v_2 = 2v_c$, is reasonable since it has been observed that velocities at the cavitation point are as much as 150% to 240% higher than the mean flow velocity (Barnes, 1956, p. 499). Solving for $\bar{v}_c$, the critical cavitation velocity, as a function of depth, yields

$$\bar{v}_c = \sqrt{\frac{2}{3} g \frac{p_1 - p_2}{\rho g} + z_1} \qquad (42)$$

in any units. For terrestrial rivers equation (42) reduces to

$$25.56\ (995.08 + z_1)^{1/2} = \bar{v}_{c_\oplus} \text{ at } 25°C \qquad (43)$$

and

$$25.56\ (1014.18 + z_1)^{1/2} = \bar{v}_{c_\oplus} \text{ at } 0°C \qquad (44)$$

(both cgs) yielding respectively average velocities of 8.06 m/sec and 8.14 m/sec to induce cavitation at one atmosphere 10^6 dynes/cm^2) pressure. For Mars, equation (42) reduces to

$$15.76\ (10.47 + z_1)^{1/2} = \bar{v}_{c_\sigma} \text{ at } 0°C \qquad (45)$$

in cgs units, yielding a velocity of 0.51 m/sec at the martian surface at 10 mb (10^4 dynes/cm^2) pressure. Figure 54 shows the dependency of critical cavitation velocity on depth for both earth and Mars, plotted from equation (42). This figure is adapted from Baker (1973, p. 135), with the martian curve added. It is interesting to note in Figure 54 that the martian critical cavitation velocity at 27 meters depth is equal to the surface terrestrial value. This is simply due to the fact that about 27 meters of water on Mars exerts 10^6 dynes/cm^2 (1 atm.) pressure. The velocity necessary to induce cavitation in water under that pressure is, of course, unique. This also implies that only at 27 meters on Mars does martian cavitation energy equal terrestrial surface cavitation energy at the same temperature.

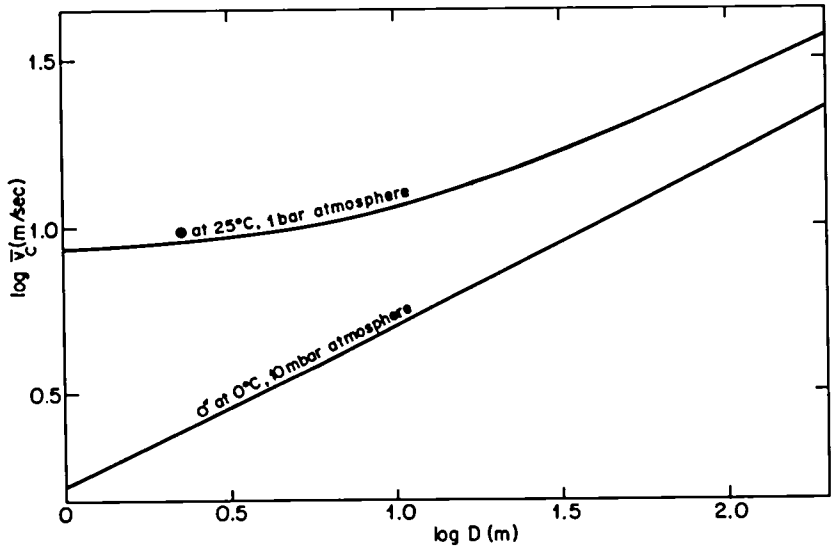

Figure 54.

Critical cavitation velocity versus depth for earth and Mars.

Pressure generated by bubble collapse

Although several authors have reported cavitation damage by melting, Knapp et al. (1970, p. 354-355) feel that the primary damage is due to the high pressure hammering due to the violent collapse of the bubbles. They report that tool steels and other materials of yield strengths of about 1.4×10^4 atmospheres (1.4×10^{10} dynes/cm^2 or 200,000 lbs/inch^2) have been pitted by cavitation, although pressures transmitted to solid boundaries adjacent to collapse centers are more typically about 10^3 atmospheres (10^9 dynes/cm^2 or about 15,000 lbs/inch^2). Terrestrial rocks have a range of unconfined compressive yield strength from roughly 1.8×10^9 dynes/cm^2 (about 26,000 lbs/inch^2) for strong rock (e.g. granites) to around 4×10^8 dynes/cm^2 for weak rocks (e.g. fissile shales) (about 5800 lbs/inch^2). The rock strengths quoted are well within the range of pressures produced by cavitation.

It has already been mentioned that surface cavitation under present martian conditions would be less energetic than terrestrial surface cavitation due to the much lower atmospheric confining pressure on Mars. It is useful, at this point, however, to derive an expression for the energy of bubble collapse and then for the pressure induced by collapse as a function of water depth for both planets. Under certain assumptions, it is then possible to compare the pressures transmitted with the compressive strengths of rock to determine the depth and velocity of martian flows necessary to cause cavitation damage.

First will be calculated the kinetic energy of a collapsing sperical bubble in a pure, incompressible fluid. Kinetic energy generated during the collapse of the bubble to a point in dyne-cm, is first expressed in its usual form

$$K_c = 1/2\ mv^2 \tag{46}$$

where m is the mass of the material entering the void during collapse in grams, and v is the average collapse velocity in cm/sec. The spherical mass which collapses into the void is expressed as

$$m = \rho V \tag{47}$$

and for a sphere

$$m = \rho \frac{4}{3} \pi R_o^3 \tag{48}$$

where R_o is the radius in cm of the bubble before collapse. The velocity of collapse is assumed here to be uniform and therefore an implicit assumption is that the collapse takes place into a vacuum. This is not strictly correct since the compression of dissolved gas or vapor within the cavity will retard the collapse and absorb some of the impact energy, converting it to heat. For this model however, the velocity can be

expressed as d/t where the distance d = R_o and t is found by the Rayleigh expression for the bubble collapse interval in an incompressible fluid,

$$t = 0.91468\ R_o\sqrt{\frac{\rho}{p_\infty}} \tag{49}$$

(Knapp et al., 1970, p. 99, equ. 4-6) in cgs units. The kinetic energy of the collapse of a bubble to a point is then from (46), (48), and (49),

$$K_c = 2.50\ R_o^3\ [p_\infty] \tag{50}$$

P_∞ is the confining pressure around the bubble and is equal to just the hydrostatic pressure plus atmospheric pressure p_o. Substituting for P_∞ , K_c becomes

$$K_c = 2.50\ R_o^3\ [\rho g h + p_o] \tag{51}$$

where ρ is the density of the fluid, g is local gravity and h is the fluid depth. All are in cgs units.

If we express pressure as the energy density of the bubble,

$$P = \frac{K_c}{V_b} = \frac{K_c}{\frac{4}{3}\pi R^3} \tag{52}$$

where V_b is the diminishing volume of the collapsing bubble of radius R, we arrive at

$$P_R = c'\ p_\infty \frac{R_o^3}{R^3} = c'\ [\rho g h + p_o]\frac{R_o^3}{R^3} \tag{53}$$

where P_R is the pressure at radius R and c' is a constant. From this simple derivation c' = 0.60. The Rayleigh derivation (Knapp et al., p. 102) in which dv/dt is not zero (v is the bubble wall velocity) has c' equal to 0.20.

A plot of collapse pressure versus depth for earth and Mars is shown in Figure 55 for R_o/R = 100. The ordinate in this graph bears explanation. Two pressure scales are used one for P_r and one for $P_{r'}$. P_r is the collapse site pressure calculated from equation (53) using the more conservative c' = 0.20. $P_{r'}$ is the effective collapse pressure at two R_o. $P_{r'}$ is used since it is very unlikely that a bubble will collapse directly on a confining surface. Rather, it is more likely to collapse near a solid boundary and have several bubble radii of fluid between the collapse site and the boundary (Knapp et al., p. 145, 354). Although Knapp et al. state that there has been no definite experimental determination of collapse pressure intensities, they cite four attenuated-collapse pressure

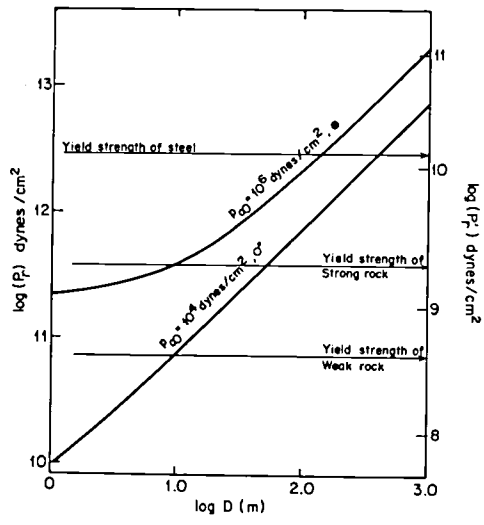

Figure 55.

Cavitation bubble pressure versus depth of flow. Left ordinate is the pressure at the bubble center, right ordinate is the effective pressure at two bubble radii. Read indicates yield strengths from the right ordinate (effective pressure values).

calculations from various sources (p. 144). The four have a mean of 0.005 $\pm$ a standard deviation of 0.003 for the ratio of the attenuated pressure and the collapse site pressure, $\frac{P_{r'}}{P_r}$, and that value is used to scale the right ordinate in Figure 55. Also indicated in Figure 55 is the range of unconfined yield strengths for rock on the $P_{r'}$ scale. Figure 55 should be taken as a rough gauge of the relative cavitation intensities of earth and Mars. It is clear, however, even with the uncertainties of the model, that for flows under current martian conditions, cavitation will occur at lower velocities, but will be as energetic as terrestrial surface cavitation only for flows deeper than 30 meters.

Discussion

Flow and sediment transport

The gravity-dependence of several important aspects of river flows have been discussed in this chapter: (1) the critical tractive velocity for a given sediment size, hydraulic radius and slope, (2) the settling velocity of sediments, and (3) the necessary power to transport suspended load and bed load versus the available power.

From equation (40) it is clear that the suspended sediment transport power of martian rivers should be enhanced by the lower gravity. This implies increased sorting of sediment in the downstream direction. Equation

(40) may also imply that martian river deltas may have lower slopes and be spread over larger areas than terrestrial ones. With ubiquitous and strong martian aeolian erosion, fine-grained, dispersed martian deltas may have short lifetimes and this may explain why very few deltaic-like features have been observed at valley mouths. Low gravity should have little to no effect on bedload transport (equation 39), and, for a given hydraulic radius, the slope necessary to transport a given sediment size should be roughly similar on the earth and Mars. The slope necessary to produce a desired discharge and a desired Reynolds number, for a given hydraulic radius, however, will be greater than on the earth by 1.62 because of the dependence of flow velocity on gravity ($v \propto \sqrt{g}$). Since the force balance equations involving turbulent flow are gravity invariant, and because martian rivers are like terrestrial rivers, expected to be fully turbulent (Figure 53), we can expect martian rivers to be, with the exception of increased suspended sediment loads and lower velocities, generally similar to terrestrial rivers.

Cavitation

Cavitation with lower than terrestrial critical velocities will occur at the surface of flows where atmospheric pressure is less than one standard atmosphere (10^6 dynes/cm^2). The intensity of such cavitation, however, will scale accordingly, as shown in Figure 55 for Mars. Low-energy cavitation ($P_r < 2 \times 10^{11}$ dynes/cm^2 or $P_{r'} < 10^9$ dynes/cm^2) should add turbulence to the flow and help entrain fine sediment, thereby helping to increase the suspended sediment load. High-energy cavitation ($P_r < 2 \times 10^{11}$ dynes/cm^2 or $P_{r'} < 10^9$ dynes/cm^2) should erode solid rock.

On Mars, the catastrophic flooding proposed to have formed the large channels such as the Chryse channels (Baker and Milton, 1975; Sharp and Malin, 1975) would have had flow velocities on the order of those experienced by the Lake Missoula floods (Baker, 1973, p. 135). Under terrestrial atmospheric conditions, these channels would probably have experienced high-energy cavitation and under martian conditions, probably both low- and high-energy cavitation, making them very muddy, turbulent, erosive flows.

For martian valleys formed under near-terrestrial atmospheric conditions, cavitation is probably of little significance due to the lower flow velocities on a given slope. If, however, local heating caused seepage and flow under less than terrestrial atmospheric pressures low-energy cavitation probably occurred, combining with the low Z_s (equation 36) to efficiently entrain and transport fine-grained sediment. The speculation then is that low discharge, cavitating flows from subsurface sources on Mars would be proportionately more erosive than such flows on the earth.

As an interesting footnote with regard to cavitation, Knapp et al., 1970 (p. 145) report that a phenomena known as "sonoluminescence" has been observed in cavitating flows. Light is produced under certain conditions by cavitation. It is thought that the light emission is due to either high pressure incandescence of gas, vapor, and trace impurity during bubble

collapse or perhaps is an electrical effect. Most interestingly, visual light emission has been reported for very high energy cavitation in the field. Knapp et al., 1970 (p. 353) report that visible light has been seen at night at Hoover Dam in the tailrace when river conditions required the release of large volumes of high pressure water into an energy dissipating structure which experienced severe cavitation. In the context of sonoluminescence, it would have been fascinating to observe both the martian and Scabland catastrophic releases at night. Also, it may be of interest to observe Icelandic Jokulhaups at night for any evidence of this phenomena, although the optical depth in muddy water is quite small.

CHAPTER VI: DISCUSSION: ORIGIN AND IMPLICATIONS OF MARTIAN VALLEYS

Data Summary and Conclusions

The surface of Mars displays two major classes of linear or sinuous depressions: channels and valleys. Channels are defined as features possessing smoothly sinuous, continuous depressions exhibiting streamlining of obstacles and parallel grooving. Topographic accordance at junctions may or may not exist. Channels may occur on cratered plains where they exist without a surrounding valley, or they may occur on valley floors.

Valleys are defined as sinuous to linear depressions showing no evidence of fluid erosion as the primary mode of valley walls destruction. Valleys may or may not have visible channels on their floors and may or may not bifurcate. Generally, however, they occur in networks. Valleys occur predominantly on heavily cratered ancient terrain and are concentrated in areas of low albedo.

Channels and valleys appear to represent two different modes of erosion. Large channels appear primarily to be the result of catastrophic floods on short timescales (Milton, 1973; Sharp and Malin, 1975) and subsequent modification over long timescales by mass movements. Valley networks do not coalesce to form large channels in a way that would imply direct movement of fluid through valleys into the large channels. There is some evidence that valleys were conduits for surface flow which may have supplied water to regolith reservoirs. Valley systems, in general, seem to be older than large channels. Small channels within valleys appear to be the result of flows within valley systems and obviously are either contemporaneous with the valley or younger than it.

Categorization of valleys

Valley systems may be divided into several categories by planimetric form. The three major categories of systems are: (1) longitudinal, (2) integrated, and (3) slope valley systems. Network systems are comprised of juxtapositions of different types of individual networks. These individual network types are: (1) parallel, (2) digitate, (3) stem, and (4) rectilinear. Radial assemblages of valley systems are termed centrifugal and centripetal (interior and exterior). The diversity of valley network types reflects heterogeneity of process, substrate and geologic structure.

Global distribution

Valley networks of the parallel and digitate type occur almost exclusively in ancient, heavily-cratered terrain. Longitudinal systems occur within a variety of terrains of varying ages. The parallel and digitate networks are most analogous to but are nevertheless distinct from terrestrial dendritic drainage patterns. These features are concentrated in the southern hemisphere, are absent from younger volcanic plains, and are inevitably flooded by the younger lavas where the valleys debouch into the plains. Integrated valleys are as old as the most ancient heavily cratered terrain.

Subsequent resurfacing and erosional processes have produced a present valley distribution on Mars which differs from the original. Thus, theories which suggest that the present valley distribution represents the result of preferential valley formation in temperate and equatorial martian latitudes cannot be supported by the observed distribution.

Parallel and digitate valley networks (Chapter I), are ubiquitous to the ancient heavily-cratered terrains. They predate the development of both the lightly cratered northern plains, and Lunae Planum plains. These valley networks postdate, but in some cases may be contemporaneous with, large basins as evidenced by both exterior and interior centripetal and centrifugal radial valley systems.

Longitudinal systems appear to have no preferential distribution with respect to terrain or latitude. The formation period of these features, as evidenced by their occurrence in young and old terrains, may span a much greater length of time than the more temporally restricted integrated networks.

Quantitative pattern analysis

An important characteristic of a drainage network is the distribution of junction angles as a function of position within the network. While other network planimetric parameters (e.g. bifurcation ratios) are useful for descriptive purposes, none can be as readily related to overall network physical properties, such as the relationship between junction angle systematics and the longitudinal profile of a drainage basin (Chapter IV). Dendritic terrestrial networks have junction angles which increase rapidly with recipient link magnitude. This is the result of small, low-magnitude links entering large high-magnitude links down-network at high angles. Such systematics are observed at all scales in terrestrial river systems.

Martian networks do not display such systematics. They possess remarkably low junction angles which appear to be totally independent of the position in the network. Low-magnitude links enter high-magnitude links at very low junction angles and are just as deep. Martian networks do coalesce downhill, both regionally and on local slopes (e.g. crater walls). There is little systematic down network widening as would be expected in a tributary

drainage system with all parts of the network active simultaneously. There is, however, a general progression in network character from angular in headward reaches to more sinuous near to the system mouth. In general, the martian networks fill space very inefficiently with large inter-valley areas remaining undissected with no evidence of divides or competition for drainage.

On the basis of these observations several conclusions may be drawn: (1) martian networks received drainage from very restricted source areas; (2) they are quite immature in development compared to terrestrial dendritic networks; (3) low junction angles at junctions with high-magnitude contrast indicate that low-magnitude tributaries are not consequent on the valley side slopes; (4) point (3) is consistent with a headward sapping mechanism for valley formation when coupled with observed amphitheater valley heads; and (5) all planimetric observations are consistent with a hypothesis of fluvial erosion fed from restricted source regions. The hypothesis of an areally uniform source, such as rainfall, has no compelling support.

Valley morphology

Features on the order of 100m across can be discerned within individual valleys. A number of general observations of morphology can be summarized: Some valleys appear to have interior channels and streamlined obstacles. These indicate erosion by flows within the valleys. Amphitheater valley heads are an important general characteristic. They appear in all valley network types. It appears that flow may have occurred in different parts of the same network at separated time intervals, although this is not a general characteristic. Mass wasting is active on valley walls in many areas. Large rockfalls are the most common type in contrast to the landslide features seen in Vallis Marineris. Valleys show both U- and V-shaped cross-sections, with both crenulated and smooth walls. Chaotic terrain exists at the up-network terminations of some valley systems. Many first-magnitude tributaries have cross-sectional areas equal to that of the recipient trunk; this is particularly true in digitate networks.

It may be argued that observations with 100 meter resolution cannot properly address the question of the source of fluid, nor the question of smaller runoff rills on inter-valley plateaus which appear undissected at lower resolution. Three observations argue against this criticism: (1) higher resolution images (~ 10m) of these valley networks show no such runoff rills adjacent to valleys or debouching into them, (2) comparable orbital images of terrestrial canyons do reveal a surface drainage system on relatively undissected plateau surfaces and (3) amphitheater valley heads have no small rills associated with them.

Generally, martian valleys appear to be the result of erosion and down-gradient transport of regolith in organized systems by a fluid. There is evidence of flow in at least some of the valleys and evidence of mass-wasting in valley interiors. Therefore, it is likely, given present surface conditions, that mass wasting continued long after the cessation of fluid flow. Present valley morphology may bear only slight resemblance to earlier valley forms. The parallelism of tributaries and the extreme length of low-magnitude tributaries suggests a restricted source region. The amphitheater valley heads suggest headward extension of tributaries by undermining of a component layer. This is consistent with the existence of the observed mass wasting debris deposits. Erosion by groundwater flowing along trends of opportunity in permeable substrata is likely to have contributed to valley formation. Surface runoff of water melted by extrusive or intrusive volcanics also probably had a part in their formation.

Physical theory

The gravity dependency of the physics of flow predicts no extreme scaling effects for martian rivers. In general, a river evolved in a martian environment, which had surface pressure and a temperature high enough to prevent sublimation or freezing, would have had much the same appearance as a terrestrial river evolved in a similar landscape. Such morphology, however, is generally absent within well-adjusted martian valleys, leading to the conclusions that such rivers never existed on Mars.

For transport to occur the critical tractive stress per unit velocity necessary to initiate grain movement must be equal to the available tractive stress per unit velocity, as is well known. Martian and terrestrial values for these numbers are identical for a given grain size, slope, and hydraulic radius in both the laminar and turbulent Reynolds number regimes. Therefore a given terrestrial river under lower gravity would initiate transport of the same size fraction of bedload and suspended load as on the earth. For particles whose Reynolds number is small enough (i.e. suspended sediment) for Stokes settling to apply, the fraction of power (energy per unit time) expended in keeping that load in suspension is lower on Mars. Martian rivers should therefore be able to transport a larger amount of fine sediment, keep it in suspension longer, and/or transport it over lower slopes. These effects may cause martian deltas to be thinner per unit area than terrestrial ones. Bedload power is unaffected by gravity scaling. Therefore sediment size-sorting downstream may be more effective on Mars. That could cause longitudinal gradients to decrease more rapidly for an equilibrium configuration, giving higher α values (rates of increase of junction angles with respect to recipient magnitude for a given magnitude tributary) than comparable terrestrial networks. This is contrary to what is observed and suggests that martian valley systems do not possess equilibrium longitudinal profiles in the terrestrial sense and that the eroding fluid was not distributed over the networks uniformly.

Cavitation is cited as a possible contributor to erosion in low velocity water flows under low martian pressures. Critical cavitation velocities

predicted are far lower than terrestrial ones for a given water depth. Two kinds of cavitation are defined: high-energy (pressures lower than 10^9 dynes/cm^2) and low energy (pressures lower than 10^9 dynes/cm^2). All natural terrestrial cavitation is by this definition high-energy cavitation. Low-energy cavitation could occur in water flow less than 27 meters deep at 10mb surface pressure and would increase turbulence and turbidity. High-energy cavitation could occur for martian flows deeper than 27 meters at 10mb surface pressure and would erode competent rock. For water flows under present martian surface pressures ($\leq$ 10mb) cavitation will occur but will be far less energetic than terrestrial surface cavitation. Deep flow cavitation (e.g. catastrophic floods) will experience energies similar to Channeled Scabland flows.

Age data

Crater counts on valley systems yield exposure ages of greater than 2 billion years before present. That fact, coupled with the nearly exclusive occurrence of valley networks on ancient cratered terrain, suggests great antiquity for these systems. The prevalence of impact craters larger than 50km in diameter in heavily cratered terrain argues for minimal ($\leq 70 \times 10^6$ yrs) exposure to and formation subsequent to any early rainfall epoch.

Hypotheses for Valley Formation

Flow versus non-flow hypotheses

Polygenetic formation processes are most likely responsible for the variety of morphology and planimetric patterns present in martian valleys. Heterogeneity of erodable materials may contribute to the varied appearance of these features, even when attacked by a single genetic process of uniform intensity. The origin of martian valleys is a complex, multivariate problem in which no single hypothesis answers all questions. An obvious approach is to ascertain which hypothesis explains most of the data by constructing a so-called "truth table" where a row of hypotheses is compared to a column of observations and entries are made in the table based on the likelihood of a particular observation fitting a given hypothesis. Such a truth table has been constructed for the observations of martian valley systems reported here and for various hypotheses proposed and is shown in Table VII. It is obvious from this table that flow or hybrid processes best explain the observed characteristics of martian valley networks.

From examining Table VII it is clear that various hypotheses have weaknesses. For example, it is likely that whatever erosion process predominated in the formation of the rectilinear networks, it was strongly influenced by structural control, since orthogonal jointing is a common pattern both on earth and Mars. The steep walls, amphitheater terminations, and the lack of interior channel argue that surface runoff did not control network orientation.

TABLE VII

Comparison of Flow and Non-Flow Hypotheses for Valley Formation

FLOW →

MODELS: OBSERVATIONS:	FLUVIAL	GLACIAL	LAVA	DEBRIS	WIND	ALKANES[9,10]	LIQUID[1] OR SOLID CO_2[2]
Distribution: found only in cratered terr.	yes	yes	maybe	yes	yes	yes	no
Planimetric Properties:							
1. coalesce downhill							
a. high slopes	yes	?[1]	yes[1]	yes[1]	no	yes	yes
b. low slopes	yes	yes	no	no	no	yes	yes
2. angular to sinuous down-network	yes	no	yes	no	no	?	?
3. high variance in junction angles	yes	?[1]	no	no	yes	?	?

TABLE VII (CONTINUED)

	NON-FLOW →		HYBRID →
MODELS: / OBSERVATIONS:	PURELY STRUCTURAL	DRY SAPPING	WET SAPPING
Distribution: found only in cratered terr.	no	yes	yes
Planimetric Properties:			
1. coalesce downhill			
a. high slopes	no	yes[2]	yes
b. low slopes	no	no	yes
2. angular to sinuous down-network	yes	yes	yes
3. high variance in junction angles	yes	yes	yes

TABLE VII (CONTINUED)

FLOW →

MODELS: OBSERVATIONS:	FLUVIAL	GLACIAL	LAVA	DEBRIS	WIND	ALKANES[9,10]	LIQUID[1] OR SOLID CO_2[2]
Morphology:							
1. interior channels	yes	yes	yes	yes	no	yes	yes
2. islands	yes	yes	yes	yes	yes	?	?
3. rectilinear networks	maybe[5]	no	no	no	no	no	no
4. amphitheater terminations	yes[6]	?[1]	no	no	no	?	?
5. sinuosity							
a. low	yes	yes	yes	yes	yes	?	?
b. high	yes	not likely	yes	no	no	?	?
6. delta forms	yes	no[3]	no	no[4]	no	?	?
7. valley head on promontories	yes	yes	yes	yes	yes	yes	yes?

TABLE VII (CONTINUED)

NON-FLOW ⟶ HYBRID ⟶

MODELS: / OBSERVATIONS:	PURELY STRUCTURAL	DRY SAPPING	WET SAPPING
Morphology:			
1. interior channels	yes	no	yes
2. islands	yes	yes	yes
3. rectilinear networks	yes	yes	yes
4. amphitheater terminations	yes[6]	yes	yes
5. sinuosity			
a. low	no[7]	yes	yes
b. high	no	possibly	yes
6. delta forms	no	yes[8]	maybe
7. valleys head on promontories	no	yes	yes

TABLE VII - FOOTNOTES

[1]It is hard to say exactly what these agents would do if there were no pre-existing stream valleys to follow.
[2]On steep slopes, sliding might expose ice which would sap uphill causing more sliding, etc.
[3]Moraines are crescentic, but are not considered "deltaic". Melt water could form a delta but this would be considered under "fluvial".
[4]Crescentic, but not deltaic.
[5]Under the influence of structure; immature system.
[6]Collapse pit or underground drainage.
[7]Shear islands and sinuosities develop in sheared grabens, but these are usually enechelon and discontinuous.
[8]Talus cones.
[9]Yung and Pinto (1978).
[10]Both possibilities are sufficiently bizarre so as to be outside the realm of conjecture with regard to resultant landforms.

Further, the existence of strongly rectilinear networks debouching into closed grabens suggests that non-flow processes were capable of forming valley networks (Table VII).

There is no compelling reason to invoke glacial erosion within any martian valley system. It is difficult, however, to completely rule it out. Terrestrially, glaciation explains the presence of boulder erratics, bedrock scour, eskers, and certain types of deposits (e.g. moraines, kames, kame terraces, kettles). On Mars such features have not as yet been observed although the resolution has not been generally high enough to allow their detection. Valley glaciers occur in mountain valleys and derive energy from the high relief. Their flow direction follows stream valleys and so it is hard to know what patterns would exist in the absence of pre-existing valley networks on flat terrain. On Mars, cirques would have had to be present in the amphitheater valley heads and continually supply a laterally restricted flow of ice over hundreds of kilometers on very low slopes ($\leq 1^{o}$).

Continental glaciers, on the other hand, may be capable of carving longitudinal troughs in pre-existing landscapes (Linton, 1963; Clayton, 1965). Linton (1963, p. 17) emphasizes the ability of glaciers to cut deeply downward, even in headward areas. He attributes this incision to the dilation of rock at the glacier base due to the removal of rock overburden and its subsequent replacement by ice, only one-third the original density. On Mars, however, this effect would be greatly reduced for a given depth of excavation since gravity is only one-third that of the earth's. Clayton (1965) discusses the formation of the Finger Lakes of New York State and attributes the formation of these overdeepended sub-parallel troughs to sub-glacial scour during Wisconsin glaciation of the Allegheny Plateau. Coates (1966, p. 472), however suggests that much of the Wisconsin glacial erosion in the Finger Lakes area exploited a topography already eroded by pro-glacial drainage from Illinoian and other ice sheets. Thus, he attributes much of the resulting present valley pattern to the diversion of ice during the most recent glacial advance into pre-existing drainage routes. Since the role of continental glaciation in eroding large valleys on the earth is ambiguous where field evidence is readily available, it is difficult to assess the probability of such an occurrence on Mars on the basis of orbital imaging alone. The sparse, open appearance of many of the martian valleys argues for local sources of eroding agent, as opposed to something as uniform and widespread as an ice-sheet. Further, coalescent glacial flows generally form parallel ice streams with arêtes and strings of nunataks marking the remnants of the lateral divides (Linton, 1963, p. 24). While martian valleys generally form in parallel configurations, they generally have flat, undissected inter-valley plateaus within valley networks exhibiting little erosion and tributary development. It is best to rule out glaciation until compelling evidence in the form of ice-contact features are observed.

Lava is not likely to form deep flat-floored rectilinear networks. Since no obvious volcanic constructs are associated with valley networks, it is likely that most valleys are not lava channels. Lava flow would tend to

reduce the variability of junction angles for a junction of a given magnitude contrast, contrary to what is observed in the junction angle statistics. Valley networks show no signs of being leveed; however, multiple flows on the flanks of many volcanic constructs on Mars do have levees (Carr, et al. 1977).

Debris flows probably explain many short parallel valleys on steep slopes, but it is difficult to believe that they could be sustained over many kilometers on intercrater plains. Debris flow organization to the degree of even the rudimentary network structure observed in martian valley systems would be highly unlikely. Debris flows are unlikely over extended distances on low slopes.

Wind has probably had a part in post-formational modification of valley networks (Cutts et al., 1977). However, wind-carved, coalescent networks are unobserved on the earth and are very doubtful for Mars. Air, being a compressible fluid, is not necessarily always deflected around obstacles. It can compress and flow over large obstacles where the height of the obstacles is comparable to the depth of the flowing layer. Slope winds of high intensity can modify already existing terrain. However, excavation by eolian erosion on the earth generally produces deflation hollows or basins which are broad and shallow features. It is unlikely that wind could initiate the excavation of a deep, sinuous, integrated network.

Lastly, liquid or solid CO_2 has been mentioned informally as a possible erosive agent and recently it has been suggested (Yung and Pinto, 1978) that liquid alkanes are theoretically permissible early in martian history. It is difficult to assess the probable efficacy of these proposed erosion agents because they are far outside the realm of terrestrial experience. Since water is readily available, and in its liquid or solid form could have facilitated the genesis of many if not all of the erosional forms associated with channels and valleys, it is unnecessary at this point to invoke the more exotic choice.

Non-flow hypotheses (e.g., structural) can explain many of the morphological characteristics of martian valleys. The main difficulty in explaining all valley networks by non-flow formational processes is the inability of these processes to provide network orientation aligned downslope, as in erosion by gravity-driven flow. This is the major objection to a purely non-flow formational hypothesis.

In summary, the complexity of planimetric network patterns of martian valley systems and their orientation downslope on low gradients are evidence for gravity-driven fluid flow. The general lack of leveed channels and associated volcanic constructs tends to rule out lava as a general erosional agent. There is no compelling evidence for invoking glacial process, since ice-contact features are absent. Observed channels within some valleys suggest fluvial flow along those valleys.

Fluvial vs pluvial

Table VIII compares two possible sources of water for eroding martian valleys: lithospheric and atmospheric. A lithospheric source would be one in which stored water from an undetermined origin is released to flow through a ground water system or is released as surface runoff. Atmospheric (pluvial) refers to water introduced to the surface as precipitation, either as rain or snow.

The hypothesis of a pluvial water source encounters trouble on several counts. An extended period of pluviality ($\geq$ 100 M.Y.) would have erased many of the impact craters seen on Mars today. The assumption of pluviality implies a substantial atmosphere and it is plausible to expect erosion rates comparable to those measured on earth. Any pluvial period of Mars must roughly predate the craters (see Chapter III). Further, the general observation of amphitheater terminations at valley heads is more consistent with erosion by undermining, rather than runoff. No shallow surficial drainage patterns are observed coalescing into valley heads. Small tributaries are not oriented as they would if they resulted from collected runoff over inter-valley areas. They enter trunk links at very shallow angles and are uniformly as deep and wide as the trunks over their entire lengths. Again, this is indicative of an erosion process operating at a particular level in the subsurface, undermining a competent layer. Inter-valley areas often appear totally undissected - smaller competing basins are always absent in these areas. Valleys exhibit little down-network widening. This observation is more consistent with a fixed contribution of water from up-network sources with little downstream addition to discharge. A restricted upstream source implies either a restricted lithospheric source, or a pluvial source with rain confined only to upstream reaches. Aside from the fact that there is typically no significant drainage basin development anywhere in the network, there is also no consistent pattern of occurrence of obstacles at the network source (i.e. mountain ranges or plateau to trigger an orthographic effect). The parallelism of tributaries in nearly all martian networks also strongly points to a restricted source area.

There are two other observations not connected to valley orientation that suggest a lithospheric water source. There are many instances of rimless circular depressions with steep walls, filled with block chaotic debris. Invariably one or more valleys penetrate the circular wall of the depression. These depressions may be buried craters which have filled with brecciated rock or sediment and subsequently covered by more competent rock, perhaps lava. Such shock-indurated craters would provide a convenient reservoir for subsurface water. When the headward extension of a valley taps this reservoir, water is released into the valley. The crater roof collapses, resulting in a chaotic deposit in the interior of a rimless depression.

Another interesting observation is the general progression of valley morphology and plan pattern from linear and angular up-network to more sinuous and smooth toward the mouth. It is possible that tectonic activity

TABLE VIII

Comparison of a Lithospheric versus an Atmospheric source

MODEL ▷ / OBSERVATIONS: ◁	LITH. SOURCE	ATMOS. SOURCE
1. Worn down ghost basins	possible	yes
2. Retention of large basins	yes	not likely
3. Parallel drainage, restricted source areas	yes	not likely
4. Amphitheater terminations	yes	no
5. Low entrance angles of small tributaries/deep incision	yes	no
6. Undissected plateaus in inter-valley areas	yes	not likely
7. Lack of sub-basin development in inter-valley areas	yes	no
8. Steep, crenulated walls	yes	no
9. Lack of distal widening down-network	yes	not likely
10. Very small networks at the margin of lava flow	yes	no
11. Valleys radial to basins	yes	yes
12. Collapsed crater roofs	yes	?
13. Progression of network character from angular to sinuous down-network	yes	not likely

associated with local heating could have penetrated a subsurface ice-rich or water-rich layer. A spring could result in which erosion by surface flow would be more effective downstream away from the source, and less controlled by associated upstream fractures. This is what appears to have happened in the Elysium area (Malin, 1976a, b).

Summary

General conclusions

The main conclusions of this dissertation are:

(1) Martian valley systems are the result of erosion by water flowing on the surface or in the subsurface from lithospheric sources.

(2) This process occurred relatively early in martian history and predated the formation of the major plains units.

(3) There is no compelling evidence from valley system distribution, morphology, or planimetric pattern for their formation by rainfall-supplied water. From orbit, at similar resolution there are no terrestrial features which are as comparably obvious as the martian valley networks. Terrestrial river networks observed at this scale have a fine subtle filigreed texture, in contrast to the crudely integrated, deeply entrenched, and coarse martian networks.

Implications and speculations

The conclusions of this thesis have some implications for martian climatic history. First, there is no conclusive evidence for rainfall, although it cannot be totally ruled out. Rain could have occurred, and is one mechanism for emplacement of water into the early cooling, brecciated, martian regolith. There is, however, no geomorphological evidence left of this early phase of martian history. On Earth, plate tectonics continually renews relief by processes ranging from the compressional formation of mountain ranges to gentle epirogenic uplift. On Mars, the absence of plate tectonics means that original relief would have been reduced rapidly under a terrestrial-like environment. Sediment transport and erosion in this early epoch could have filled early impact craters leaving broad shallow depressions which may have been reservoirs for subsurface volatiles. Such depressions are characterized today by the presence of chaotic terrain and radial (centripetal) valley networks. These depressions are quite subtle and probably very old.

A second implication to martian climatic history is that less atmosphere is necessary to allow surface flow of water than is required to transport the quantities of water necessary to initiate rain-supplied drainage systems. For example, the severity of the climatic change required to produce a 50mb or 100mb atmosphere is logically less than that required to produce 750mb or 1000mb atmosphere.

Third, if the source of water for valley erosion is in the regolith, it appears that, since the valleys are generally quite old, this source has not provided an eroding fluid recently. A question arises as to what has turned this source off. It is likely that the early martian heat flow was higher than it is today and that the crust was the thinner and warmer (F.P. Fanale, pers. comm. 1978). Active groundwater systems would have been more likely under those conditions, even at very low surface temperatures. Moderate pressures are necessary for uncovered flows. However, an ice cover as hypothesized by Wallace and Sagan (1977) could allow flow even under low atmospheric pressure conditions. It is likely then, particularly in a warmer, high pressure environment, with more geothermal heat available, that conditions favored the development of valleys by erosion from nonpluvial surface runoff and groundwater seepage and undermining. Subsequent modification of these valleys then could occur by dry, sublimative loss of water directly to the atmosphere. Dessication of exposed layers rich in water ice would be diffusion-limited and therefore probably slow. Dessicated layers would become weaker since their supporting strength would be reduced due to volume reduction and loss of grain cementation, both effects caused by loss of interstitial water over time. Valleys could then erode headward and laterally in the absence of flow. Valley floors would become debris choked. If much of the subsurface is composed of fine-grained regolith, as has been suggested (Malin, 1976a, b), it is possible that the debris residue evolved from this process could be transported out of the valleys by wind. It has been observed that valley networks are concentrated in low albedo areas. The author has argued in the past (Pieri, 1976) and here in Chapter II that the concentration of valleys in dark areas is an observational selection effect. It has been clearly observed from Viking that high-albedo cratered terrain is mantled (e.g. west of Syrtis Major, and west of Hellas). Obviously, at the present time, assuming these mantles are of wind transportable sediment, the high-albedo cratered terrain is not generally undergoing deflation. If sublimative erosion and subsequent wind transport of sediment are occurring, these processes can be occurring only in the dark low-albedo areas. Increased visibility of valley systems in low-albedo cratered terrain is certainly due to the thinner debris mantles, but may also be due in part to increased scouring of detritus derived from sublimative erosion. The relatively high equatorial temperatures would increase water mobility in the upper or outer few centrimeters of the ground and would tend to increase the dessication at these latitudes, relative to more poleward areas.

APPENDIX I

EXPLANATION OF RELATIVE INCREMENTAL PLOTTING FORMAT

One format used here for presenting the size-frequency distribution of crater populations is the relative size-frequency distribution plot suggested by Woronow et al. (1978). In this format crater diameter (D) is plotted against relative size-frequency distribution R(D) defined as

$$R(D) = \frac{F(D)}{S(D)}$$

where F(D) is the number of craters per unit area (ΔN) in a given size interval (ΔD). S(D) is a model reference distribution of crater diameters and was taken here to be

$$S(D) = D^{-3} .$$

D^{-3} is used since, as Woronow et al. point out, the log-log slope of the size-frequency distribution for most craters fall between -2 and -4. Hence, using D^{-3} yields a roughly horizontal line which thereby accentuates departure from that line. Assuming a simple production function (such as D^{-3}), then departures from the curve could be interpreted as changes in crater obliteration rates (e.g. deposition or erosion).

Substituting in (1) yields

$$R(D) = \frac{\Delta N}{\Delta D} \cdot \frac{1}{S(D)} = \frac{C(D_2) - C(D_1)}{(D_2 - D_1) \cdot S(D)}$$

where $C(D_n)$ is the cumulative number of craters per km^2 with diameters greater than or equal to D_n. S(D) is evaluated at the geometric mean of the interval $D_2 - D_1$ (i.e. $(D_2 - D_1)^{1/2}$), thus

$$S(D) = D_2 D_1^{-3/2}$$

Therefore,

$$R(D) = (D_2 D_1)^{3/2} \frac{C(D)_2 - C(D_1)}{(D_2 - D_1)}$$

All data presented here has been plotted as log R(D) against log (D). Crater diameters are binned in $\sqrt{2}$ intervals following the procedures outlined by Woronow et al. (1978).

Confidence intervals for the log R(D) versus log (D) plots are determined in the following way. If the number of craters per km^2, N, is assumed to be Poisson distributed over the region examined (Soderblom et al., 1974; Woronow et al., 1978; Hartmann, 1973) then one standard deviation (1σ) is represented by $N \pm \sqrt{N}$.

If $R(D) \pm \Delta R$ is the 1σ confidence interval of R(D), then

$$R(D) + \Delta R = \frac{\Delta N \pm \sqrt{N}}{\Delta D \quad S(D)}$$

$$= R \pm \frac{\sqrt{N}}{\Delta D S(D)} \cdot \frac{\sqrt{N}}{\sqrt{N}}$$

Therefore,

$$R(D) + \Delta R = \left(R \pm \frac{R}{\sqrt{N}}\right)$$

To correlate R(D) values with models for impact history and therefore with absolute age, which are usually expressed in cumulative statistics, it is convenient to determine the correspondence between R(D) and both the number of 4-10 km craters and the total number of craters greater than 1 km.

A given log(R) interval can be easily converted into a cumulative number of craters. From above, the integral of the size-frequency distribution (i.e., the total number of craters greater than a given diameter, C(D)) is

$$C(D) = \int_D^\infty F(D)dD$$

where as before, $F(D) = \Delta N / \Delta D$. Substituting for F(D) from equation (1) yields

$$C(D) = \int_D^\infty R \cdot S(D)dD \ .$$

Here, R is taken as a constant since the desired result is a correspondence between a given R and C(D). Therefore

$$C(D) = R \int_{D}^{\infty} S(D)dD \ .$$

Since the data are binned in finite intervals, the integral equation can be converted to a sum of finite differences. This conversion yields

$$C(D) = R \sum_{n=1}^{\infty} S(D)\Delta D \ . \tag{12}$$

Recalling that $S(D) = D^{-3}$ evaluated at the geometric mean of the bin limits and that the data are binned $\sqrt{2}$ intervals yields

$$C(D) = R \sum_{n=1}^{\infty} \left(\sqrt{2}^{n}D \cdot \sqrt{2}^{n-1}D\right)^{-3/2} \cdot \left(\sqrt{2}^{n}D - \sqrt{2}^{n-1}D\right) \ , \tag{13}$$

which reduces to the convergent infinite series

$$C(1) = R \sum_{n=1}^{\infty} \left(2^{[3/4-n]}\right) (0.29289)\ D^{-2} \tag{14}$$

for all craters greater than 1 km in diameter.

This infinite series can be generalized so that for a given ratio between adjacent diameter bin ranges, a (e.g. $a = \sqrt{2}$), and a given slope for the log-log incremental reference size frequency distribution, b (e.g. $b = -3$),

$$C(D) = R \sum_{n=1}^{\infty} \left(a^{n}Da^{n-1}D\right)^{b/2} \cdot \left(a^{n}D - a^{n-1}D\right) \ , \tag{15}$$

which reduces to

$$C(D) = R \sum_{n=1}^{\infty} a^{n(b+1)-b/2}D^{(b+1)} \left(1 - \frac{1}{a}\right) \tag{16}$$

Further, for a given diameter size range, D_c to D_d, (e.g. for the cumulative number of craters per km^2 between 4 and 10 km, D_c = 4 km and D_d = 10 km) the following general equations hold:

$$C(D_c - D_d) = C(D_c) - C(D_d) \tag{17}$$

and therefore

$$C(D_c) - C(D_d) = R \sum_{n=1}^{\infty} a^{[n(b+1)-b/2]} \left(1 - \frac{1}{a}\right)\left[D_c^{(b+1)} - D_d^{(b+1)}\right] . \tag{18}$$

For D_c = 4 km, D_d = 10 km, a = $\sqrt{2}$, and b = -3,

$$C(4) - C(10) = R(0.02586) \tag{19}$$

Absolute ages from the impact flux history model of Soderblom et al. (1974) (figure 21) are assigned to log R values in Figure 22, using

$$T = \frac{C(4) - C(10) \times 10^6 \text{ km}^2 - 5}{80} \tag{20}$$

for C(D) less than 350 and

$$T = \frac{C(4) - C(10) \times 10^6 \text{ km}^2 + 7886}{2230} \tag{21}$$

for C(D) greater than 350 craters per 10^6 km^2. T is the absolute age in billions of years before present.

APPENDIX II

LIST OF VARIABLES USED IN CHAPTER V

all cgs units

a - radius of a spherical particle or bubble
ρ_s - density of a particle of sediment
v_s - settling velocity of particle of sediment
v - velocity of fluid
μ - absolute viscosity
υ - kinematic viscosity
t - time in seconds
g - acceleration of gravity
r_L - resisting force for Stokes settling
r_t - resisting force for turbulent settling
C_D - drag coefficient
R_{e_p} - particle Reynolds number (see equation 33, p. 229)
F_d - downhill force of water due to its own weight
L - channel segment length
D - channel depth
w - channel width
F_r - resisting stress
R_h - hydraulic radius
τ_t - shear stress exerted by turbulent flow
S - slope of energy grade line (i.e. water surface)
τ_L - shear stress exerted by laminar flow
W_c - energy required to move a particle on a stream bed
d - particle diameter
u_* - shear velocity
F_c - critical tractive force
θ_o - dimensionless critical shear stress
Re_* - shear Reynolds number
ϕ - critical shear stress ratio
I - dynamic transport rate
M_b - bedload mass
I_b - bedload dynamic transport rate
Ω_b - rate of work
β - angle of channel bed
α - angle of internal friticion for particles
v_s - particle settling velocity
v_d - vertical downslope component of the flow velocity
Z_s - ratio of power expended in supporting suspended load

Z_a - ratio of available power for sediment transport
Z_b - ratio of power expended in transporting bedload
$\bar{v}_c$ - critical cavitation velocity
K_c - kinetic energy of cavitation bubble collapse
P_∞ - confining pressure around a cavitation bubble
P_o - atmospheric pressure
h - fluid depth
V_b - volume of collapsing bubble
P_r - bubble collapse pressure at some radius R
$P_{r'}$ - effective bubble collapse pressure at two R_o
R_o - initial radius of bubble before collapse
R - arbitrary bubble radius

BIBLIOGRAPHY

Baker, V.R., 1971, Paleohydrology of catastrophic Pleistocene flooding in Eastern Washington: Geol. Soc. Am. Special Paper, 144, 79 p.

Baker, V.R., 1973, Erosional forms and processes for the catastrophic Pleistocene Missoula floods in Eastern Washington, in Fluvial Geomorphology, M. Morisawa, ed., Publ. in Geomorphology, State Univ. N.Y., Binghamton, N.Y., p. 123-148.

Baker, 1976, personal communication.

Baker, V.R., 1978, Hydrodynamics of erosion by catastrophic floods: in NASA Tech. Memo, 79729, Reports of Planetary Geology Program, 1977-79, pp. 248-250.

Baker, V.R. and Kochel, R.C., 1978, Morphometry of streamlined erosional forms in terrestrial and martian channels: in NASA Tech. Memo, 79729, Reports of Planetary Geology Program, 1977-78, p. 251 (abstr.).

Baker, V.R. and Milton, D.J., 1974, Erosion of catastrophic floods on Mars and Earth: Icarus, 23, p. 27-41.

Barnes, H.L., 1956, Cavitation as a geological agent: Amer. Jour. of Science, 254, pp. 493-505.

Basset, A.B., 1910, on the descent of a sphere in a viscous liquid: The Quarterly Journal of Pure and Applied Mathematics, 41, pp. 369-381.

Bretz, J.H., Smith, H.T.U., and Neff, G.E., 1956, Channeled Scablands of Washington; new data and interpretations: Geol. Soc. Amer. Bull., 67, pp. 957-1049.

Carr, M.H., Masursky, H., Baum, W.A., Blasius, K.R., Briggs, G.A., Cutts, J.A., Duxbury, T., Greeley, R., Guest, J.E., Smith, B.A., Soderblom, L.A., Veverka, J., and Wellman, J.B., 1976, Preliminary Results from Viking Orbiter Imaging Experiment: Science, 193, pp. 766-776.

Carr, M.H., and Schaber, G.G., 1977, Martian permafrost features: Jour. Geophys. Research, 82, pp. 4039-4054.

Carson, M.A., and Kirkby, M.J., 1972, Hillslope form and process, Cambridge Univ. Press.

Chapman, C.P., 1974, Cratering on Mars, 1, Cratering and obliteration history, Icarus, 22, pp. 264-271.

Chapman, C.R., and Jones, K.L., 1977, Cratering and obliteration history of Mars: Ann. Rev. Earth Planet Sci., 5, pp. 515-540.

Christensen, E.J., 1976, Martian topography derived from occulation, radar, spectra, and optical measurements: Jour. Geophys. Research, 80, pp. 2909-2913.

Clayton, K.M., 1976, Glacial Erosion in the Finger Lakes Region (New York State, U.S.A.), Zeit. für Geomorph., Nf9, pp. 50-52.

Coates, D.R., 1966, Discussion of K.M. Clayton "Glacial Erosion in the Finger Lakes Region (New York State, U.S.A.)", Zeit. für Geomorph., Nf10, pp. 469-474.

Cutts, J.A., Blasius, K.R., and Roberts, W.J., 1978, Chaotic terrain and channels associated with Chryse Planitia, Mars: An alternative erosional model: in NASA Tech. Memo., 79729, Reports of Planetary Geology Program, 1977-78, p. 277 (abstr.)

Dryden, H.L., Murnaghan, F.D., and Bateman, H., 1956, Hydrodynamics, Dover Publications, Inc., a republication of Bulletin 84 of the National Res. Council.

Easterbrook, D.J., 1969, Principles of Geomorphology, McGraw-Hill, San Francisco, Ca., 462 p.

Embleton, C. and King C.A.M., 1968, Glacial and Periglacial Geomorphology, St. Martin's Press, New York, 608 p.

Fanale, F.P., 1978, personal communication.

Flint, J.J., 1974, Stream gradient as a function of order, magnitude, and discharge: Water Resources Research, 10, pp. 969-973.

Florenski, C.P., Basilevski, A.T., Kuzmin, R.O., Chernaya, I.M., 1975, Geomorphological analysis of some martian surface images from the Mars 4 and 5 automatic stations: Icarus, 26, pp. 219-229.

Graf, W.H., 1971, Hydraulics of Sediment Transport, McGraw-Hill Book Co., New York, 513 p.

Gregory, K.J. and Walling, D.E., 1973, Drainage Basin Form and Process, Edward Arnold, London, 456 p.

Hack, J.T., 1957, Studies of Longitudinal Stream Profiles in Virginia and Maryland: U.S. Geol. Survey Prof. Paper, 294-B, 97 p.

Hartmann, W.K., 1973, Martian cratering, 4, Mariner 9 initial analysis of cratering chronology: Jour Geophys. Research, 78, pp. 4096-4116.

Hartmann, W.K., 1974, Geological observations of martian arroyos: Jour. Geophys. Research, 79, pp. 3951-3957.

Hartmann, W.K. and Raper, O., 1974, The New Mars, NASA SP-337, 179 p.

Horton, R.E., 1932, Drainage basin characteristics. Am. Geophys. Union Tr., pp. 350-361.

Horton, R.E., 1945, Erosional development of streams and their drainage basins; hydrophysical approach to quantitative morphology: Geol. Soc. Am. Bull., 56, pp. 275-370.

Howard, A.D., 1971, Optimal angles of stream junction: Geometric stability to capture, and minimum power criteria: Water Resources Research, 7, pp. 863-878.

Jones, K.L., 1974, Evidence for an episode of crater obliteration intermediate in martian history: Jour. Geophys. Research, 79, pp. 3917-3931.

Knapp, R.T., Daily, J.W., Hammitt, F.G., 1970, Cavitation, McGraw-Hill, New York, 578 p.

Leopold, L.B., and Langbein, W.B., 1962, The concept of entropy in landscape evolution: U.S. Geol. Surv. Prof. Paper, 500-A, 20 p.

Leopold, L.B. and Miller, J.P., 1956, Ephemeral streams, Hydraulic factors and their relation to the drainage net: U.S. Geol. Survey Prof. Paper, 282-A, 36 p.

Leopold, L.B., Wolman, M.G., and Miller, J.P., 1964, Fluvial Processes in Geomorphology, Will. Freeman, and Co., 522 p.

Linton, D.L., 1963, The Forms of Glacial Erosion, Institute British Geographers Trans. and Papers, no. 33, p 1-28.

Lubowe, J.K., 1964, Stream junction angles in the dendritic drainage pattern: Am. Jour. of Science, 262, pp. 325-339.

Malin, M.C., 1974, Salt weathering on Mars: Jour. Geophys. Research, 79, pp. 3888-3894.

Malin, 1976a, Ph.D. Thesis, California Institute of Technology, Pasadena, Ca., 176 p.

Malin, M.C., 1976b, Age of martian channels: Jour. Geophys. Research, 81, pp. 4825-4845.

Martin, M.E., 1912, The Ways of the Planets, Harper and Bothers, New York, 272 p.

Masursky, H., 1973, An overview of geological results from Mariner 9: Jour. Geophys. Research, 78, pp. 4009-4030.

Masursky, H., Boyce, J.M., Dial, A.L., Schaber, G.G., and Strobell, M.E., 1977, Classification and time of formation of martian channels based on Viking data: Jour Geophys. Research, 82, pp. 4016-4038.

McCauley, J.F., Carr, M.H., Cutts, J.A., Hartmann, W.K., Masursky, H., Milton, D.J., Sharp, R.P., and Wilhelms, D.E., 1972, Preliminary Mariner 9 Report on the Geology of Mars: Icarus, 17, pp. 289-327.

Milton, D.J., 1973, Water and processes of degradation in the martian landscape: Jour. Geophys. Research, 78, pp. 4037-4049.

Murray, B.C., Soderblom, L.A., Sharp, R.P., Cutts, J.A., 1971, The surface of Mars, 1, Cratered terrains, Jour. Geophys. Research, 76, pp. 313-330.

Mutch, T., Arvidson, R., Head, J., Jones, K., and Saunders, R., 1976, The Geology of Mars, Princeton Univ. Press, 400 p.

Mutch, T.A., Arvidson, R.E., Binder, A.B., Guiness, E.A., and Morris, E.C., 1977, The geology of the Viking Lander 2 Site: Jour. Geophys. Research, 82, pp. 4452-4467.

Neukum, G. and Wise, D.U., 1976, Mars: a standard crater curve and a possible new time scale: Science, 194, pp. 1381-1387.

Nummedal, D., 1977, Entrainment of Sediment by Fluid Flows on Mars, in NASA Tech. Memo, X3511, Reports of the Planetary Geology Program, 1976-77, pp. 162-163.

Parker, R.S., 1977, Experimental study of drainage basin evolution and its hydrologic implications: Hydrology Paper, no. 90, Colo. St. Univ, Fort Collins.

Pieri, 1974, unpublished manuscript.

Pieri, D., 1976, Distribution of small channels on the martian surface: Icarus, 27, pp. 25-50.

Pieri, D., 1978, Junction angles of martian channels: NASA Tech. Memo, 79729, Reports of the Planetary Geology Program, 1977-78, p. 268.

Potter, D.B., 1976, Geologic map of the Hellas quadrangle: U.S. Geo. Survey Misc. Investigations I-441 (MC-28).

Sagan, C.E. and Bagnold, R.A., 1975, Fluid transport on earth and aeolian transport on Mars: Icarus, 26, pp. 209-218.

Sagan, C.E., Toon, O.B., and Gierasch, P.J., 1973, Climatic change on Mars: Science, 181, pp. 1045-1049.

Saunders, R.S., 1978, personal communication.

Schumm, S.A., 1956, Evolution of drainage systems and slopes in bedlands at Perth Amboy, New Jersey: Geol. Soc. Am. Bull., 67, pp. 597-646.

Schumm, S.A., 1978, The Fluvial System, John Wiley & Sons, 338 p.

Scott, D.H., and Carr, M.H., 1977, Geological Map of Mars: U.S. Geol. Survey Misc. Geol. Inv. Map I-1083.

Sharp R.P., 1973, Mars: Fretted and chaotic terrains: Jour. Geophy. Research, 78, pp. 4073-4083.

Sharp, R.P. and Malin, M.C., 1975, Channels on Mars: Geol. Soc. of Amer. Bull., 86, pp. 593-609.

Shreve, R.L., 1967, Infinite topologically random channel networks: Jour. Geol., 75, pp. 179-186.

Smart, J.S., 1972, Channel networks: Advances in Hydroscience, 8, pp. 305-346.

Soderblom, L.A., Condit, C.D., West, R.A., Herman, B.M., and Kriedler, T.J., 1974, Martian planetwide crater distributions: Implications for geologic history and surface processes: Icarus, 22, pp. 239-263.

Soderblom, L.A., Kriedler, T.J., and Masursky, H., 1973, Latitudinal distribution of debris mantles on the martian surface: Jour. Geophys. Research, 78, pp. 4117-4122.

Soderblom, L.A., and Wenner, D.B., 1978, Possible fossil H_2O liquid ice interfaces in the martian crust: Icarus, 34, pp. 622-637.

Toon, O.B., Ward, W.R., and Burns, J.A., 1977, Climatic change on Mars: hot poles at high obliquity: 8th Annual Meeting, Division for Planetary Sciences, American Astronomical Society, Honolulu, Ha., 19-22 Jan. 1977 (abstr.).

UNESCO, 1976, World Catalog of Very Large Floods: A Contribution to the International Hydrological Program, UNESCO Press, Paris, 424 p.

Wallace, D. and Sagan, C.E., 1977, Evaporation of ice-choked rivers: application to martian channels, in NASA Tech. Memo, X3511, Reports of Planetary Geology Program, 1976-77, p. 161

Ward, W.R., 1973, Large-scale variations in the obliquity of Mars: Science, 181, pp. 260-262.

Ward, W.R., 1974, Climatic variations on Mars, 1, Astronomical theory of insolation: Jour. Geophys. Research, 79, pp. 3375-3386.

Wolman, M.G., 1955, The Natural channel of Brandywine Creek Pennsylvania: U.S. Geol. Survey Prof. Paper, 271, 54 p.

Woronow, A., 1975, A size-frequency study of large martian craters: Lunar and Planetary Laboratory Report, University of Arizona, Tucson, 31 p.

Woronow, A., Arvidson, R., Boyce, J., Chapman, C., Cintala, M., Fulchignoni, M., Moore, H., Neukum, G., Schultz, P., Soderblom, L.A., Strom, R., and Young. R., 1978, Standard Techniques for presentation and analysis of crater size-frequency data; NASA Tech. Memo, 79730, 20 p.

Woronow, A. and King, E.A., 1972, Size-frequency distribution of martian craters and relative age of light and dark terrains, Science, 175, pp. 755-757.

Yung, Y.L. and Pinto, J.P., 1978, Primitive atmosphere and implications for the formation of channels: Nature, 273, pp. 730-732.

SECTION II

VOLCANO-ICE INTERACTIONS ON THE EARTH AND MARS

by

Carlton Carl Allen

A Dissertation Submitted to the Faculty of the

DEPARTMENT OF PLANETARY SCIENCES

In Partial Fulfillment of the Requirements
For the Degree of

DOCTOR OF PHILOSOPHY

In the Graduate College

THE UNIVERSITY OF ARIZONA

1 9 7 9

STATEMENT BY AUTHOR

This dissertation has been submitted in partial fulfillment of requirements for an advanced degree at The University of Arizona and is deposited in the University Library to be made available to borrowers under rules of the Library.

Brief quotations from this dissertation are allowable without special permission, provided that accurate acknowledgment of source is made. Requests for permission for extended quotation from or reproduction of this manuscript in whole or in part may be granted by the head of the major department or the Dean of the Graduate College when in his judgment the proposed use of the material is in the interests of scholarship. In all other instances, however, permission must be obtained from the author.

SIGNED: 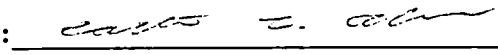

PREFACE

Few countries on Earth offer the diversity of volcanic landforms awaiting the investigator in Iceland. Located astride the Mid-Atlantic Ridge, this is one of the most active volcanic regions in the world. Major eruptions occur several times per decade, and thermal zones with hot springs and geyers continually attest to the presence of magma not far beneath the surface. By contrast, some 11% of this island on the Arctic Circle lies beneath ice sheets which are remnants of much broader Pleistocene glaciation. Glacial meltwater rivers roar through precipitous canyons and suddenly spread onto wide flood plains, while nearby the winds form immense patterns in the sand and ash of cold volcanic deserts.

This country offers another distinct advantage to the geologic investigator. The descendents of the Vikings who settled Iceland in the ninth century were among the most adventurous, literate and observant people of their time. Armed with a written historical record spanning 1100 years, Icelandic geologists have a nearly unparalleled opportunity to analyze the long-term behavior of the forces which affect their island. Untutored farmers understood many of the salient features of local volcanology and glaciology centuries before scientists in mainland Europe, and the tradition of important scientific observations by laymen continues to this day. Within the past fifty years detailed studies of Icelandic geology by scientists from many countries have led to a realization of the importance of this island to research ranging from plate tectonics to geothermal energy production.

Iceland has of late also been "discovered" by planetary scientists. The uniqueness of this volcanic island, both as a training ground for astronauts and as a prime site for analog studies aimed at the Moon and terrestrial planets, is being recognized. The work described here, which began in Iceland and reaches to Mars or perhaps far beyond, bears witness to that fact.

ACKNOWLEDGMENTS

The completion of any piece of research reflects the contributions of many individuals. I owe large debts of gratitude to a number of good friends and scientific colleagues.

First, I wish to thank Professor Robert Strom -- friend, teacher and capable advisor. The other members of my dissertation committee, to whom I could turn for support and advice, are Dr. William Bull, Dr. Charles Glass, Dr. Bradford Smith and Dr. Laurel Wilkening. Dr. Michael Drake made available several experimental facilities and Ms. Gail Georgenson provided considerable help in the Space Imagery Center. Special thanks go to Ms. Nancy Moore as typist, efficient departmental secretary and all around good person.

Field research in Iceland was approved by the Icelandic National Research Council, with Dr. Sigurdur Thorarinsson acting as research advisor. Dr. Oddur Sigurdsson and Dr. Kristjan Saemundsson gave generously of their expertise in matters of local geology. I particularly appreciate the assistance of Mr. Svienn Thorgrimsson.

Research at The University of Arizona was partially funded by NASA Grant NGL 03-002-191 to Professor Strom. The Scanning Electron Microprobe Quantometer Laboratory was established under NSF Grant DES 74-23721. NASA funding also helped to support the field studies in Iceland, for which I am grateful to Mr. Steven Dwornik. Additional assistance was provided by the Scholarship Committee of Trinity Presbyterian Church and by my parents, Dr. and Mrs. Carlton Allen. My debt to them goes far beyond the financial.

I am proud to acknowledge the inspiration provided by the late Dr. Gordon Macdonald. His teaching opened my eyes to volcanology and the discussion of subglacial eruptions in Volcanoes was the spark for this entire study.

Finally, let me thank Jaclyn Allen, my wife, co-worker and constant source of support. This work is dedicated to her.

TABLE OF CONTENTS

LIST OF TABLES

LIST OF ILLUSTRATIONS

ABSTRACT

The interaction of volcanism with ice and water produces a suite of landforms with morphologies highly characteristic of their origin. They include large flood channels, distinctive mountains and ridge systems, and fields of steam explosion craters. Features similar to these in form, size and geologic setting occur on Mars and have proved to be valuable indicators of the history of water on that planet.

Eruptions of Katla, a subglacial volcano in Iceland, have been followed by devastating meltwater floods. Rapid melting of large masses of ice by heat from the eruption is the only viable process for producing the water volumes and flow rates observed. Floods associated with a number of subglacial heat sources have created impressive channels and depositional zones across Iceland.

Central vent eruptions beneath glaciers in Iceland and North America built steep-sided, flat-topped "table mountains". The typical eruptive sequence commenced with a hot gas phase which melted a small cavity in the ice, followed by the extrusion of lava into the meltwater, forming basaltic pillows. As the pillow pile built to within a few hundred meters of the top of the ice the style of eruption shifted from effusive to explosive. This change resulted from a combination of vesiculation and chilling of the magma by water, and produced a fine glassy tuff. When the ice surface was finally reached and water was denied access to the vent the eruption products changed again to include pillow breccia and basalt flows. Postglacial volcanism capped many table mountains with additional flows, craters and cones.

A similar sequence resulted in the formation of ridges by subglacial fissure eruptions. Such ridges are composed almost wholly of glassy tuff. They rarely built high enough to completely penetrate the overlying ice, so capping lava is usually not present. These ridges sometimes occur individually, but in other cases the products from a number of eruptions combine to form extensive masses of tuff.

Lava flowing over wet ground can cause the water to boil explosively. Such steam explosions in Iceland produced a variety of cones and tumuli known collectively as pseudocraters. Thermal calculations indicate that near-surface ice can be nearly as effective as water in forming these features.

The melting of ground ice by shallow magma intrusions has been proposed to account for certain channels on Mars. Such a mechanism does not appear

feasible, based on heat flow requirements and geologic observations. An alternative model, which invokes slow melting of ice and subsequent release of water under pressure, is favored.

Analogs to terrestrial table mountains, ridges and pseudocraters have been identified on Viking imagery of Mars, notably in Acidalia Planitia. Photointerpretation of this region has led to the formulation of a consistent geologic history. An ice-rich regolith once overlay the present plains surface, and may still exist in the adjacent highlands. Volcanic eruptions beneath this layer produced the Martian analogs to table mountains and ridges. Estimates of the heights of these features indicate that the regolith averaged approximately 500 m thick. At some time changes in climate or subsurface heat flow led to melting of the ice and breakdown of the regolith. Subsequently the exposed lowlands were extensively resurfaced by thin lava flows.

A similar history is postulated for all of the northern plains of Mars, based on the occurrence of geologic features resembling those in Acidalia Planitia. The ice-rich regolith required by this model could have contained 8×10^{21} cm^3 of water. This is several times the total volume thought to have been outgassed by the planet, based on atmospheric measurements. A serious discrepancy thus exists between interpretations of geologic and atmospheric data concerning the history of water on Mars.

CHAPTER 1

INTRODUCTION

Research on the interaction of volcanism with ice was motivated by the continuing debate among planetary scientists concerning the importance of water in the surface history of Mars. During the course of two years of study it has proven possible to understand, both qualitatively and quantitatively, a poorly studied class of terrestrial landforms. In addition, the recognition of similar features of Mars has provided important new data on that planet's evolution.

The current evidence for significant amounts of ground ice on Mars is derived mainly from photointerpretation of large scale geologic features. These include flood channels with their associated source areas, the planet-wide dichotomy between the old southern uplands and the younger, lower northern plains, and the ubiquitous rampart craters with ejecta blankets which appear to have contained entrapped volatiles. The present research concerns a fourth class of landforms which have proven useful in identifying regions formerly covered by ice, namely those landforms which result from volcanic eruptions into an ice-rich environment.

The term "volcano-ice interaction features" is used in this study to denote three major types of landforms. First are those which result directly from the rapid melting of large volumes of ice. These include collapsed source areas, flood channels and alluvial deposits. A second group of features includes the steep-sided "table mountains" and serrated ridges of glassy tuff and pillow breccia which are the volcanic constructs built by sub-ice central vent and fissure eruptions. Finally, a varied group of landforms produced by steam explosions is discussed under the general designation of "pseudocraters".

The research for this dissertation was divided into three overlapping phases, extending over a period of approximately two years. The initial phase consisted of field research in Iceland, where a number of volcano-ice interaction features were examined on a reconnaissance basis. This study was complemented by a literature search and interpretation of aerial photographs of such features from sites in Iceland and elsewhere. The second phase involved a mathematical analysis of subglacial volcanism. This work also included laboratory analysis of rock samples from Iceland, as well as experiments designed to simulate the behavior of magma in a glacial environment. The purpose of this phase of the research was twofold -- to verify the sequence of events in a subglacial eruption as indicated by field observations and to provide a quantitative basis for analyzing volcano-ice

interactions on Mars. The third phase was the Mars study itself. Thousands of images from the two Viking orbiting spacecraft were examined in a search for analogs to the landforms seen in Iceland. Photointerpretation of the regional geology associated with such features was carried out and the mathematical models were employed to study the evolution of volcanism and gound ice on the Martian surface.

Subglacial volcanic eruptions have been described or postulated in many parts of the world, including the continental United States and Alaska, Canada, Ecuador, Spitsbergen and Jan Mayen islands and Antarctica. Iceland was chosen as the site for field research for several reasons. First, being one of the most volcanically active regions on Earth, and having been almost totally covered by glacial ice during the Pleistocene, the country displays a wide variety of subglacial volcanic landforms. Second, and equally important, a number of these features have been well studied by Icelandic geologists, several of whom provided considerable assistance in the present investigation.

Research on Icelandic subglacial volcanism is still in an early, largely descriptive stage. The basic interactions involved have been recognized for many years (e.g., Noe-Nygaard 1940), and the submarine eruptions which formed the island of Surtsey (Thorarinsson 1964) filled in many details of the process. However, most field studies have concentrated on the peculiarities of individual localities rather than stressing the basic features common to all or most subglacial eruptions. In addition, the majority of these investigations lack even the most basic mathematical, physical and thermal analyses. Two major contributions of the present study are the definition of a common eruptive sequence for subglacial volcanoes and the introduction of mathematical modeling and modern analysis techniques to this field.

This research goes on to make use of the large-scale landforms produced by volcano-ice interactions to study the geology of Mars. One the major current questions in planetary science concerns the history of water on or below the Martian surface. In the years since Mariner 9 revealed that this planet was once subjected to massive floods (Milton 1973) theories of the source and fate of water on Mars have proliferated. Sharp (1973a, 1973b) was among the first to postulate the importance of ground ice in the formation of a number of Martian surface features. With the acquisition of thousands of high resolution images from the Viking orbiters (Carr et al., 1976) the detailed search for additional indications of subsurface ice and water became possible.

Geologic features which may reflect ice beneath the Martian surface are abundant on the Viking photographs. Masursky et al. (1977) summarized the evidence from the channels, while Carr et al. (1977) did the same for the craters. Carr and Schaber (1977) described a large number of landforms which resemble those found in permafrost environments on Earth. The present study is the first to employ volcano-ice interaction features to probe the evolution of Martian ground ice in both space and time.

CHAPTER 2

TERRESTRIAL GEOLOGIC STUDIES

Reconnaissance field studies of a number of sites in Iceland were carried out during a three week period in the summer of 1978. Fig. 1 shows the locations of features discussed in the following chapters. The field work was supplemented by the study of high resolution aerial photographs, geologic and topographic maps, and the published observations of many previous investigators.

2.1 Subglacial Volcanism

Volcanic eruptions beneath glacial ice have been common occurrences throughout much of the geologic history of Iceland. One manifestation of such an eruption is the "jokulhlaup", or glacial burst -- a meltwater flood of short duration and large volume. Thorarinsson (1960a) stated that jokulhlaups which result from major eruptions of the subglacial volcano Katla are among the largest floods ever to have been witnessed by human beings.

The volcanic construct resulting from a subglacial eruption is much less easy to observe. Shortly after the 1934 eruption of the Grimsvotn caldera, however, a team of Danish and Icelandic scientists reached the site and reported a spectacularly drained glacial lake and an impressive outpouring of lava and tephra (Nielsen 1937). These researchers also discussed a probable eruption at another site beneath the glacier -- activity which apparently did not produce sufficient heat to melt through the ice. While observations such as these yield some information on the products of subglacial volcanism, most of our knowledge comes from the study of volcanic piles remaining after the glaciers' retreat.

Iceland has a long history of volcanic activity and widespread glaciation, which has yielded many landforms resulting from subglacial eruptions. Two very distinctive landforms, comprising over one hundred features, have been identified with eruptions of this type. Table mountains, or "stapis" in Icelandic, are steep-sided, flat-topped piles of glassy basaltic tuff and pillow lava, often capped by flat-lying basalt flows. Narrow, serrated ridges of the same basaltic glass composition are also common. The basaltic glass is characteristically altered by the process of palagonitization to a yellow-brown material known in Iceland as "moberg", literally brown rock (Jakobsson 1978).

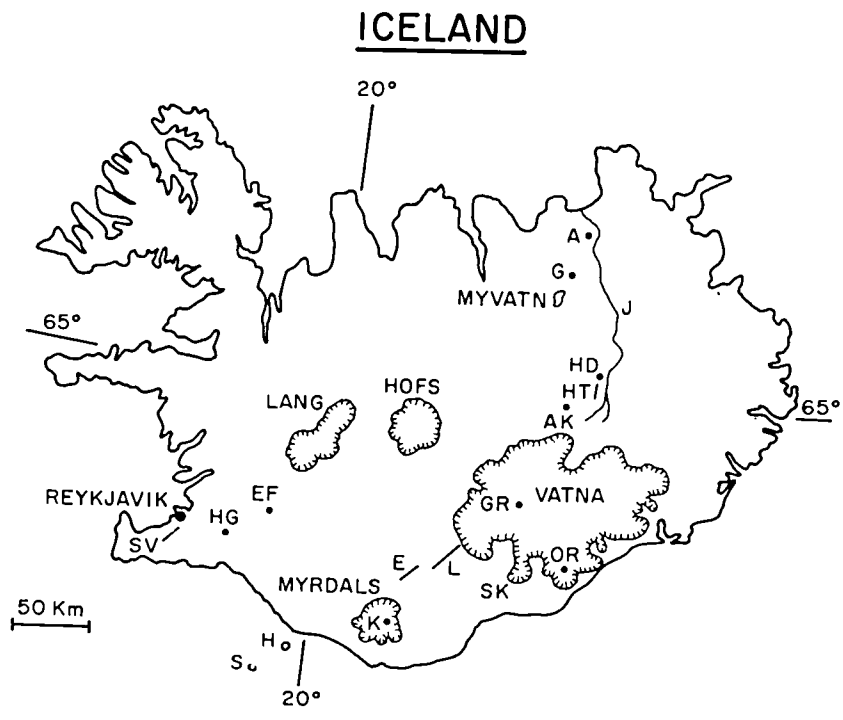

Subglacial volcanoes
- GR Grimsvotn
- K Katla
- OR Oraefajokull

Volcanic islands
- H Heimaey
- S Surtsey

Table mountains
- EF Efstadalsfjall
- G Gaesafjoll
- HD Herdubreid
- HG Hengill

Eruptive fissures
- E Eldga
- L Laki

Moberg ridges
- HT Herdubreidtogl
- SV Sveifluhals

Caldera
- AK Askja

Icecaps
- Hofs
- Lang
- Myrdals
- Vatna

Outlet glacier
- SK Skeidarar

River
- J Jokulsa a Fjollum

Lake
- Myvatn

Flood channel
- A Asbyrgi

Capital city
- Reykjavik

Fig. 1. Field Study Locations in Iceland

The moberg mountains and ridges have been variously attributed to tectonics, i.e., horsts (Nielsen 1933, Einarsson 1962), or erosion (Doorninck 1935), but they were first considered to be subglacial volcanoes by Pjetursson (1900). Most investigators who have carefully studied the table mountains and ridges have come to accept this latter origin (Noe-Nygaard 1940, Bemmelen and Rutten 1955, Saemundsson 1967, Sigvaldason 1968 and Jones 1970). The results of the present investigation also support this theory.

Most of Iceland's table mountains and ridges have lateral dimensions of a few kilometers. Much larger moberg deposits occur, however, particularly beneath present icecaps. These deposits apparently represent the combined products of many eruptions from numerous vents which occurred over the long periods of glaciation.

Another type of feature common in Iceland is the pseudocrater. This is a crater similar in appearance to a cinder or spatter cone, but formed when a relatively thin lava flow covers wet ground, producing steam explosions (Thorarinsson 1960b). While minor in scale compared to the other features, pseudocraters are important to this study both as characteristic interaction features and because of their usefulness in studying conditions on the surface of Mars.

2.2 Jokulhlaups

Floods bursting from beneath glaciers are not uncommon in many parts of the world, though the Icelandic name jokulhlaup has become something of a generic term. Most of these floods have nothing to do with volcanic heating, but may result from rockslides into glacial lakes or the breaking or lifting of an ice dam (Preusser 1976, pp. 140-141). Floods in regions of active volcanism may be caused by melting of snow and ice by lava or tephra (Preusser 1976, p. 139) or by eruptions through a crater lake (Macdonald 1972, pp. 429 ff.). In Iceland, however, two other mechanisms are responsible for the largest and most devastating floods.

The volcano Katla, located beneath 400 m of ice near the southeast edge of the Myrdals glacier, is thought to initiate floods composed mostly of meltwater produced during its eruptions (Thorarinsson 1960a). Eruptions in 1625, 1660, 1722, 1823, 1860 and 1918 were quickly followed by water discharges up to 2×10^9 m^3, with peak flood rates exceeding 10^5 m^3/sec (Preusser 1976, Table 21). The usual time elapsed between the initial appearance of an eruption cloud and the peak of the flood is approximately two days (Barth 1950, p. 10).

Explosive eruptions of the Oraefajokull caldera in 1362 and 1727 produced disastrous floods and ash falls. In addition, the 1727 activity was accompanied by the extremely rapid advance of two of the outlet glaciers of the Vatna icecap (Bardarson 1974, pp. 70-78).

The characteristic cycle of recent floods from the Grimsvotn caldera, however, is based on a very different mechanism. Thorarinsson (1960a) has determined that the jokulhlaups from Grimsvotn are semi-periodic. Since 1934 such floods have occurred every 4-6 years, with the last one in 1972 (Bullard 1976, p. 303). While Grimsvotn has not erupted in over three decades, continuous solfatara (i.e., hot gas) activity within the caldera melts the adjacent ice and snow, forming a large lake. Recent studies have shown that, upon reaching a sufficient depth, the hydraulic pressure of the lake water lifts a section of the bounding ice and opens an escape channel beneath the Skeidarar glacier (O. Sigurdsson, National Energy Authority of Iceland, personal communication, 1978). Thus the resulting floods are not dependent on a volcanic eruption.

The key features formed in connection with a jokulhlaup, for the purposes of geomorphic analysis, are the source area, flood channels and deposition area. The source of the Grimsvotn floods is a lake which may grow as large as 35 km^2 and 500 m deep (Bardarson 1974, pp. 54-57). A small Katla flood in 1955 was accompanied by the formation of two circular depressions one kilometer across by 80 m deep in ice 400 m thick (Thorarinsson 1960a). Thorarinsson and Rist (1955) described a probable subglacial eruption near Grimvotn which formed a depression in the ice 2.5 km long and over 100 m deep.

The floods from Katla and Grimsvotn which emerge onto the southern outwash plains cut channels in sand and gravel as much as 10 m deep and hundreds of meters wide near the glaciers (Nummedal et al. 1974). Boulders and ice blocks tens of meters across are transported for short distances (Thoroddsen 1925), and huge scour patterns are formed around obstacles (Nummedal et al. 1974). Lewis (1936), however, noted that in the loose gravel of the outwash plains flood waters do not cut down so much as spread laterally, sometimes for many kilometers. Thus, while traveling the road which comes within six kilometers of the points at which the Katla and Grimsvotn floods emerge from beneath the glaciers, the present author observed only very wide jokulhlaup channels which were not more than 2-3 m deep.

Jokulhlaup erosion can be much more spectacular where the flood channel is confined by solid rock. Floods, probably triggered by eruptions beneath the northern section of the Vatna icecap, follow the course of the river Jokulsa a Fjollum north to the sea (Thorarinsson 1960c). The small coastal plain has been flooded numerous times in the last several centuries. Just south of this plain the river flows through a deep gorge, and to the west of this gorge is the 3.5 km long valley of Asbyrgi with its 100 m high dry waterfalls cut into solid basalt (Fig. 2). Immediately south of the falls the abandoned channel is pocked with large scour marks. Within 10 km of Asbyrgi aerial photography reveals a number of other former channels and falls which display features of erosion and deposition reminiscent, on a somewhat reduced scale, of the channeled scabland of Washington State (Baker and Nummedal 1978). While Torarinsson (1960c) attributed the erosion of Asbyrgi to river cutting along lines of tectonic weakness, recent work suggests that massive jokulhlaups may have been responsible (Sigurdsson, personal communication, 1978).

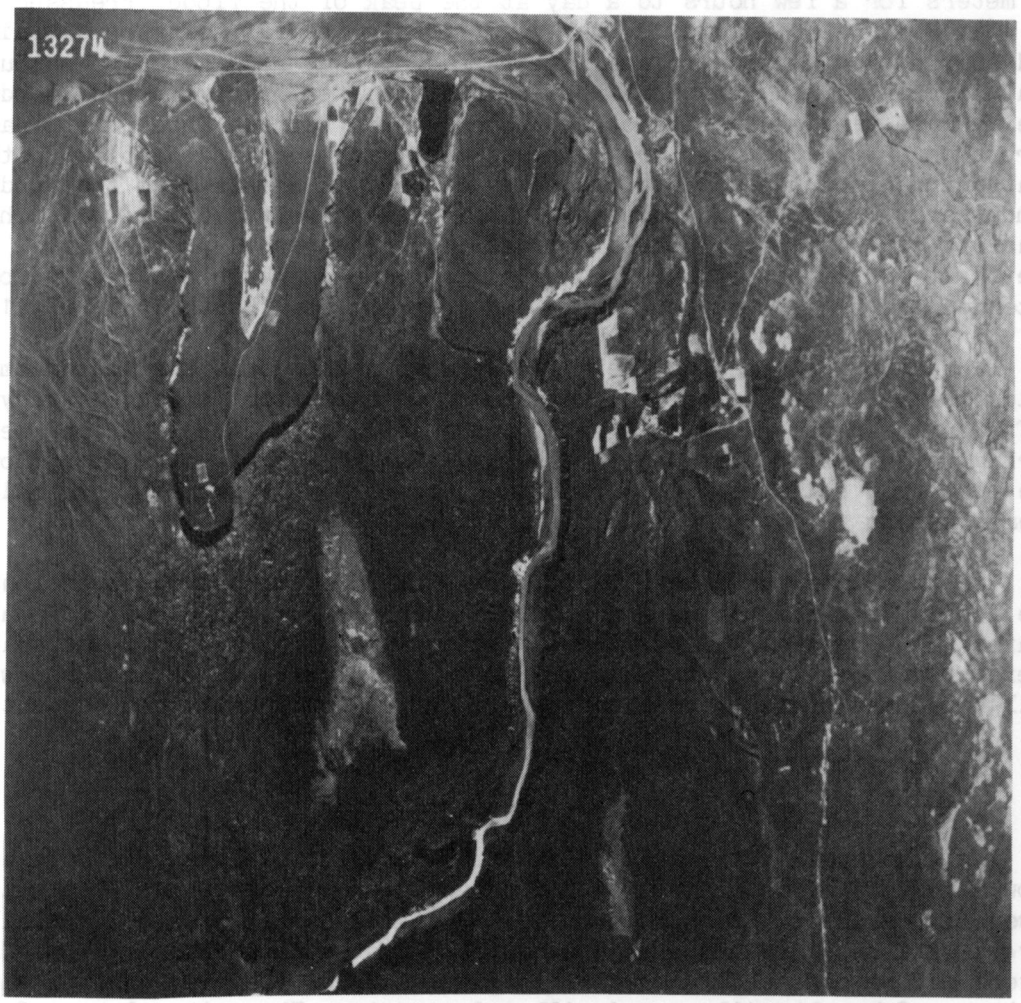

Fig. 2. Asbyrgi

The valley of Asbyrgi is 3.5 km long and has a 100 m high dry waterfall at its southern end. Downstream from the falls scour marks in the basalt show evidence of the floods which formed this feature. The present course of the river Jokulsa a Fjollum lies about 2 km to the east of Asbyrgi.

Most Icelandic jokulhlaups, however, appear to be considerably more important as agents of deposition than erosion. Upon emerging from beneath the ice the flood waters generally spread for kilometers across the flat outwash plains, or "sandur". Water may cover these plains to depths of tens of meters for a few hours to a day at the peak of the flood (Preusser 1976, p. 164; Barth 1950, Plate 2), but very rapidly the rate of flow diminishes and only a wide expanse of shallow braided streams remains. Two sandur plains form the southern coast of Iceland, one fed by rivers and floods from the Myrdals glacier and the other by those from Vatna. These flat, dark stretches, 30-50 km wide, are composed mostly of sand and pebbles, with a scattering of boulders up to one meter across. A sample from the Myrdals sandur showed that the pebbles are almost exclusively basalt, while the sand consists of fragments of the black basaltic glass known as tachylite. Since the first settlement of this area a millenium ago jokulhlaup deposition has extended the plain over two kilometers into the sea (Barth 1950, p. 11).

In summary, studies of Katla and Grimsvotn show that the mechanisms by which these two subglacial volcanoes produce meltwater floods are very different. In the first case most of the water is derived from ice melted during an eruption. The second case, however, involves not an eruption but the heat from solfataras slowly melting ice to form a lake which finally breaks out in flood.

The three major features of each type of jokulhlaup are depressions in the ice marking the source areas, flood channels and large depositional plains. The channel may be of two distinct varieties -- broad and shallow where they cross loose sand and gravel or relatively narrow and deep with well-developed signs of erosion where confining rock walls are encountered.

2.3 Table Mountains

Table mountains, the subglacial equivalents of small shield volcanoes, show a variety of shapes, sizes and compositional variations. Typically the lower, interior portions are composed of pillow basalt masses, overlain by layers of finely-divided orange basaltic glass (sideromelane). The glass layers may be essentially free of larger rocks, or they may contain varying mixtures of basalt pillows and pillow fragments. The outer slopes of the mountain, especially near the top, are commonly mantled with a scree of such fragments. Many table mountains are capped with a series of flat-lying basalt flows, and some display summit cones and craters. Fig. 3. shows Gaesafjoll, a typical large table mountain in northern Iceland, which is discussed in detail below (Section 2.3.2).

The first recognition of the subglacial origin of table mountains was by Pjetursson (1900), followed by qualitative confirmation through the field studies of Noe-Nygaard (1940) and Kjartansson (1943). The first and still most extensive modern study was that of Bemmelen and Rutten (1955), which surveyed the mountains in the north central section of Iceland. Kjartansson's (1960a) work is a worthwhile review of the knowledge of subglacial eruption mechanisms to that time. Several recent studies of

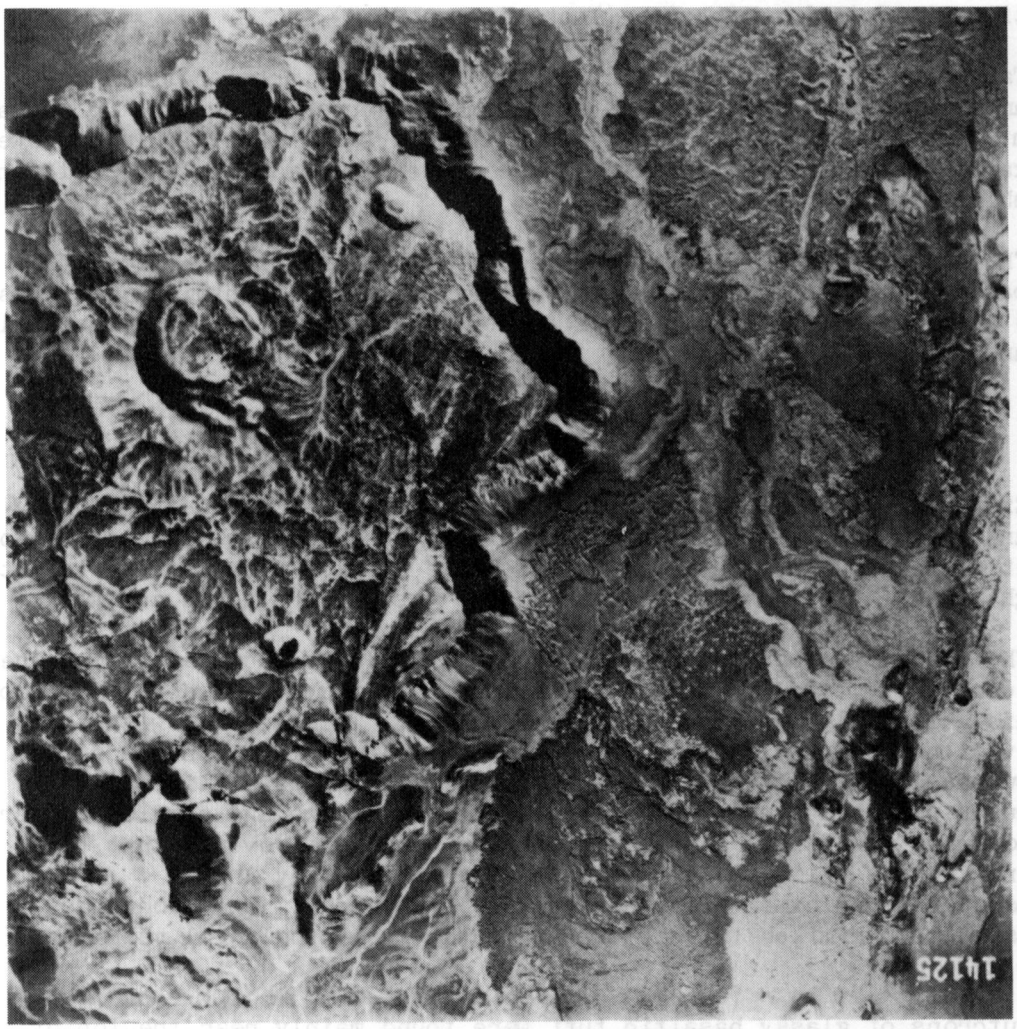

Fig. 3. Gaesafjoll

The table mountain Gaesafjoll, approximately 7 km long by 5 km wide, is bounded by 200 m high moberg cliffs. Caprock and postglacial lavas were erupted from three summit craters, the largest of which occupies a breached cone.

table mountains (Jones 1970, Sigvaldason 1968, Saemundsson 1967) presented clearer insights into the eruptive process than had been available previously. The building of the island of Surtsey by submarine eruptions which began in 1963 produced a striking counterpart to a subglacial eruption. This activity, commencing beneath the sea rather than in glacial meltwater, demonstrated the mode of formation of almost every major constituent of table mountains (Thorarinsson 1964).

Table mountains have been identified in several areas outside of Iceland. Mathews (1947) located seven such features in British Columbia. Recently Hoare and Coonrad (1978) identified a table mountain in southwest Alaska. Carlisle (1963) discussed a formation on Quadra Island, British Columbia, very similar to Surtsey.

The present investigation combined field research in Iceland with photoanalysis of several of the North American table mountains. By these means a scenario was developed for the evolution of a "typical" subglacial volcano.

2.3.1 Efstadalsfjall

Efstadalsfjall is a simple table mountain located in south central Iceland. The mountain rises from a roughly circular base 5 km across to a height of some 500 m (Fig. 4). This feature has not been studied in detail, though Jones (1970) investigated mountains just to the north and west.

The present author ascended Estadalsfjall by the southeast slope, next to a deep gully. Pillow basalt which forms the mountain's core was exposed in this gully well over halfway to the summit. This accords with the observations of Jones (1970) concerning the volumetric dominance of the pillow basalt piles in nearby table mountains. The basalt is black and vesicular with a medium porphyritic texture. Olivine and plagioclase are the dominant minerals. Electron probe microanalysis reveals that the olivine is Fo_{83} while the plagioclase is approximately An_{82}. Microscopic chromium-rich spinel crystals also occur. The groundmass composition is similar to that of basalts in many subglacial volcanoes (see Table III, p. 211).

Outcrops of glassy basaltic tuff were found mainly near the top of the mountain. This glass, orange-brown sideromelane, has a composition close to that of the pillow basalts, but has been strongly palagonitized. Microscopic plagioclase and spinel crystals are scattered among the moderately angular glass fragments, which generally measure around 0.5 mm across.

The mountain is mantled for almost its entire height with several meters of a mixture of glass fragments and vesicular black pillow basalt breccia. This unit occurs in pronounced layers parallel to the local dip of the mountain slope, and matches the description of "foreset breccia" described on the nearby table mountains by Jones (1970). Breccia layers on

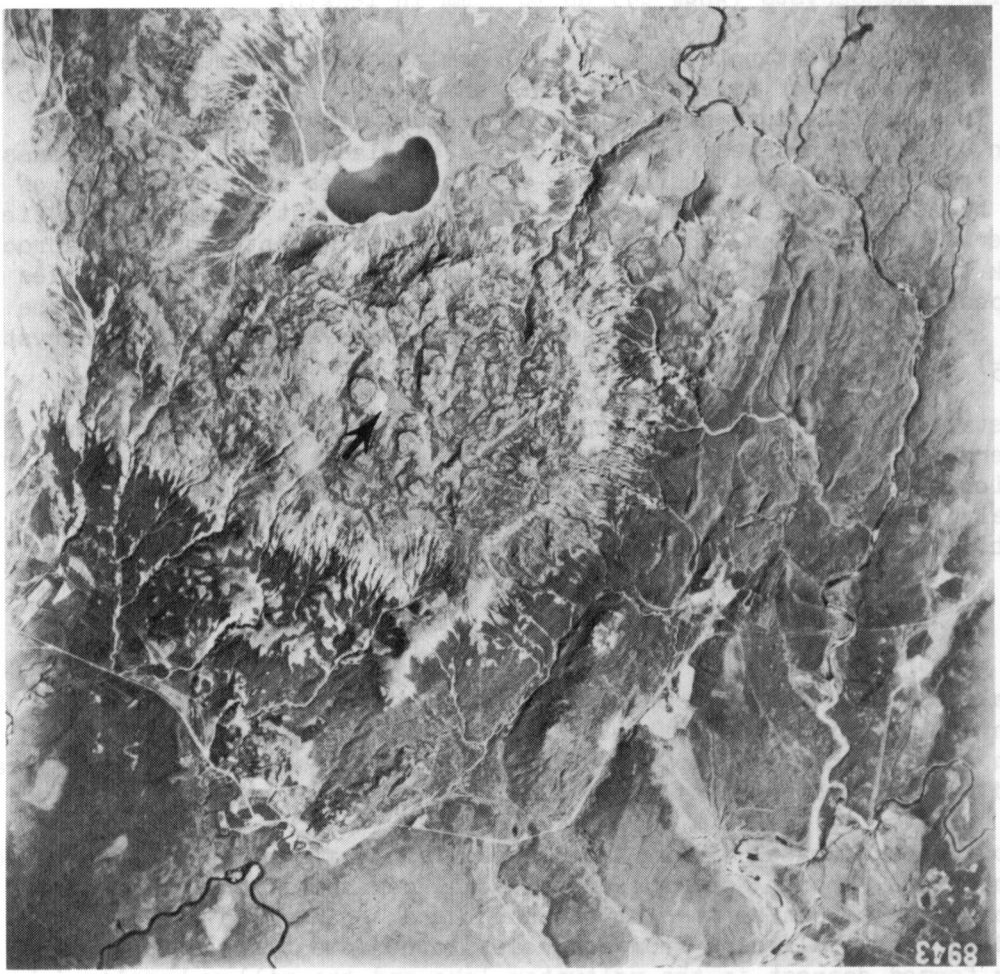

Fig. 4. Efstadalsfjall

The table mountain Efstadalsfjall measures 5 km across and 500 m in height. The caprock has been heavily eroded by glaciation. A small lake (arrow) may mark the location of the eruptive vent.

Efstadalsfjall occasionally alternate with layers composed exclusively of pillow basalts. These may represent individual flows which entered the meltwater or somewhat later intrusions into wet deposits. The basalt and the glass in the foreset breccias have compositions approximating those of other units on the mountain. Both basalt and glass contain abundant plagioclase phenocrysts (An_{84-87}) up to 1 mm in length.

The caprock, or "topplateau" in the terminology of Bemmelen and Rutten (1955), is composed of several flows of dense, gray basalt totalling 4-5 m thick. This unit is apparently contemporaneous with the rest of the mountain, since it has been heavily scarred by glacial erosion (Kjartansson 1962). Prominent NE-SW trending near-vertical faults offset sections of the caprock by as much as 2 m. No summit crater is evident either in the field or on aerial photographs, though a small lake in the center of the caprock may mark the location of the vent. A swarm of sub-parallel feeder dikes has been exposed by erosion near the top of the mountain. The basalt of the caprock is porphyritic, with abundant millimeter scale olivine phenocrysts (Fo_{65-85}) and 10 μm crystals of anorthite, clinopyroxene and spinel.

As stated above, this is a simple table mountain, apparently formed by a single eruptive sequence. While the caprock has been strongly modified by glaciation and the outer slopes are deeply gullied, the preservation of relatively thin breccia layers on the slopes indicates that Efstadalsfjall has lost little mass since the time of its formation.

2.3.2 Gaesafjoll

Gaesafjoll is a large, complex table mountain located approximately 15 km north of Lake Myvatn in northern Iceland. Studied extensively by Bemmelen and Rutten (1955, pp. 41-52), this imposing structure (Fig. 3) has received little subsequent attention.

No outcrops of basal pillow basalt are visible along the southwest side of the mountain, though Saemundsson (personal communication, 1978) stated that such material can be seen at the north end. Since the terrain surrounding Gaesafjoll dips from southeast to northwest the northern end probably formed deepest in the meltwater lake and the pillow basalt might be expected to be more extensive there.

Gaesafjoll is bounded on the west, north and east sides by steep cliffs 100-200 m high composed almost exclusively of millimeter sized fragments of glassy tuff. Most of this glass appears to be sideromelane, and it shows a fairly minor degree of palagonitization. The cliffs display massive layers of essentially monomict glass fragments, separated by sharply defined horizontal beds several meters thick composed of basalt pebbles and pillow fragments. This well-sorted bedding is strongly indicative of deposition in water rather than by airfall.

In a valley on the southwest flank of Gaesafjoll the massive beds of relatively uncontaminated tuff give way to alternating layers of tuff and mixed tuff and breccia, some of these layers being as much as 10 m thick. The breccia contains both pillow fragments and unbroken pillows up to 70 cm across. The pillows display well-defined chilled rims of tachylite as well as numerous vesicles. The mode of association of the uncontaminated tuff with pillow breccia layers indicates that the pillows were formed by lava flows into a meltwater lake, rather than as intrusions.

Evidence of intrusion is visible on the south face of Litla Karfla, a small moberg mountain immediately adjacent to the south end of Gaesafjoll. Here a prominent basalt dike within a layer of clean fragmented glass displays prominent columnar structure with a variety of orientations. This dike is interpreted as an intrusion into a wet deposit, possibly at a time when the meltwater lake still surrounded the mountain.

The caprock of Gaesafjoll is tens of meters thick and composed of gray olivine basalt. This lava was probably somewhat eroded by glacial ice, and it was subsequently buried by post-glacial eruptions.

The postglacial lava, a dense, gray pahoehoe with prominent olivine phenocrysts, erupted from at least two of the three summit craters and built a prominent cone around the largest. This lava overflowed the sides of the mountain in several places and can be identified on the plains below (Bemmelen and Rutten 1955, p. 45).

Gaesafjoll is cut by dominant NNE-SSW and subordinant ESE-WNW high-angle faults which apparently controlled the shapes assumed by the summit craters. The orientations of some cliff faces may also be controlled by collapse along lines of structural weakness.

This mountain differs from Efstadalsfjall mainly in the relative importance of basal pillow basalt versus massive layers of sideromelane tuff. In Gaesafjoll the glass appears to be the dominant phase, indicating a long period of explosive eruption and deposition within the glacial lake.

2.3.3 Herdubreid

Herdubreid, the most impressive and best known of Iceland's table mountains, is located in the east central part of the country, some 50 km north of the Vatna icecap. Rising 1000 m above the surrounding lava plains, this is the tallest and most precipitous such feature in the region. Bemmelen and Rutten (1955, pp. 90 ff.) considered the present mountain to be the remnant of a larger structure partially destroyed by glacial erosion.

Access to the summit of Herdubreid is blocked by the sheer cliffs of the caprock except for a narrow breach on the northwest face. Due to constraints of time and equipment, the present investigation was restricted to the lower slopes, mainly in a prominent stream valley on the mountain's northeast side. Most of the major rock units were sampled, however, either in place or from material brought down by the stream.

Neither the present author nor Bemmelen and Rutten (1955) located a massive unit of pillow basalt at the base of Herdubreid. Sigvaldson (1968), however, asserted that such a unit does underlie the mountain, and extends to within about 200 m of the caprock. If so, glacial erosion and subsequent mass wasting prevented the recognition of the basal pillow lavas on the northeast slope.

The lower slopes of Herdubreid are extensively mantled by scree composed mainly of broken pillows. Approximately 100 m above the plains in the stream valley several layers of in situ pillows were encountered. This unit, as much as 4 m thick, apparently formed by intrusion into wet deposits of glassy tuff. At approximately the same level dikes and chimneys of basalt with poorly-formed columnar jointing are visible, probable indications of intrusion into dry sediments.

Large exposures of sideromelane, containing plagioclase (An_{67-89}) and olivine (Fo_{80}) phenocrysts but few pillow fragments, are common in the lower several hundred meters of the mountain. The higher slopes, which were not reached, show a much more ragged erosion pattern than their counterparts on Gaesafjoll. This observation, coupled with the large amount of pillow breccia encountered in the stream bed, indicates that the upper sections of Herdubreid may be composed largely of a glass and pillow basalt mixture. Boulders of such a composition, some containing whole pillows over one meter across, dot the lower slopes. The cliffs below the caprock are hundreds of meters high and do not appear to contain discrete layers. Apparently, due perhaps to limited access of water to the vent, this phase of the eruption was less explosive and produced more lava in relation to glass than other table mountains. Rounded basalt pebbles, possibly eroded by the glacier, were also incorporated into the eruptive products during this phase.

The Herdubreid caprock, tens of meters thick, forms a prominent escarpment girdling the entire mountain. This basalt is gray with a medium porphyritic texture. Large plagioclase (An_{71-74}) and olivine (Fo_{79}) crystals are scattered throughout the groundmass. The compositions of phenocrysts and matrix in this lava are strikingly similar to those of rocks nearly 1000 m lower in the sequence.

The postglacial lava which covered the south half of the caprock and formed a striking 150 m high cone was not sampled in the present investigation. Bemmelen and Rutten (1955, p. 95) reported that this lava is a very scoriaceous, porphyritic basalt, quite distinct from the underlying caprock unit.

Herdubreid's summit lavas display NNE-SSW trending faults which parallel the strike of fissures in the surrounding terrain. The postglacial cone lies along the extension of a line of eruptive vents capping Herdubreidtogl, the moberg ridge south of the mountain (Section 2.4.3). Bemmelen and Rutten (1955, p. 95) theorized that the Herdubreid cone is simply one vent on a fissure several kilometers long. The fact that the lava from this vent had to penetrate vertically through an additional kilometer of moberg deposits to reach the surface illustrates the weakness of this material.

Field observations and photogeologic studies indicate that a significant fraction of this mountain has been lost to glacial erosion. Bemmelen and Rutten (1955, p. 93) noted that Herdubreid was not a nunatak, since the caprock displays evidence of glaciation. Thus, at some time after its formation Herdubreid was enveloped by ice over one kilometer deep. This mass of ice was apparently responsible for considerable lateral erosion, as indicated by exposed dikes on the lower slopes and the lack of foreset breccias.

2.3.4 Hengill

The last major table mountain visited during the present field study was Hengill, a massive structure in southwest Iceland. Saemundsson (1967) published a comprehensive report on this complex feature. Arnason et al. (1969) and Barth (1950, pp. 102-113) noted the many active solfatara fields which dot the mountain.

Hengill is not an isolated table mountain, but rather the largest member of a complex which includes ridges, graben and recent eruptive vents. In exploring Hengill the path chosen ascended from the main graben on the northeast flank to the top of the second highest peak, 768 m above sea level.

No basal pillow basalt was observed in the area studied, though its existence was inferred by Saemundsson (1967). Several 2 m thick layers of pillows, interpreted as intrusive, were encountered. These outcrops of black, porphyritic lava were observed about two thirds of the way up the mountain slope. Saemundsson (1967) noted pillow basalts of picritic texture on Hengill which showed marked gravitational settling of olivine and other phenocrysts.

Thin layers of relatively uncontaminated sideromelane tuff were observed at the level of the solfataras somewhat less than half the distance up the slope, and again just beneath the summit. The glass, which has been strongly palagonitized, contains pillow fragments as well as rounded basalt pebbles.

Massive foreset breccia deposits tens of meters thick mantle most of the north slope of Hengill. Pillow lavas in the breccia are gray and porphyritic, with 1 mm plagioclase crystals occurring both in the interiors of the pillows and within the tachylite cooling rims.

The caprock basalt is black and dense, with aphanitic texture. Saemundsson (1967) described it as a tholeiite. Only a small patch 2-3 m thick caps the northern peak, while the geologic map (Kjartansson 1960b) shows another patch farther south. No source craters were seen, and none are shown on the map. One basalt flow which apparently originated from the caprock was sighted in a north-trending valley, indicating that significant stream erosion had taken place before eruption ceased.

This mountain has been strongly affected both by glacial and fluvial erosion. Glaciation apparently removed most of the caprock basalts and erased evidence of the vent or vents. Streams have eroded steep valleys 50 m deep. Prominent NNE-SSW trending faults, extensions of the still active regional system, have cut Hengill and the neighboring mountains.

2.3.5 Heimaey

The Vestmann Islands, lying about 15 km off the southern coast of Iceland, were formed almost exclusively by submarine volcanic eruptions. The largest island, Heimaey, however, also includes two large cones plus the 270 m high peak of Heimaklettur which may have been at least partly formed subglacially (Jakobsson 1968).

Heimaklettur is a rather simple structure composed of two main units. The lower portion is built of strongly palagonitized tuff containing a small admixture of basalt fragments and intercalated basalt layers, possibly intrusions. The glassy material forms near-vertical sea cliffs which display occasional settling layers and evidence of local sagging of the material after emplacement.

The upper section of the formation is dominated by massive flows of dense gray basalt separated from the tuff in a few places by a thin layer of poorly formed pillows. Plagioclase phenocrysts up to 1 cm long and smaller crystals of olivine are common within the flows. No craters are visible anywhere in the formation, although Jakobsson (1968) identified five separate centers of eruption. He reported that the Heimaklettur caprock series is some 20 m thick.

This part of the island bears no evidence of later lavas. However, Heimaey's newest volcano, one kilometer south of Heimaklettur, was formed in 1973.

No evidence was found at Heimaklettur which would distinguish between a subglacial or submarine origin for this feature. The lack of foreset beds and eruption craters suggests a major loss of material due to cliff retreat, leaving behind only the core of the original structure. Recent observations on the nearby island of Surtsey, however, show that even before the erosion very little actually distinguishes a submarine volcano from a table mountain.

2.3.6 Surtsey

Surtsey is the name given to the island at the south end of the Vestmann chain formed by submarine eruptions between 1963-67. It is included in this study because of the striking similarity of its eruption products to those observed in table mountains. Due to its importance as a site for observing biological development Surtsey is off limits to all but a few scientists. The following description is derived from Thorarinsson (1964).

The first signs that a submarine eruption was taking place off the south coast of Iceland were jets of black tephra sighted from a nearby fishing boat on the morning of 14 November 1963. Within one day the eruption, originating from a fissure some 500 m long, built a small island a few meters above sea level. Since the depth of the ocean at the eruption site was 130 m, quite a high volcanic pile was apparently built before any evidence of eruption was detected. Seismic records show weak activity possibly associated with Surtsey a week before the tephra phase began, but the tranquility of the initial eruption was striking. This quiet eruption may have corresponded to the initial pillow lava phase in table mountains (Thorarinsson 1966), though pillow lavas have not yet been recovered from the base of Surtsey.

The growing island continued in explosive eruption for over four months, producing glassy tuff and lava bombs when sea water had easy access to the vent. On those occasions when the water was blocked temporarily lava fountaining and gas jetting occurred. Thus both steam explosions and gas release from the magma affected the final state of the lava.

After April, 1964 access of water to the vent was effectively cut off by the growing mass of the island, and effusive activity commenced. Layers of basaltic lava capped the tuff and assured the survival of the island against wave erosion. At the ocean's edge some lava streams continued to flow into the water, while others were chilled and broken into pillow forms and glass fragments resembling the foreset breccias of table mountains.

As the Surtsey observations demonstrate, eruptions into a few hundred meters of sea water or glacial meltwater follow quite similar courses. Therefore, this island can be classified as a table mountain in all but name.

2.3.7 British Columbia

Mathews (1947) described seven volcanoes in northern British Columbia for which he suggested an origin by subglacial eruption. This hypothesis was based on reconnaissance field work and subsequent recognition of similarities between these mountains and those in Iceland.

Analysis of aerial photographs of four of the seven features supports the observations of Mathews concerning their morphologic similarity to some Icelandic table mountains.

As described by Mathews (1947) the table mountains, or "tuyas", are capped by flat-lying basalt flows 3-30 m thick. Underlying these caprocks are beds of fragmental material of basaltic composition. This unit dips steeply and is apparently free of interbedded flows. While its composition is not listed in detail, the gross description matches that of the foreset breccias seen in Iceland. Pillow basalt occurs at the base of at least one lava flow and pillow fragments are scattered through the foreset breccias.

One noteworthy location at which pillows were found is the summit of Ash Mountain, well over one kilometer above the surrounding terrain. If these pillows are part of a foreset breccia unit they indicate that the ice in this area was once over a kilometer thick.

Aerial photographs of Tuya Butte and Isspah Butte show them to be steep-sided, flat-topped structures similar to several of the Icelandic features described above. Glacial erosion has removed evidence of the source craters and formed cirques in the upper walls. Steep cliffs with scree slopes at their feet indicate that the material beneath the caprocks erodes similarly to the tuffs of Gaesafjoll and Herdubreid. Two other tuyas, Ash Mountain and Kawdy Butte, are much more complex and deeply eroded. While their gross morphologies are not diagnostic of an origin by subglacial volcanism, the work of Mathews (1947) shows that they are also table mountains. These two features may well be equivalent in their development to Hengill (Section 2.3.4).

2.3.8 Alaska

Hoare and Coonrad (1978) identified a single isolated tuya in the Togiak Valley of southwest Alaska. This feature stands 300 m high and was probably considerably larger than its present 15 km^2 before being severely eroded by glaciation. The authors suggested that, unlike its Icelandic and Canadian counterparts which formed beneath relatively stationary ice sheets, the Alaskan feature was built by eruptions into an active valley glacier.

The Togiak tuya is capped by flat-lying flows of alkali olivine basalt. Three aligned lakes in the caprock probably mark the vent locations. This caprock is underlain by pillow basalts and breccias on the south end and by palagonitized glassy tuffs further north. No exposures of basal pillow basalt were located.

Hoare and Coonrad (1978) doubted that other table mountains will be found in Alaska, except possibly on the Seward Peninsula. However, P. J. Cannon of the University of Alaska (personal communication, 1978) suggested the Wrangell Mountains in the east central part of the state and the volcanoes on the west side of Cook Inlet as the sites of possible subglacial eruptions.

2.3.9 Summary

The "normal" evolution of a table mountain, as summarized by Preusser (1976, pp. 118 ff.) and modified by the present author's observations, is as follows. A single vent or a short fissure opens beneath an ice sheet hundreds of meters thick, and a portion of the ice immediately overhead is melted by the initial rush of hot gas. This is soon followed by the intrusion of basaltic magma into the cavity containing a subglacial lake. Upon contact with water the lava cools rapidly, forming pillow basalt. This relatively quiet eruption into a confined pocket of water within the ice may

continue for several weeks, with heat released from the cooling lava slowly melting the confining glacial ice both overhead and laterally. In this manner the pillow mass may build to within a few hundred meters of the top of the glacier.

As the mountain increases in height the pressure of the overlying water decreases and gas within the magma expands. At the same time this more open structure of the magma allows meltwater to gain access to the interior of the vent where it chills the molten rock. A critical point is reached when vesiculation, aided by steam explosions, fragments the magma and the eruption enters an explosive phase. The chief product is now tephra composed of finely-divided sideromelane glass, with a varying admixture of pillow basalt fragments. After the top of the glacier is breached glass and rock fragments are blown high into the air. Those which fall back into the meltwater lake may form well-defined beds due to differential settling.

This phase of the eruption continues for days or weeks until the mountain has essentially reached the level of the lake surface and access of water to the vent become sporadic. Eruption products now alternate between glass and basalt which quickly flows into the water and forms pillows and pillow breccia. Sometimes these layers of foreset breccia mantle the volcano's outer slopes from top to bottom.

Eruption often continues subaerially after the lake level has been surpassed, and a caprock of flat-lying basalt flows is formed. The caprocks of most table mountains are somewhat scarred by subsequent glaciation, and lateral glacial erosion may carry away whole sections of the edifice. Long after the glacier has disappeared eruptions may resume, mantling the caprock with much younger cones, flows and craters.

The relative amounts of basalt and glassy tuff are quite variable among the table mountains studied. A representative composition is 60% tuff and 40% basalt by volume.

Many table mountains are distinctive enough in their large-scale morphology to be immediately recognizable on aerial photographs. Indeed, large features such as Gaesafjoll can be distinguished at the 80 m resolution of Landsat imagery. The key morphologic features of table mountains are their flat tops and steep sides. Many of these mountains also exhibit summit flows, cones and craters indicative of renewed eruptions after the formation of the main structure. Table mountains are characteristically less than 10 km wide, with heights which reflect the thickness of the ice sheet.

2.4 Moberg Ridges

The dominant style of volcanism in Iceland, as elsewhere on Earth, is the fissure eruption. Iceland's central graben, actually part of the median rift valley of the Mid-Atlantic Ridge, is cut by thousands of fissures which trend NE-SW in the southern part of the country and north-south farther

north. While no shield volcanoes have been active in Iceland for over 3500 years (Thorarinsson 1960b), innumerable fissure eruptions have taken place, the most recent in 1975.

Some fissure eruptions apparently involve a quiet effusion of lava with little associated explosive activity. The product in such a case is a thin, widespread flow which may totally conceal its source. Commonly, however, explosive eruptions from individual points along a fissure precede the flow of lava. Here forms a line of cinder and spatter cones tens of kilometers long. Lava pours from these craters and the flows may coalesce into extensive sheets. The Laki eruption of 1783 (Thorarinsson 1970) and the "Myvatn fires" of 1724-29 (Rittman 1938) were of this type.

Subglacial fissure eruptions produce landforms very different from crater rows and lava sheets. As described by Kjartansson (1960a) the features are "ridge shaped, often serrated mountains or low hills, or straight lined, more or less continuous rows of such mountains." A small group of ridges just north of Gaesafjoll is shown in Fig. 5. Some of the largest ridge systems in Iceland, just west of the Laki fissure, are up to 35 km long, 2-4 km wide and 200-400 m in height (Preusser 1976, p. 249).

While moberg ridges are common in Iceland due to the predominance of young eruptive fissures, such ridges have not been reported elsewhere. However, P. Hammond of Portland State University (personal communication, 1978) has identified one such feature in the Cascades and believes that others may be found in the region. Thorarinsson (1970) has suggested that many of the linear features which parallel the mid-ocean rift system on the sea floor may be the submarine counterparts of Icelandic moberg ridges.

2.4.1 Sveifluhals

Sveifluhals is a prominent 23 km long ridge which strikes NE-SW across the Reykjanes peninsula south of Reykjavik. The author climbed the steep eastern slope, near the south end of Lake Kleifarvatn, to a point just below the 395 m peak.

This ridge, with a net elevation of over 200 m, covers a layer of basal pillow basalt. One outcrop of this material was located in a roadcut near the north end of the lake. The pillow structure is poorly developed in dense, medium gray lava. Millimeter scale plagioclase phenocrysts (An_{84-87}) occur in the matrix.

Siderromelane tuff, exhibiting varying degrees of alteration, was seen mainly on the lower slopes. This unit contains occasional broken pillows and many small basalt fragments around 2 mm across. The glass itself is highly vesicular and contains numerous large plagioclase (An_{78-79}) laths. In addition the glass of this mountain is unique among the present samples in incorporating microcrystals some 10 μm long directly into its structure. The compositions of these microcrystals of olivine (Fo_{80-82}) and plagioclase (An_{72-76}) were used to derive the eruption temperature of the glass (Section 3.1.5).

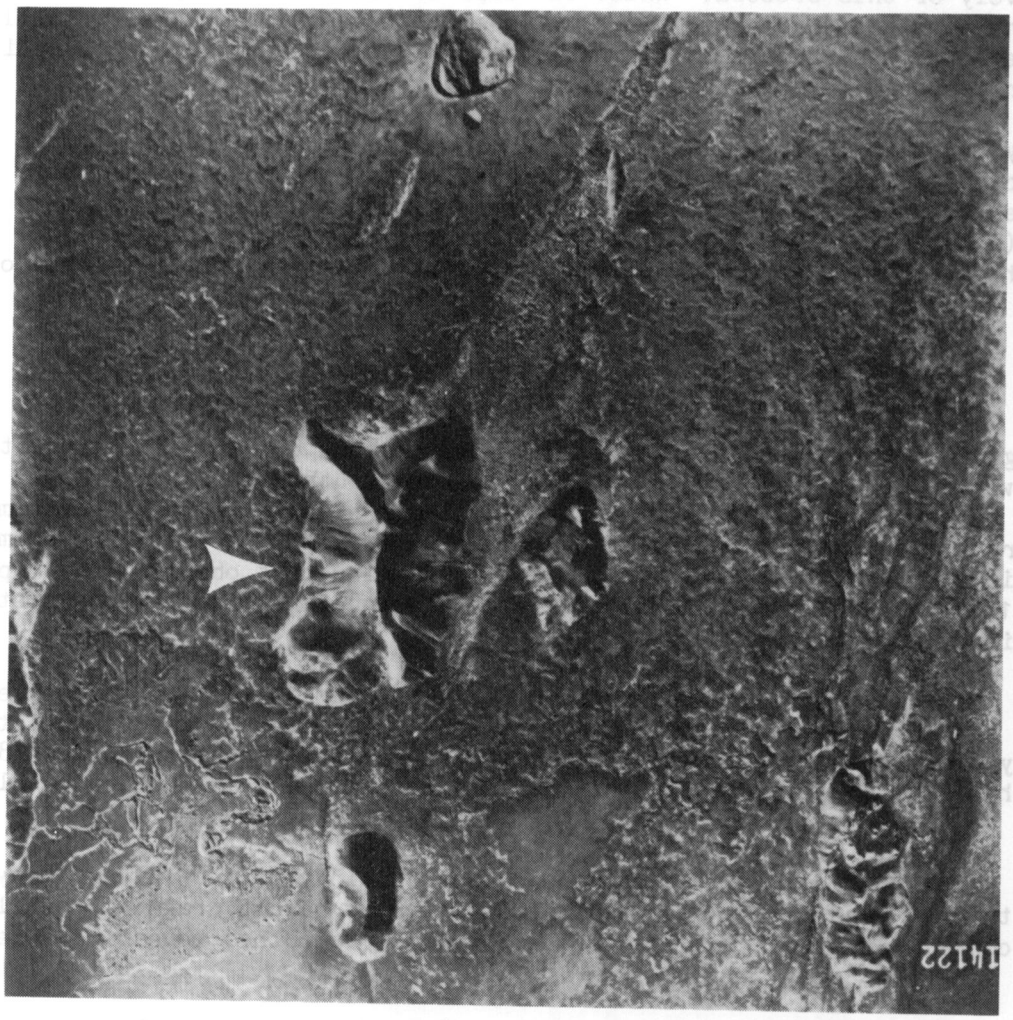

Fig. 5. Thorunnarfjoll

The moberg ridge Thorunnarfjoll (arrow) is approximately 2 km in length and 280 m high. A number of smaller, parallel moberg ridges are also shown. The crater to the north of Thorunnarfjoll is the main vent of a small shield volcano.

Sveifluhals may have reached close to water level during its eruption, since steeply-dipping beds of probable foreset breccia mantle the slopes. These beds may simply represent local variations in the tuff-pillow fragment mix, however, since at least one such bed grades laterally into much less contaminated tuff. In the area examined, the ridge crest consisted almost exclusively of this breccia. While the dips of the foreset layers are accordant with the underlying slope at lower altitudes, the highest beds lie contorted into many bizarre attitudes. Water turbulence during the eruption or later tectonic movement are possible explanations.

Many eruptive fissures on the Reykjanes peninsula have been active in postglacial times. While Sveilfuhals bears no lava caprock, linear vents on both the northwest and southeast slopes have produced cinder and spatter ridges (Kjartansson 1960b). A subordinate moberg ridge also parallels Sveifluhals at the base of its southeast side, indicating that more than one fissure may have been active beneath the glacier.

2.4.2 Eldga

Eldga is a 27 km long system of explosive graben, possibly the largest in the world (Schwarzbach 1964, p. 65). Located southwest of the Laki fissure and striking nearly parallel to it, Eldga bisects the great system of moberg ridges between the Vatna and Myrdals icecaps (Fig. 6). The 8 km long main rift was studied on a day when low-hanging mist obscured the tops of the 140 m high cliffs. The simple internal structure of one ridge system was obvious, however.

The rift apparently penetrates to pre-glacial basalt, for massive layers with no pillow or columnar structure were observed. Glassy tuff appears to directly overlie this material. Saemundsson (personal communication, 1978) noted that many other ridges in this region also lack a basal pillow basalt unit.

The ridges cut by Eldga seem to be composed mainly of tuff layers many meters thick. Some layers show minimal addition of basalt fragments, while others contain prominent rounded cobbles, probably smoothed beneath glacial ice.

At least one 10 m thick basalt flow is visible part way up the graben wall. This flow may mark a point in the eruption when the meltwater drained away. Water subsequently reentered the vents, however, because the moberg pile continues above the flow and extends to the ridge top. None of the ridges in this region bear lava caprocks. The basalt flows within Eldga itself are associated with the formation of the graben, which occurred long after the ridges were built (Preusser 1976, p. 249).

2.4.3 Herdubreidtogl

Immediately south of Herdubreid stands the 8 km long ridge Herdubreidtogl. This 2-3 km wide feature is composed of a broad lower

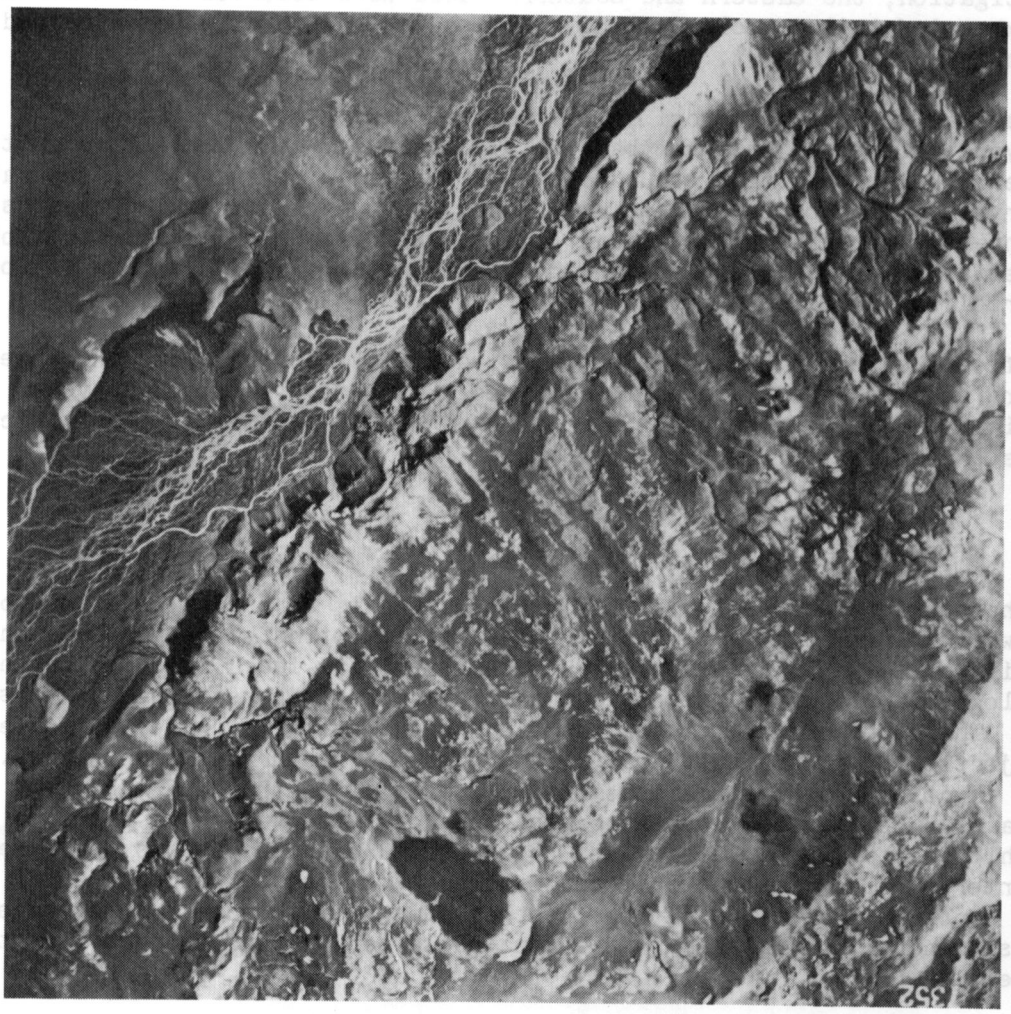

Fig. 6. Giljabrunir

Giljabrunir is one of the large moberg ridges which occur between the icecaps of Vatna and Myrdals. This ridge segment, approximately 6 km long and up to 250 m high, lies parallel to and about 25 km NNE of the Eldga graben.

plateau and a central spine which rises to 470 m above the surrounding countryside. In plan view the ridge appears to be composed of two sections, the southern portion trending NNE-SSW and the northern striking almost north-south. While Herdubreidtogl was not climbed during this investigation, the eastern and southern faces were observed from a distance of 3 km. A detailed geological description may be found in Bemmelen and Rutten (1955, pp. 96-98).

Basically, Herdubreidtogl is composed of glassy tuff and breccia overlying a layer of columnar basalt. Two features complicate this pattern, however. First, a double sequence of tuff overlain by breccia is separated by varved lake deposits. Bemmelen and Rutten (1955) interpreted this as evidence for two distinct eruptive phases, well separated in time but both subglacial. Second, the eruptions built this mountain high enough to form a subaerial caprock.

After the region became free of ice, activity resumed along the same fissure and scoriaceous lava flows capped the ridge. As noted above (Section 2.3.3), this eruption also appears to have formed the cone which crowns the summit of Herdubreid.

2.4.4 Summary

The course of a subglacial fissure eruption is apparently similar to that which forms a table mountain. An initial venting of hot gases along the rift melts an elongated cavity in the overlying ice. In some instances a pillow lava phase may follow, but many ridges show no evidence of this unit. The major portion of the eruption is an explosive phase, dominated by the ejection of glassy tuff and pillow fragments in varying percentages. These eruption products are essentially identical to those of table mountains. Few fissure eruptions continue long enough for the ridge to breach the water level, so foreset breccias and caprock basalts are rarely encountered. Occasionally the reactivation of a fissure in postglacial times deposits lava flows on the crest or flanks of a ridge. An average composition for moberg ridges is estimated to be 90% tuff and 10% basalt by volume.

Moberg ridges are less distinctive in their morphologies than table mountains. The ridges are characterized chiefly by linearity and alignment with other features in the vicinity, especially fissures and eruptive vents. Some ridges are single, isolated features and some form complex systems. Many have a serrated appearance, due both to erosion and to the eruption of a number of individual vents. Moberg ridges range up to 35 km in length. Their heights are generally less than the presumed thickness of the overlying ice at the time of their formation.

2.5 Massive Moberg Deposits

The volcanic products of subglacial eruptions do not always take the form of isolated table mountains or ridges. Just as lava flows from a

number of vents may combine to create a vast basalt plateau, the tuff and breccia from many eruptive centers and fissures beneath an ice sheet may combine into widespread moberg deposits.

Several broad expanses of moberg material are apparent on geologic maps of Iceland. The ridge system between the Vatna and Myrdals glaciers, including the Eldga region, caps one such mass (Fig. 7). This area of ridges and valleys, 20 km wide and 50 km in length, is almost totally mantled by layers of tuff and breccia with a net relief of 200-400 m (Kjartansson 1962).

A second region, denoted the "palagonite highlands" by Preusser (1976, pp. 286-288), runs north for 200 km from Vatna to the sea. In this case the maximum width is some 75 km and the relief reaches 400 m. Deposits from numerous ridges and table mountains unite to form a nearly continuous moberg layer (Saemundsson 1977).

On a smaller scale, the caldera of Askja, north of Vatna, tops a 275 km^2 massif of tuff, basalt layers and pillows (Sigvaldason 1968, Bemmelen and Rutten 1955, pp. 99-123). As noted by these authors, as well as during the present reconnaissance, numerous vents on this mountain remain active to the present time. Such activity was also prevalent during the Pleistocene, as a number of massive subglacial eruptions appear to be represented.

Evidence indicates that the four major remnant ice sheets in Iceland are at least partially underlain by moberg deposits. Geologic maps of Vatna, Lang and Hofs glaciers (Kjartansson 1965, Kjartansson 1962) show this material fringing portions of the glaciers and protruding through as nunataks. The evidence in the case of Myrdals is even more compelling.

This glacier is almost completely surrounded by moberg deposits, and the same material is exposed in ridges which penetrate deep into the ice. Along the southern coast, where the moberg mass almost reaches the sea, its thickness approaches 1000 m. While Katla is the only presently active volcano known to underlie this glacier, the ice does cover extensions of several recent fissure systems. A small basalt caprock and numerous jokulhlaup channels at the glacier's edge suggest the presence of additional vents.

A noteworthy feature of this massif is the array of isolated moberg plateaus which border its southern and western edges (Kjartansson 1962). Several of these, notably Petursey and Dyrholaey, show evidence of being eruptive sites, either submarine or subglacial. Others, including Hafursey and Hjorleifshofied, appear to be erosional remnants, cut off from the main plateau by jokulhlaup channels (Thorarinsson, personal communication, 1978).

Truly massive layers of subglacial volcanic products have been noted in Antarctica. Here the exposures consist of cliffs some 2000 m high (Hamilton 1972), and such material has been estimated to extend 5 km below the present ice cap in some localities (Le Masurier 1972). While the origin of these deposits has not yet been established, it is assumed that they represent the products of a number of voluminous subglacial fissure eruptions.

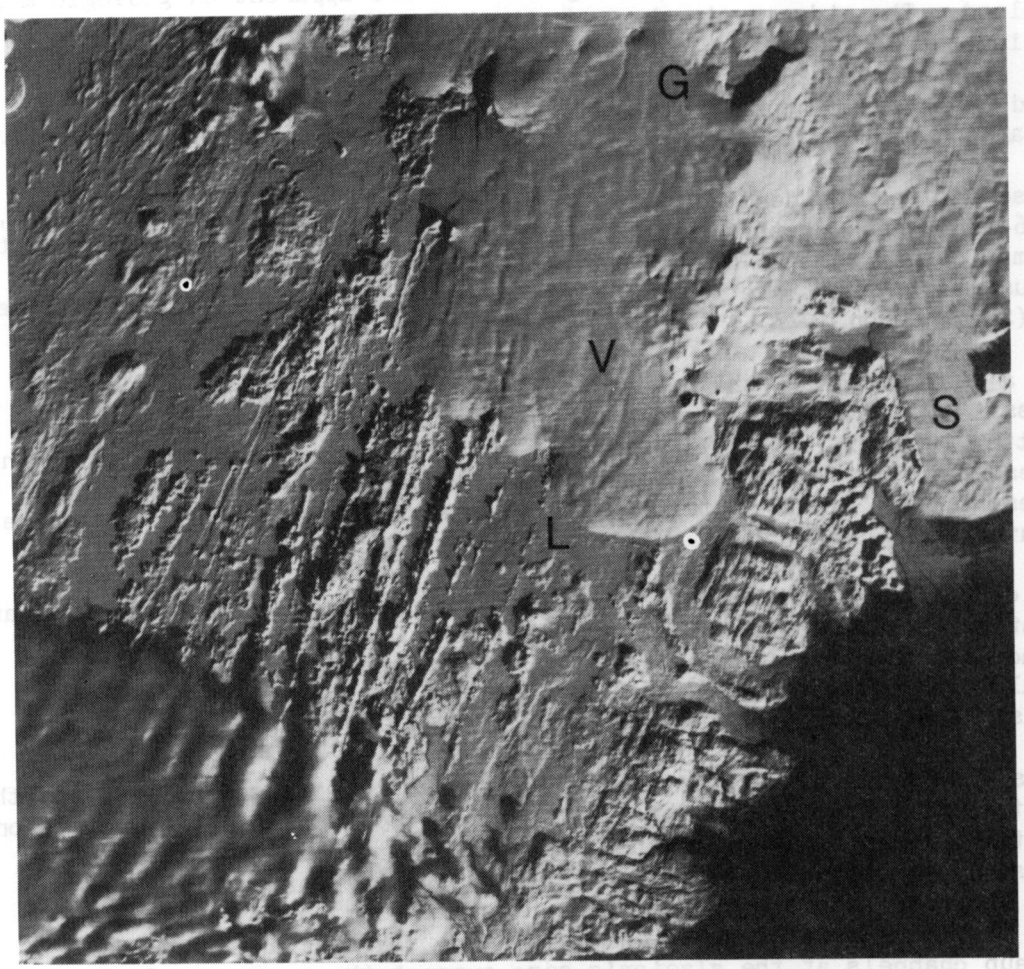

Fig. 7. Moberg Ridge System Between Vatna and Myrdals

The 20 km by 50 km system of moberg ridges between the icecaps of Myrdals (cloud covered) and Vatna (V) is shown in this Landsat image. Topographic variations are accented by the low sun angle and continuous snow cover. Other features of interest include the Laki fissure (L), the Grimsvotn caldera (G) and the Skeidarar outlet glacier (S). Landsat frame E-1192-12082-6.

2.6 Pseudocraters

Many of the Earth's volcanic regions are dotted with craters formed by steam explosions. Eruptions near the ocean or lava flowing into the sea commonly produce tuff rings or littoral cones. The Hawaiian and Galapagos Islands contain many such features. The encounter of magma with ground water at depth can yield spectacular maars and explosion-collapse depressions such as the Pinacate craters of Sonora, Mexico.

Tuff rings and maars are found in Iceland, but a third type of steam explosion crater seems unique to that country. This is the pseudocrater, a landform resulting from explosions caused by lava flowing over water-saturated ground (Thorarinsson 1960b). While not formed strictly by volcano-ice interaction, pseudocraters indicate the presence of near-surface water in volcanic terrain and therefore are relevant to the study of Martian landforms.

The type locality for pseudocraters is Lake Myvatn. The southern shore and islands of this shallow lake are dotted with over 1000 of these small cones (Fig. 8). They range up to 30 m in height and have basal diameters of as much as 320 m. The average Myvatn pseudocrater, however, rises no more than 5-10 m and is approximately 50 m across the base.

While the pseudocraters at Myvatn are the best known, similar features occur in many parts of Iceland. Examination of the 1:250,000 geologic quadrangles which now cover about two thirds of the country reveals at least eight other fields of these features. Several cones on the floor of the Eldga rift may also be pseudocraters, formed as lava flowed over a river which occupied the valley.

Field examination of previously mapped pseudocraters at Myvatn, east of Reykjavik and at several locations along the southern coast showed that these features are diverse in terms of composition, size and morphology. A broad central crater is common, often approximately one half of the basal diameter across. Not even the crater form is requisite, however. Many of the features in southern Iceland have no summit pits, but are merely tumuli several meters in height. Most pseudocraters are composed primarily of spatter, indicating that the explosions occurred while the bulk of the lava was still molten or at least semi-plastic. However, several cones were encountered which appeared to be simply loose piles of cinders. In one case a coherent basalt layer over a meter thick had been uplifted and contorted without breaking.

The flow which produced the pseudocraters at Myvatn has the texture of pahoehoe and contains collapsed segments of lava tubes. Steam explosions occurred over an area of approximately 25 km^2, though the flow itself is considerably more widespread (Preuser 1976, p. 242). The minimum flow thickness in the pseudocrater field is estimated to be 3-5 m.

Individual pseudocraters are similar in many respects to small cinder and spatter cones, though their origin is significantly different.

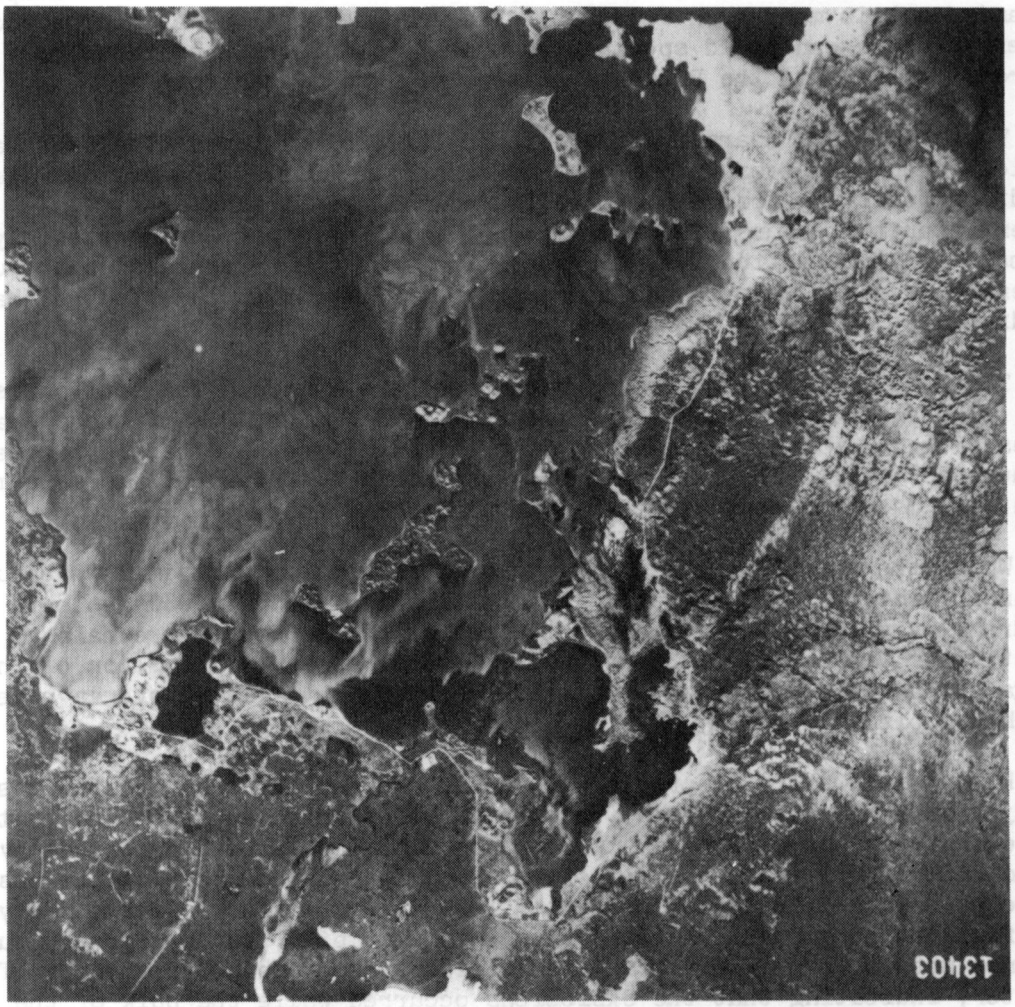

Fig. 8. Myvatn Pseudocraters

Pseudocraters as large as 320 m in basal diameter occur along the southern shore and on the islands of Lake Myvatn.

Morphologic evidence for an origin by steam explosion includes small size, large crater diameter/basal diameter ratio, lack of alignment among craters and confinement to a single flow.

2.7 Conclusions

Volcano-ice interactions in Iceland produce massive floods by two distinct mechanisms. Historical eruptions of Katla and Oraefajokull have been followed immediately by jokulhlaups as great quantities of glacial ice were rapidly melted. At Grimsvotn, conversely, the floods result from semi-periodic filling and rapid draining of a meltwater lake. The water is derived from ice melted over a period of years by solfatara activity within the caldera.

Table mountains and moberg ridges are the subglacial equivalents of shield volcanoes and fissure flows, respectively. The major geologic units which compose these features are basal pillow basalt, sideromelane tuff containing pillow fragments, foreset breccia and basaltic caprock. All of these components result from the same eruptive sequence, with the different products reflecting changing modes of interaction between water and magma. Many of these former subglacial volcanoes are capped by later flows, cones and craters which indicate reactivation of the vents.

The products of a number of closely-spaced subglacial eruptions may combine to form widespread moberg deposits. Such units probably underlie parts of the present ice caps in Iceland and Antarctica. Similar deposits, exposed by the retreat of Pleistocene ice sheets, cover thousands of square kilometers.

Pseudocraters are cones or tumuli formed by steam explosions beneath still-molten lava flows. These features are highly diverse in composition, size and morphology.

Field studies and photointerpretation of this suite of volcano-ice interaction features provide the basis for the analytical and experimental work described in the following chapter. This combined effort subsequently creates a framework within which to interpret similar features on the planet Mars.

CHAPTER 3

ANALYTICAL AND EXPERIMENTAL STUDIES

Phase two of the research on volcano-ice interactions concentrated on analyzing the physical processes implied by geologic evidence. This represents a considerable departure from previous work, which has been mainly descriptive. Two considerations motivated these analyses -- to better understand and quantify the entire process of subglacial volcanism and to derive data on the surface history of Mars.

Most studies of the moberg mountains and ridges in Iceland have concentrated on descriptive field work and petrographic analysis. The engineer and geologist Trausti Einarsson, however, reduced subglacial volcanism to a problem in heat transfer and mechanics and claimed to have found a fundamental objection to the process (Einarsson 1966). He stated that the initial eruption of basalt is so rapid with respect to the rate of heat transfer on the ice that sufficient volume cannot be melted to accomodate the growing lava pile. Furthermore, he showed that the magma pressure is insufficient to lift an overlying ice sheet more than 50-100 m thick, implying that subglacial eruptions might be rapidly suppressed by the sheer weight of the overlying ice. Einarsson (1966) described the composition of a typical table mountain as "flat-lying layers of fluviatile sediments alternating with lavas up to middle height", a characterization somewhat at odds with the observations discussed in Chapter 2. While his mechanism for forming the isolated mountains is not clear, it appears to involve local upthrust (Einarrson 1962).

The second aim of these analyses, and indeed of the entire dissertation study, is to use analogs to terrestrial volcano-ice interaction features to study the Martian surface. Viking photographs of Mars provide data on morphology, size, shape, orientation and location of particular features. In order to make quantitative statements concerning past conditions on that planet, significant parameters for terrestrial volcanoes and ice were derived and related to the Viking measurements.

Four aspects of the suite of landforms described in Chapter 2 were chosen for this anlysis. The first concerns the phenomena of jokulhlaups, specifically the effectiveness of eruptions versus long term heating in producing large meltwater floods. Next is a study of pillow lavas, concentrating on the efficiency of heat transfer from lava to ice. Third the explosive eruption phase is addressed. Finally, a model is developed for the formation of pseudocraters.

3.1 Physical Parameters

Table I lists the material parameters used in the following numerical modeling. Many of these numbers are well known and have been taken directly from the literature. Other values were derived as described below. Table II concerns parameters specific to a "model" subglacial eruption which produces a "typical" table mountain or moberg ridge. Table III lists characteristic compositions of several eruption products from the Sveifluhals ridge (Section 2.4.1). Samples collected by the author were prepared as thin sections and analyzed using the University of Arizona Scanning Electron Microprobe Quantometer.

3.1.1 Density

The densities of a number of samples were determined by measuring the volume of water displaced by a given mass of material. Tachylite from a Herdubreid pillow crust yielded a density of 2.9 $\pm$ 0.1 gm/cm^3, as compared to an average of 2.8 gm/cm^3 for plateau basalt glass (Nafe and Drake 1968). Basalt from the interior of the same pillow had a density of 2.7 $\pm$ 0.1 gm/cm^3, close to the average crustal density in Iceland of 2.78 gm/cm^3 (Walker 1974). A density of 2.6 gm/cm^3 for liquid lava of the same composition was derived by the method of partial volumes described by Bottinga and Weill (1970). Five samples of sideromelane tuff from a number of mountains had an average density of 2.23 $\pm$ 0.14 gm/cm^3.

3.1.2 Viscosity

Macdonald (1972, pp. 61-64) discussed the many factors influencing magma viscosity. Values listed range over four orders of magnitude. A viscosity of 10^3 poise was chosen because it lies between the values for a pure basaltic liquid and a mixture of liquid and crystals (Shaw et al. 1968). Using the method of Bottinga and Weill (1972) a viscosity of 1.6×10^3 poise was calculated for the pillow basalt composition of Table III at a temperature of 1200 ^{o}C.

3.1.3 Heat Capacity

The heat capacities of basalt and glass are composition dependent, and a number of empirical formulae have been derived to relate these parameters. The method of Morey (1954, pp. 211-212) was used to calculate the heat capacities of pillow basalt and glass samples from Sveifluhals (Table III). The derived values, 7.5×10^6 erg/gm ^{o}K for both samples, are close to typical values for basalt.

3.1.4 Thermal Conductivity

Morey (1954, p. 219) presented a formula for deriving the thermal conductivity of glass from its composition. Employing the same glass

Table I
Physical Parameters

Parameter	Symbol	Value	Source*
Temperature			
Melt ice	T_i	0 °C	1
Melt basalt	T_m	1065	2
Boil water (at 49 atm)	T_b	264	3
Latent heat of melting			
Ice	h_w	3.3×10^9 erg/gm	1
Basalt	h_b	3.3×10^9	4
Glass	h_g	3.3×10^9	4
Latent heat of vaporization			
Water	h_v	2.2×10^{10} erg/gm	1
Density			
Air (dry, STP)	ρ_a	1.3×10^{-3} gm/cm^3	3
Ice	ρ_i	0.9	5
Water	ρ_w	1.0	3
Lava	ρ_l	2.6	5
Basalt	ρ_b	2.7	5
Glass	ρ_g	2.8	5
Tuff deposit	ρ_t	2.2	5
Olivine (Fo_{80}) crystal	ρ_c	3.4	6
Viscosity			
Lava	η_l	10^3 poise	5
Heat capacity			
Air (dry)	c_a	1.2×10^4 erg/gm °K	3
Water	c_w	4.2×10^7	3
Steam	c_s	8.0×10^7	1
Lava	c_l	1.2×10^7	7
Basalt	c_b	7.5×10^6	5
Glass	c_g	7.5×10^6	5
Thermal conductivity			
Glass	k_g	9.2×10^4 erg/cm sec °K	5

*Sources

1 Robie et al. 1978
2 Macdonald 1972
3 CRC Handbook of Chemistry and Physics 1978
4 Walker et al. 1976
5 Measured or derived in present study
6 Bloss 1952
7 Mueller and Saxena 1977

Table II

Model Subglacial Eruption Parameters

Parameter	Symbol	Value
Eruption temperature	T_e	1200 °C
Total heat released	h_e	10^{25} ergs
Rate of heat release	q_e	10^{18} erg/sec
Eruption rate	r_e	10^8 cm^3/sec
Volume erupted		
Central vent	V_c	5.1×10^{15} cm^3
Fissure	V_f	2.7×10^{15} cm^3
Mass erupted		
Central vent	M_c	1.2×10^{16} gm
Fissure	M_f	6.1×10^{15} gm
Composition (by volume)		
Table Mountain		basalt 40 / tuff 60
Ridge		basalt 10 / tuff 90
Ice thickness	d_i	500 m
Ice temperature	T_i	0 °C (isothermal)
Ice density	ρ_i	0.9 gm/cm^3

TABLE III

Characteristic Compositions of Eruption Products from Sveifluhals

	Pillow basalt[1]	Tachylite[1]	Sideromelane[1]	Plagioclase[2]	Olivine[2]
Na_2O	2.96	2.14	2.20	2.60	0.04
K_2O	0.32	0.22	0.22	0.14	0.08
CaO	13.18	11.89	12.02	15.77	0.34
Al_2O_3	17.94	14.56	14.27	31.72	0.02
SiO_2	52.52	47.99	47.97	49.32	39.75
MgO	4.59	7.70	7.58	0.23	44.42
Cr_2O_3	0.07	0.04	0.04	0.00	0.06
FeO	7.85	12.27	12.55	0.76	17.64
TiO_2	1.21	1.81	1.85	0.02	0.00
Total	100.64	98.62	98.70	100.56	102.35

[1]Mean of 3 samples

[2]Analysis of 1 sample -- crystal in glass (Fig. 10a)

composition as was used above for heat capacity yields a conductivity value of 9.2×10^4 erg/cm sec ^oK.

3.1.5 Eruption Temperature

Slow cooling of a basaltic melt through its liquidus temperature results in the formation of crystals whose compositions are related to the bulk composition of the liquid. As cooling proceeds both liquid and crystal compositions change in a manner which is temperature dependent. Thus, the compositions of a basaltic glass and the crystals which were in equilibrium with it at the time of glass formation may be used to derive the temperature which had been reached when rapid chilling set in.

In the present study a sample of Sveifluhals glass proved particularly useful for such a temperature determination. Fragments of this sideromelane are shown in Fig. 10a (p. 222). The glass contains olivine and plagioclase microcrystals approximately 10 μm long. These crystals were incorporated in the melt at the moment it was chilled to glass by contact with water. Due to their small size they are assumed to be late-forming crystals which were essentially in equilibrium with the liquid. Hence these crystal and glass compositions (Table III) should allow the derivation of a realistic eruption temperature.

At least three methods exist for deriving temperatures from composition data. The approach of Kudo and Weill (1970) fits glass and plagioclase compositions to an experimentally determined temperature curve. Drake (1976, eqns. 1-3) obtained improved values for the regression parameters, which were used in the present analysis. Roeder and Emslie (1970) described a similar geothermometer based on glass and olivine compositions. Finally, M. J. Drake and C. Hostetler of the Lunar and Planetary Laboratory, University of Arizona, have developed a technique which yields a liquidus temperature from the glass composition alone. Their method is based on a determination of the shape of the liquidus surface in temperature-composition space (Hostetler, personal communication, 1978). All three methods were employed and the eruption temperatures derived for Sveifluhals sideromelane are as follows:

Glass and Plagioclase:	1153 ± 55 ^oC
Glass and Olivine:	1198 ± 23 ^oC
Glass:	1197 ± 21 ^oC

For ease of computation an eruption temperature of 1200 ^oC was adopted.

3.1.6 Total Heat

Macdonald (1972, p. 60) summarized estimates of the total energy released during a number of eruptions. Values range from approximately 10^{18} - 10^{27} ergs, with a modal value of around 10^{25} ergs. Total energy is partitioned among several effects, including heating, explosive

disruption of magma and seismic energy. Most historical eruptions in Iceland have been relatively aseismic, due in part to the high degree of fracturing in the crust. The modal value of 10^{25} ergs has been adopted as "typical" of the total heat produced during a single major eruptive sequence. The building of a large volcanic construct may require several such eruptions.

3.1.7 Rate of Heat Release

Estimates of the rate of thermal energy release of a number of eruptions were listed by Macdonald (1972, p. 60). These values span a wide range, from 8×10^{15} - 8×10^{25} erg/sec, and include radiation, heat transport by gases and conduction into the surrounding rocks. Estimates of the heat energy released from high temperature zones in Iceland (Bodvarsson 1960) range from some 10^{14} erg/sec on the Reykjanes peninsula to 10^{16} erg/sec at Grimsvotn. Thorarinsson (1964, p. 43) estimated that the rate of energy release during the first four months of the Surtsey eruption equalled approximately 10^{18} erg/sec. This value appears characteristic of the basaltic volcanism of Iceland and will be used in the calculations below.

3.1.8 Eruption Rate

Rates of eruption have been published for a number of Icelandic volcanoes. Walker (1973) estimated that the shield volcanoes were built by eruptions averaging 10^6 cm^3/sec. Flow during the lava phase at Surtsey was about 2×10^7 cm^3/sec (Thorarinsson 1964, p. 51), while the effusion rate at Askja in 1961 averaged 6×10^8 cm^3/sec (Wood et al. 1977). The massive Laki fissure lavas initially poured out at some 5×10^9 cm^3/sec, though the average rate was probably an order of magnitude lower (Thorarinsson 1970). A value of 10^8 cm^3/sec was adopted for the present study to represent both the effusive and explosive phases of a "typical" Icelandic eruption.

3.1.9 Total Volume and Mass

Thorarinsson (1967a) estimated that the mean volume for the ten largest shield volcanoes in Iceland is 5.5 km^3 (5.5×10^{15} cm^3). Using a density for basalt of 2.7 gm/cm^3 yields an average mass of 1.5×10^{16} gm.

The volumes of six table mountains were calculated from topographic data. The mean value is 5.1 km^3, with a standard deviation of 2.1 km^3. Modeling these mountains as 40% basalt and 60% tuff by volume gives an average mass of 1.2×10^{16} gm.

Three of the largest fissure eruptions in Iceland, those of Thorsja, Laki and Eldga, produced 15, 12 and 9 km^3 of lava respectively (Thorarinsson 1960d, Thorarinsson 1979, Rittmann 1962). The masses of these flows range from 2.4 - 4.1×10^{16} gm.

The mean volume of three moberg ridges is 2.7 $\pm$ 1.8 km^3. Assuming a composition of 90% tuff and 10% basalt yields a mean mass of 6.1 x 10^{15} gm. Thus, the eruptions which produced many of the Pleistocene subglacial ridges were somewhat less voluminous than the largest postglacial fissure flows.

3.1.10 Ice Thickness

Thorarinsson (1976b, Fig. 12) plotted the mean altitudes of 27 table mountains in northern and southern Iceland, as well as the average altitude of the surrounding terrain. The difference between the two regression lines, i.e., the net height of the table mountains, increases from the coast inland. Since the caprock of a table mountain represents the approximate level of the surrounding ice this finding was interpreted in terms of increasing glacier thickness toward the interior. This suggests that the ice sheet was 200-300 m thick near the coast and over 1000 m thick 150 km inland. A value of 500 m has been adopted for the present model.

3.1.11 Ice Temperature

An isothermal profile at 0 ^{o}C is assumed for the ice sheet in this model. Actual temperatures, at least in temperate glaciers, follow the pressure melting curve for ice, approximately -6 x 10^{-4} $^{o}C/m$ (Shreve and Sharp 1970). For 500 m of ice this amounts to only -0.3 ^{o}C.

3.1.12 Ice Density

Ice density is assumed to be a constant 0.9 gm/cm^3 throughout the glacier. While actual values are somewhat variable, depending on compaction, trapped air and fissures within the ice, this value is average for many glaciers (Embleton and King 1975a, p. 125). Ice phase transitions are unimportant here, since they occur at pressures in excess of 2000 atm. Beneath 500 m of ice the pressure is about 49 atm.

3.2 Jokulhlaups

The first question to be addressed in this model is whether the volume of meltwater released in a large jokulhlaup can be formed by a single volcanic eruption, or whether a large part of it must come from long term melting or other sources. Both the total heat and the rate of heat release are important parameters, and will be treated separately.

Katla and Oraefajokull are the two volcanoes most likely to have produced jokulhlaups by eruption alone. The historic Oraefajokull eruptions are too poorly documented to provide data for numerical testing. Katla, however, has produced floods several times during the present century and has been well studied. A representative total discharge for a large Katla

flood is 2 x 10^{15} cm^3 (Thorarinsson 1970). A constraint on the rate of heat release is provided by the observation that essentially all of this volume of water reaches the outwash plain within two days of the first visible sign of eruption (Thorarinsson 1970).

3.2.1 Total Heat

A simple model for the melting of ice by a subglacial eruption assumes a point source of heat beneath a glacier of infinite lateral dimensions. Two extreme cases can be envisioned. All meltwater may remain within the growing hemispherical chamber or all water may drain away immediately. Since the time scale for Katla floods is only a few days the second case appears more important for the study of these floods, and will be the only one treated. This case yields a minimum value for required heat release, since the water is assumed to escape before being heated above 0 °C.

Heat loss to the air above the glacier and to the underlying rocks are also assumed to be negligible. The first assumption is reasonably good as long as the eruption continues into a closed cavity in the ice. After the roof of this cavity collapses, however, most additional volcanic heat will be lost to the air. Neglect of heat loss into the rocks is based on the high efficiency of heat transfer by radiation and thermal convection of air as opposed to transfer by conduction into basalt. These simplifying assumptions will also result in minimum values for the amount of heat required to melt the glacial ice.

Heat transfer is thus assumed to take place by means of radiation and convection only. While the cavity remains closed all heat will go toward melting ice or heating air. As each cubic centimeter of ice melts the water escapes and is replaced by a like volume of air at an initial temperature of 0 °C.

Heating dry air requires 1.2 x 10^4 erg/gm °K, although the value for moist air is somewhat higher. Air density at sea level is approximately 1.3 x 10^{-3} gm/cm^3. Mean air temperature within the cavity is dependent upon the thermal gradient. For the extreme case of a linear gradient from a 1200 °C central source to a hemispherical boundary at 0 °C this mean temperature is 300 °C. Therefore, each cubic centimeter of air will absorb around 4.7 x 10^3 ergs as it is heated to the mean temperature of the chamber. The melting of ice requires 3 x 10^9 erg/cm^3. Thus, to a good approximation all of the heat in this model goes toward melting ice.

The observed total volume of a Katla flood is about 2 x 10^{15} cm^3 of water. Melting the equivalent amount of ice requires 6.6 x 10^{24} ergs. The total heat adopted in section 3.1.6 for a typical large eruption is 10^{25} ergs. Thus, on the basis of this model, eruption melting is a reasonable mechanism for the production of jokulhlaups from Katla.

3.2.2 Rate of Heat Release

The question of heat flux remains. For the present model a value of 10^{18} erg/sec was initially adopted, based mainly on observation at Surtsey. Ice was assumed to melt instantly when its temperature exceeded 0°C and heat transfer by radiation and convection were also assumed to be instantaneous. As noted previously, descriptions of Katla floods indicate that essentially all of the water reaches the plains within two days (1.7×10^5 sec) of the first appearance of an eruption cloud. At the flux rate cited above, however, only 1.7×10^{23} ergs would be released in this period of time, less than 3% of the total required by the observed water volume.

Several alternative scenarios for ice melting may be envisioned. Possibly the first phase of Katla eruptions are quiescent, with the eruption cloud being a rather late stage phenomenon. In such a case, however, the quiet phase would be expected to produce heat at a lower rate than an explosive eruption, and would need to last for tens or hundreds of days to melt the required volume of ice.

The slow accumulation of meltwater resulting from continuing solfatara activity, similar to the case at Grimsvotn, is also possible. Thorarinsson (1960a) described a 1955 Katla flood with a volume of 2.8×10^{13} cm^3 which could have had such a source. Solfatara heating appears unlikely as a source for the major jokulhlaups, however. Bodvarsson (1960) showed that there is no high-temperature zone at Katla with a heat flux of more than 2×10^{14} ergs. Even at this maximum rate of heating the requisite amount of ice could not be melted in less than 1000 years. Thus, while solfatara activity may produce a portion of the meltwater included in floods which average about 49 years apart, it appears inadequate to account for a substantial fraction.

Precipitation likewise is inadequate to supply the flood waters. While over 5×10^{15} cm^3 of water falls on the Myrdals glacier annually (Preusser 1976, Fig. 15), almost all of it is in the form of snow. Therefore, the heat requirements for producing liquid water remain essentially the same.

A portion of the water in the jokulhlaups is probably derived from melting within the subglacial channels by which the floods reach the outwash plains. The maximum amount of heat available for such melting by water at 0 °C equals the change in potential energy of the water as it drops from the volcano to the plains. For a mass of 2×10^{15} gm falling from the 900 m altitude of Katla to sea level this energy equals 1.8×10^{23} ergs, or about 3% of the total required for ice melting.

3.2.3 Summary

Most of the melting supplying major floods from Katla is apparently due to an extremely energetic eruptive phase. Other mechanisms appear to be

totally inadequate to supply the heat flux required by the present conservative model. Melting of enough ice to provide 2 x 10^{15} cm^3 of water in two days requires that large eruptions of Katla supply heat at a rate of 3.8 x 10^{19} erg/sec. This is approximately 40 times the rate characteristic of Surtsey.

3.3 Pillow Basalts

The initial phase of many subglacial eruptions appears to consist of the quiet effusion of basaltic lava. Field observations at Efstadalsfjall (Section 2.3.1) and the descriptions of Jones (1970) and Sigvaldason (1968) show that such an effusive phase often results in a massive basal unit of pillow lava. As described by Macdonald (1972, pp. 100-104) and many other authors, this form of basalt is highly indicative of the contact of magma with abundant water. Pillow formation may occur as a lava flow passes from land into a lake or ocean, as well as upon initial submarine eruption. As described in Chapter 2, both types of pillow basalts were observed in this study of table mountains.

A primary objection to the ability of a subglacial eruption to form a table mountain is that heat transfer from lava to ice becomes very inefficient as soon as a cooling crust forms on the magma. At this point the ice cannot be melted rapidly enough to make room for additional volcanic material and pressure from the ice above may suppress the eruption (Einarsson 1966). This hypothesis can be tested by the thermal modeling described below.

The model is designed to yield the maximum heat flux consistent with field observations. The case treated is that of an isolated mass of lava cooling and forming a single pillow. Fig. 9 shows a pair of pillows on Gaesafjoll. They are separated by several centimeters of tuff, and thus were almost completely surrounded by water-saturated deposits at the time of formation. Each has a mean diameter (d) of around 25 cm and a tachylite cooling crust 1 cm thick (d_c). For ease of computation pillows will be modeled as spherical.

Upon initial injection into water a tachylite crust will form essentially instantaneously. This involves cooling the outer 1 cm of lava with heat capacity c_1 from the eruption temperature of 1200 °C (T_e) to the melting temperature of 1065 °C (T_m) and removing the heat of crystallization (h_g). The thermal energy released at this stage, h_1, is given by:

$$h_1 = [\pi (d - d_c)^2 \cdot d_c] \cdot \rho_g \cdot [(T_e - T_m) \cdot c_1 + h_g] \qquad (1)$$

using the values given in Table 1, h_1 = 2.5 x 10^{13} ergs.

At this point the interior of the pillow is still at 1200 °C and heat is being lost by conduction through the crust. Since the rate of heat flow is dependent on the temperature gradient across this crust, the temperature of the water must be estimated. Water in the vicinity of the vent will be

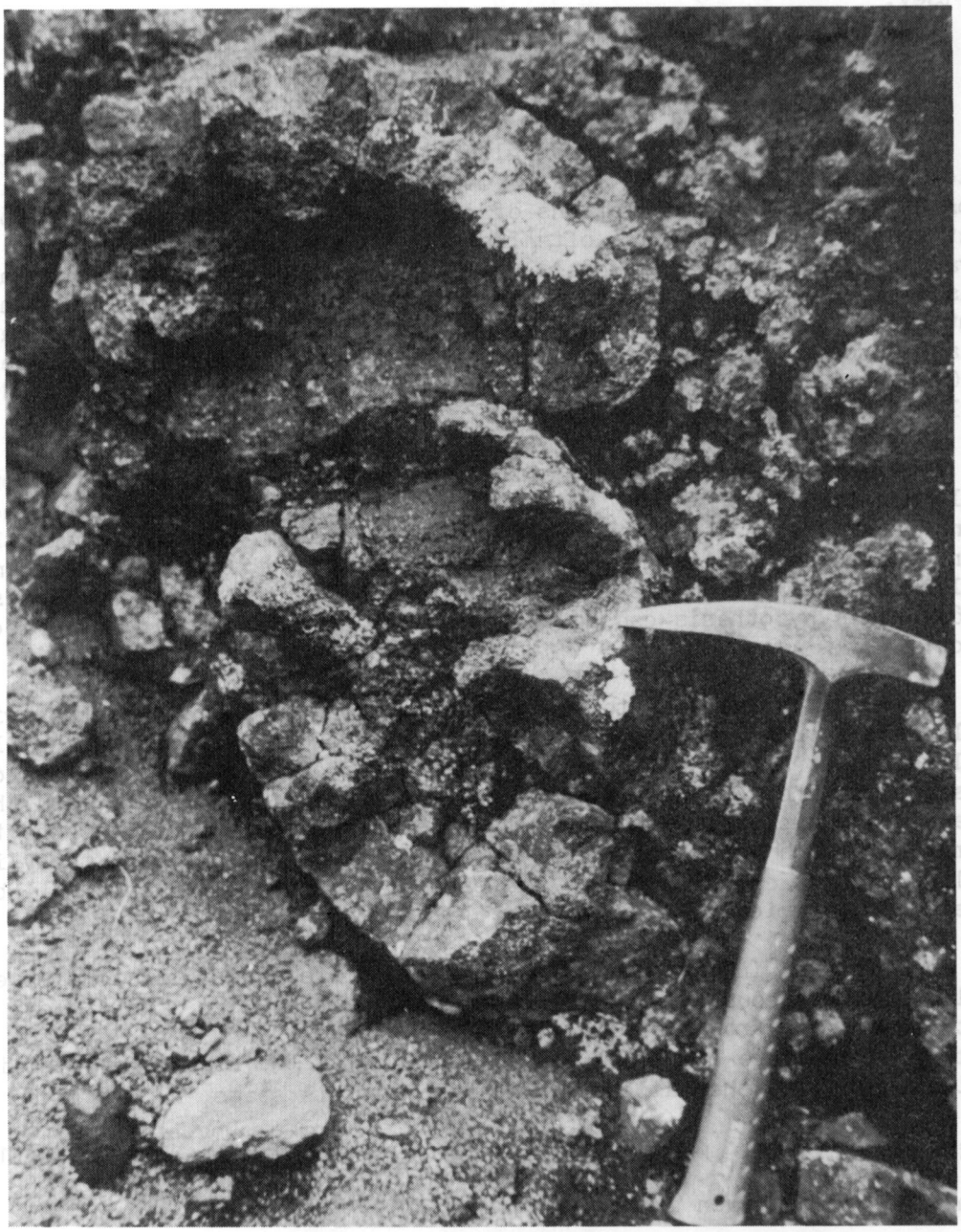

Fig. 9. Pillow Basalts

This pair of pillows, surrounded by sideromelane tuff, was found on the southwestern slope of Gaesafjoll. Hammer length equals 33 cm.

heated to its boiling point and then rise as bubbles of superheated steam, to be immediately replaced by more water. Thus the maximum water temperature appears to be that of boiling (T_b), which under the pressure of 500 m of water equals approximately 264 °C. The initial rate of heat loss from the entire pillow, q_0, is thus:

$$q_0 = [\pi(d - 2d_c)^2] \cdot [(T_e - T_b)/d_c] \cdot k_g \qquad (2)$$

where k_g is the thermal conductivity of the tachylite crust. This model gives an initial heat flux of 1.4×10^{11} erg/sec, and the rate will decrease as the interior temperature drops. At the melting temperature of 1065 °C the flux will have dropped to 1.2×10^{11} erg/sec. The presence of a thin, distinctive glass crust on most pillows, combined with an interior lacking concentric layering, indicates that solidification probably did not progress inward from the crust, but rather occurred at essentially the same time throughout the mass of lava. Therefore the heat flow may be modeled down to the melting temperature by an "average" flux value of 1.3×10^{11} erg/sec.

The time needed to solidify the interior of this pillow may be calculated from the heat flux and a knowledge of the total thermal energy released during cooling and solidification. This energy value, h_2, is calculated in the manner of Eqn. 1 using the interior volume of the pillow.

$$h_2 = [\pi(d - 2d_c)^3 /6] \cdot \rho_b \cdot [(T_e - T_m) \cdot c_1 + h_b] \qquad (3)$$

Thus, $h_2 = 8.5 \times 10^{13}$ ergs, which will be released from the cooling pillow in under 11 minutes. Adding h_1 and h_2 gives the total heat released from the pillow through the point of solidification, some 1.1×10^{14} ergs. After the entire pillow solidifies the heat flux drops to a nearly negligible value.

The total volume of the pillow is 8.2×10^3 cm^3. Melting the same volume of ice requires 2.4×10^{13} ergs. However, the formation of pillow lava requires the presence of water in contact with the lava, so heat radiated by the rock is partitioned between melting ice and heating water to the mean temperature within the cavity. Again assuming a linear gradient in temperature between lava at 1200 °C and ice at 0 °C, the mean water temperature equals 300 °C. Raising the temperature of water requires 4.2×10^7 erg/gm °K. Therefore to melt 8.2×10^3 cm^3 of ice and raise the temperature of the resulting water by 300 °C requires a total of 1.2×10^{14} ergs. Thus, for this extreme case, the heat released by a single pillow during the first 11 minutes of cooling is nearly sufficient to remove its own volume of ice. If the mean temperature of the water is not 300 °C, but closer to 0 °C, only about 2.4×10^{13} ergs will be required to melt the ice volume corresponding to a single lava pillow. In this case the energy released by the cooling pillow is more than sufficient to melt the ice.

The calculated 11 minutes solidification time for an average pillow may be compared to geologic observations. Saemundsson (1967) noted some pillow

lavas on Hengill showed evidence of significant crystal settling. While exact values of crystal size and settling distance are not available, the process can be modeled using reasonable estimates.

Stokes' law predicts the terminal settling velocity, v, for a spherical crystal of diameter d and density ρ_c in a melt of density ρ_1. The liquid viscosity is given by η_1 and g is the acceleration of gravity (981 cm/sec^2).

$$v = 2_g \cdot d^2 \cdot (\rho_c - \rho_1)/9\eta_1 \qquad (4)$$

For 1 mm olivine crystals, using the parameters in Table 1, v = 1.7 x 10^{-3} cm/sec. At this rate the crystal can sink 10 cm in 96 minutes.

This estimate of a characteristic settling time is by no means exact. Olivine crystals one centimeter across are not uncommon in Icelandic lavas. Such crystals would sink one hundred times faster than those in the model above. On the other hand, the viscosity of 10^3 poise used in this calculation may be much too low. As the lava in the pillow cools and crystallization begins, the effective viscosity of the liquid-crystal mixture rises by an order of magnitude or more (Shaw 1969). The observation of Sigvaldason (1968) that crystal settling within pillows is relatively uncommon in Icelandic basalts indicates that cooling generally takes place more rapidly than crystal sinking. Rapid eruptions, resulting in the formation of piles of still warm pillows, may slow the cooling rate enough to permit large scale settling of crystals.

The present very conservative model indicates that an "average" pillow can release at least 92% of the heat necessary to accommodate its own volume by melting ice in less than 11 minutes. This near equality is heavily model dependent, however. Increasing the thickness of the tachylite cooling crust will decrease the rate of heat flow in direct proportion. Decreasing the size or changing the shape of the pillow will raise the cooling rate as the ratio of surface area to volume increases. Most important, the insulating effect of adjacent masses of lava can slow the rate of heat transfer and might prevent ice melting from keeping up with the rate of magma intrusion. If such a condition continues the volume problem noted by Einarsson (1966) could become acute.

The solution apparently lies in the extra thermal energy provided by hot gases, both before and during the effusion of lava. Observations of fissure eruptions, especially those near Myvatn in 1724 (Rittmann 1938), have shown that the first products are mainly gases, and that sometimes very little lava is erupted for days or weeks. This probably reflects the opening of the fissure before the magma has had time to rise to the surface.

The amount of heat available from an exsolved gas phase may be roughly calculated. Macdonald (1972, pp. 44-54) indicated that basaltic magmas often release gas equal to 1% of the magma weight. Sigvaldason and Elisson (1968) analyzed eleven samples of gas from Surtsey and found it to be mainly water, 83% by volume. The present model assumes therefore that water is the

only important constituent of magmatic gas and that 0.005 gm of water is liberated as steam for each gram of lava erupted. Assuming that this steam is initially superheated to 1200 °C and cools to the boiling temperature of 264 °C approximately 4.8×10^8 ergs of heat will be released per gram of lava. This translates to just over 10% of the heat required to melt ice equivalent in volume to the lava and raise the temperature of the resulting water to 264 °C. Thus, the exsolution of even a tiny amount of hot gas as the magma cools may be able to overcome the volume deficit between lava and ice.

In summary, the objections to subglacial volcanism in terms of low rates of heat transfer from lava to ice are probably not valid. Historic eruptions in Iceland often commence with a hot gas phase. In a subglacial eruption such a phase would melt a cavity in the ice into which initial basalt effusion could take place. During this effusion the cooling of pillow lavas and the exsolution of magmatic gas should be marginally adequate to make room for the growing volcanic pile by melting overlying ice.

3.4 Explosive Phase

The geologic observations in Chapter 2 show that the major portion of most table mountains and almost the entire mass of every moberg ridge are composed of glassy tuff with a variable admixture of pillow fragments. The Surtsey eruption showed that this material was probably formed by explosive eruptions caused by water gaining access to the volcanic vent. In the study of this eruptive phase three questions are addressed. First, will the glass particles release enough heat to melt through the ice? Second, what is the detailed mechanism by which a quiet effusive eruption switches to one of explosive violence? Finally, is this change of eruptive sytles dependent on water pressure?

3.4.1 Total Heat

The question of adequate heat output may be addressed in the same manner as for the pillow basalt calculations. Microscopic observations of individual glass fragments (Figs. 10a,b, p. 222) show that they are homogeneous particles on the order of 0.5 mm across by 0.04 mm thick, with a volume (V) of around 10^{-5} cm^3. The homogeneity of the particles indicates that chilling from eruption temperature to the temperature of the surrounding boiling water (T_b = 264° C) took place almost instantly. The total heat per particle, released in a fraction of a second, is thus:

$$h = V \cdot \rho_g \cdot [(T_e - T_m) \cdot c_1 + h_g + (T_m - T_b) \cdot c_g] \qquad (5)$$

Inserting appropriate values into this equation gives $h = 3.1 \times 10^5$ ergs, or 3.1×10^{10} erg/cm^3. The total heat required to melt a cubic centimeter of ice and raise the water temperature by 300 °C is 1.4×10^{10} ergs. Conservatively, therefore, as long as the subglacial cavity remains closed, the glass fragments formed during the explosive phase of the

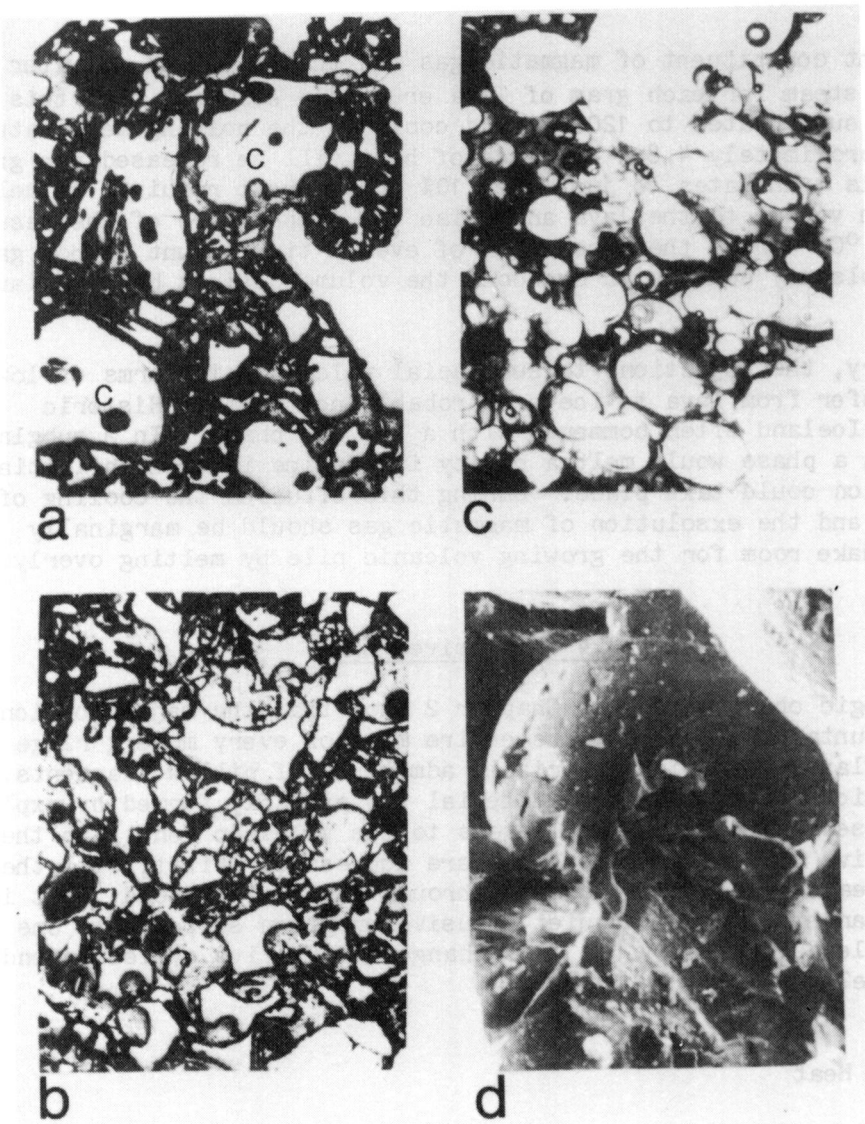

Fig. 10. Sideromelane Tuff

a. Tuff fragments from Sveifluhals. Several fragments contain microcrystals of olivine and plagioclase (C) approximately 10 μm long. Reflected light photomicrograph, frame width approximately 1 mm.

b. Tuff fragments from Herdubreid. Reflected light photomicrograph, frame width approximately 1 mm.

c. Highly vesicular glass from Sveifluhals. Transmitted light photomicrograph, frame width approximately 1 mm.

d. Broken vescicle in tuff from Herdubreid. Scanning electron micrograph, frame width 0.37 mm.

eruption liberate enough heat to account for 2.2 times their own volume of ice. For a mean water temperature of 0 °C this factor increases to 12.2 times the glass volume. Once the top of the glacier is thinned to the point of collapse, however, most heat dissipation from the eruption column will be into the air above the ice, and little additional enlargement of the cavity will take place.

3.4.2 Triggering Mechanism

The mechanism by which a subglacial or submarine eruption enters its explosive phase apparently involves access of water to the vent (Thorarinsson 1964, p. 42; Sigvaldason 1968). The physical meaning of this statement is somewhat obscure, however. During quiet effusion some water of necessity has access to the rising magma at some level in the vent. The change from effusion to explosion appears to occur instantaneously and seems irreversible as long as water is present. Those pillow lavas which are intercalated with the tuff on mountains such as Herdubreid and Hengill have the appearance of intrusions into wet sediments.

Macdonald's (1972, pp. 104-105) discussion of the textures of glassy fragments bears on this question of mechanism. He noted that fragments of volcanic ash produced by explosive vesiculation display many curved surfaces which formerly bounded the expanding bubble. Conversely, fragments of glass spalled from lava as a result of contact with water and thermal contraction of the rock contain few vesicles and are generally flat with angular outlines.

Fig. 10 shows characteristic fragment shapes from tuff deposits on Herdubreid and Sveifluhals. Vesiculation has obviously been of great consequence in forming many of these fragments. Fig. 10c in particular displays evidence that gas bubbles within the magma can expand to the point of volumetric dominance. Explosive eruption due to the expansion of entrained gases cannot be the sole cause of glass formation, however. If this were the case the percentage of glassy tuff in subaerial eruptions would be much higher.

The simple contact of magma with water is likewise inadequate to produce the observed glass textures. This was demonstrated by a series of experiments using furnaces in the Experimental Petrology Laboratory of M. J. Drake. Samples weighing about 0.05 gm of tachylite and caprock basalt from Herdubreid were heated to 1210 $\pm$ 10 °C and held at that temperature for five minutes -- sufficient time for melting to occur. Some samples were then allowed to cool in air while others were dropped into water at 100 °C or 0 °C. In each case the product was a basaltic glass bead with a vesicular texture. Vesiculation took place during the melting process, and the presence or absence of water as a cooling medium had no apparent effect on glass texture.

These observations suggest that the initiation of explosive eruption involves both magmatic gas and water. As magma approaches the surface gas

is liberated from solution and expanding bubbles form within the melt. In a typical subaerial eruption most of the gas bubbles leave the magma and either escape from the vent or from the surface of the lava as it flows. For this reason, lava which has flowed some distance is often effectively degassed and can enter a body of water without causing explosions (Holcomb et al. 1974, p. 81).

Conditions change dramatically, however, when water is introduced into the ascending magma. Approximately 1.3×10^{10} ergs are instantaneously released by the chilling of 1 cm^3 of magma to glass at 1065 °C. The total energy required to heat a cubic centimeter of water from 0 °C to boiling at 264 °C and further heat the steam to 1065 °C is 9.7×10^{10} ergs. Thus the injection of a volume of water equal to 13% of the volume of the magma can instantly chill the basaltic liquid to glass. The resulting material might be expected to have a texture similar to that shown in Fig. 10c.

This delicate structure of the vesicular glass is not usually preserved, however. As the glassy froth rises further overlying pressure decreases and the vesicle walls are shattered by the expanding gas within. In addition, steam explosions mark the boiling of water injected into the vent. These two factors account for the violently explosive phase of the eruption. Thermal modeling by Sigvaldason (1968) led to similar, though more restricted, conclusions.

3.4.3 Pressure Dependence

The pressure of several hundred meters of water and/or ice can have a significant effect on the degree of vesiculation of magma. Thus the onset of explosive eruption might be expected to be somewhat pressure dependent.

Walker (1974) noted that at depths below one kilometer water pressure makes the exsolution of gas from lava unlikely. Jones (1969) found a correlation between the vesicularity of table mountain pillow basalts and presumed water depth. The present study provided further evidence of the effectiveness of water pressure in preventing gas exsolution. Two fragments of non-vesicular tachylite from a pillow basalt unit located some 600 m below the caprock on Herdubreid were heated to 1217 $\pm$ 3 °C and held for five minutes before being allowed to cool in air. In both cases the volumes of the samples nearly doubled after melting as a result of vesiculation. Similiar tests on caprock lava evoked a much smaller volume change. The significant difference between conditions at the time of tachylite chilling originally and during remelting was a drop in pressure. The laboratory experiments were carried out at one atmosphere pressure, while the first chilling of this glass was under water with a pressure which may have exceeded 50 atmospheres. Thus, as lava rises into contact with a deep glacial lake a significant amount of magmatic gas may remain for later release.

The water depth at the point in a particular eruption at which activity switched from effusive to explosive may be approximated from field

observations. Assuming that the water level remained constant throughout the explosive phase, this depth is close to the difference in altitude between the top of the pillow basalt pile and the lowest caprock layer. Locating the highest pillow basalts is often not possible, however, because tuff overlies these lavas. The estimates given below should thus be considered maximum applicable water depths.

Jones (1970) found basal pillow lavas within about 100 m of the presumed water level in the table mountains which he investigated. The evidence of a basal pillow unit at the north end of Gaesafjoll places an upper limit of 240 m on water depth there. The pillow basalt pile at Herdubreid was mapped as extending to within approximately 200 m of the top by Sigvaldason (1968), and a similar altitude difference was seen at Efstadalsfjall during the present study. At the Sveifluhals ridge pillows were exposed some 200 m below the ridge crest, but this ridge probably never penetrated the water surface. In contrast, the Surtsey eruption commenced in water 130 m deep and probably did not enter its explosive phase until the volcanic pile was much closer to the surface. A quiet eruption ENE of Surtsey built a ridge to within 23 m of sea level (Thorarinsson et al. 1964). Thus, for many but not all Icelandic subglacial and submarine volcanoes, a transition from effusive to explosive eruption took place at water depths of around 100-200 m.

3.4.4 Summary

The explosive phase of subglacial and submarine eruptions is characterized by the production of tuff consisting mainly of fragments of sideromelane glass. The heat released by the formation of this glass is clearly adequate to melt the equivalent volume of ice, so that the eruption can proceed with no volume problems. The abrupt transition from effusive to explosive volcanism is triggered by a combination of extreme magma vesiculation and chilling of the magma to glass. This transition is somewhat pressure dependent, apparently occurring in most cases at a depth of 100-200 m.

3.5 Pseudocraters

The formation of pseudocraters by steam explosion is now well accepted by most workers in the field. Discussions of energetics, however, have not proceeded past a qualitative recognition of the fact that such explosions can be immensely powerful. In the present study modeling was done both to study the formation of this rather rare class of geologic phenomena and to provide a basis for interpreting similar features on Mars.

The model pseudocrater discussed here is typical of the features studied at Lake Myvatn (Section 2.6). A basal diameter of 50 m was chosen, along with an interior diameter of 25 m at ground level. Interior and exterior slopes stand at an angle of 30° to the horizontal, giving the rim a height of 3.6 m. A 5 m thick basalt flow is emplaced instantaneously over

water-saturated ground and a single steam explosion occurs while the lava is still molten. The entire mass of lava within the 25 m diameter circle is disrupted and ejected by the explosion.

The volume of lava ejected in this model equals 2.5×10^9 cm^3, representing a mass of 6.4×10^9 gm. The cone contains 2.7×10^9 cm^3 of semi-consolidated fragments. Assuming a mean porosity of 20% for this material gives a density of 2.2 gm/cm^3. The mass of the cone is therefore about 5.7×10^9 gm. Thus over 11% of the disrupted mass of lava is either ejected beyond the crater walls or falls back into the center. For a 5 m thick flow no underlying rock need be ejected. This agrees with the observation at Myvatn which shows that essentially all of the material forming the cones was emplaced in a molten or semi-plastic state.

The next question concerns the generation of steam at the contact between lava and water-saturated ground. Jaeger (1959) calculated temperatures at the base of a lava flow for a number of geologically important cases, including several similar to the present one. For a lava flow at 1000 ^oC in contact with saturated sandstone, in a condition which prevents the escape of water vapor, the contact temperature at the time of emplacement is 674 ^oC. The mean temperature attained by a near surface water layer initially at 0 ^oC should be about 337 ^oC. Since this is above boiling temperature for water at the pressure provided by 5 m of overlying lava, essentially all water near the surface will flash to superheated steam.

The pressure of steam at 337 ^oC is approximately 1.4×10^8 $dyne/cm^2$. The downward pressure exerted by the weight of the lava equals 1.3×10^6 $dyne/cm^2$. If the flow is assumed to be liquid, i.e., with zero shear strength, the steam pressure is clearly sufficient to eject the lava mass.

The minimum energy required to form the model pseudocrater is given by the change in potential energy of the lava as it is raised to its new location in the cone. The mean change in height $\Delta h = 3.7$ m, and the change in potential energy, ΔE, is computed by the formula:

$$\Delta E = m \cdot g \cdot \Delta h \qquad (6)$$

For the model cone this minimum emplacement energy $\Delta E = 2.1 \times 10^{15}$ ergs.

The change in energy produced by expansion of the steam is expressed as:

$$\Delta E = p \cdot \Delta V \qquad (7)$$

where p is pressure and ΔV equals change in volume. If the effect of the steam explosion is modeled as the lifting of the 5 m thick lava disc until it clears the flow surface, followed by disruption, $\Delta V = 2.5 \times 10^9$ cm^3. Eqn. 7 then yields $\Delta E = 3.4 \times 10^{17}$ ergs. Therefore this hypothetical steam explosion exceeds the minimum emplacement energy requirement by over two orders of magnitude.

A related question concerns the viability of the steam explosion process if water in the soil is replaced by ice. While this case was not treated by Jaeger (1959), a rough calculation based on the model treated above will suffice to indicate that near-surface ice can indeed produce pseudocraters.

Melting one gram of ice at 0 °C requires 3.3×10^9 ergs. Heating the same gram of water to 100 °C, vaporizing the water and heating the steam to a temperature of 337 °C uses approximately 4.5×10^{10} ergs. Thus the heat needed to create superheated steam by melting ice is only 7% more than that required for liquid water at the same initial temperature.

The case of an ice layer buried beneath several meters of regolith is of particular interest for Mars studies. Jaeger (1959) showed that, for an appropriate combination of rock and ice parameters, the maximum temperature attainable at a depth equal to half the lava flow thickness is 336 °C. The mean temperature in a meltwater layer above ice at this depth would then be 168 °C. Under these conditions such a temperature would provide barely enough heat to produce any steam at all from the ice layer. Thus burial at a depth equal to around half the thickness of the overlying flow appears to be a limiting condition on the initiation of steam explosions from ground ice.

The main result of this analysis is that steam explosions are more than energetic enough to account for the formation of pseudocraters. Further, the possibility of initiating such explosions by emplacement of a lava flow over near-surface water or ice is demonstrated.

3.6 Conclusions

Thermal modeling of the initiation of jokulhlaups from the volcano Katla supports the conclusion, based on observations of eruptions and floods, that heat from the eruption itself is responsible for melting most of the ice. In addition, the large volumes of water and short durations of these floods imply that Katla eruptions are characterized by extremely high heat fluxes.

Hot gas and lava in combination can form the basal units of subglacial volcanoes, in accord with field observations. While the heat fluxes needed to melt ice to accommodate the growing volcanic pile are available, the balance is close. The presence of a thick ice sheet may in fact have suppressed eruptions in Iceland or elsewhere.

The explosive phase of a subglacial or submarine eruption is initiated by the exsolution of magmatic gas and the concurrent chilling of the magma by water. Shattering of the basaltic glass by the internal gas pressure and steam explosions produces the tuff which forms the bulk of most subglacial volcanoes. Initiation of the explosive phase is somewhat dependent on the pressure of overlying water, and normally commences at a depth of 100-200 m.

Pseudocraters of the size and morphology which characterize the features at Lake Myvatn can be formed by steam explosions. The heat of a lava flow

is sufficient to trigger steam explosions in water or ice within a few meters of the surface.

These models of volcano-ice interaction features confirm the interpretations of their formation mechanisms derived from geologic field studies. In addition, the mathematical treatments provide the basis for comparative studies of Martian analogs under the physical conditions found on that planet.

CHAPTER 4

MARTIAN GEOLOGIC STUDIES

The study of Martian geology is a product of the space age. Before 1965 the surface of this planet, Earth's third nearest neighbor in space, was almost totally unknown. Telescopes showed variable light and dark markings, fluctuating polar caps and occasional planet-wide dust storms, but little else. Since that time nearly a dozen American and Soviet spacecraft have revealed a planet of striking geologic diversity.

The large-scale geology of Mars was first seen during the Mariner 9 mission, which mapped the planet from orbit with a resolution of 1-3 km. Fig. 15 (p. 246) is a map of the major geologic units in the equatorial regions derived from Mariner 9 imagery. As discussed by Mutch et al. (1976, pp. 56-91), the planet's southern hemisphere is dominated by a heavily cratered highlands unit. Tharsis, a broad plateau topped with shield volcanoes hundreds of kilometers in diameter, is centered near the equator and 110° longitude. A second major volcanic province is Elysium Planitia, located near 25° N latitude and 210° longitude. Much of the Martian northern hemisphere is covered by relatively young plains units. The polar regions display complex stratigraphic sequences formed predominantly by aeolian erosion and deposition. The polar caps consist of varying mixtures of water ice and solid CO_2.

Four Viking spacecraft reached Mars in 1976. The two orbiters continued the planet-wide survey begun by Mariner 9. Meanwhile the landers returned the first surface data from the plains of Chryse and Utopia. Table IV is an up-to-date comparison of some physical properties of the Earth and Mars.

The primary data set for the present investigation is the Viking orbiter imagery. Some 20,000 individual frames and nearly one hundred photomosaics were examined in a survey of possible volcano-ice interaction features. A great deal of this imagery has ground resolution of 50-100 m, which makes detailed photointerpretation of small geologic features possible for the first time.

4.1 History of Water

Mariner 9 revealed a planet with widespread volcanism similar to that which dominates the Earth and the Moon. This volcanism, coupled with a small scale degassing directly from the regolith, was probably the source for most of the present Martian atmosphere as well as the unknown mass of volatiles, including water, now located in non-atmospheric sinks.

Table IV

Planetary Data

Parameter	Earth	Mars	Source*
Mean radius	6.37×10^8 cm	3.39×10^8 cm	1
Surface area	5.10×10^{18} cm^2	1.44×10^{18} cm^2	
Volume	1.08×10^{27} cm^3	1.63×10^{26} cm^3	
Mass	5.98×10^{27} gm	6.43×10^{26} gm	1
Acceleration of gravity	981 cm/sec^2	373 cm/sec^2	1
Atmospheric pressure (reference level)	1.0×10^6 dyne/cm^2	6.1×10^3 dyne/cm^2	1,2
Mean surface temperature	15 °C	-63 °C	1
Atmospheric composition (surface)	N_2 78.1%	CO_2 95.3%	1,3
	O_2 20.9	N_2 2.7	
	Ar 0.9	Ar 1.6	
	H_2O <1 variable	O_2 0.1	
		CO 0.1	
		H_2O 0.03 variable	

*Sources

1 Goody and Walker 1972
2 Seif and Kirk 1977
3 Owen et al. 1977

The Viking lander mass spectrometers gave the first in situ analyses of the Martian atmosphere. Measurements of nitrogen and noble gas isotope abundances proved to be particularly useful indicators of the total amount of volatiles degassed during the planet's history. The results, based to an extent on the terrestrial degassing record, are somewhat model dependent. Owen et al. (1977) assessed the various uncertainties and estimated that the total amount of water degassed by Mars is approximately 10^{21} cm^3. This is equivalent to a layer of water ten meters deep covering the entire planet. Other degassing models, based on the same Viking data, yielded estimates as much as an order of magnitude higher (McElroy et al. 1977).

A number of sinks for Martian water have been identified. The present atmosphere, according to Viking measurements, contains about 1.3×10^{15} cm^3 of water, though this value is somewhat variable (Farmer et al. 1977). The amount of water lost to space via dissociation and thermal escape has been estimated at 4×10^{20} cm^3 over the age of the planet (McElroy 1972). Viking thermal mapping has shown that the present residual north polar cap is composed of water ice, while the southern cap probably consists of frozen CO_2 (Kieffer et al. 1977). The northern cap has an area around 10^{16} cm^2 (Cutts 1973) and an unknown thickness. A 500 m thick cap, for example, would contain 5×10^{20} cm^3 of ice. The upper few meters of the regolith may also be a major volatile sink, either through adsorption, hydration or catalysis of H_2O dissociation. One estimate of the effectiveness of this sink concluded that as much as $10^{20} - 10^{23}$ cm^3 of water might be removed from circulation (Huguenin 1976).

These studies suggest the presence of sinks for much of the water outgassed during the history of Mars. Another possible sink of potentially major importance is the deeper regolith and underlying bedrock within several kilometers of the surface. Present Martian surface temperatures rarely exceed 0 °C, so the regolith generally acts as a cold trap for water. Fanale (1976) noted that at latitudes above approximately $\pm 40^{\circ}$ water ice can exist in equilibrium with the present atmosphere, and Smoluchowski (1968) demonstrated the effectiveness of a fine grained regolith in preventing ice loss at even lower latitudes. Thus, under present Martian conditions, a ground ice layer within a few meters of tens of meters of the surface could be stable.

Soderblom and Wenner (1978), using heat flow values based on terrestrial studies, theorized that much of the Martian surface may be underlain by a mixture of ice and rock to a depth of 1-2 km. Below this depth they estimated that planetary internal heat flow would raise the temperature above the melting point of ice and a liquid water layer could exist. A layer of ice and rock equivalent to one kilometer of pure ice across the whole planet would contain over 10^{23} cm^3 of water. Thus, determination of the existence, depth and areal extent of any ground ice layer is of utmost importance in understanding the history of water on Mars.

4.2 Indicators of Ground Ice

A number of features have been interpreted by photogeologists as evidence for a significant ground ice layer on Mars. The most conspicuous are the large channels, first seen on Mariner 9 imagery (Milton 1973). While channels of many morphologic types and proposed origins exist, those which display large scale flow features and originate in areas of collapsed, or "chaotic", terrain are usually ascribed to massive water floods. Many investigators believe that this water was derived from the melting of subsurface ice (Carr 1978; Masursky et al. 1977).

Mars displays a marked global asymmetry between the young plains which dominate the northern hemisphere and the considerably older, higher terrain to the south. These two major geologic units are separated in many places by a scarp 1-2 km high. One interpretation of this relationship (Soderblom and Wenner 1978) is that an ancient planet-wide highlands unit was underlain by a thick layer of ice and rock which became thermally unstable. Progressive scarp retreat, due to ice breakdown and removal of the incorporated rocky material, left behind a lower plains unit. Resurfacing of these plains by volcanic and aeolian action produced the present surface.

Another probable indicator of subsurface ice is the characteristic morphology of ejecta deposits surrounding many Martian impact craters. These "rampart craters" display lobate ejecta blankets with raised distal edges, extending 1-2 crater diameters from their crater rims, and are unlike ejecta deposits surrounding lunar and Mercurian craters. Carr et al. (1977) ascribed this morphology to emplacement of the ejecta along ballistic trajectories followed by ground flow. This flow is believed by them to have been aided by entrapped gases derived from impact vaporization of subsurface ice and water. Rampart craters occur on all major geologic units of the planet, and their formation spans a significant portion of Martian geologic history, probably up to the present (Allen in press). If rampart craters are indeed indicators of ground ice, it must be or have been distributed essentially planet wide.

Certain landforms indicative of the interaction of volcanism with ice and water also occur on the surface of Mars. Among such features are possible analogs to the jokulhlaup channels, large moberg deposits, table mountains, moberg ridges and pseudocraters of Iceland. The identification and interpretation of these landforms provide valuable data on the history and evolution of volatiles at the Martian surface.

4.3 Floods

Masursky et al. (1977) studied the large variety of channels on Mars and proposed modes of origin for these features. Of particular interest to the present study are channels which originate in box canyons littered with chaotic material and which display downstream patterns resembling those associated with high flood discharges on Earth (Baker and Nummedal 1978). Fig. 11 is a Viking photomosaic of such a channel located in the highlands

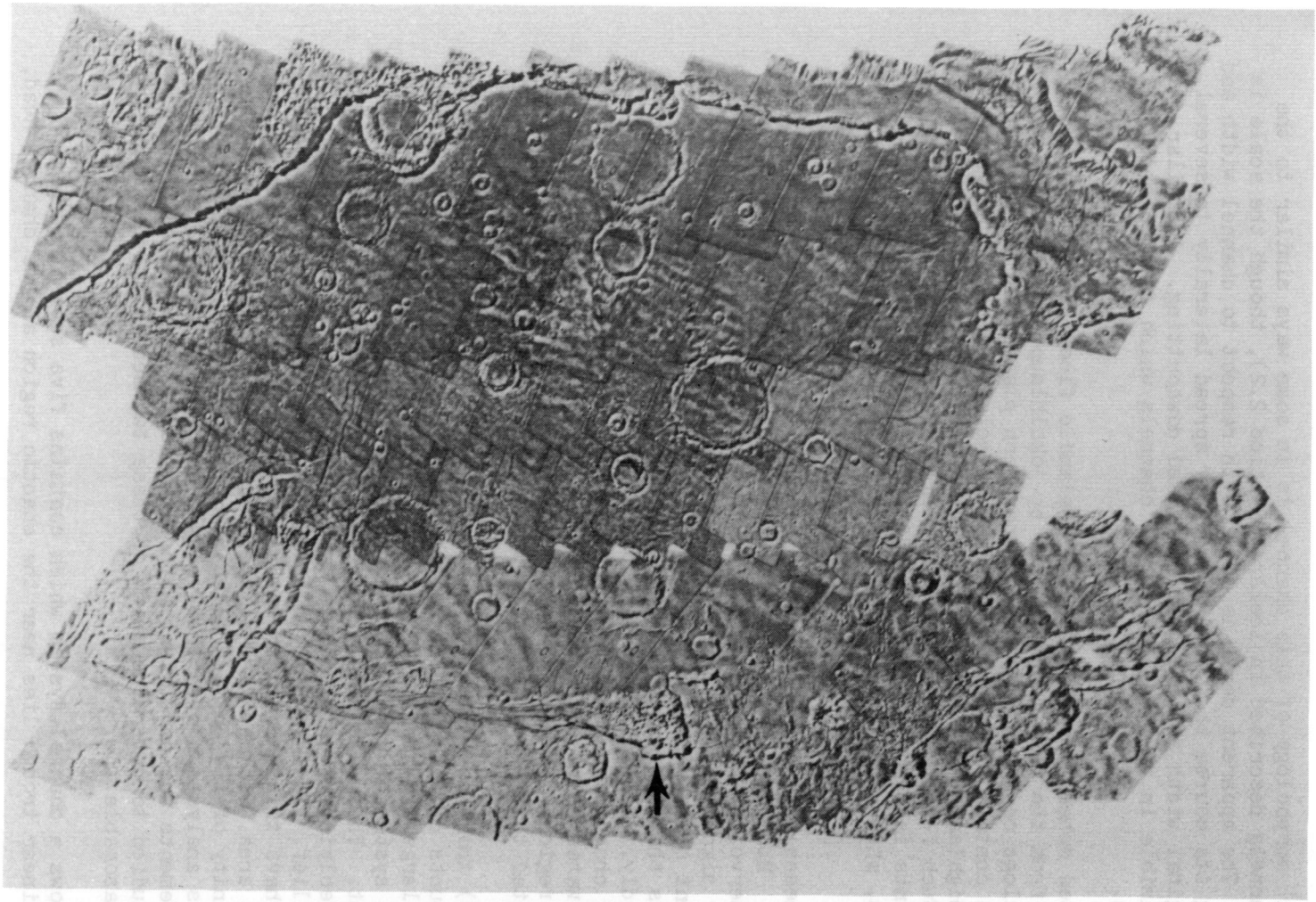

Fig. 11. Chaotic Terrain and Channel

This 200 km long channel originates in a 40 km by 70 km region of chaotic terrain (arrow) in the highlands south of Chryse Planitia. Viking photomosaic 211-5001.

south of Chryse Planitia. This channel, small by Martian standards, starts in a collapsed area 40 km across and extends for over 200 km before entering a large depression known as the Hydroates Chaos.

The overall morphology of this channel is in some ways similar to the jokulhlaup channels described in Iceland (Section 2.2), though the scale is much greater. The apparent depth is small with respect to channel width and part way along its course the flood apparently spread laterally to several times its original width and essentially ceased downcutting. A similar sequence is visible in the Icelandic flood channels which debouch onto the outwash plains.

The isolated moberg mountains on the Icelandic flood plains (Section 2.5), cut off from the main mountain mass by jokulhlaup erosion, also may have their analogs on Mars. The Martian northern plains near the highland boundary scarp contain numerous mesas which correlate in height and apparent age with the highland terrain (Fig. 12, Viking orbiter frames 34A71, 675B42-46). Such features have been identified (Guest et al. 1977) as highland remnants isolated by erosion. Similar mesas, in the vicinity of major channels, show obvious evidence of lateral erosion and streamlining by floods.

Two hypotheses have been advanced to account for this class of Martian flood channel. Both ascribe the erosion to catastrophic water flow from a subsurface reservoir. The mechanisms for producing the water and its sudden release differ significantly, however. Masursky et al. (1977) suggested that emplacement of a subsurface magma body could melt overlying permafrost. As the underground lake grew it might intersect a cliff face and drain rapidly. Overlying terrain would then collapse forming the characteristic chaotic morphology seen at the channel heads. In this model the volume of water released should roughly equal the volume removed from the collapsed region. Masursky's rough calculations for two large channel systems indicated that the estimated volumes are indeed similar.

Carr (1978) took issue with the adequacy of the collapsed terrain to supply the amounts of water implied by the flood channel morphology. He proposed that large expanses of ground ice were at one time underlain by an interconnected system of pore water maintained in the liquid state by geothermal heat. This water could have been under considerable pressure, due both to overlying material and to the hydraulic head provided by topographic relief. Thus a break in the ice layer, possibly by meteorite impact, could have triggered rapid release of a large volume of water from beneath a wide area. In such a case the size of the collapsed area in the immediate vicinity of the outflow point might be much less than the water volume. Carr's analyses showed that volumes and flow rates derived from channel measurements are consistent with this model. The channel shown in Fig. 11 was studied to determine which of these two mechanisms for melting ice is more reasonable.

Fig. 11 shows a channel system which contains five separate areas of collapse. A linear trough lies near the chaotic region at the channel head,

Fig. 12. Highland Boundary Scarp

The southern highlands near latitude 44° N and longitude 325° are separated from the northern plains by a distinct scarp. Mesas near the scarp, similar in height and apparent age to the highland terrain, were probably cut off by erosion. Frame width approximately 215 km. Viking orbiter frame 675B46.

while two large rounded collapse depressions and a smaller elongated one occur downstream. The elongated troughs, the line connecting the pair of circular depressions, and the longer wall of the main channel are parallel. They strike ENE-WSW, along a local line of structural weakness as well as the topographic gradient. Thus the locations and shapes of the collapsed regions may be either tectonically or slope controlled.

The volume of the largest collapsed area was calculated to estimate the heat required for ice melting. The solar altitude in these images is around 28^{o} above the horizon, and the sun's rays appear to just graze some of the walls of the depression. A slope angle of 28^{o}, close to the value of 25^{o} estimated by Masursky et al. (1977) for other canyons, implies a depth of 250 m for the collapsed area. The characteristic cross-canyon width is about 40 km and the length of the collapsed region is 70 km. The volume percentage of ice in terrestrial permafrost zones ranges up to 80% (Embleton and King 1975b, pp. 33 ff.), and a value of 50% was employed for the present model. This value appears conservative based on the volume deficit in the chaotic region. If 50% of the material in this region consisted of ice with a density of 0.9 gm/cm^3 the resulting flood would have a volume of 3.2×10^{17} cm^3 of water. According to estimates of other Martian floods (Masursky et al. 1977) this one was rather small, but it is still over 150 times the volume of a large Katla flood in Iceland.

As described in Section 3.2.1, flood volumes can be translated directly into minimum values for the heat needed to melt the requisite amount of ice. In the present case the requirement for simple melting is 1.0×10^{27} ergs. Assuming that this heat was produced by a near-surface intrusion equal in area to the chaotic region, and ignoring all heat sinks except ice, the heat released would amount to 3.7×10^{13} erg/cm^2. In Iceland the highest heat flow rates, exclusive of active eruptions, are approximately 2×10^{4} erg/cm^2 sec (Bodvarsson 1960). At such a rate almost 59 years would be required to melt the ice in this Martian canyon. However, the largest high temperature area in Iceland has an area of only 100 km^2, compared to the 2800 km^2 required by this model.

Melting could proceed considerably more rapidly if heat fluxes characteristic of volcanic eruptions were applicable. At the rate of 3.8×10^{19} erg/sec estimated for Katla (Section 3.2.2), the required volume of ice could be transformed to water in about ten months. However, Fig. 11 shows no evidence in the vicinity of any of the collapsed areas of surface volcanic activity.

This analysis suggests that the heat required to form water for even a small Martian flood would strain the capacity of one of the most thermally active areas on Earth. Larger floods elsewhere on Mars have been estimated to involve in excess of 10^{19} cm^3 of water (Masursky et al. 1977). While many Martian volcanoes are mammoth by terrestrial standards, the lack of surface manifestations of volcanism in the vicinity of chaotic terrain makes the subsurface intrusion mechanism suspect.

The model of Carr (1978) appears better able to satisfy the geologic requirements. This model does not require anomalous heat sources or chaotic regions with volumes comparable to those of the floods which issued from them. The apparent alignment seen in Fig. 11 could represent collapse along lines of local weakness due to the withdrawal of subsurface water. The three chaotic areas within the main flood channel may have been formed as a result of the flood itself. If water under significant pressure existed beneath the surface in these areas, removal of even a small part of the overburden by flood erosion could trigger local episodes of outburst and collapse, resulting in features such as those shown.

4.4 Massive Moberg Deposits

Indirect evidence suggests the possibility that massive deposits of volcanic material similar to palagonitized basaltic glass may exist on the surface of Mars. Indications come from spectroscopy, in situ analysis and photogeology. Definitive knowledge of the composition of Martian surface materials will probably have to await a sample return mission. However, the implications of a moberg-like composition and structure for significant amounts of the regolith call for careful examination of this question.

Soderblom and Wenner (1978) pointed out similarities between the infrared spectra of palagonitized basaltic material and spectra of Mars. While the match for the samples used was not close enough to constitute an identification, further analysis is warranted and is underway (Wenner, personal communication, 1978).

Soderblom and Wenner (1978) also noted that palagonitized samples dehydrate rapidly in a vacuum and lose much of their coherence. Under Martian conditions such material could distintegrate into particles which would be widely distributed during dust storms. Toulmin et al. (1977) stated that the Viking soil analyses are suggestive of weathered material derived from palagonitized basalts. Gooding and Keil (1978) examined the thermodynamics of such weathering and found them to be favorable under present Martian conditions.

Finally, Hodges and Moore (in preparation, 1979) have suggested that a massive layer of palagonitized tuff forms the base of Olympus Mons. This massive volcano, approximately 600 km across, is bounded at the base by a steep scarp approximately 2 km high. These authors consider Olympus Mons to be a giant table mountain, with the scarp marking the moberg layer and the rest of the volcano corresponding to the caprock. Hodges and Moore have theorized that the Martian north pole was once much nearer the location of Olympus Mons (18° N latitude, 133° longitude) and that the initial eruptions at this site took place beneath a thick icecap.

The present author is skeptical of this theory. A 600 km wide, 2 km high moberg layer seems an unlikely geometry for a central eruption. Moreover, the melting of the required 6×10^{20} cm^3 of ice would have produced innumerable jokulhalup channels, some of which should still be visible.

4.5 Pseudocraters

The modeling of pseudocrater formation in Section 3.5 shows that these features can form as a result of lava flowing above a layer of ground ice. Indeed, the ice need not be at the surface, but may be buried beneath a regolith up to half as thick as the lava. On Mars, with surface gravity less than 40% that of Earth and a much more tenuous atmosphere, pseudocraters several times larger than their terrestrial counterparts might be expected, due to the increased ballistic range (McGetchin et al. 1974).

Greeley and Theilig (1978) noted a group of mounds in southern Chryse Planitia which they believed to be analagous to the tumuli pseudocraters of southern Iceland (Viking frames 6A61-63, 4A19-20). Lucchitta (1978) proposed the same origin for scattered craters on a flow surface in Deuteronilus Mensae. During the present study several flows dotted with probable pseudocraters were located in Acidalia Planitia (Viking frame 455B1, mosaics 211-5025, 211-5557). The same identification was arrived at independently by Frey et al. (1979).

The criteria for recognizing pseudocraters include size, crater diameter/basal diameter ratio, lack of alignment, and restriction to individual flows (see Fig. 8). These criteria are met by the Acidalia cones, a number of which are shown in Fig. 14 (p. 241). Most of these features measure some 600 m across the base, or double the size of the largest Myvatn pseudocrater. They are simple, occasionally overlapping cones with craters about half their basal width. The cones are morphologically distinct from primary and secondary impact craters of the same size, as well as from the small shield volcanoes in the region.

4.6 Table Mountains and Ridges

A major goal of the present investigation was to locate Martian analogs to terrestrial table mountains and moberg ridges. In the case of many Icelandic features large scale morphology is sufficiently distinctive to permit their identification on aerial photographs and even Landsat imagery. Thus, with high resolution (50-100 m) Viking photographs similar landforms on Mars should be recognizable.

The morphologic characteristics which were required for tentative identification of a table mountain analog included steep slopes and a relatively flat caprock. Further, in order to distinguish such mountains from mesas formed by other mechanisms, some indication of subsequent eruption through the caprock was required. By analogy to Icelandic table mountains, such indications included capping flows, cones or craters (Section 2.3.9). Since size as well as morphology was considered diagnostic, mountains smaller than 1 km or larger than 20 km across were not considered analogous to table mountains.

The distinguishing characteristics of moberg ridges are general linearity and alignment with other ridges and fissures nearby (Section

2.4.4.). Most of the Icelandic features are many times as long as they are wide and often display several segments or a serrated crest indicative of multiple eruption centers. Similar morphologies were required of possible Martian analogs, along with the condition that they not be greatly dissimilar in size to the moberg ridges of Iceland.

4.6.1 Morphologic Analogs

Fig. 13 is a Viking image showing a mountain in central Acidalia Planitia which is almost a twin of Gaesafjoll (Fig. 3). The main plateau is bounded on two sides by apparently steep slopes and is topped by a large cone containing a shallow crater. The lower plateau measures 7 km by 4.8 km, while the cone is about 2 km on a side. Lack of stereo imagery makes an accurate height determination impossible. An estimate of the height can be derived by analogy to terrestrial table mountains, however. The slopes of the moberg cliffs of a number of these mountains were measured and a mean value of around 35° was derived. Assuming that this slope is relevant to table mountain analogs on Mars, the height of the plateau in Fig. 13 is approximately 500 m. The volume of this mountain is thus around 16 km^3, as compared to 5.1 km^3 for the average table mountain in Iceland (Section 3.1.9).

Many other table mountain analogs were located at various points in the northern plains. Table V (p. 247) gives location and imagery data for a selection of these features. In addition, data for several moberg ridge analogs are included.

One important example of these ridges is shown in Fig. 14. This feature, also located in Acidalia Planitia, lies within 150 km of the highland boundary. The ridge consists of two segments offset in strike by approximately 30°, similar to the structure of Herdubreidtogl (Section 2.4.3). The overall form of the Martian feature, however, more closely resembles the somewhat smaller ridge shown in Fig. 5. The Martian ridge is 6 km long and 2.2 km in width. Assuming a slope of 27°, consistent with mean values for Icelandic ridges, the height is approximately 530 m. The volume is thus around 3.5 km^3, close to the figure of 2.7 km^3 which is representative of moberg ridges in Iceland (Section 3.1.9). Several smaller ridges and fissures parallel the main Martian ridge. In addition, a set of roughly radial fractures indicate doming of the topography beneath this feature.

4.6.2 Geologic Prerequisites

While landforms strikingly similar to terrestrial table mountains and moberg ridges have been located on Mars, their size and morphology are not sufficient criteria for identification. The formation of such features requires a rather specialized set of geologic circumstances, including volcanic eruption, ice and erosion.

Fig. 13. Table Mountain Analog

This steep-sided, flat-topped mountain is located near latitude 45° N and longitude 21° in central Acidalia Planitia. A large cone with a shallow crater caps the mountain. The main plateau measures approximately 7 km by 4.8 km. Viking orbiter frame 26A28.

Fig. 14. Moberg Ridge Analog

This ridge is located near latitude 38° N and longitude 13° in Acidalia Planitia. Several smaller ridges and fissures parallel the main feature. The length of this ridge is approximately 6 km and its maximum width is 2.2 km. Numerous 600 m wide cones, probably analagous to pseudocraters, dot nearby flows. Viking orbiter frame 72A02.

Volcanism has been widespread throughout much of Martian history. Evidence ranges from shield volcanoes hundreds of kilometers across to apparently vesicular rocks at the Viking landing sites. Small mountains, similar in size and morphology to the Icelandic shields, can be seen in many locations (Viking orbiter frames 4A79, 115A24). Large areas of the planet's surface are covered with thin, lobate flows analogous to those produced by terrestrial fissure eruptions (Viking orbiter frames 583A76-80). On Earth such volcanoes are the subaerial equivalents of table mountains and moberg ridges.

Two additional conditions are implied by the formation of features like those in Iceland. First, a thick layer of ice or ice-rich material must have been in place above the eruption site. Secondly, this layer must have subsequently disapppeared, in order for the volcanic construct to be visible. On Earth the ice was in the form of Pleistocene glaciers, and the disappearance of these glaciers revealed the volcanic mountains. On Mars evidence of glaciation is lacking, though glacial valleys, moraines, drumlins and eskers might be identifiable at the resolution of Viking imagery. Therefore, a different geologic history must be invoked.

Hodges and Moore (1978) noted that landforms resembling table mountains are concentrated in Acidalia Planitia, and this is confirmed by the present investigation. Excellent Viking imagery and a number of photomosaics (211-5557, 211-5024,5) of this region reveal a sequence of events which accord well with the presence of sub-ice eruption features.

Acidalia Planitia displays several indications that a widespread surface unit once overlay the plains and has been subsequently stripped away. As noted above, this terrain is lower and younger than the adjacent highlands. The boundary between the two units has the appearance of an erosional scarp, with numerous outliers of highland terrain dotting the plains. In addition, some sections of the plains exhibit "pedestal craters". These appear to be impact craters a few kilometers in diameter perched atop individual measa. While the suggestion has been made that these are actually table mountains (Carr, personal communication, 1978), a different origin is more often proposed. This involves the crater ejecta blanket acting as a protective cap which prevents erosion of the underlying material (McCauley 1973). These pedestal craters on the plains may thus preserve remnants of an older, higher surface.

The nature of this former surface layer, and indeed its very existence, are called into question when the problem of removing it is considered. A layer consisting solely of rock or breccia on the order of a kilometer thick and covering vast areas cannot be removed without leaving massive amounts of debris somewhere in the vicinity. The lack of such a debris deposit has led to theories that the planet-wide topographic discontinuity actually reflects either a thinner northern crust (Mutch et al. 1976, pp. 316 ff.) or "subcrustal erosion" due to mantle convection (Wise et al. 1979).

An alternative hypothesis, which recognizes the apparent erosional origin of the highland boundary scarp, is that of Soderblom and Wenner

(1978). As discussed above, they interpreted the stripping of the plains as the removal of a layer of regolith containing a large percentage of ground ice and underlain by meltwater. During some phase of Martian history such a layer could have become thermally unstable, especially where exposed in crater walls or cliff faces. Progressive melting of ice and escape of meltwater could lead to the formation of a retreating scarp. Incorporated regolith material, especially that previously brecciated by meteorite impacts, might be further broken down and dispersed by fluvial and aeolian action. Cutts and Blasius (1978) identified streamlined mesas in northern Acidalia Planitia which they attributed to aeolian erosion, but which might instead have been formed during the breakdown of an ice-rich layer.

Additional evidence that a layer containing ice once covered much of Acidalia Planitia is provided by the pedestal craters. The diameters of the pedestals, and hence the crater ejecta blankets, are generally about three times the crater diameter. Such an extended ejecta range is characteristic of Martian rampart craters, thought to be indicators of ground ice or water (Carr et al. 1977). Pedestal craters thus may be the eroded remains of craters formed in an ancient ice-rich surface which has since been removed by breakdown and erosion.

The percentage of ice in this layer cannot be determined with presently available data. By analogy to terrestrial permafrost and by examination of Martian chaotic regions, a figure of 50% ice by volume may be adopted (Section 4.3).

The studies of subglacial eruptions in Chapter 3 are based on the thermal characteristics of pure ice. On Mars eruptions may have taken place into a layer which is modeled as consisting of half ice and half incorporated blocks of basaltic breccia. Such Martian eruptions would differ from their terrestrial counterparts in several respects.

The combination of ice and rock will have a mean density of around 1.8 gm/cm^3, as compared to 0.9 gm/cm^3 for pure ice. Under Martian gravity, however, the weight of such a layer would be only 76% of the weight of a glacier of the same thickness on the Earth. Thus, to the extent that initiation of the explosive phase of the eruption is pressure dependent, Martian table mountains might have thicker tuff layers than similar terrestrial features.

Eruptions into a layer consisting of 50% rock would encounter volume problems much more severe than if the layer were pure ice. Effusion of basalt might in some cases be suppressed by the overlying rock and ice, since even complete melting of the ice would remove only half the overlying material. An explosive eruption, however, would be characterized by higher rates of heat transfer and ice melting along with a more easily dispersed product, and so should be better able to melt sufficient ice to accommodate itself.

Finally, the effective heat capacity of a mixed ice and basalt layer is somewhat lower than that of pure ice. The difference is approximately one

third for the case of material initially at 0 ^{o}C and subsequently heated to 300 ^{o}C. Thus, for a given heat output, the Martian eruption would be more effective than its terrestrial counterpart.

Eruptions into an ice-rich surface layer on Mars, therefore, would take place under somewhat different physical conditions than the subglacial eruptions of Iceland. The differences, however, appear generally favorable to the formation of features similar to table mountains and moberg ridges.

At least one region of the Martian surface, therefore, appears to contain the major geologic prerequisites for the formation of table mountain and moberg ridge analogs. These include volcanic eruptions of the proper scale, an overlying layer of ice-rich material and its subsequent removal. Excellent Viking imagery of this region provides the data necessary to reconstruct a consistent geologic history of Acidalia Planitia.

4.7 Evolution of Acidalia Planitia

Early in the history of Mars the crustal rocks were subjected to intense bombardment by meteorites, which left a brecciated regolith possibly several hundred meters deep across the planet. Temperatures were low enough for the surface to act as a cold trap for water released from the planet's interior by volcanic eruptions. Over millions of years a substantial percentage of ice was incorporated into the upper crust. Below approximately one kilometer, however, the internal heat flux caused this ice melt, providing a large reservoir of liquid water.

In the area of Acidalia Planitia the ice rich zone of the regolith was about 500 m thick. A number of relatively small eruptions into this layer produced masses of glassy tuff, and where the volcanic pile built to the surface level lava flows capped these mountains. Small impacts, coming at a much lower rate than in earlier times, marked the surface with craters displaying ramparts at the edges of their ejecta blankets.

The table mountains and ridges preserved today on Acidalia Planitia probably represent only a portion of the sub-ice volcanism which occurred during this time. Large scale fissure eruptions are also likely to have taken place, adding significant masses of partially-consolidated glassy tuff to the regolith.

During a period of climatic change or increased internal heat flow the ice-rich layer in the northern hemisphere became thermally unstable. The ice melted, creating widespread floods. Some water entered the atmosphere and was distributed among a number of planet-wide sinks. The remainder percolated into the newly exposed lowland surface where it remained until another change in conditions brought about the formation of ice in this portion of the crust. The rocky material from the former top layer, already brecciated by impact and periglacial weathering, was further disaggregated and widely distributed by floods and winds. Mixed with this material was a portion of the basaltic glass from eruptions into the ice. These fragments

were altered by palagonitization and over many millenia were spread across the planet by the winds.

The plains which remained after loss of the ice-rich layer were extensively resurfaced by thin lava flows, but otherwise suffered no major changes. Pedestal craters, table mountains and moberg ridges marked the former level of ice and rock on these plains, and a scarp with outlying remnants of the highlands showed where the breakdown of this layer ceased. Impacts on the plains formed rampart craters, suggesting that a subsequent ice-rich zone formed. In some places this zone extended so near the surface that later lava flows were rent by explosions as the ice flashed to steam.

4.8 Planet-Wide Survey Results

The search for volcano-ice interaction features involved a survey of over 20,000 Viking images, taken between the start of the mission and revolution 780 (orbiter 1) and 705 (orbiter 2). The morphological criteria required for the tentative identification of table mountain and ridge analogs are listed in Section 4.6. Fig. 15 shows the results of this survey. Locations of probable sub-ice volcanic mountains within 65° of the Martian equator are plotted on a map of major geologic boundaries simplified from the work of Scott and Carr (1978). One additional feature, near the south pole, will be discussed separately below. Table V gives location and image data for these features.

Fig. 15 shows that all recognizable sub-ice eruption landforms within the map boundaries are located in the northern plains. Some of these features, such as those in Amazonis and northern Acidalia Planitia, are many hundreds of kilometers from the highland boundary. Others are found close to the scarp, in association with the "knobby material" which marks major areas of highland terrain breakdown. The geologic history thoughout the nothern plains is interpreted as similar to that described above for Acidalia Planitia (Section 4.7). D. U. Wise of the University of Massachusetts (personal communication, 1979), in mapping western Acidalia near Tempe Fossae, has interpreted the formation of table mountain analogs in a like manner. Differences in the areal density of table mountain and ridge analogs probably reflect variation in local rates of eruption, erosion and resurfacing of the plains.

An area of the northern plains which displays evidence of particularly active volcanism is Elysium Planitia. Landforms resembling table mountains are visible near the volcano Hecates Tholus (Fig. 16) and a large ridge system occupies part of the Phlegra Montes (Fig. 17). These ridges are morphologically similar to those shown in Fig. 6. A wide range in landform dimensions illustrates the variability of volcanic activity in this region of Mars.

A number of possible table mountains and moberg ridges were noted in the Martian polar regions, but verification was hampered by low photographic resolution or poor atmospheric conditions. One feature of particular

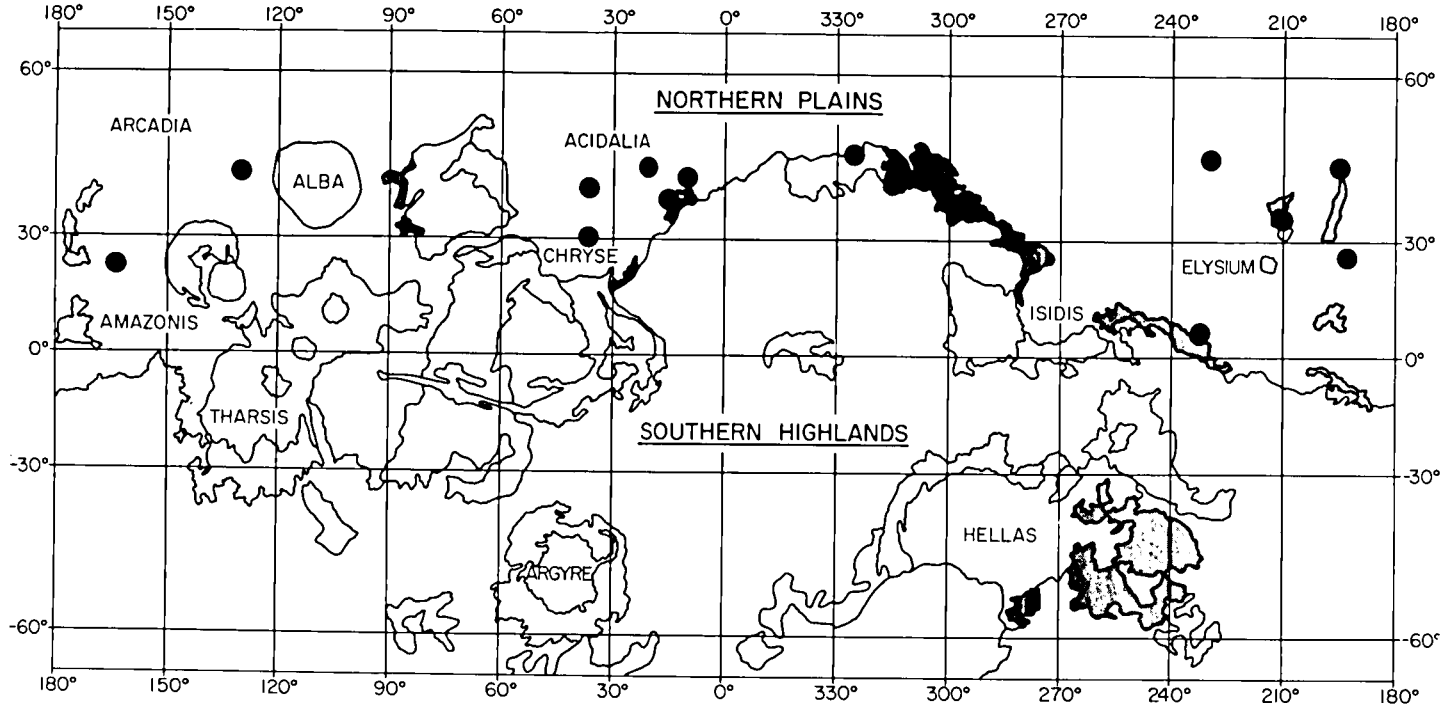

Fig. 15. Locations of Table Mountain and Moberg Ridge Analogs

Black dots indicate the locations of table mountain and moberg ridge analogs within 65° of the Martian equator. Stippling shows regions of "knobby material", a geologic unit which marks the breakdown of highland terrain. The geologic map was simplified from the work of Scott and Carr (1978).

Table V

Martian Table Mountain and Moberg Ridge Analogs

Table Mountains			Moberg Ridges		
Viking Frame	Latitude	Longitude	Viking Frame	Latitude	Longitude
9B10,15	47 N	230	7B77	44 N	130
26A28 (Fig. 13)	45 N	21	9A61	43 N	10
86A39,41 (Fig. 16)	34 N	210	58B51	47 N	326
545A14	26 N	194	66B82	6 N	233
583A55,57	24 N	164	72A02 (Fig. 14)	38 N	13
595A22	41 N	37	76B71-73 (Fig. 17)	46 N	195
655A38	25 N	160			
669A60	29 N	37			
			Mariner 9 DAS 0804433 (Fig. 18)	81 S	64

Fig. 16. Table Mountain Analogs Near Hecates Tholus

A number of table mountain analogs (T) are located near the base of the volcano Hecates Tholus (H) in Elysium Planitia. Frame width approximately 41 km. Viking orbiter frame 86A39.

Fig. 17. Moberg Ridge Analogs in the Phlegra Montes

This large ridge system is located in the northern Phlegra Montes, at the eastern edge of Elysium Planitia. The main ridge consists of a number of segments, and it is paralleled by a smaller segmented ridge to the west. Frame width approximately 88 km. Viking orbiter frame 76B71.

interest, however, was photographed well on the Mariner 9 mission. This is a system of rectilinear ridges near the south pole, informally named "Inca City" by Mariner geologists (Fig. 18).

Inca City lies in the "etched plains", which are interpreted as remnants of a vast unlayered deposit of sediments severely eroded by the wind (Mutch et al. 1976, pp. 254 ff.). Overlying this unit is a layered deposit which in turn is overlain by the south polar cap. The ridge system consists of 3-5 roughly parallel features some 50 km long by 2 km wide, locally connected by short perpendicular segments. The entire structure rests atop a low plateau which shows evidence of aeolian erosion. Inca City has beeen interpreted (Mutch el al. 1976, p. 255) as a set of dikes exposed by stripping of the overlying terrain. Alternatively, it may represent the result of fissure eruptions beneath an enlarged polar icecap. The system of moberg ridges between Iceland's Myrdals and Vatna glaciers (Fig. 7) is similar both in form and scale to this Martian feature.

4.9 Implications for Water on Mars

The motivation of this research program has been the continuing debate over the existence and extent of ground ice beneath the Martian surface. The results discussed in this chapter provide a new basis for approaching the question.

If the mountains and ridges which have been located in the Viking imagery are indeed analogous to terrestrial subglacial volcanoes a former thick ground ice layer mantling the northern plains is strongly indicated. Ice within the present regolith is probably not an adequate substitute. The voluminous supply of meltwater and the lateral confinement supplied by glacial ice or its Martian equivalent appear to be necessary for the development of table mountains and moberg ridges.

The thickness of the ice-rich layer at a number of points across the planet may be inferred from the heights of table mountain plateaus and ridge crests. As dicusssed above, the features shown in Figs. 13 and 14 yield estimates of about 500 m for the thickness of this layer at two locations in Acidalia Planitia. Other landforms in the same area indicate that the thickness varied from 250-500 m. The appropriate figure for Chryse Planitia is approximately 400 m, for Amazonis around 300 m and for the regions near Alba Patera and Elysium about one kilometer. The Inca City ridges are approximately 500 m high, which gives a lower limit to the thickness of an extended south polar cap.

The implications of these findings for the study of Martian water and ice are far reaching. Current degassing models (Owen et al. 1977) indicate that approximately 10^{21} cm^3 of water reached the surface over Mar's history. However, if the present interpretations are correct this number may have to be revised upward significantly. The sub-polar northern plains cover approximately one fourth of the planet's surface. If this area was once mantled by a 500 m thick layer containing 50% ice by volume, 8×10^{21}

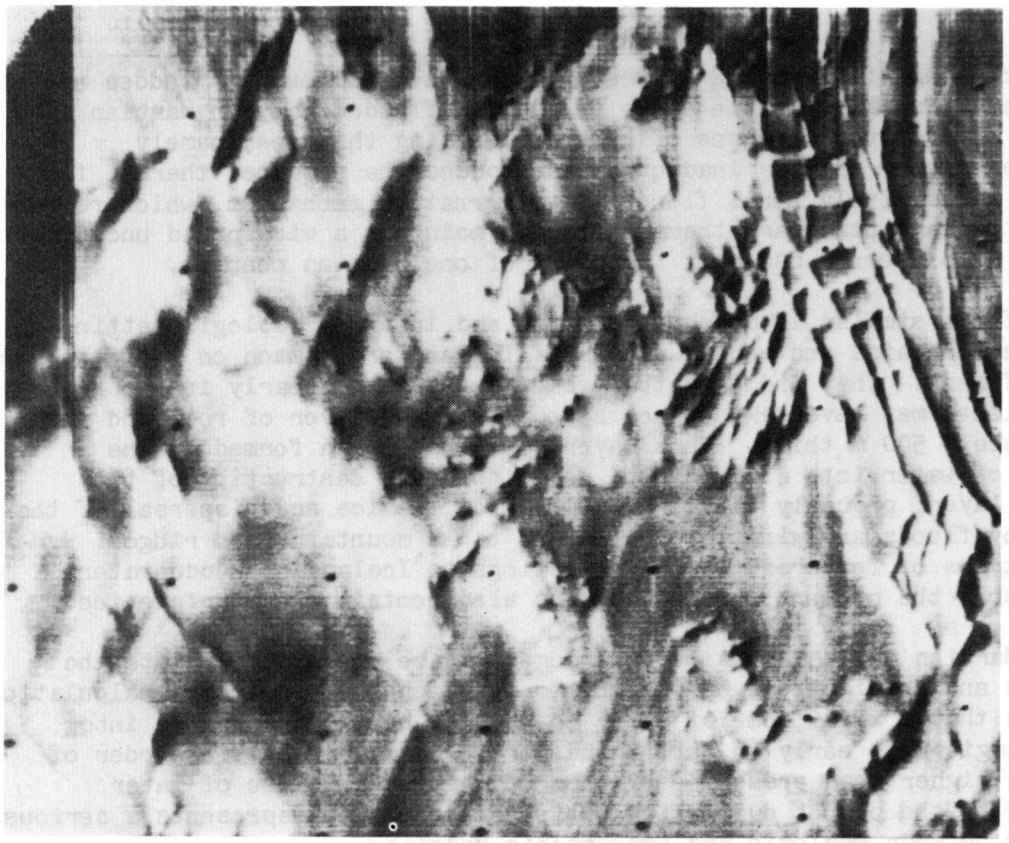

Fig. 18. Inca City

Inca City is a 50 km long system of roughly parallel ridges connected by short perpendicular segments. The ridges cap a low plateau. Inca City is located near latitude 81° S and longitude 64°, close to the edge of the south polar cap. Mariner 9 frame DAS 08044333.

cm^3 of water was involved. Thus, neglecting all other sinks and neglecting strong evidence that the highlands also contain significant ice and water, the entire predicted H_2O inventory of the planet could be accounted for several times over by this one rather localized unit.

4.10 Conclusions

The melting of large quantities of ground ice followed by sudden release of the water is the probable cause of massive floods early in Martian history. One proposed source of heat for melting this ice, namely subsurface magma, appears inadequate to produce the required thermal flux for even a relatively small flood. An alternative mechanism, which requires only the average planetary thermal flux to maintain a widespread underground aquifer, is preferred based on the study of one Martian channel.

Landforms similar in morphology, size and inferred geologic setting to the table mountains and moberg ridges of Iceland are common on the northern plains of Mars. They indicate that volcanic eruptions early in the history of the planet may have taken place beneath a mixed layer of rock and ice approximately 500 m thick. This layer could have been formed by the freezing of water into a brecciated regolith. The destruction of the ice-rich layer, probably caused by melting of the ice and dispersal of the breccia by floods and winds, revealed the table mountains and ridges. Several types of features, including analogs to Icelandic pseudocraters, suggest that the present northern plains also contain near-surface ice.

The Martian table mountains and ridges can be used to calculate the thickness and areal extent of the former ice-rich layer. Such a calculation indicates that 8×10^{21} cm^3 of water could have been incorporated into this geologic unit early in Martian history. This is nearly an order of magnitude higher than present estimates of the total volume of water outgassed by the planet during its entire history, and represents a serious disparity between geologic and atmospheric modeling.

CHAPTER 5

PERSPECTIVE AND FUTURE RESEARCH

All research, and especially interdiciplinary studies such as this one, builds on a broad foundation of past work. At some point it is important to set such projects in perspective and identify which pieces of a synthesis are in fact original contributions to knowledge.

The present study of volcano-ice interactions is somewhat unique in its attempt to fit a variety of features and processes into a single fairly simple scheme. By concentrating on the similarities, rather than the differences, among the Icelandic field sites a model for subglacial volcanism was developed which not only fits features in Canada and Alaska but is also useful for Mars. While many parts of this model eruption sequence have been previously identified by other workers, two points are new. One of these is the recognition of a hot gas phase as the solution to the volume problem encountered by a subglacial volcano. The second concerns the mechanism by which explosive eruptions are triggered due to vesiculation and interaction of the magma with water.

The laboratory and numerical analyses of various aspects of subglacial volcanism and pseudocrater formation, while relatively straightforward, are almost without precedent in this field. Many problems of Icelandic geology demand the application of similar techniques, but have not yet received such attention. Considering the importance of this island to both terrestrial and planetary geologic problems, this situation calls for immediately reply.

The recognition of subglacial volcanism as a likely process and a useful probe of the Martian surface was slow in coming. The only exception was a continuing qualitative reference to volcanic heating of permafrost as a possible source for the ancient floods. This author's suggestion (Allen 1977) that Martian analogs to table mountains and moberg ridges were likely was the initial mention of these features in a planetary context. Two years later at least three other research groups are involved with problems specifically addressed in this study.

Future work can take many forms. Geologic field studies of most subglacial volcanic landforms are woefully inadequate. The Canadian table mountains in particular deserve careful attention. Recognition within the past year of subglacial volcanic forms in Alaska and the Cascades should help make American geologists more aware of this potentially significant process. The massive moberg deposits of Antarctica, and their implications for polar glaciology and climatic history, remain poorly studied.

A corollary to subglacial volcanism is the submarine variety. The Surtsey experience and topographic studies of seamounts suggest that table mountains may have numerous equivalents on the ocean floor. Considerable work remains, however, before the similarities and differneces between these types of features can be sorted out. One important study, scheduled for 1979, is the coring of Surtsey. Questions concerning a basal pillow basalt unit below this island should be soon answered (Wenner, personal communication, 1979).

Palagonitization, both as a geologic process and as an analog to Martian soil weathering, is receiving considerable attention. No fewer than four planetology research programs will be underway in 1979-80 investigating some phase of this question. With the return of surface samples from Mars a distinct possibility within the next two decades, a great deal of interest in the weathering of basaltic material may be anticipated.

A further study of Martian surface processes, using data from the Viking continuation mission, could profitably be undertaken. Many regions of interest still have not been photographed with the resolution or atmospheric clarity necessary for detailed geologic interpretation. In addition, valuable data on surface composition, thermal properties and topography have yet to be be made available in a usable form.

The growing disparity between the volumes of water apparently demanded by photogeologic interpretation and allowed by degassing models needs to be specifically addressed. Understanding of the evolution of both surface and atmosphere of Mars depend critically on a knowledge of this number.

Two future Mars mission possibilities would be particularly beneficial for studies such as the present one. The first is the return of a sample, preferably a core, which would provide many clues to geologic products and processes. The usefulness of datable rocks from a number of sites, allowing absolute calibration of cratering chronologies, cannot be overestimated. A second mission, one to establish a seismic network, may one day permit identification of the proposed thick regolith and ice-rich zones presently hidden from view.

Finally, it should be recognized that the Earth and Mars may not be the only solar system bodies on which volcanic eruptions beneath icy material have occurred. G. J. Consolmagno, presently of the Harvard College Observatory (personal communication, 1977), has noted that such a process could well have helped to shape the surfaces of the Galilean satellites of Jupiter. Europa especially might have an ice crust a few kilometers thick and an interior capable of producing volcanism. The 1979 Voyager imaging experiments may be capable of detecting large table mountains and ridges, and could certainly show flood channels of a Martian scale. Even better data may be anticipated from the Galileo mission of the next decade.

The present study has taken one rather neglected terrestrial phenomenon and used it to probe the history of a neighboring planet. One day perhaps, if mankind's quest for knowledge continues unabated, the validity of these interpretations may be proved.

LIST OF REFERENCES

Allen, C. C., Interactions of volcanism and ice -- Earth, Mars and icy satellites (abstract), Bulletin of the American Astronomical Society, 9, 541, 1977.

Allen, C. C., Areal distribution of Martian rampart craters, Icarus, (in press).

Arnason, B., Theodorsson, P., Bjornsson, S., and Saemundsson, K., Hengill, a high temperature thermal area in Iceland, Bulletin Volcanologique, 33, 245-259, 1969.

Baker, V. R. and Nummedal, D., (editors), The Channeled Scabland, NASA, Washington, 1978.

Bardarson, H. R., Ice and Fire -- Contrasts of Icelandic Nature, Reykjavik, 1974.

Barth, T. F. W., Volcanic Geology Hot Springs and Geyers of Iceland, Carnegie Institution, Washington, 1950.

Bemmelen, R. W. van, and Rutten, M. G., Tablemountains of Northern Iceland, E. J. Brill, Leiden, 1955.

Bloss, R. D., Relationship between density and composition in mol per cent for some solid solution series, American Mineralogist, 37, 966-981, 1952.

Bodvarsson, G., Hot springs and the exploitation of natural heat sources, in On the Geology and Geophysics of Iceland, Guide to excursion no. A2, pp. 46-54, International Geological Congress XXI Session, Reykjavik, 1960.

Bottinga, Y., and Weill, D. F., Densities of liquid silicate systems calculated from partial molar volumes of oxide components, American Journal of Science, 269, 169-182, 1970.

Bottinga, Y., and Weill, D. F., The viscosity of magmatic silicate liquids: a model for calculation, American Journal of Science, 272, 438-475, 1972.

Bullard, F. M., Volcanoes of the Earth, University of Texas Press, Austin and London, 1976.

Carlisle, D., Pillow breccias and their aquagene tuffs, Quadra Island, British Columbia, Journal of Geology, 71, 48-71, 1963.

Carr, M. H., Formation of Martian flood features by release of water from confined aquifers (abstract), in Reports of Planetary Geology Program, 1977-1978, NASA Technical Memorandum TM 79729, pp. 260-262, 1978.

Carr, M. H., Crumpler, L. S., Cutts, J. A., Greeley, R., Guest, J. E., and Masursky, H., Martian impact craters and emplacement of ejecta by surface flow, Journal of Geophysical Research, 82, 4055-4065, 1977.

Carr, M. H., Masursky, H., Baum, W. A., Blasius, K. R., Briggs, G. A., Cutts, J. A., Duxbury, T., Greeley, R., Guest, J. E., Smith, B. A., Soderblom, L. A., Veverka, J., and Wellman, J. B., Preliminary results from the Viking orbiter imaging experiment, Science, 193, 766-776, 1976.

Carr, M. H., and Schaber, G. G., Martian permafrost features, Journal of Geophysical Research, 82, 4039-4054, 1977.

CRC Handbook of Chemistry and Physics, CRC Press, Inc., West Palm Beach, Fla., 1978.

Cutts, J. A., Nature and origin of layered deposits of the Martian polar regions, Journal of Geophysical Research, 78, 4231-4249, 1973.

Cutts, J.A., and Blasius, K. R., Chaotic terrain and channels on Mars: an alternative model, Contribution #98, Planetary Science Institute, Pasadena, Cal., 1978.

Doorninck, N. H. van, Die Enstetehung der Schildvulkane und der vulkanischen Tafelberge Islands, Proceedings, Koninklijke Akademie van Wetenschappen te Amsterdam, 38, 77-87, 1935.

Drake, M. J., Plagioclase-melt equilibria, Geochimica et Cosmochimica Acta, 40, 457-465, 1976.

Einarsson, T., Upper Tertiary and Pleistocene rocks in Iceland, Visindafelag Islendinga, 36, 1-196, 1962.

Einarsson, T., Physical aspects of sub-glacial eruptions, Jokull, 16, 167-174, 1966.

Embleton, C., and King, C. A. M., Glacial Geomorphology, John Wiley and Sons, New York, 1975a.

Embleton, C., and King, C. A. M., Periglacial Geomorphology, John Wiley and Sons, New York, 1975b.

Fanale, F. P., Martian volatiles: their degassing history and geochemical fate, Icarus, 28, 179-202, 1976.

Farmer, C. B., Davies, D. W., Holland, A. L., LaPorte, D. D., and Doms, P.E., Mars: water vapor observations from the Viking orbiters, Journal of Geophysical Research, 82, 4225-4248, 1977.

Frey, H. V., Chase, S. A., and Lowry, B., Phreatic eruptions on Mars (abstract), in Lunar and Planetary Science X, pp. 400-401, Lunar and Planetary Institute, Houston, Tex., 1979.

Gooding, J. L., and Keil, K., Alteration of glass as a possible source of clay minerals on Mars, Geophysical Research Letters, 5, 727-730, 1978.

Goody, R. M., and Walker, J. C. G., Atmospheres, Prentice Hall, Inc., Englewood Cliffs, N. J., 1972.

Greeley, R., and Theilig, E., Small volcanic constructs in the Chryse Planitia region of Mars (abstract), in Reports of Planetary Geology Program, 1977-1978, NASA Technical Memorandum TM 79729, p. 202, 1978.

Guest, J. E., Butterworth, P. S., and Greeley, R., Geological observations in the Cydonia region of Mars from Viking, Journal of Geophysical Research, 82, 4111-4120, 1977.

Hamilton, W., The Hallett volcanic province, Antarctica, U.S. Geological Survey Professional Paper 456-C, C1-C62, 1972.

Hoare, J. M., and Coonrad, W. L., A tuya in Togiak Valley, southwest Alaska, Journal of Research of the U.S. Geological Survey, 6, 193-201, 1978.

Hodges, C. A., and Moore, H. J., Tablemountains of Mars (abstract), in Lunar and Planetary Science IX, pp. 523-525, Lunar and Planetary Institute, Houston, Tex., 1978.

Hodges, C. A., and Moore, H. J., Tablemountains of Mars (in preparation), U.S. Geological Survey, Menlo Park, Ca., 1979.

Holcomb, R. T., Peterson, D. W., and Tilling, R. I., Recent landforms of Kilauea volcano, in Geologic Guide to the Island of Hawaii, pp. 49-86, NASA, Washington, 1974.

Huguenin, R. L., Mars: chemical weathering as a massive volatile sink, Icarus, 28, 203-212, 1976.

Jaeger, J. C., Temperatures outside a cooling intrusive sheet, American Journal of Science, 257, 44-54, 1959.

Jakobsson, S. P., The geology and petrography of the Vestmann Islands. A preliminary report, Surtsey Research Progress Reports IV, 113-129, 1968.

Jakobsson, S. P., Environmental factors controlling the palagonitization of the Surtsey tephra, Iceland, Bulletin of the Geological Society of Denmark, 27, 91-105, 1978.

Jones, J. G., Pillow lavas as depth indicators, American Journal of Science, 267, 181-195, 1969.

Jones, J. G., Intraglacial volcanoes of the Laugarvatn region, southwest Iceland, II, Journal of Geology, 78, 127-140, 1970.

Kieffer, H. H., Martin, T. Z., Peterfreund, A. R., Jakosky, B. M., Miner, E. D., and Palluconi, F. D., Thermal and albedo mapping of Mars during the Viking primary mission, Journal of Geophysical Research, 82, 4249-4291, 1977.

Kjartansson, G., Arnesinga Saga I. Natturulysing Arnessyslu., Yfirlit of Jardsaga, Reykjavik, 1943.

Kjartansson, G., The Moberg Formation, in On the Geology and Geophysics of Iceland, Guide to excursion no. A2, pp. 21-28, International Geological Congress XXI Session, Reykjavik, 1960a.

Kjartansson, G., Geological map of Iceland, Sheet 3, South-west Iceland, Museum of Natural History, Reykjavik, 1960b.

Kjartansson, G., Geological Map of Iceland, Sheet 6, South-central Iceland, Museum of Natural History, Reykjavik, 1962.

Kjartansson, G., Geological Map of Iceland, Sheet 5, Central Iceland, Museum of Natural History, Reykjavik, 1965.

Kudo, A. M., and Weill, D. F., An igneous plagioclase geothermometer, Contributions to Mineralogy and Petrology, 25, 52-65, 1970.

Le Masurier, W. E., Volcanic record of Cenozoic glacial history, Marie Byrd Land, International Union of Geological Sciences (Pub.) Series B, 1, 251-259, 1972.

Lewis, W. V., Nivation, river grading, and shoreline development in south-east Iceland, Geographical Journal, 88, 431-447, 1936.

Lucchitta, B. K., Survey of cold-climate features on Mars (abstract), in Second Colloquium on Planetary Water and Polar Processes, pp. 48-51, NASA, Washington, 1978.

Macdonald, G. A., Volcanoes, Prentice-Hall, Inc., Englewood Cliffs, N. J., 1972.

Masursky, H., Boyce, J. M., Dial, A. L., Schaber, G. C., and Strobell, M. E., Classification and time of formation of Martian channels based on Viking data, Journal of Geophysical Research, 82, 4016-4038, 1977.

Mathews, W. H., "Tuyas", flat-topped volcanoes in northern British Columbia, American Journal of Science, 245, 560-570, 1947.

McCauley, J. F., Mariner 9 evidence for wind erosion in the equatorial and mid-latitude regions of Mars, Journal of Geophysical Research, 78, 4123-4137, 1973.

McElroy, M. B., Mars: an evolving atmosphere, Science, 175, 443-445, 1972.

McElroy, M. B., Kong, T. Y. and Yung, Y. L., Photochemistry and evolution of Mars' atmosphere: a Viking perspective, Journal of Geophysical Research, 82, 4379-4388, 1977.

McGetchin, T. R., Settle, M., and Chouet, B. A., Cinder cone growth modeled after Northeast Crater, Mount Etna, Sicily, Journal of Geophysical Research, 79, 3257-3272, 1974.

Milton, D. J., Water and processes of degradation in the Martian landscape, Journal of Geophysical Research, 78, 4037-4047, 1973.

Morey, G. W., The Properties of Glass, Reinhold Publishing Co., New York, 1954.

Mueller, R. F., and Saxena, S. K., Chemical Petrology, Springer-Verlag, New York, Heidelberg, Berlin, 1977.

Mutch, T. A., Arvidson, R. E., Hed, J. W. III, Jones, K. L. and Saunders, R. S., The Geology of Mars, Princeton University Press, Princeton, N. J., 1976.

Nafe, J. E., and Drake, C. E., Physical properties of rocks of basaltic composition, in Basalts, Volume 2, pp. 483-502, Wiley Interscience, New York, 1968.

Nielsen, N., Contributions to the physiography of Iceland. With particular reference to the highlands west of Vatnajokull, Det Kongelige Danske Vindenskabernes Selskabs Skrifter, 9. Raekke, Naturvidenskagelig of Mathematisk Afdeling, 4, 185-286, 1933.

Nielsen, N., A volcano under an ice-cap. Vatnajokull, Iceland 1934-36, Geographical Journal, 90, 6-23, 1937.

Noe-Nygarrd, A., Sub-glacial volcanic activity in ancient and recent times, Folia Geographica Danica, 1, 1-67, 1940.

Nummedal, D., Boothroyd, J. C., Hine, A. C., and Hayes, M. O., Iceland geology -- slide set no. 3, University of Southern Carolina, Columbia, S. C., 1974.

Owen, T., Biemann, K., Rushneck, D. R., Biller, J. E., Howarth, D. W., and LaFleur, A. L., The composition of the atmosphere at the surface of Mars, Journal of Geophysical Research, 82, 4635-4639, 1977.

Pjetursson, H., The glacial palagonite-formation of Iceland, Scottish Geographical Magazine, 16, 265-293, 1900.

Preusser, H., The Landscapes of Iceland: Types and Regions, Dr. W. Junk, The Hague, 1976.

Rittmann, A., Die Vulkane and Myvatn in Nord-Island, Bulletin Volcanologique, 2, 1-38, 1938.

Rittmann, A., Volcanoes and Their Activity, Wiley Interscience, New York, 1962.

Robie, R. A., Hemingway, B. S., and Fisher, J. R., Thermodynamic properties of minerals and related substances at 298.15 k and 1 bar (10^5 pascals) pressure and at higher temperatures, Geological Survey Bulletin 1452, 1978.

Roeder, P. L. and Emslie, R. F., Olivine-liquid equilibrium, Contributions to Mineralogy and Petrology, 29, 275-289, 1970.

Saemundsson, K., Vulkanismus and Tektonik des Hengill-Gebietes in Sudwest-Island, Acta Naturalia Islandica, 2, 1967.

Saemundsson, K., Geological Map of Iceland, Sheet 7, North-east Iceland, Museum of Natural History, Reykjavik, 1977.

Schwarzbach, M., Geologenfahrten in Island, Ludwigsburg, 1964.

Scott, D. H., and Carr, M. H., Geologic Map of Mars, U.S. Geological Survey, Reston, Va., 1978.

Seif, A., and Kirk, D. B., Structure of the atmosphere of Mars in summer at mid-latitudes, Journal of Geophysical Research, 82, 4364-4378, 1977.

Sharp, R. P., Mars: troughed terrain, Journal of Geophysical Research, 78, 4063-4072, 1973a.

Sharp, R. P., Mars: fretted and chaotic terrains, Journal of Geophysical Research, 78, 4073-4083, 1973b.

Shaw, H. R., Rheology of basalt in the melting range, Journal of Petrology, 10, 510-535, 1969.

Shaw, H. R. Wright, T. L. Peck, D. L., and Okamura, R., The viscosity of basaltic magma: an analysis of field measurements in Makuopuhi lava lake, Hawaii, American Journal of Science, 266, 225-264, 1968.

Shreve, R. L., and Sharp, R. P., Internal deformation and thermal anomalies in Lower Blue Glacier, Mount Olympus, Washington, U.S.A., Journal of Glaciology, 9, 65-86, 1970.

Sigvaldason, G. E., Structure and products of subaquatic volcanoes in Iceland, Contributions to Mineralogy and Petrology, 18, 1-16, 1968.

Sigvaldason, G. E., and Elisson, G., Collection and analysis of volcanic gases at Surtsey, Iceland, Geochimica et Cosmochimica Acta, 32, 797-805, 1968.

Smoluchowski, R., Mars: retention of ice, Science, 159, 1348-1350, 1968.

Soderblom, L. A., and Wenner, D. B., Possible fossil H_2O liquid-ice interfaces in the Martian crust, Icarus, 34, 622-637, 1978.

Thorarinsson, S., On the predicting of volcanic eruptions in Iceland, Bulletin Volcanologique, 23, 45-52, 1960a.

Thorarinsson, S., The postglacial history of the Myvatn area and the area between Myvatn and Jokulsa a Fjollum, in On the Geology and Geophysics of Iceland, Guide to excursion no. A2, pp. 60-69, International Geological Congress XXI Session Reykjavik, 1960b.

Thorarinsson, S., Der Jokulsa-Canyon und Asbyrgi, Petermanns Geographische Mitteilungen, 104, 154-162, 1960c.

Thorarinsson, S., The postglacial volcanism, in On the Geology and Geophysics of Iceland, Guide to excursion no. A2, pp. 33-45, International Geological Congress XXI Session, Reykjavik, 1960d.

Thorarinsson, S., Surtsey the New Island in the North Atlantic, Almenna bokafelagid, Reykjavik, 1964.

Thorarinsson, S., Some facts about the Surtsey eruption, Naturufraeding-urinn, 35, 153-181, 1966.

Thorarinsson, S., Hekla and Katla, in Iceland and Mid-Ocean Ridges, Visindafelag Islendiga, Reykjavik, 190-199, 1967a.

Thorarinsson, S., Some problems of volcanism in Iceland, Geologische Rundschau, 57, 1-20, 1967b.

Thorarinsson, S., The Lakagigar eruption of 1783, Bulletin Volcanologique, 33, 910-929, 1970.

Thorarinsson, S., Einarsson, T., Sigvaldason, G., and Elisson, G., The submarine eruption off the Vestmann Islands 1963-64, Bulletin Volcanologique, 27, 435-445, 1964.

Thorarinsson, S., and Rist, S., Skaftarhlaup i September 1955, Jokull, 5, 37-40, 1955.

Thoroddsen, T., Die Geschichte der islandischen Vulkane, Det Kongelige Danske Videnskabernes Selskabs Skrifter, 9. Raekke, Natutvidenskabelig og Mathematisk Afdeling, 8, 1925.

Toulmin, P., III, Baird, A. K., Clark, B. C., Keil, K., Rose, H. J., Jr., Christian, R. P., Evans, P. H., and Kelliher, W. C., Geochemical and mineralogical interpretation of the Viking inorganic chemical results, Journal of Geophysical Research, 82, 4625-4634, 1977.

Walker, D., Longhi, J., Kirkpatrick, R. J., and Hays, J. F., Differentiation of an Apollo 12 picrite magma, Proceedings of the Lunar Science Conference, 7th, 1365-1389, 1976.

Walker G. P. L., Lengths of lava flows, Philosophical Transactions of the Royal Society (London), A 274, 107-118, 1973.

Walker, G. P. L., Eruptive mechanisms in Iceland, in Geodynamics of Iceland and the North Atlantic Area, pp. 189-201, D. Reidel Publishing Co., Dordrecht-Holland, Boston, 1974.

Wise, D. U., Golembek, M. P., and McGill, G. E. Structural sequence, timing, and a model for the evolution of the Tharsis province of Mars (abstract), in Second International Colloquium on Mars, p. 89, NASA Conference Publication 2072, 1979.

Wood, C. A., Whitford-Stark, J. L., and Head, J. W., Iceland Field Itinerary, NASA, Washington, 1977.

SECTION III

WASHINGTON UNIVERSITY

Department of Earth and Planetary Sciences

THE STRATIGRAPHIC SEQUENCE OF VOLCANIC AND SEDIMENTARY UNITS IN THE NORTH POLAR REGION OF MARS

by

Michael Edward Botts

A thesis presented to the
Graduate School of Arts and Sciences
of Washington University
in partial fulfillment of the
requirements for the
degree of Master of Arts

November, 1979

Saint Louis, Missouri

TABLE OF CONTENTS

LIST OF FIGURES

ACKNOWLEDGEMENTS

This research was funded in part by NASA grants NSG-7545 and NSG-7087 from the Planetary Division of the Office of Space Sciences (OSS) of NASA Headquarters to Washington University in St. Louis, Missouri, and was conducted at the NASA Regional Space Imagery Center at Washington University. The results of this research were submitted to Washington University as partial fulfillment of the requirements for the degree of Master of Arts in the Department of Earth and Planetary Sciences.

I would like to thank my thesis advisor, Dr. Raymond E. Arvidson, for his valuable advice and criticism, and more importantly, for allowing me the freedom to pursue my own intuitions. Likewise, a very special appreciation is reserved for Pat Jacobberger, who typed this manuscript and provided the moral support needed to complete this endeavor.

The final preparation of this report was conducted while I was employed as a Research Associate in the Space Sciences Laboratory of George C. Marshall Space Flight Center, Alabama. The personal interest shown during this tenure by Dr. William W. Vaughan, Chief of the Atmospheric Division, is acknowledged. I also wish to thank Dr. Nicholas C. Costes, Geotechnical Research Laboratory, for the continued technical and moral support, encouragement, and advice received from him during this time.

ABSTRACT

Based on photogeologic mapping of Viking Orbiter images of Mars, four distinct informal stratigraphic units can be defined for the region north of 70°N latitude. They are: (a) bulbous plains, (b) mantled plains, (c) dune deposits, and (d) layered deposits/perennial ice.

The bulbous plains unit underlies all other north polar units and represents a sub-unit of the mottled cratered plains. Based on crater size-frequency data, bulbous plains is equivalent in age to the relatively old cratered plains unit at Tempe Plateau (90°W, 30°N). The low albedo of bulbous plains and the appearance of what appears to be a dike suggest that bulbous plains has a volcanic origin. Cumulative crater size-frequency distribution functions for bulbous and mantled plains display two-segment curves with a crater-production slope of -2.0 and a cratering-obliteration equilibrium slope of -0.7. This supports the interpretation that mantled plains were formed by dust blanketing of bulbous plains. As calculated from crater size-frequency distribution functions, the relative surface-obliteration rates are 1:9:88 for bulbous, moderately mantled, and heavily mantled plains, respectively.

The layered deposits probably represent a facies of mantled plains in which dust has been deposited onto the perennial ice cap rather than directly onto the ground. Thus, the areal extent of the layered deposits at the north and south poles may indicate the maximum extent of the perennial ice caps as controlled by changes in Martian orbital parameters.

Dune deposits occur in the form of longitudinal, transverse, and barchan dunes, and possibly as sheet sand deposits. Actual dunes are generally confined to mantled plains, suggesting that mantling provides a proper substratum for dune accumulation.

Surface winds for the north polar region were determined from dune orientations to flow predominantly counterclockwise around the polar cap, although there is evidence for dune modification by secondary winds spiralling clockwise off of the cap.

A gradation from densely spaced transverse dunes to more dispersed barchan and transverse dunes implies a general thinning of circumpolar dune deposits downwind of extensive areas mapped as bulbous plains. The author suggests that dune material is being stripped from bulbous plains and is accumulating as dunes downwind on mantled plains.

BACKGROUND

Telescopic Observations

Man first became interested in the polar regions of Mars when white polar spots were reported by Cassini in 1666 and again by Huygens in 1672. In 1784, Sir William Herschel studied the changing size of the polar caps with seasons and interpreted the polar spots as seasonal accumulations of ice and snow. The melting of the polar caps was found to be intimately related to the "wave of darkening" of the Martian surface during summer (1).

Although Wilhelm Beer and Johann Mädler reported the presence of a dark band around the receding north pole of Mars in 1830, little further attention was given to the observation until 1894 when Percival Lowell reported a similar band around the south polar cap. This sparked controversy as to whether the dark bands were real features of the Martian surface or just an optical illusion (2). Since the circumpolar bands were interpreted as moistened ground, their presence would imply actual melting of the retreating polar water ice rather than sublimation (1). Lowell envisioned his Martian "canals" as an irrigation system designed to bring water from the melting caps to the arid lower latitudes (2).

Two distinct types of Martian polar "caps" have been recognized since 1907. The spring and summer caps are surface deposits whereas the "caps" observed in autumn and winter are cloud mantles (i.e. the polar hood). The polar hood begins forming as the summer ends and disappears rather abruptly at vernal equinox (1).

Two major differences between the north and south polar ice caps have been recognized from telescopic observations. Whereas the north polar cap is centered almost precisely on the rotation axis of Mars, the center of the south polar cap deviates from the rotation axis by 5°. Also, the north polar cap is larger than the southern cap, probably due to the fact that the subsolar latitude during perihelion is presently in the southern hemisphere. It is probable that during this period of excess insolation in the southern hemisphere, the north polar cap grows at the expense of the southern cap (3).

Mariner Mission Results

Neither polar cap was imaged by the 20 pictures returned by the Mariner 4 Mars flyby mission in 1965. However, spectrometry data taken during Mars occultation determined that the Martian atmosphere was essentially carbon

dioxide at a few millibars. This led many to argue that the polar caps may also be primarily carbon dioxide (2).

The first "close-up" images of the south polar cap were taken by the Mariner 7 spacecraft as it flew by Mars in 1969. No dark circumpolar band was observed for the south polar region, placing serious doubt on the possibility that a dark "melt band" might occur around the north pole (2).

The Mariner 9 orbiting spacecraft photographed Mars from November 1971 to March 1972, and provided excellent south polar coverage. This was, in part, due to the fact that the south pole was the only feature clearly seen through the global dust storm which enshrouded Mars during the early mission, and because the orbit of the spacecraft traversed the south pole every revolution during the orbit's periapsis. The entire south pole was imaged at 3-4 km resolution with 20% covered by 300-400 m resolution (3).

One of the most striking features of the south pole is the "quasi-linear, swirl-like" pattern seen in the ice cap. The north polar cap was later found to display an even more pronounced swirl pattern (see figure 1). Based on Mariner 9 images, several mechanisms have been proposed to account for these features. Murray and Malin (4) proposed that the curvilinear features represented the edges of stacked plates of ice and suggested that an offsetting of these plates provided evidence for polar wandering. Others believed the features represented troughs rather than the edges of plates, and suggested spiralling polar winds (5), or mass-wasting (6) as the dominant erosion mechanisms.

The excellent Mariner 9 coverage of the south polar region provided a clear understanding of its stratigraphic sequence (7). The ancient cratered terrain, which is the oldest unit on Mars and covers most of the southern hemisphere, underlies the south polar region as well. Massive (i.e. unlayered) blankets, probably composed of fine, wind-transported dust, overlie the ancient cratered terrain in the south polar region. These blankets have been extensively eroded to form pitted terrain and etched terrain (8). The massive blankets are overlain, sometimes unconformably, by layered deposits which have been subsequently eroded to expose the layering in troughs and scarps. In addition to the thin mantles of CO_2 ice which advance and retreat each year (7), permanent ice caps cover both poles though Mariner 9 investigations could not determine whether the permanent caps consist of H_2O or CO_2 ice.

The layered deposits probably form by cyclic deposition of wind-blown dust carried in from the mid-latitudes (9). Deposition models using 50,000 and 95,000 year climatic cycles have been proposed to account for the layers (4), although Cutts concludes that such a period is too short to allow transport of sufficient material to the poles. However, a 2 million-year cycle of orbital ellipticity of Mars may modify the intensity of global dust storms enough to cause the layering, and allow time for a sufficient amount of material to be transported to the poles (9).

Compared to the south polar coverage, Mariner 9 coverage of the north pole of Mars was relatively poor. Not only was the spacecraft's orbit much higher over the north pole compared to the orbital range during south polar traverses, but the polar hood obscured the north polar region during most of the standard mission. Although visibility improved greatly during the Mariner 9 extended mission, north polar coverage was severely limited because of a shortage in the spacecraft's attitude-control gas.

Mariner 9 imagery products showed the north polar cap and its associated layered deposits to be very similar to deposits of the south pole. Minor differences include the most pronounced "swirl-like" pattern of the north polar cap and the greater extent of the northern permanent ice cap. Layered deposits in the north are most extensively covered by permanent ice than at the south pole.

Although the lack of a dark circumpolar band in the south has placed serious doubt on the pressence of such a band in the north, a very low albedo band around the northern pole was confirmed by Mariner 9. However, the feature was found to be fixed in position, rather than a halo surrounding a retreating ice cap. Sagan et. al. (10) attributed the presence of the dark band to the scouring of a thin layer of bright dust by strong polar winds.

Mariner 9, for the first time, allowed determination of the stratigraphic sequence of the north polar region (11). Like the south polar region, the sequence in the north was found to include an underlying cratered unit, a massive deposit interpreted as wind-blown dust, and layered deposits capped by permanent ice.

However, the underlying moderately cratered unit is not the ancient cratered terrain, but rather a younger unit designated as mottled cratered plains. These plains are characterized by Soderblom et. al. (11) as having an abundance of small craters (10-20 km diameter), lower average albedo than most of Mars, and a highly mottled appearance which results from numerous bright and dark streaks and bright material highlighting crater rims and interiors. As mapped by Soderblom et. al. the mottled cratered plains are distributed rather extensively between 55° to 80° north latitudes.

Overlying the mottled cratered plains is a bright debris mantle which was subdivided into smooth, etch-pitted, and rippled plains (11). Rippled and etched-pitted plains were interpreted as depositional and erosional modifications of smooth plains. Because of the severely limited extent and poor quality of the Mariner 9 north polar coverage, the geologic mapping of Soderblom et. al. (11) is labelled by the authors as "preliminary" and contains numerous implied boundaries between units.

Viking Mission Results (August 1976-November 1978)

Compared to Mariner 9, the Viking Orbiter spacecrafts, particularly VO2, provided much improved coverage of the north polar region of Mars.

Following the successful landings of Viking Landers 1 and 2, the inclination of the orbit of Viking Orbiter 2 was changed from 55° to 75° in order to permit extensive north polar coverage before polar hood formation (33). Ground resolution of the north polar images taken with the VO2 in this orbit was 100-180 meters as compared to 300-400 meters for Mariner 9 high-resolution coverage of the south pole (3). During the extend Viking mission, the orbital inclination of VO2 was further increased to 80° and the periapsis lowered from 1500 km to 778 km (33). This improved the ground resolution of the north polar imagery to about 60 meters.

In addition to the Viking Orbiter imaging capabilities, the Orbiters included an infrared thermal mapper (IRTM) which provided conclusive evidence that the residual ice cap at the north pole was composed of a "dirty water ice" (12). Summer temperatures at the south pole have not dropped low enough to allow a similar determination of the composition of the south polar cap (34).

The spiral patterns within the polar caps have continued to intrigue Viking investigators. Although it is now generally accepted that these features are troughs rather than plate edges, there is still much controversy as to the origin of the troughs. As an alternate hypothesis to the rotating wind erosion and mass wasting processes mentioned earlier, Howard (13) has suggested that isolation-controlled ice ablation and accumulation could account for the spiral pattern of the troughs, with wind action only serving to redistribute dust across layered deposits.

The circumpolar dark band, which has been confirmed by Mariner 9 investigations, was determined from Viking images not to be a deflation feature as had been predicted earlier, but corresponded instead to large dune fields partially surrounding the north polar ice cap (14). It will be shown in this paper, however, that not all of the dark areas can be explained by the presence of visible dunes.

Determining the source of such a large supply of dune material has become a very intriguing problem. Any model attempting to define the source of the north polar dune deposits must consider: (a) the unique geographic association of large fields with the north polar region, (b) the very low albedo of the dune deposits ($A_L \leq 0.20$) (12), and (c) the particle size required for saltation in the Martian environment (diameter = 200-250 μm; 15). An added complication to the grain size requirement is that sands appear to be absent at the Viking Landing sites, possibly due to self-destruction of saltating grains during the impacts with rocks (i.e. the "kamikaze" effect; 16). Therefore, the model must account for sand-sized particles being present at high latitudes while apparently absent at lower latitudes. Source models proposed fall into three general categories: (a) dune sands have been transported from lower latitudes predominantly by saltation (14), (b) dune material consists of aggregates of atmospherically-derived dust, which have been deposited either directly onto the ground as "dirty iceballs" (17), or onto the polar cap where it is subsequently eroded from the layered deposits (14), and (c) dune sands have a regional source implying processes unique to the north polar region (15, this paper). Each model proposed has certain problems which must be accounted for.

Blasius et. al. (35) have suggested that aeolian carving of many of the channels leading into Chryse Planitia may have supplied both suspended and saltating material to the northern plains. Although conditions may have been different in the past, neither wind streak data (3, 10) nor atmospheric models based on present conditions (18, 19) support such an atmospheric flow direction.

A major complication with the proposed atmospheric-dust models is that they require aggregation of fines to form sand-sized particles, using aggregate bonding mechanisms such as electrostatics (20), ice (17), or evaporites (14). A more serious problem is that the atmospheric-dust models fail to account for the low albedo of the dune deposits, since atmospheric dust on Mars is commonly known to have a high albedo.

A regional-source model must explain the uniqueness of the large supply of dune material in the north polar region, by assuming either a unique source unit, a unique polar process, or both. Squyres (15) has suggested that a regional source of "coarse-grained" basalt may produce low-albedo dune material which retains its sand-size and low albedo because of low UV weathering rates. Retention of an adequate sand supply may be aided by high mechanical weathering rates which result from freeze-thaw processes and glacial grinding.

Based on the improved coverage by the Viking Orbiter spacecrafts, Squyres (15) revised the stratigraphic sequence in the north polar region to include dune material. Following much the same sequence as set forth by Soderblom et. at., Squyres divided the stratigraphy into moderately-cratered plains material, debris mantle (massive deposits), dune material, laminated (layered) deposits, and perennial ice. Using results derived through photogeologic mapping and from crater size-frequency distribution data, it will be shown in this paper that the stratigraphic mapping of Squyres is inconsistent with his description of the units.

The results of the present paper were primarily obtained from photogeologic mapping of Viking Orbiter imagery in the form of mosaics and individual enlarged frames. The goals of the research were (a) to redefine and map distinct informal stratigraphic units in the north polar region of Mars (i.e. $>70^{\circ}$N latitude), (b) to define and interpret crater size-frequency distribution functions for particular units, (c) to map the directions of dune-driving winds based on the orientation and form of circumpolar dunes, and (d) to infer a source for the north polar dune deposits based on the relationships between dune-driving winds and the distribution of stratigraphic units.

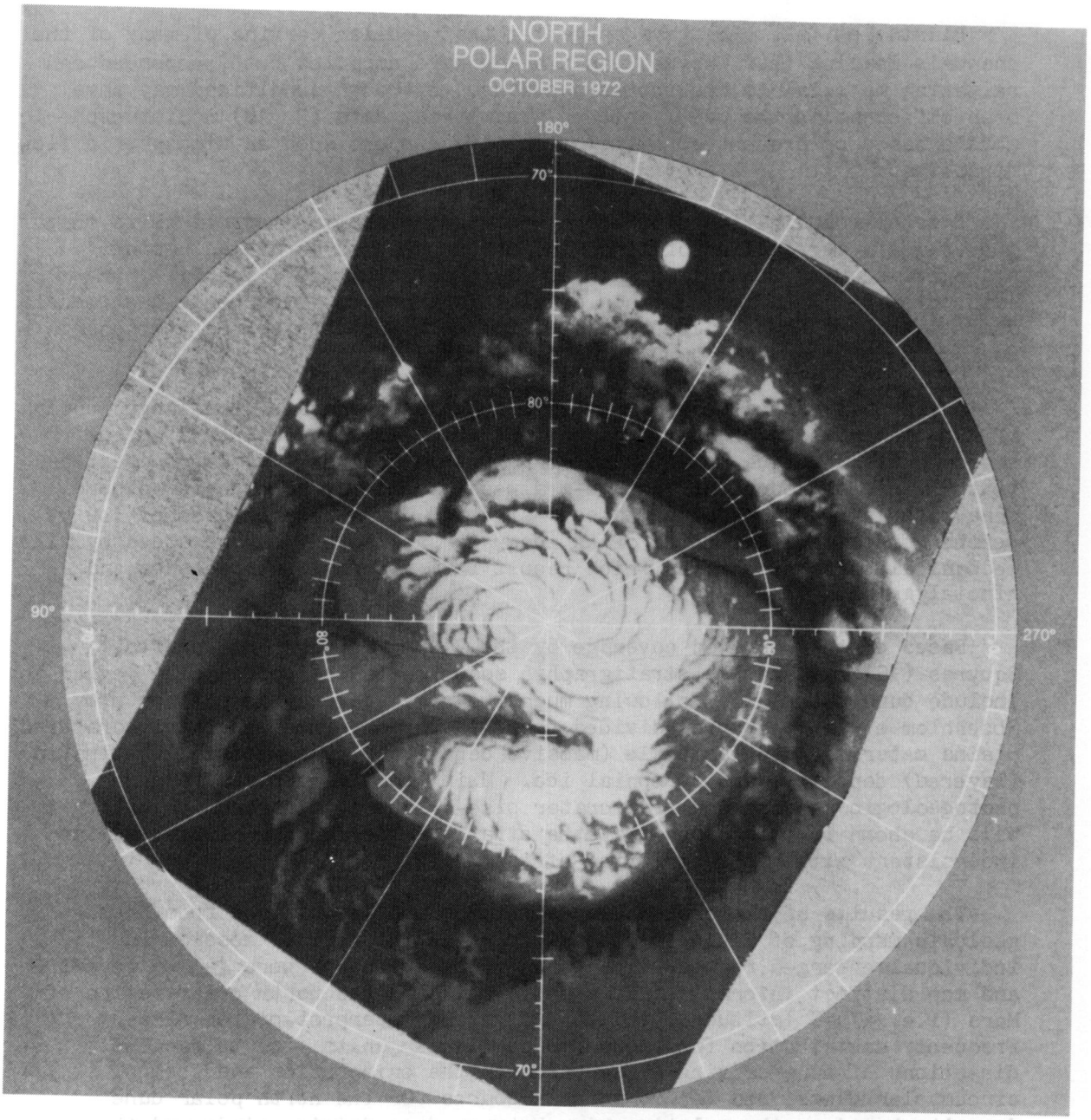

Figure 1: Mariner 9 mosaic of the north polar region of Mars (from Mars as Viewed from Mariner 9, NASA SP-329, 1976). Note the well developed spiral pattern within the ice cap. The low-albedo band surrounding the cap corresponds in part to the presence of dune fields.

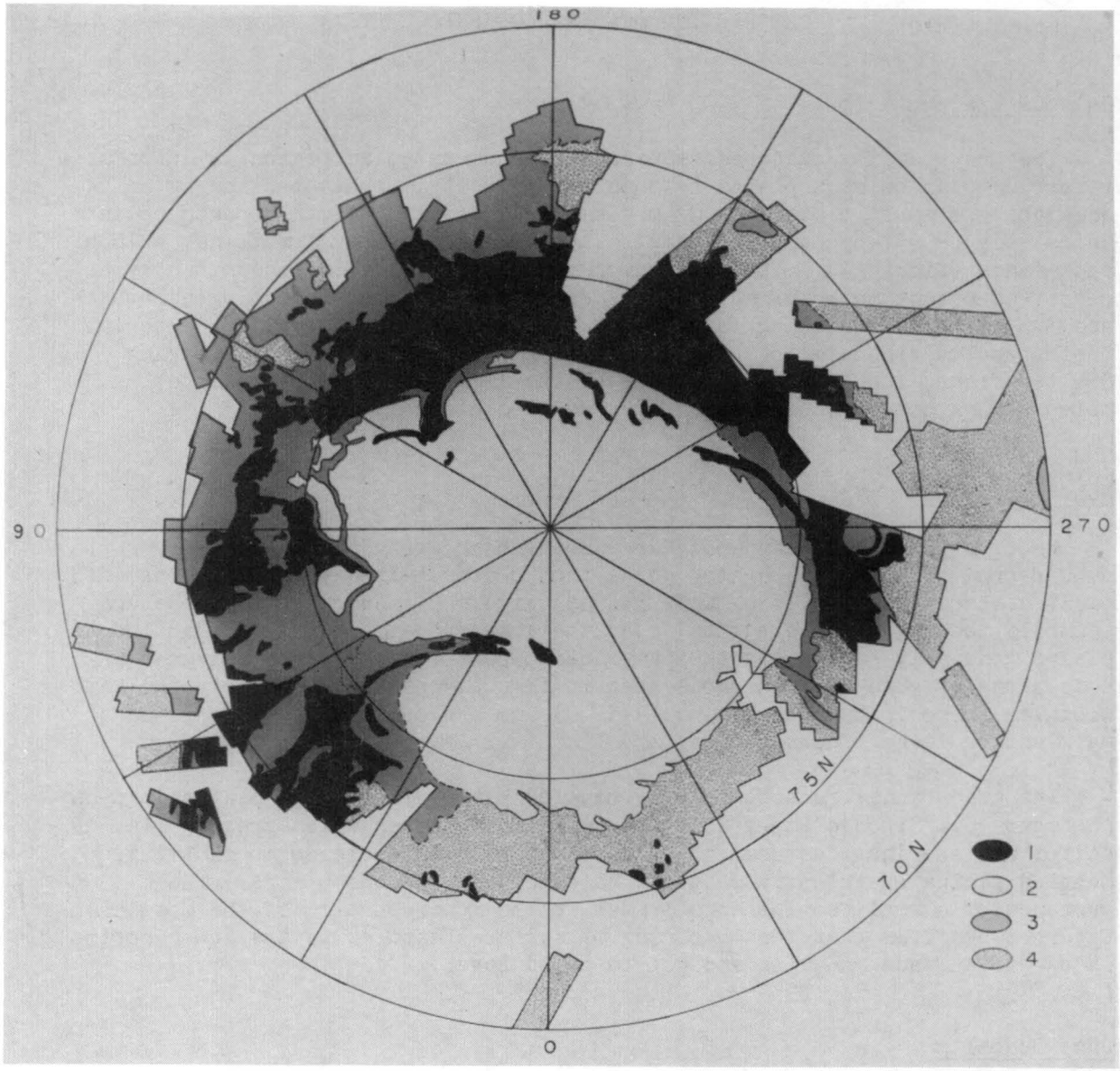

Figure 2: Stratigraphic map of the north polar region of Mars: (1) dunes, (2) layered deposits/perennial ice, (3) mantled plains, and (4) bulbous plains. Mantled plains include moderately- and heavily-mantled plains; bulbous plains include bulbous and lightly-mantled bulbous plains.

DESCRIPTION OF STRATIGRAPHIC UNITS

Bulbous Plains

The most heavily-cratered terrain in the north polar region is informally referred to as bulbous plains by this author. It is characterized by an abundance of small craters (<2 km diameter) relative to other north polar units (figure 9), by numerous debris-flow craters, and by a mottled, bulbous appearance (figure 3). The mottled, bulbous appearance is predominantly a result of bright material surrounding dark, highly irregular polygons, which are 3-8 km wide. Mottling is also due to concentrations of bright material inside and on the exterior rims of many craters. Within the same Viking Orbiter frame, the albedo of bulbous plains is generally intermediate between dark dune deposits and bright mantled plains.

Mantled Plains

Mantled plains display a higher albedo than either bulbous plains or dune deposits, and has a crater population characterized by a deficiency of small craters relative to bulbous plains (figure 9) and by shallow craters commonly lacking visible ejecta (i.e. the appearance of burial). Mantled plains generally have a smooth appearance except for mesas and polygons in some areas (figure 4). Polygons seen in figure 4 are approximately the same width as those in bulbous plains (2-6 km) and are outlined by low-albedo markings or large troughs.

The gradational relationship of mantled plains to bulbous plains is seen in figure 5. Since craters and other surface features which are high in relief are the last features to be obscured with an increase in mantling, mantled plains are clearly shown to be overlying bulbous plains. The presence of a small bowl-shaped crater in the lower portion of the mosaic in figure 5 confirms that the obscuring of surface features in the lower portion is due to surface mantling and not to cloud cover.

Dune Deposits

Dune deposits are characterized by a very low albedo relative to all other north polar units and commonly, though not always, by the presence of linear and arcuate patterns which have been interpreted as dunes (14). An excellent example of the relationship of dunes to mantled and bulbous plains is seen in figure 6.

Layered Deposits/Perennial Ice Cap

Figure 7 shows an example of the layered deposits and the overlying perennial ice cap in the north polar region. The reader can refer to

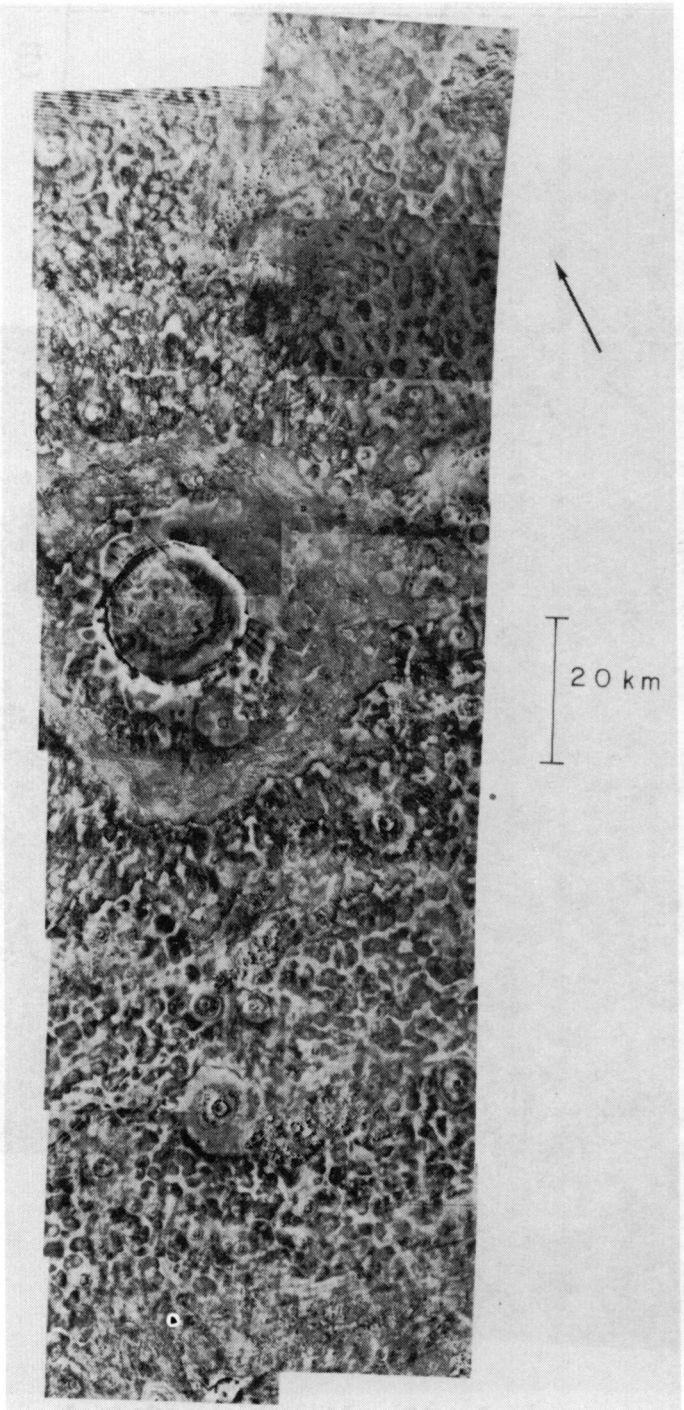

Figure 3: Type area for bulbous plains at 72°N, 290°W (Viking frames 538B01-538B16). Note the characteristic mottled, bulbous appearance resulting from bright material within and on the rims of craters and surrounding highly-irregular polygons.

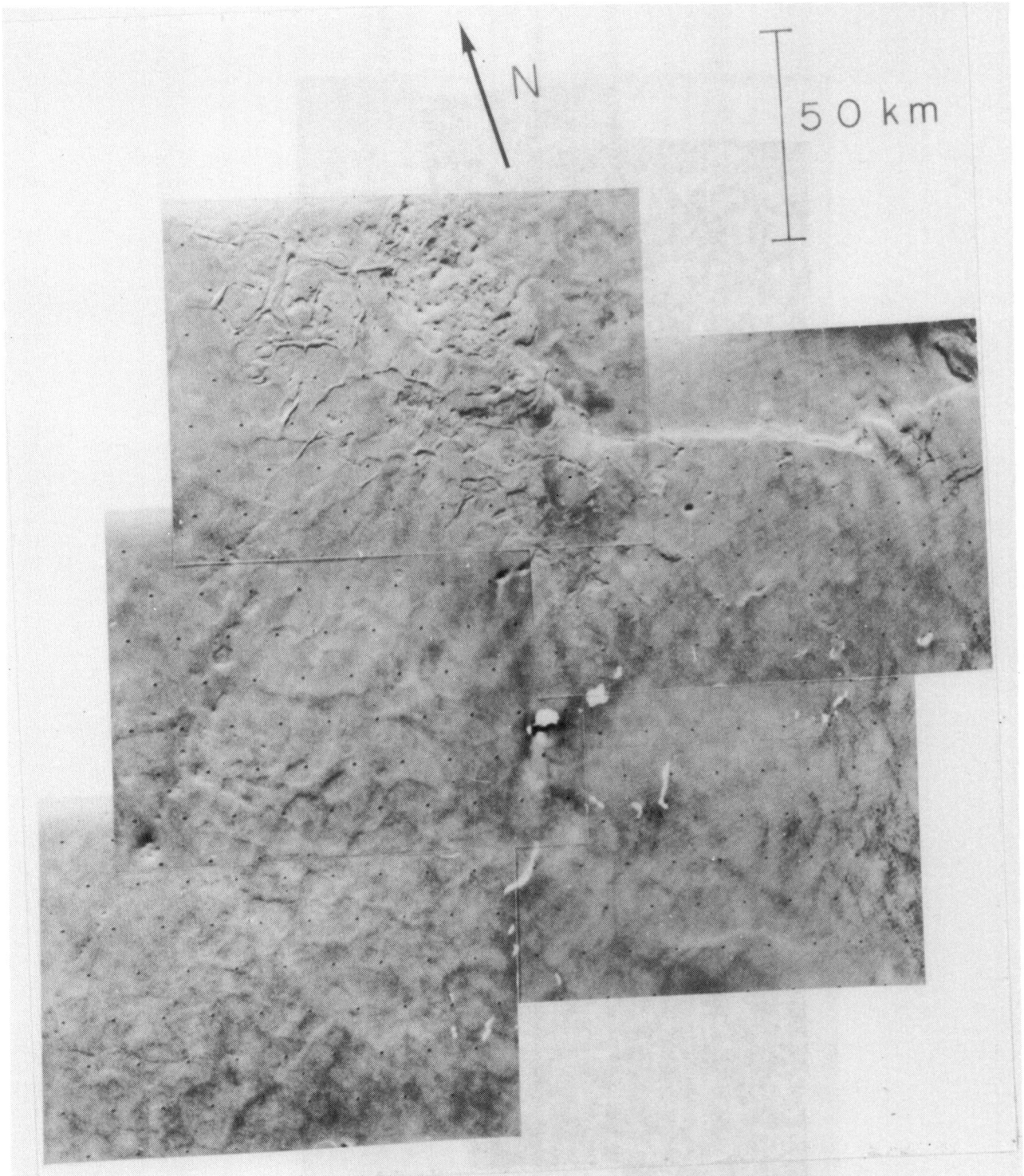

Figure 4: Type area for heavily-mantled plains, at the "mouth" of Borealis Chasma, 80°N, 65°W (Viking frames 70B31-70B35). Note polygons within mantled plains and layering in the scarp wall at the top of the mosaic (illumination is from the bottom right of the mosaic).

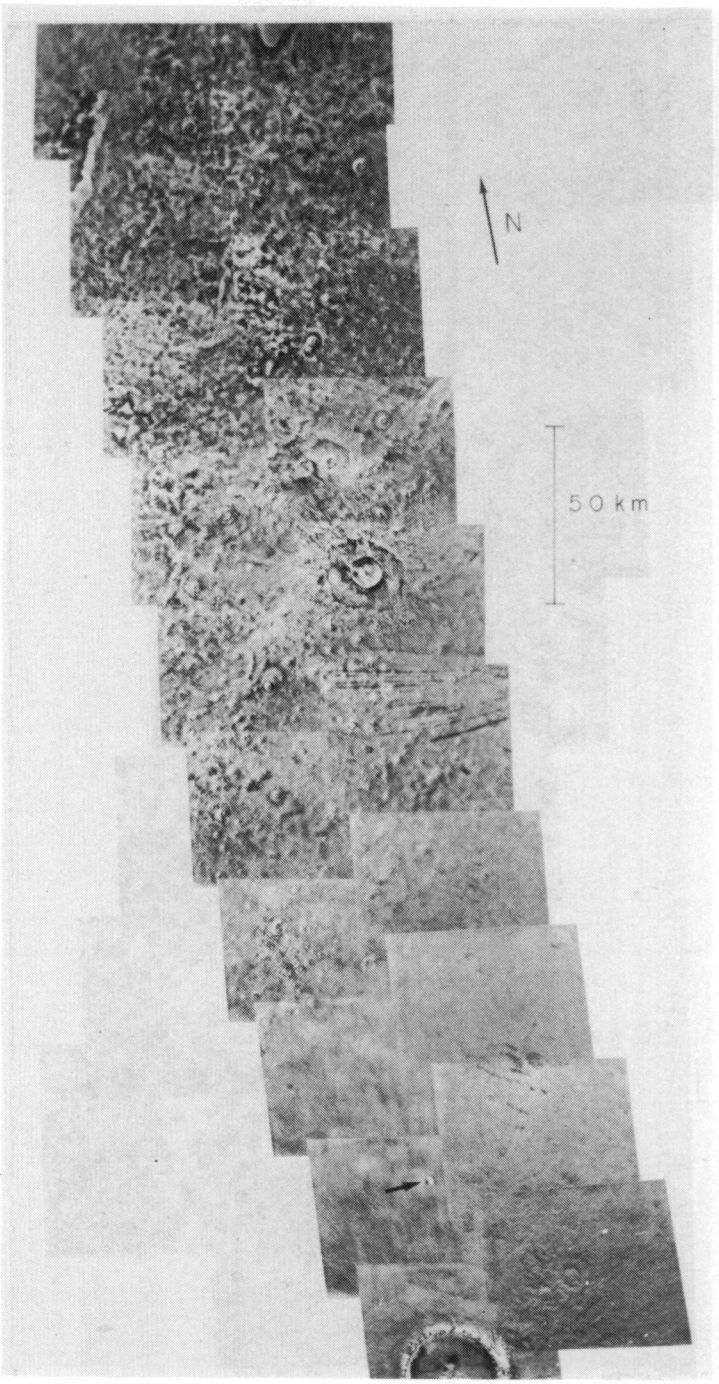

Figure 5: Viking Orbiter mosaic showing gradation of bulbous plains in the upper part of the mosaic to heavily-mantled plains in the lower part; at 70°N, 260°W (frames 576B10-576B20). The sharp appearance of the bowl-shaped crater (marked by arrow) indicates that the area is mantled rather than obscured by clouds. Also, note the two large "survivor" craters protruding through bulbous plains in the upper part of the mosaic.

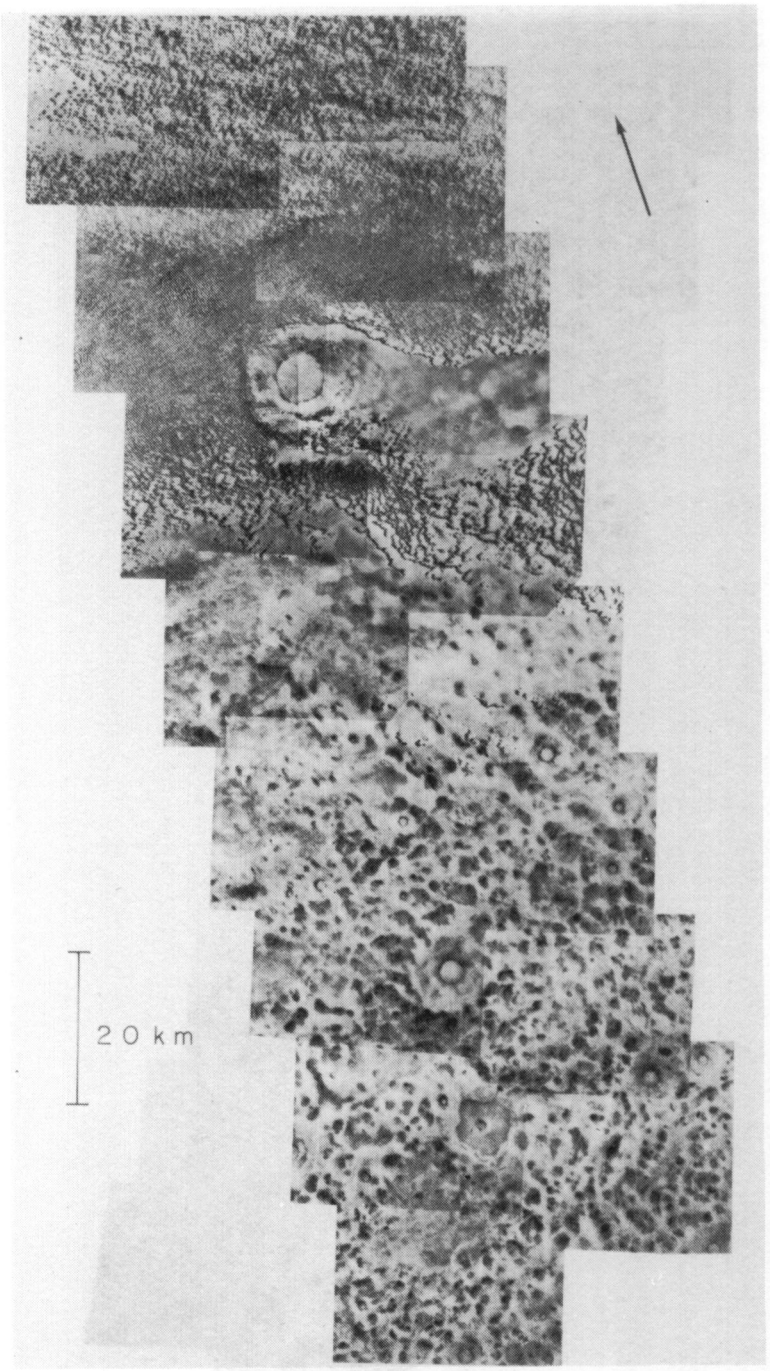

Figure 6: Excellent example of the relationships among bulbous plains, mantled plains, and dunes; at 72°N, 59°W (Viking frames 525B01-525B16). There is a relatively rapid gradation from bulbous plains near the bottom of the mosaic (south) to bright mantled plains and dark dunes in the north. Dunes in this mosaic are transverse and barchan dunes. Note the close correlation between the presence of dunes and the presence of mantled plains.

Figure 7: Viking Orbiter frame showing the bright perennial ice cap overlying layered deposits, which are exposed in the walls of troughs within the ice cap (frame 56B61).

numerous other papers (8, 13, 14, 15) for detailed description and discussion of these units. The present paper will not examine these deposits in detail but will instead concentrate on stratigraphic units surrounding the north polar cap.

INTERPRETATION AND DISTRIBUTION OF STRATIGRAPHIC UNITS

Bulbous and Mantled Plains

a. Interpretations from visual observations

Though certainly not the only possible interpretation, bulbous plains are interpreted here as having a volcanic origin. This is based primarily on its generally low albedo, though a history of near-surface igneous activity is also suggested by the presence of what appears to be an exposed dike (figure 8). Large "survivor" craters from the underlying older terrain can be seen protruding through bulbous plains in figure 8 and figure 5.

The highly-irregular polygons which characterize bulbous plains are somewhat different from polygons seen in lower latitudes. A belt of polygonal ground occurs between 40° and 50° N latitude, with typical polygons up to 20 km across (21). Polygons within bulbous ground are generally not larger than 8 km in diameter. Also, the patterned nature of bulbous plains appears to be more irregular than the polygonal appearance in the lower latitude belt, although this could be a result of the characteristic mottling of bulbous plains which tends to accent the irregular polygonal nature. As will be shown below, this mottling probably results from bright dust filling the low areas surrounding polygons and within craters. Thus, as the amount of dust-filling increases, polygon centers can be seen to stand out as highs.

The presence of the polygons in the lower latitudes of Mars has been attributed to contractive lava cooling or freeze-thaw ice wedging in a permafrost layer (21), although a scale problem exists when comparing Martian polygons to terrestrial analogs. Polygons formed by ice wedging or lava contraction on Earth are typically 100 m wide, whereas those in the 40° -50° N latitude belt of Mars are up to 20 km across (21). Although the highly irregular polygons within bulbous plains are generally not larger than 8 km, this is still larger than terrestrial analogs. Still, the interpretation that polygonal ground on Mars may have formed by lava contraction or ice wedging is plausible. The unique occurrence of polygonal ground at latitudes greater then 40° N tends to favor the interpretation that polygonal ground on Mars results from ice wedging (21). However, since bulbous plains are confined to the northern latitudes, and may be volcanic, it is reasonable that either process might have formed its characteristic polygons.

As seen in figure 5, there is a gradation between mantled and bulbous plains, such that mantled plains range from lightly-mantled plains, in which

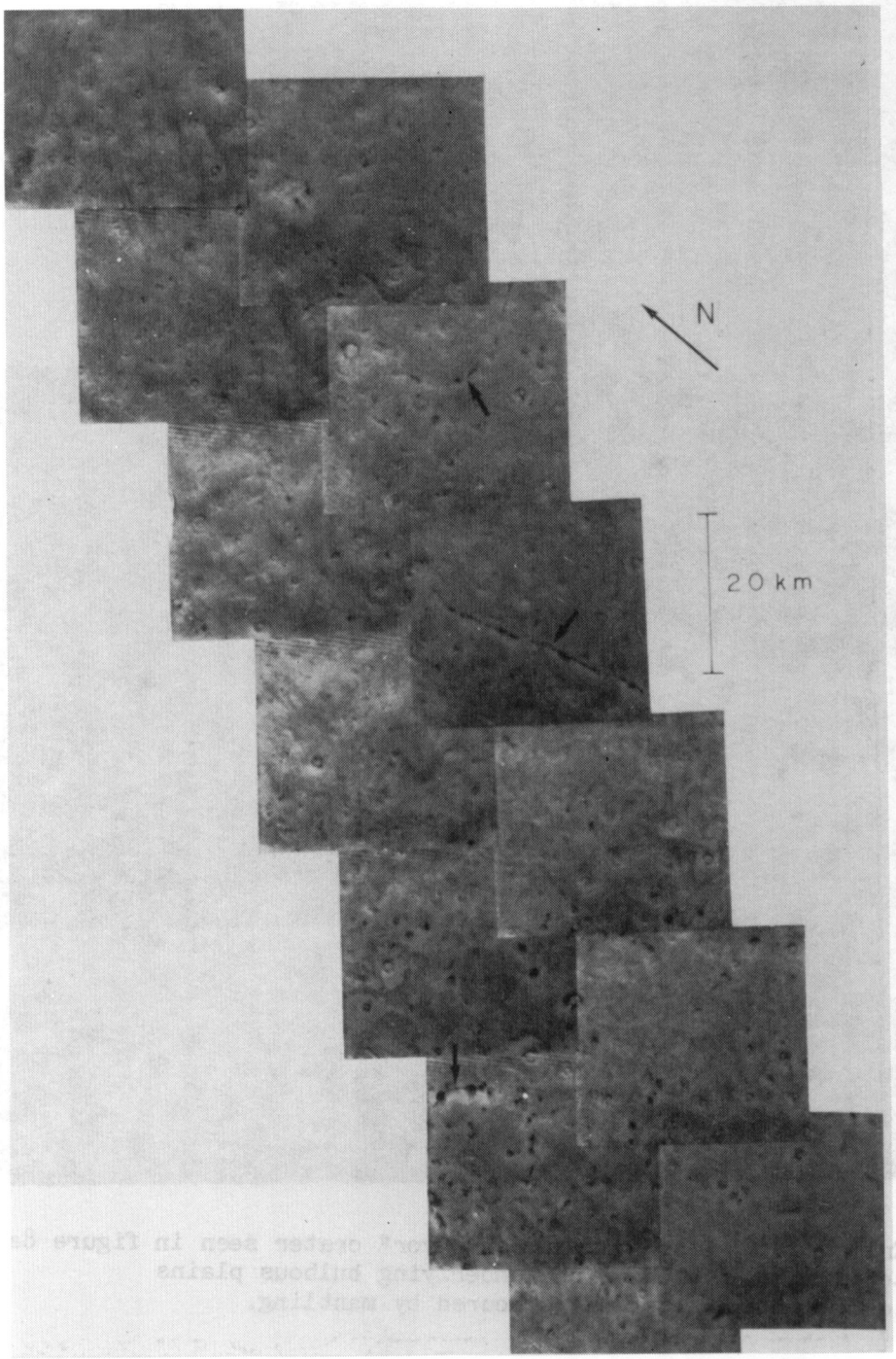

Figure 8a: Viking Orbiter mosaic showing what appears to be a linear dike and two "survivor" craters within lightly-mantled to moderately-mantled bulbous plains; at 70°N, 244°W (frames 505Bo1-505B13). Figures 8b and 8c are enlargements of these features and allow better discrimination of the underlying bulbous nature of the area.

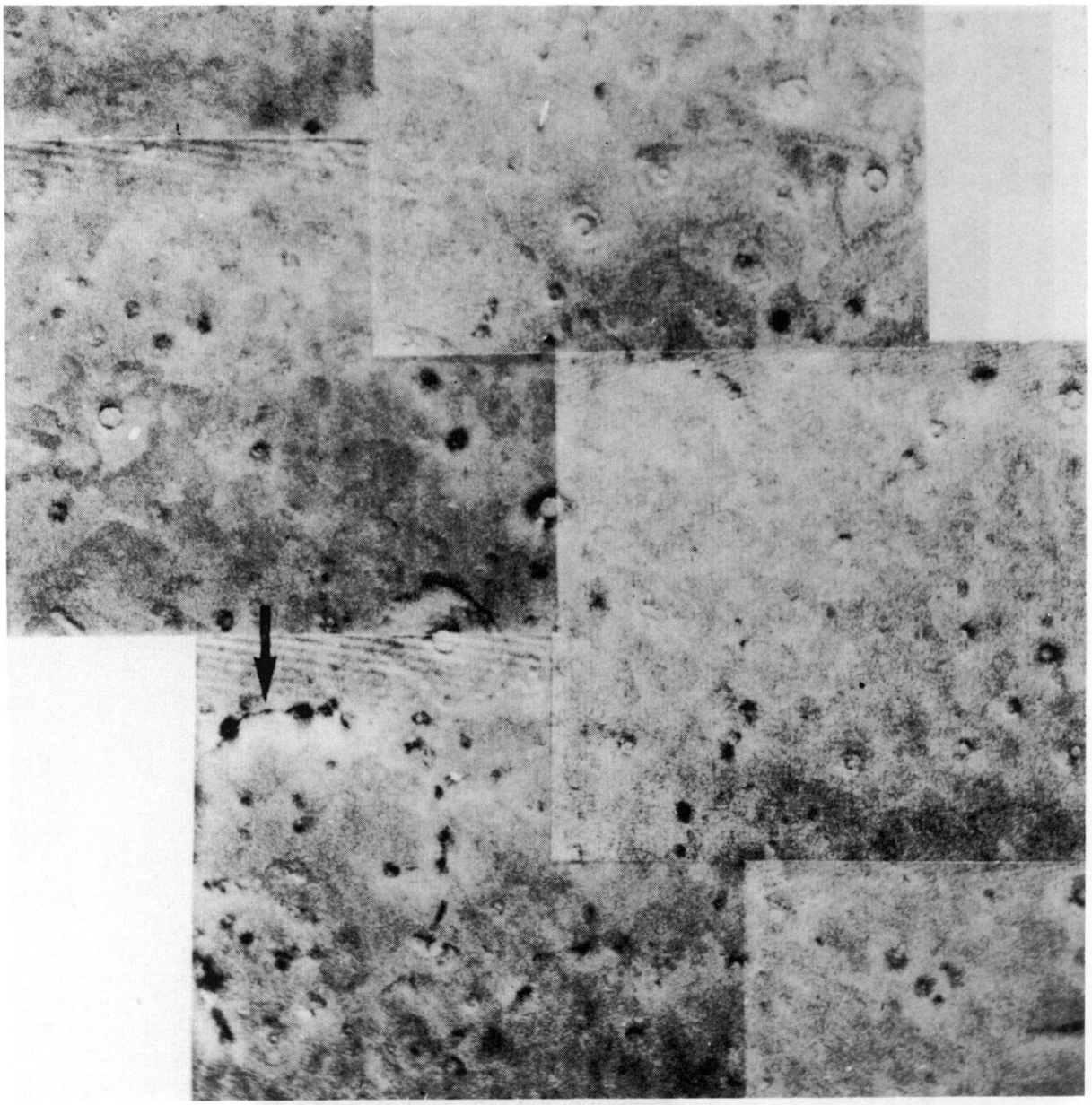

Figure 8b: Enlargement of an ancient "survivor" crater seen in figure 8a, allowing better discrimination of the underlying bulbous plains characteristics, which are somewhat obscured by mantling.

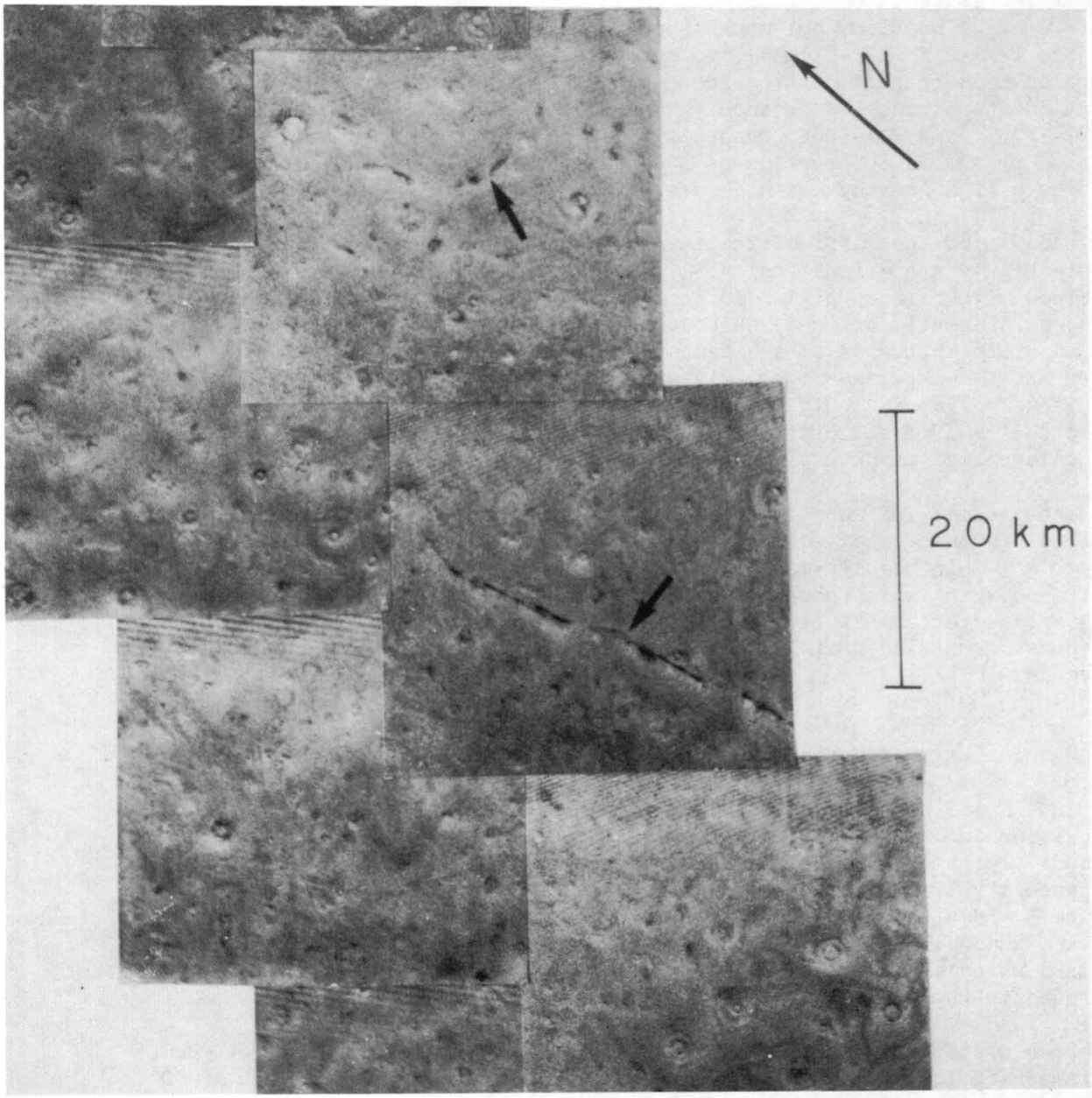

Figure 8c: Enlargement of a possible linear dike seen in figure 8a. Note that the length of the feature is greater than 20 km. The dike apparently protrudes through the mantling and the bulbous plains.

some features of bulbous plains, such as a relative abundance of small craters and a mottled, polygonal appearance, are retained (reference Viking Orbiter frames 531B21-531B36), to moderately- and heavily-mantled plains, where bulbous characteristics are replaced by a relatively smooth, crater-deficient appearance (reference Viking mosaics 211-5573 (frames 71B61-71B62; 71B41-71B45) and 211-5562, respectively). Due to this blanketing nature, mantled plains is interpreted as a deposit of wind blown dust covering bulbous plains in varying thickness.

Because of the difficulties involved in defining distinctive boundaries within highly gradational units, lightly-mantled plains are henceforth combined with bulbous plains to form a distinct mappable unit (figure 2). Thus, as presently defined, bulbous plains include all terrain which retain the characteristics of an abundance of small craters and a mottled, bulbous appearance. Likewise, moderately-and heavily-mantled plains, which as will be discussed later, could be arbitrarily separated on the basis of relative deficiencies of small craters, are for convenience combined into a single map unit called mantled plains.

The presence of mesa-like landforms within mantled ground suggests that mantled plains have experienced a period of deflation. The origin of the polygons within heavily-mantled plains is as poorly understood as the origin of the polygons which characterize bulbous plains. The similarity in size, however, suggests that either the process of formation is similar, or the polygons of mantled plains are controlled by underlying bulbous plains polygons.

b. Cumulative crater size-frequency distributions

Cumulative size-frequency distribution plots for small craters (<10 km) on bulbous and mantled plains are presented in figure 9. The two plots for bulbous plains (figures 9a and 9b) represent the areas seen in figures 3 and 6, respectively. Clusters of similar-sized craters, like those seen in figure 3, result from secondary impact of ejecta from large impact events, and are generally not representative of the unit as a whole. Therefore, all craters which appeared to be associated with crater clusters were not included in the counts.

Both plots for bulbous plains display a power-law slope of about -2.0. A linear fit to the data gives a one-kilometer intercept "age" (22) of 4000 craters per 10^6 km^2.

An unrealistic decrease in the number of small craters counted in images can result from imagery degrading as crater diameters approach the resolution limits of the images. This results in a shallower slope, or a "rolling over," of the cumulative size-frequency distribution curve at small diameters. However, "rollover" due to resolution degradation for Viking Orbiter imagery occurs at 6 times the pixel resolution (23), or at 1.7×10^{-1} km for figure 9a. Since in figure 9a the break in slope occurs at 27 times the pixel resolution, or at 7.6×10^{-1} km, the slope of -0.7 for smaller crater diameters is probably a true feature of the crater population and not a resolution effect.

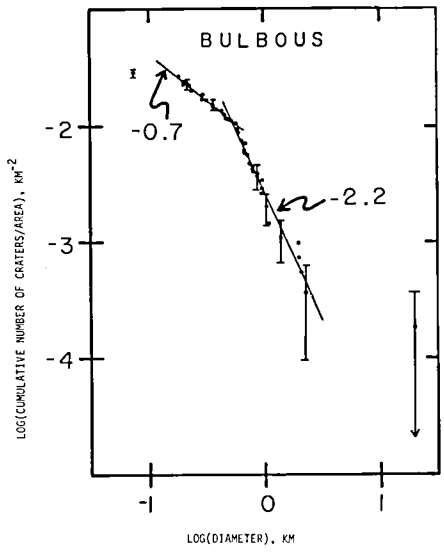

Figure 9a: Cumulative size-frequency distribution plot for small craters on bulbous plains. Area represented is from the bulbous plains type area seen in figure 3. N = 156 craters; total area = 5,419.1 km^2. Error bars signify one standard deviation confidence intervals and equal $\pm \sqrt{n}$ for the nth crater.

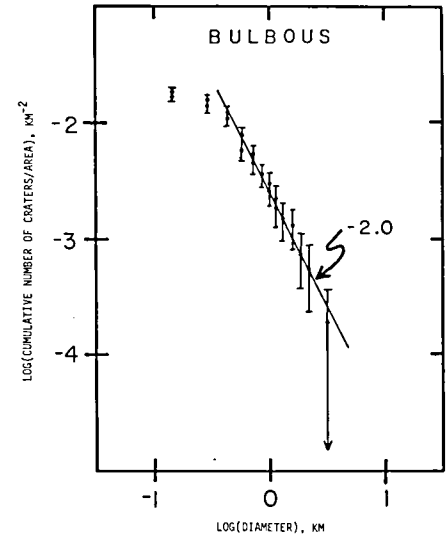

Figure 9b: Cumulative size-frequency distribution plot for small (< 4 km) craters on bulbous plains, representing the area seen in figure 6. N = 97 craters; total area = 5,400.7 km^2.

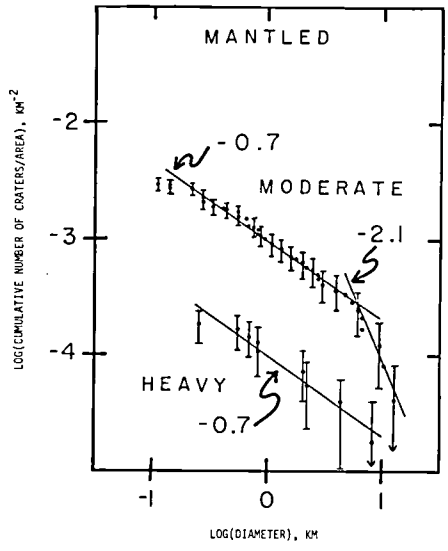

Figure 9c: Cumulative size-frequency distribution plots for small (< 13 km) craters on mantled plains. The heavily-mantled plains plot represents the type area at Borealis Chasma seen in figure 4. N= 9 craters; total area = 55,120.6 km^2. The curve for moderately-mantled plains is for the area at 76°N, 90°W (Viking frames 70B04, 71B61-71B64). N = 71 craters; total area = 24,344.6 km^2.

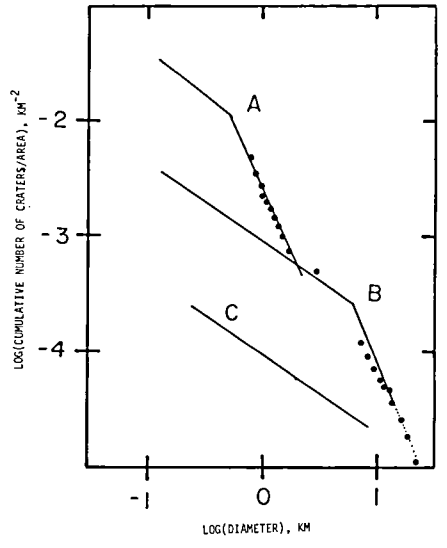

Figure 9d: Composite of cumulative crater size-frequency distribution curves seen in figures 9a and 9c. Curve A - bulbous plains; curve B - moderately-mantled plains; curve C - heavily-mantled plains. Data points are from Neukum and Wise (22) for a cratered plains unit at Tempe Plateau, 30°N, 90°W.

Crater size frequency distributions for mantled plains are seen in figure 9c, with the plot for heavily-mantled plains representing the area at the mouth of Borealis Chasma (figure 4). The plots for both moderately- and heavily-mantled plains show a repetition of the shallow -0.7 slope observed for smaller craters of bulbous plains. Moderately-mantled plains also display a two-segment distribution curve, with a slope of -2.1 for crater diameters larger than about 6 km. A slope of -2.1 is equivalent to the -2.0 to -2.2 slope values for large craters of bulbous plains.

A composite of figures 9a and 9c is seen in figure 9d. The curve segments are for bulbous (curve A), moderately-mantled (curve B), and heavily-mantled (curve C) plains. When adjusted for cumulative size-frequency functions rather than differential size-frequency functions, the Jones and Chapman model for crater obliteration (24) states that two segment curves, such as A and B in figure 9d, represent a balance between a production function,

$$\Psi(x) = \int_D^{\infty} c_d(x) \int_{T-t_e}^{T} c_t(t)\, dx\, dt \qquad (1)$$

and a cratering-obliteration equilibrium function,

$$\Psi(x)_e = \left[c_t(T) \,/\, o(T)\right] \int_D^{\infty} a(x)\, c_d(x)\, dx \qquad (2)$$

where x = the crater diameter, t_e = the retention age of a crater of a given diameter, $c_t(T)$ = the time dependence of the cratering rate, $c_d(x)$ = the diameter dependence of the cratering rate ($c_d(x) = D^{-k}$), o(T) = the obliteration rate, and a(x) = the amount of obliteration needed to render a crater indiscernible. Since the amount of obliteration, a(x), needed to remove a small crater is less than that needed for a larger crater, the cumulative size-frequency plot for an obliterated (e.g. dust-mantled) surface would show a shallow slope for small diameters, and a steep slope for larger diameters. Such is the case for curves in figure 9d. The repetition of -2.0 and -0.7 slopes for plots of both bulbous and mantled plains strongly suggests that the curves represent an equilibrium, or post-transient, cratering-obliteration process. Thus, using the Chapman-Jones model, -2.0 would define the slope of the production function, while the slope of -0.7 would represent a cratering-obliteration equilibrium function.

The repetition of the -0.7 equilibrium slope for all crater size-frequency distribution plots given above implies that the functions D^{-k} and a(x) do not change from one area to another. Otherwise, the slopes would not be the same. Thus, making the reasonable assumption that the time-dependent cratering rate, $c_t(T)$, is also constant for all areas of concern, then the value of the equilibrium function, $\Psi_e(T)$, for a given diameter range, is dependent only on the obliteration rate, o(t). Thus, the ratio of equilibrium frequencies, Ψ_e, for two such areas, would allow a relative obliteration rate, o(t), to be calculated:

$$\frac{\Delta\Psi(x)_{e_1}}{\Delta\Psi(x)_{e_2}} = \frac{[c_t(T)_1 \,/\, o(T)_2] \int_{D_a}^{D_b} a(x)_1 \, c_d(x)_1 \, dx}{[c_t(T)_2 \,/\, o(T)_2] \int_{D_a}^{D_b} a(x)_2 \, c_d(x)_2 \, dx} \qquad (3)$$

(For $c_t(T)_1 = c_t(T)_2$, $a(x)_1 = a(x)_2$, and $c_d(x)_1 = c_d(x)_2$:

$$\frac{\Delta\Psi(x)_{e_1}}{\Delta\Psi(x)_{e_2}} = \frac{o(T)_2}{o(T)_1} \qquad (4)$$

From figure 9d, the relative obliteration rates for bulbous : moderately-mantled : heavily-mantled plains are calculated as 1:9:88.

The change of slope of about 1 between crater-production and obliteration-equilibrium functions of the north polar units is consistent with the simple dust-filling model of Chapman (25). This supports this author's interpretation that mantled plains are deposits of wind-blown dust covering bulbous ground in varying thicknesses. The break in slope between crater-production and obliteration-equilibrium functions is a result of the presence of "survivor craters" which have not been obscured by the obliteration process (22). Thus, if dust mantling is the only obliterating process acting, the diameter at which the function slope changes (i.e. the "kink point") should be an indication of the average thickness of the dust mantle. Based on crater data for the Martian surface, Cintala and Mouginis Mark (26) empirically derived that the crater depth = 0.104 x diameter$^{0.962}$ for craters less than 12.3 km in diameter. By substituting the kink-point diameter for moderately-mantled plains into the equation, the thickness of the dust layer comprising moderately-mantled plains is calculated to be about 600 m. Since the crater-function kink for heavily-mantled plains does not occur within the range of diameters plotted, the thickness of dust deposited in this region is, at least, the depth of the largest crater measured, or 770 m. These values are somewhat higher than the 200 m maximum predicted by Squyres (15).

The data points seen on the composite plot (figure 9d) are not data from north polar units, but are instead the data from Neukum and Wise (22) for a cratered plains unit at Tempe Plateau (30°N, 90°W). The excellent correlation between their data and the composite plot for bulbous and moderately-mantled plains suggests first that the crater function for bulbous plains may follow the moderately-mantled plains curve in the region of diameters greater than 5 km. Since only smaller craters would be buried by an obliteration episode, this is a reasonable assumption if moderately-mantled plains result from obliteration of bulbous plains. However, such a theory should certainly be tested by plotting the crater distribution curve for greater than 5 km craters on bulbous plains.

Of more importance is that the correlation of the bulbous plains crater plot with that of the cratered plains unit at Tempe Plateau, places bulbous plains within the Martian global stratigraphic sequence as one of the relatively old cratered plains units. According to the time scale of Neukum and Wise (22), bulbous plains has an "absolute" age of 3.8 b.y. (note: according to the same scale, the oldest cratered plains unit, Lunae Planum, is 3.9 b.y.).

Dune Deposits

Dunes in the north polar region of Mars are predominantly transverse and barchan dunes, although some longitudinal dunes are also present. They are similar in size to megadunes (draa) found in the Sahara, Arabia, and the Algodones dune fields on Earth (36).

As suggested below, dune deposits might also occur as "sheet-sand" deposits. Figures 1 and 2 show the stratigraphic map and a Mariner 9 mosaic of the north polar region of Mars. A visual comparison between the stratigraphic map and the Mariner 9 image between 30° - 290° W longitude confirms that the dark circumpolar band seen in the mosaic correlates well with the presence of dunes. However, in the region 290°-0°-30° W longitude, the dark band extends into much of the area mapped as bulbous plains, whereas other areas of bulbous plains, including the type area, are not as dark. Though this region was often cloudy during much of the Viking Orbiter imagery sequences, some relatively clear images (e.g. 531B21 - 531B36) confirm the duneless, bulbous nature of the area. The presence of the low-albedo band in duneless terrain suggests either a very thin "sheet-sand" deposit of dark dune material overlying much of the most northern exposures of bulbous plains, or that the albedo of bulbous plains in other areas is more influenced by a thin mantling of bright dust. Notice that even the type area for bulbous plains appears to have dust in many depressions (figure 3).

Actual dunes are generally confined to mantled regions, as illustrated in figure 6 and the stratigraphic map in figure 2. If dune deposits overlie bulbous plains, they occur predominantly as "sheet sand" deposits rather than dunes. This suggests that, unlike bulbous plains, mantled plains provide the proper substratum for the accumulation of dunes. Mantling probably creates a smooth, crater-deficient surface with might favor dune formation.

An observed eastward gradation from densely-spaced to more dispersed dunes provides valuable information for determining the source of the circumpolar dune deposits. Fields in the region of 130°-270° W longitude are extensive, uninterrupted fields with distinct boundaries and consisting of transverse dunes with very narrow interdune areas (figure 10, and Viking Orbiter Mosaics 211-5269 (rev.61), 211-5272 (revs. 60,61), 211-5431 (revs. 62,63), and 211-5583 (rev. 72)). Dunes within the 30°-130° W longitude region occur in more dispersed fields and are generally transverse and barchan dunes with wide, bare interdune areas

Figure 10: Viking Orbiter frame showing circumpolar dune field typical of those within the area between 130° and 270° W longitude (frame 59B35). Dunes in this region are predominantly uninterrupted and closely-spaced transverse dunes. Also note the crisscross pattern of the northwestern dunes indicating modification from secondary winds sweeping off the cap.

(figure 11 and Viking Orbiter Mosaics 211-5269 (rev. 59), and 211-5562 (revs. 50,69)). Between 30°-0°-270° W longitude, dune deposits are predominantly in the form of very isolated dunes, or possibly as sheet sands. The overall view is one of counterclockwise gradation from dense transverse dunes in the region between 270° and 150° W longitude to more highly dispersed transverse and barchan dunes and eventually to possible sheet sands and isolated dunes. Although the presence of mantling appears to be required for dune formation, the degree of mantling does not appear to control the morphology of the dune fields. On Earth, transitions from transverse to barchan dunes and from narrow to wide interdune areas are generally related to a decrease in the supply of dune material (27). This relationship is typically encountered as one moves progressively away from the source of sediment. Thus, the situation observed in the north polar region may be one of a counterclockwise thinning of the supply away from the source.

Layered Deposits

The layered deposits are probably a facies of mantled plains in which wind-blown dust is deposited onto the perennial ice cap rather than directly onto the ground (15). Although it is not clearly understood which changes in Mars' orbital parameters most affect the eventual growth and decay of the perennial ice caps (3), the extent of layered deposits at the poles probably indicates the maximum extent of the perennial ice caps in the past.

Relationships of units at Borealis Chasma may illustrate an interfingering of mantled plains and layered deposits. Layering can be seen in the scarp which overlies mantled plains at the "mouth" of Borealis Chasma (figure 4). However, the surface of much of Borealis Chasma does not display the laminations within minor topography as is typical of north polar layered deposits. The surface of Borealis Chasma instead has the appearance of mantled plains, suggesting a transition from mantled plains to layered deposits and back to mantled plains. Such a transition is not unreasonable since the extent of the perennial ice cap is expected to fluctuate with time.

Comparison with Previous Research

The north polar stratigraphy presented in this paper has been compared to the stratigraphy proposed by Soderblom et. al. (1), and that of Squyres (15). Although the preliminary stratigraphic map of Soderblom et. al. has been greatly altered, their basic stratigraphic sequence for the north polar region has not changed drastically. Bulbous plains are certainly a sub-unit of the "mottled cratered plains" unit which includes a large portion of the northern hemisphere. However, bulbous plains with their characteristic highly-irregular polygonal appearance are probably confined to the northern portion of the mottled cratered plains. Mantled plains are equivalent to the debris mantle and etch-pitted plains in the stratigraphic sequence of Soderblom et. al., whereas dune deposits replace the rippled plains.

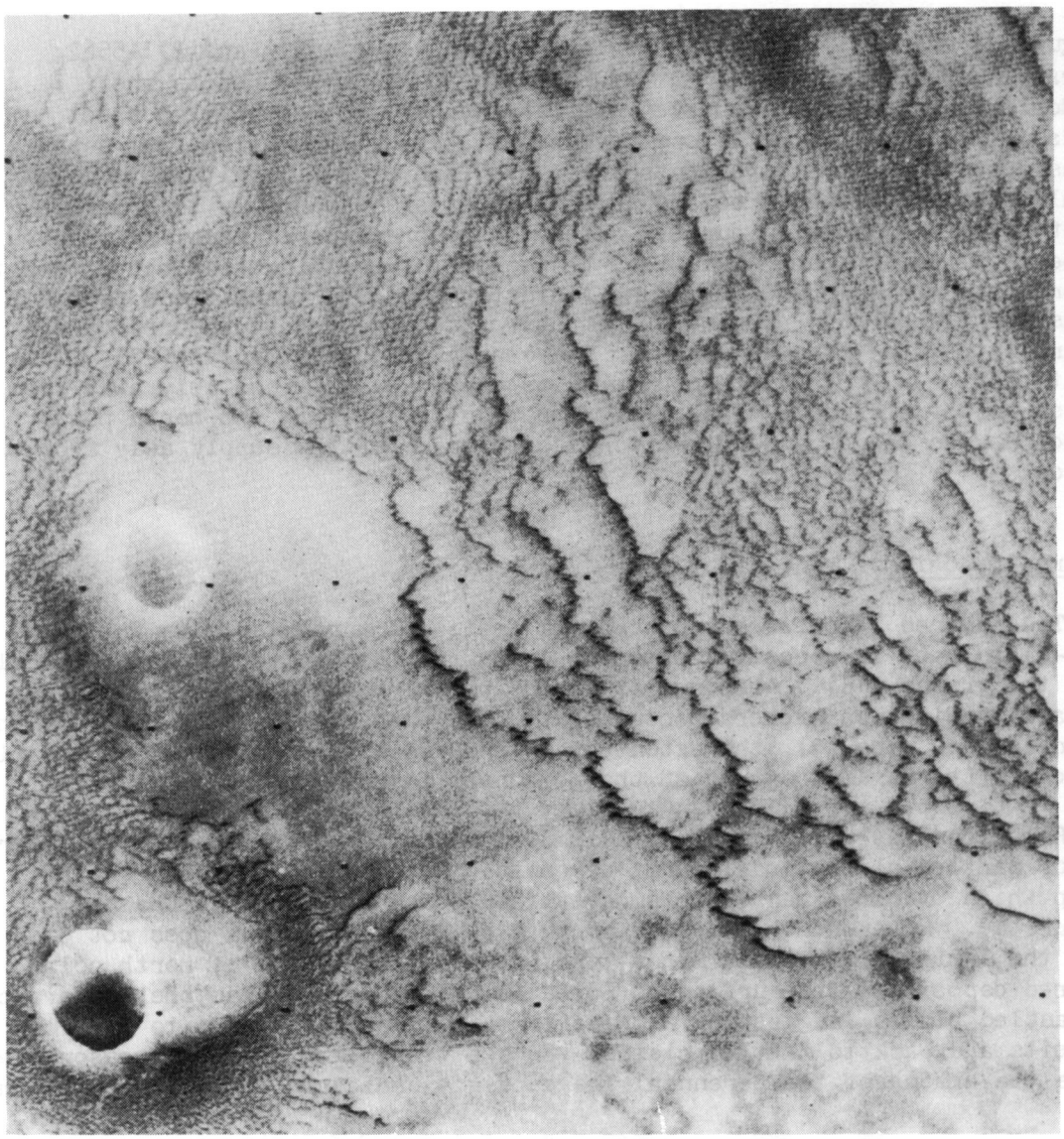

Figure 11: Typical dune field within the north polar region between 30° and 130° W longitude (Viking frame 71B64). These dunes are barchan and transverse dunes with wide interdune areas, indicating a sparseness of supply.

Although the stratigraphic sequence proposed in this paper agrees in theory with that proposed by Squyres (15, 28), there are very serious discrepancies in the defining and mapping of the cratered plains and mantled units. The previous author's type locale and only exposure of his underlying "cratered plains" unit is at the mouth of Borealis Chasma. This same area, seen in figure 4 and represented by the crater plot for heavily-mantled plains in figures 9c and 9d, is the present author's most heavily-mantled unit in the north polar region. Both the imagery and the crater size-frequency distribution data for this area show an obvious deficiency of craters relative to moderately-mantled and bulbous plains. Also, as discussed earlier, the shallow slope of -0.7 confirms that the unit is a highly-obliterated surface, probably resulting from a dust mantling which may be at least about 700 m thick. Units represented by curves A and B in figure 9d are one to two orders of magnitude more cratered than the "cratered plains" unit of Squyres. Both units represented by curves A and B have been mapped by the previous author as a debris mantle which formed by dust obliteration of craters on the "cratered plains" unit represented by curve C. Such an interpretation of these units is obviously not consistent with the crater size-frequency distribution function for these areas.

WIND DIRECTIONS

Numerous investigators (29, 30, 31), including the present author (this paper), have independently inferred near-surface wind directions within the north polar region of Mars, on the basis of dune orientations. Figure 12 shows dune orientations mapped from orthographic images which minimize distortions resulting from "oblique viewing" of the spacecraft. The map presents data in the form of orientations of arcuate (barchan) dunes and the trend of linear (transverse and longitudinal) dunes. The crisscross pattern of the dunes between 150° and 210° W longitude can be seen in figure 10.

Caution must be exercised when interpreting wind directions based on dune orientations derived from Viking Orbiter images. In such cases, barchan forms provide the most reliable indicators of near-surface wind orientations. Transverse and longitudinal dunes in the circumpolar images generally only allow determination of a wind trend rather than a wind direction. Thus, interpretations based on transverse and longitudinal dunes must rely on indirect evidence, such as wind streaks or directions based on nearby barchan dunes. Tsoar et. al. (31) have attempted to determine absolute wind directions based on the asymmetry of transverse dunes. However, it is again cautioned that the resolution of Viking north polar images may not allow reliable separation of true dune slope asymmetry from illusory effects due to shadows or oblique viewing.

In figure 13 is the present author's interpretation of wind directions based primarily on orientations shown in figure 12. Interpretations of wind directions for the transverse dune fields between 120° and 240° W longitude relied on the assumption of a continuity of wind flow relative to barchan dunes which occur at the edge of the field. Wind directions in figure 13 indicate a predominantly counterclockwise flow of dune-driving

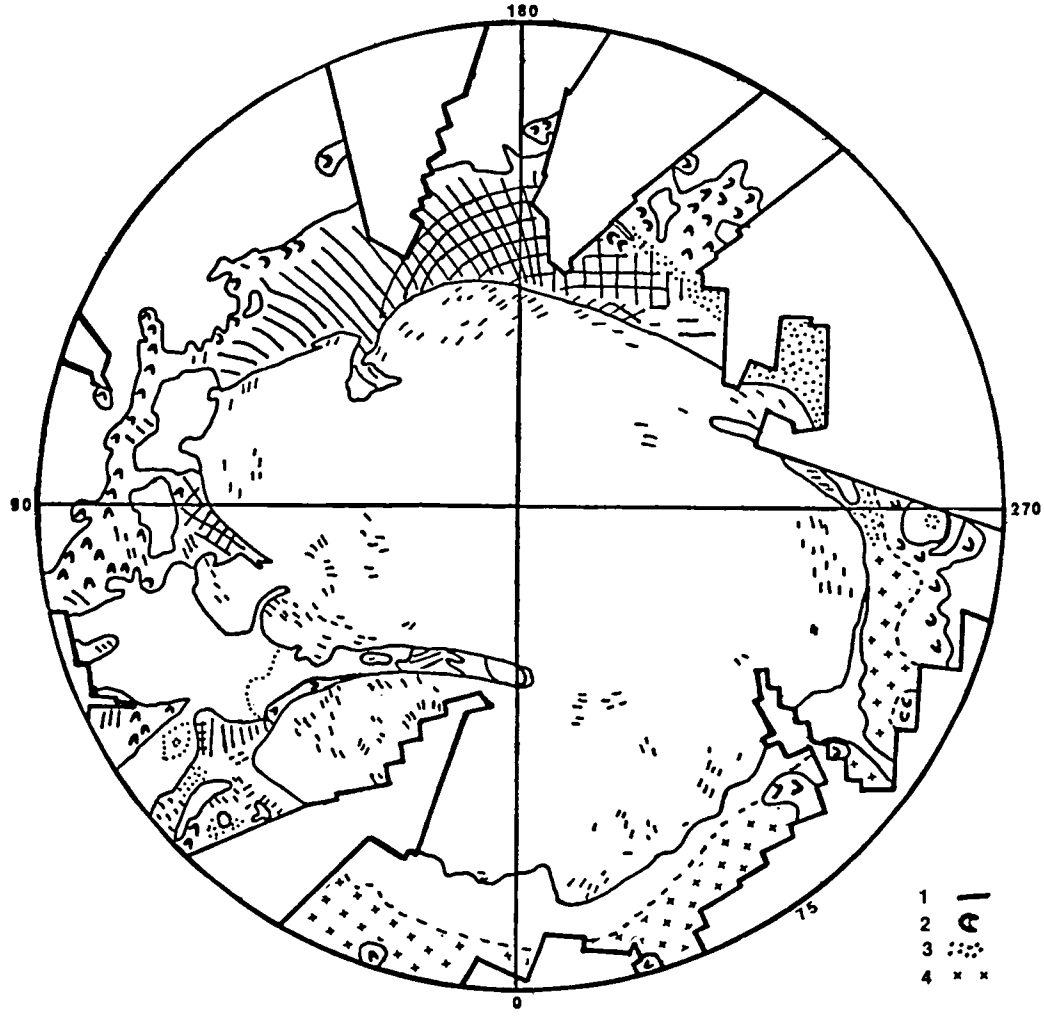

Figure 12: Dune trends within the north polar region of Mars. (1) linear trends within dune fields, and grooves in ice, (2) direction of arcuate forms in dunes (asymmetry of symbols corresponds to asymmetry observed), (3) complex dunes with no distinct linear or arcuate patterns, and (4) possible sheet sand deposits. Symbols signify general trends of dunes rather than individual dunes.

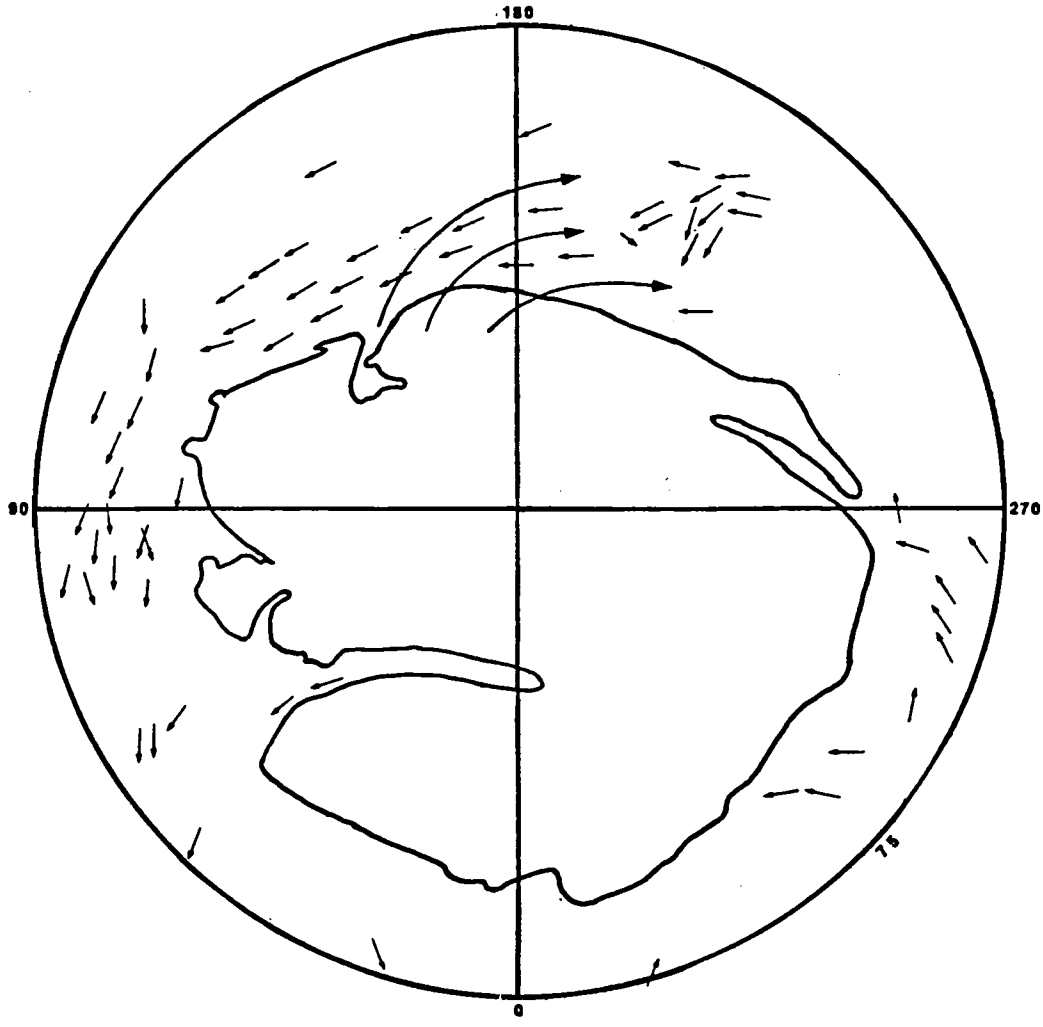

Figure 13: Near-surface wind directions based primarily on orientations seen in figure 12. There is a predominant counterclockwise direction of flow around the ice cap, with modification by winds spiralling off the cap.

winds around the ice cap along with dune modifying winds which spiral clockwise off of the ice cap, possibly during a change in season. Such an interpretation of wind directions is consistent with north polar wind circulation patterns derived from streak orientations (29), from lee cloud orientations (32; R.G. French, personal communication, 9/25/79), and from other interpretations based on dune orientations (29, 30, 31). Leach (30) attributes the clockwise pattern to the influence of Coriolis force acting on katabatic winds spiralling off the ice cap.

Thus, data derived from dune, wind streak, and lee cloud orientations indicate a polar atmospheric circulation pattern consisting of winds travelling around the ice cap in a counterclockwise direction, modified by katabatic winds spiralling clockwise off of the ice cap. Such a pattern is similar to the wind circulation around the Antarctic ice cap on Earth (30).

IMPLICATIONS FOR THE SOURCE OF CIRCUMPOLAR DUNE MATERIAL

As discussed earlier, the gradation of extensive, uninterrupted transverse dune fields to scant fields with widely spaced transverse and barchan dunes implies a general decrease in the supply of dune material as one moves eastwardly (or counterclockwise) away from the area between 270° and 180° W longitude. Circumpolar winds were found to flow predominantly counterclockwise, suggesting a general thinning of dune deposits in a downwind direction. This, combined with the presence of extensive exposures of bulbous plains upwind of extensive dune fields, may indicate that dune material is stripped from bulbous plains and deposited on mantled regions.

Such a conclusion might be further supported if one considers the dark circumpolar band extended into duneless bulbous plains areas. Two possible interpretations were suggested earlier to account for this, one being that a very thin sheet sand deposit of dark dune material blankets bulbous plains in this area, and the other suggesting that bulbous plains in this area are more completely stripped of a thin bright dust layer than bulbous plains in other areas. The first interpretation is consistent with dune material being continually derived from bulbous plains only to be slowly stripped from the region and deposited onto mantled plains downwind. If the second interpretation were true it would lend very strong support to the suggestion that bulbous plains are the source of the dune deposits. Not only would it provide evidence that this possible source area is significantly stripped, but more importantly it would indicate that bulbous plains and dune deposits have the same low albedo.

CONCLUSION

The stratigraphic sequence of the north polar region of Mars can be separated into four distinct informal units: (a) bulbous plains, (b) mantled plains, (c) dune deposits, and (d) layered deposits/perennial ice.

Bulbous plains is a relatively old "mottled" cratered plains unit equivalent in crater-distribution age to the cratered plains unit at Tempe

Plateau (90°W, 30°N). According to the time scale of Neukum and Wise, the "absolute age" of bulbous plains is 3.8 b.y.. Due to its relatively low albedo and because of near-surface volcanics suggested by the presence of what appears to be a dike, bulbous plains are interpreted as having a volcanic origin. Polygons within bulbous plains are 3-8 km and may have formed by contractive cooling of lava or freeze-thaw ice wedging within a permafrost layer.

Mantled plains are interpreted as wind-blown dust deposits covering bulbous plains in varying thicknesses. A deficiency of small craters seen in crater size-frequency distribution functions for bulbous and mantled plains supports the interpretation that mantled plains formed by obliteration of bulbous plains, while a change of slope of about 1 between crater-production and obliteration-equilibrium functions for north polar units is consistent with obliteration by dust-filling. The relative surface-obliteration rates are 1:9:88 for bulbous, moderately-mantled, and heavily-mantled plains, respectively.

Previous stratigraphic mapping proposed by Squyres for the north polar region of Mars is inconsistent with interpretations based on crater size-frequency distribution data. Such evidence strongly supports that his "cratered plains" unit at the mouth of Borealis Chasma is instead a heavily-mantled plains, whereas many areas mapped by the previous author as "debris mantle" are instead cratered plains.

Layered deposits probably represent a facies of mantled plains in which dust is deposited onto the perennial ice cap rather than directly onto the ground. Thus, the extent of the layered deposits at the north and south poles may indicate the maximum extent of the perennial ice caps in the past. A possible interfingering of layered deposits and mantled plains can be seen at the mouth of Borealis Chasma.

Dunes in the north polar region of Mars have a very low albedo and occur as transverse, barchan, and to a minor extent, as longitudinal dunes. Actual dunes are generally confined to mantled plains, suggesting that mantling provides a proper substratum for dune formation. The extension of the dark circumpolar band into duneless areas mapped as bulbous plains suggests that thin sheet sand deposits overlie bulbous plains in this area or that the most northern exposures of bulbous plains have been more effectively stripped of bright dust than bulbous plains in other areas. If the latter interpretation is true, it indicates that the albedo of bulbous plains is similar to the albedo of the dunes. The distribution of dune forms and dune field styles reveals thinning of the supply of dune material in an eastward direction away from the area between 270° and 180° W longitude.

As determined from dune orientations, near-surface north polar winds consist of a counterclockwise flow around the ice cap modified by katabatic winds spiralling clockwise off the cap. This is analogous to the atmospheric circulation pattern around the Antarctic ice cap on Earth.

The results above suggest a general thinning of the supply of dune material downwind of the area between 270° and 180° W longitude. Immediately upwind of this area are extensive exposures of bulbous plains. Thus, the author suggests that dune material is being stripped from bulbous plains and is accumulating as dunes downwind on mantled plains.

BIBLIOGRAPHY

(1) Slipher, E.C. (1962) The Photographic Story of Mars, Sky Publishing Corporation, Massachusetts.

(2) Hartmann, W.K., and O. Raper (1974) The New Mars: The Discoveries of Mariner 9, NASA SP-337, 108-122.

(3) Mutch, T.A., R.E. Arvidson, J.W. Head III, K.L. Jones, R.S. Saunders (1976) The Geology of Mars, Princeton University Press, New Jersey, 17-18, 86-91, 250-254.

(4) Murray, B.C., and M.C. Malin (1973) Polar wandering on Mars?, Science, 179, 997-1000.

(5) Cutts, J.A. (1973) Wind erosion in the Martian polar regions, J. Geophys. Res., 78, 4211-4221.

(6) Cutts, J.A., and W.L. Michalsky (1975) Mars: A new type of landscape feature in the south polar region, Final Report, contract 954189, Jet Propulsion Lab., Pasadena, CA.

(7) Murray, B.C., L.A. Soderblom, J.A. Cutts, R.P. Sharp, D.J. Milton, and R.B. Leighton (1972) A Geological framework for the south polar region of Mars, Icarus, 17, 328-345.

(8) Sharp, R.P. (1973) Mars: south polar pits and etched terrain, J. Geophys. Res, 78, 4222-4230.

(9) Cutts, J.A. (1973) Nature and origin of layered deposits in the Martian polar regions, J. Geophys. Res., 78, 4231-4249.

(10) Sagan, C., J. Veverka, P. Fox, R. Dubisch, R. French, P. Gierasch, L. Quam, J. Lederberg, E. Levinthal, R. Tucker, B. Eross, and J.B. Pollack (1973) Variable features on Mars 2, Mariner 9 global results, J. Geophys. Res., 78, 4163-4196.

(11) Soderblom, L.A., M.C. Malin, J.A. Cutts, and B.C. Murray (1973) Mariner 9 observations of the surface of Mars in the north polar region, J. Geophys. Res., 78, 4197-4210.

(12) Kieffer, H.H., T.Z. Martin, A.R. Peterfreund, B.M. Jakosky, E.D. Miner, and F.D. Palluconi (1977) Thermal and albedo mapping of Mars during Viking primary mission, J. Geophys. Res., 82, 4249-4291.

(13) Howard, A.D. (1978) Origin of the stepped topography of the Martian poles, Icarus, 34, 581-599.

(14) Cutts, J.A., K.R. Blasius, G.A. Briggs, M.H. Carr, R. Greeley, H. Masursky (1976) North polar region of Mars: imaging results from Viking 2, Science, 194, 1329-1337.

(15) Squyres, S.W. (1979) The geology of the Martian north polar region, Unpublished report, Cornell University.

(16) Sagan, C., D. Pieri, P. Fox, R.E. Arvidson, and E.A. Guinness (1977) Particle motion on Mars inferred from the Viking Lander cameras, J. Geophys. Res., 82, 4430-4438.

(17) Pollack, J.B., D. Colburn, R. Kahn, J. Hunter, W. Van Camp, C.E. Carlston, and M.R. Wolf, (1977) Properties of aerosols in the Martian atmosphere, as inferred from Viking Lander imaging data, J. Geophys. Res., 82, 4479-4496.

(18) Haberle, R.M., C.B. Leovy, J.B. Pollack (1979) A numerical model of the Martian polar cap winds, (in press).

(19) French, R.G., and P.J. Gierasch (1979) The Martian polar vortex: seasonal variation and observations of eolian features, J. Geophys. Res., 84, 4634-4642.

(20) Greeley, R. and R. Leach (1978) A preliminary assessment of the effects of electrostatics on aeolian processes, Reports of Planetary Geology Program 1977-1978, NASA TM 79729, 236-237.

(21) Carr, M.H. and G.G. Schaber (1977) Martian permafrost features, J. Geophys. Res., 82, 4039-4054.

(22) Neukum, G., and D.U. Wise (1976) Mars: A standard crater size-frequency distribution curve and a possible new time scale, Science, 194, 1381.

(23) Masursky, H., J.M. Boyce, A.L. Dial, G.G. Schaber, and M.E. Strobell (1977) Classification and time of formation of Martian channels based on Viking Data, J. Geophys. Res., 82, 4016-4038.

(24) Chapman, C.R., and K.L. Jones (1977) Cratering and obliteration history of Mars, Ann. Rev. Earth Planet. Sci., 5, 515-540.

(25) Opik, E.J. (1975) Mariner IV and craters on Mars, Irish Astron. Jour., 7, 92-104.

(26) Cintala, M.J., and P.J. Mouginis-Mark (1979) New depth/diameter data for fresh Martian craters and some interplanetary comparisons (Abstract), Report of Planetary Geology Program, 1978-1979, NASA TM 80339, 182-184.

(27) Glennie, K.W. (1970) Desert Sedimentary Environments; Developments in Sedimentology 14, Elsevier Publishing Co., New York, Chap. 6.

(28) Squyres, S.W. (1979) The evolution of dust deposits in the Martian north polar region, Icarus, 40, (in press).

(29) Wolfe, R.W. (1979) Orientation of eolian features in the north polar region of Mars: A preliminary assessment (Abstract), Lunar and Planetary Science X, 1364-1366.

(30) Leach, J.H.J. (1979) Dune forms and patterns of wind circulation in the north polar region of Mars (abstract), Second International Colloquium on Mars, NASA CP 2072, 52.

(31) Tsoar, H., R. Greeley, and A.R. Peterfreund (1979) Wind patterns and cyclone formation in the north polar region of Mars: analysis from sand dune morphologies (abstract), Reports to the Planetary Geology Program (1978-1979); NASA TM 80339, 316-318.

(32) French, R.G., P.J. Gierasch, B. Popp, R. Yerdon (1979) Cloud forms on Mars (abstract), Bulletin of the American Astronomical Society, Vol. 11, No. 3, 572.

(33) Snyder, C.W. (1977) The missions of the Viking Orbiters, J. Geophys. Res., 82, 3971-3983.

(34) James, P.B., G. Briggs, J. Barnes, and A. Spruck (1979) Seasonal recession of Mars' south polar cap as seen by Viking, J. Geophys. Res., 84, 2889-2922.

(35) Blasius, K.R., J.A. Cutts, and W.J. Roberts (1978) Large scale erosive flows associated with Chryse Planitia, Mars: source and sink relationships, Reports of Planetary Geology Program, 1977-1978, NASA TM 79729, 275-276.

(36) Tsoar, H., R. Greeley, R. Papson, and S. Squyres (1977) Sand dunes of the north polar region of Mars (Abstract), Lunar and Planetary Science X, 1242-1244.

APPENDIX A

List of Viking Orbiter Imagery Used in Research

Viking Mosaic	Frames From Mosaic
211-5269	59B61-80 ; 60B21-40 ; 61B21-42
211-5270	56B71-90 ; 57B21-40 ; 58B26-42
211-5272	59B31-44 ; 60B01-14 ; 61B01-15 ; 62B22-33
211-5273	56B51-69 ; 57B01-18 ; 58B01-17
211-5283	COMPOSITE
211-5337	77B81-94
211-5359 A,B,C,D,E,F,G,H,	COMPOSITES
211-5429	56B91-95 ; 57B41-45 ; 58B43-45 ; 59B81-83
	60B41-45 ; 61B42-44 ; 62B62-64 ; 63B43-45
	65B73-75
211-5431	62B41-62 ; 63B21-42 ; 65B51-72
211-5453	52B61-80 ; 84B01-21 ; 84B31-43 ; 84B51-55
211-5559	77B21-44 ; 77B51-70 ; 80B11-28 ; 80B31-38
211-5560	76B11-31 ; 76B41-53 ; 76B61-65
211-5562	70B01-17 ; 70B23-35 ; 70B41-45
211-5563	73B11-28 ; 73B41-60 ; 75B51-54
211-5569	50B21-38 ; 69B01-18
211-5572	77B81-94
211-5573	71B11-26 ; 71B41-53 ; 71B61-65
211-5574	82B22-28 ; 82B31-38 ; 83B11-26 ; 83B31-44
	83B51-62
211-5575	81B51-74 ; 81B77-96 ; 82B12,14,16,18
211-5576	79B43-63 ; 79B65-76 ; 79B79-83
211-5580	64B01-08 ; 66B01-14 ; 67B01-12
211-5583	72B01-16 ; 72B31-42 ; 72B51-54
211-5584	74B31-44 ; 74B51-57
211-5585	78B11-30 ; 78B41-52 ; 78B61-65
211-5641	488B21-34 ; 487B05-14
211-5718	518B37-52
211-5719	120B21-38 ; 120B41-58 ; 120B61-76
	120B81-94
211-5720	122B01-23 ; 122B31-41 ; 122B51-75
	122B81-91
211-5733	561B74-84
211-5744	525B01-16 ; 541B21-34 ; 544B01-16
211-5746	538B01-16 ; 541B01-14 ; 551B83-98
211-5752	499B41-60 ; 514B41-70
211-5753	518B44-81 ; 560B53-66 ; 560B67-80
	560B82-97
211-5758	538B01-16
211-5765	536B21-36 ; 536B41-56 ; 560B41-60
	560B61-80

211-5776	532B21-36 ; 541B21-36 ; 579B75-94
211-5805	570B01-20 ; 574B01-20 ; 576B01-20
211-5806	579B55-74 ; 580B01-20 ; 582B01-20
211-5808	560B81-98 ; 566B61-80 ; 577B71-90
211-5810	669B01-24 ; 672B25-48 ; 672B51-72
211-5812	710A71-94 ; 714A01-22 ; 717A21-40
211-5814	672B01-24 ; 672B25-48 ; 672B51-72
211-5846	501B01-20
211-5854	676B01-24 ; 676B25-48 ; 676B49-72
211-5857	705B01-20 ; 726A41-57 ; 771A21-30
211-5869	560B41-60
211-5875	801A21-26 ; 801A41-46 ; 804B01-06
	806B21-26
211-5885	753A11-54 ; 756A21-36

Individual Viking Frames Reproduced

070B31-35
505B01-16 ; 505B17-40
514B01-20
516B88-94
518B27-36
523B21-34 ; 523B41-56
524B01-16 ; 524B21-36
525B01-16
531B21-36
532B21-36
538B21-16
541B01-14
544B01-16
551B83-98
560B72-80
576B01-20 ; 576B41-60
580B16-20 ; 580B21-34
669B01-24

APPENDIX B

Computer Programs for Crater Size-Frequency Distributions

```
C     ********************************************************************
C
C     SUBROUTINE CRMOD1.FTN   (CRATER DISTRIBUTION MODULE #1)
C
C     ********************************************************************
C
C
C
C     >>>>>>> CUMULATIVE SIZE-FREQUENCY DISTRIBUTION PLOT <<<<<<<
C
C
C                     MIKE BOTTS      2/11/79
C
C
C     COMPLETE SUBROUTINE FOR CALCULATING AND PLOTTING CUMULATIVE
C        SIZE-FREQUENCY DISTRIBUTION DATA (ALONG WITH ERROR BARS).
C
C     OUTPUT INCLUDES TABLE OF VALUES NEEDED FOR PLOTTING CUMULATIVE
C        SIZE-FREQ. DISTRIBUTION, AND GRAPH OF VALUES AND ERROR LIMITS.
C
C     INPUT:  D = ARRAY OF UNBINNED CRATER DIAMETERS ARRANGED IN
C                     DESCENDING ORDER
C             N = NUMBER OF CRATERS
C             NDIM = ROW DIMENSION GIVEN 'CUMPLT' IN MAIN PROGRAM
C                     (DIMENSION GIVEN 'BARCUM' SHOULD BE 2*NDIM)
C             A = TOTAL AREA (KM**2) OF CRATER COUNTS
C             XAXIS1 = LOWER BOUND OF X-AXIS
C             XAXIS2 = UPPER BOUND OF X-AXIS
C             YAXIS1 = LOWER BOUND OF Y-AXIS
C             YAXIS2 = UPPER BOUND OF Y-AXIS
C
C     NOTES: IF LIMITS OF GRAPH ARE NOT KNOWN, SET XAXIS1 AND XAXIS2
C              EQUAL TO 0.0 .PROGRAM PLOT.FTN WILL THEN COMPUTE
C              ITS OWN INCREMENTS.
C            X INCREMENT = (XAXIS2 - XAXIS1)/100.
C            Y INCREMENT = (YAXIS2 - YAXIS1)/50 .
C             (PROGRAM WILL ASK IF YOU DESIRE A REPLOT).
C
C     RETURNS :
C             DIA = DIAMETERS OF CRATERS
C             CUM = CUMULATIVE NUMBER OF CRATERS LARGER OR EQUAL TO
C                     DIAMETER AT THAT POINT
C             DIALOG = LOG (D)
C             CUMLOG = LOG (CUM)
C             ERRLOG = LOG (1ST SET OF ERROR LIMITS)
C             AIRLOG = LOG (2ND SET OF ERROR LIMITS)
C             CUMPLT = 2-COLUMN ARRAY OF MEASURED DATA WHERE:
C                     CUMPLT(I,1) = DIALOG(I)
C                     CUMPLT(I,2) = CUMLOG(I)
C             BARCUM = 2-COLUMN ARRAY OF ERROR BAR DATA WHERE:
C                     BARCUM(I,1) = DIALOG(I)
C                     BARCUM(I,2) = ERRLOG(I)
C                     BARCUM(I+1,1) = DIALOG(I)
C                     BARCUM(I+1,2) = AIRLOG(I)
C             J = DIMENSION VARIABLE OF DIALOG,CUMLOG,ERRLOG,AIRLOG
C
C     SUBROUTINES NEEDED:
C             CUMFRQ.FTN      (CALCULATES VALUES NEEDED FOR PLOT)
C             SQUEEZ.FTN      (PREPARES MEASURED DATA FOR PLOTTING PROGRAMS)
C             SQUISH.FTN      (PREPARES ERROR BAR DATA FOR PLOTTING PROGRAMS
C             PLOT.FTN        (PLOTS DATA + ERROR BARS)
C
C     SISTER PROGRAMS:
C             CRMOD2.FTN      (DIFFERENTIAL SIZE-FREQUENCY PLOT)
C             CRMOD3.FTN      (BINNED RELATIVE SIZE-FREQUENCY PLOT)
```

```
C       ------------------------------------------------------------------
        SUBROUTINE CRMOD1(D,N,NDIM,A,XAXIS1,XAXIS2,YAXIS1,YAXIS2,DIA,CUM,
       1DIALOG,CUMLOG,ERRLOG,AIRLOG,CUMPLT,BARCUM,J)
        DIMENSION D(N),DIA(N),DIALOG(N),CUM(N),CUMLOG(N),ERRLOG(N),AIRLOG(N),
       1CUMPLT(NDIM,2),BARCUM(2*NDIM,2)
C       .....................................................................
C       CALL ROUTINE FOR CALCULATING CUMS
C
        CALL CUMFRQ(D,N,A,DIA,DIALOG,CUM,CUMLOG,ERRLOG,AIRLOG,J)
C       .....................................................................
C       LIST VALUES NEEDED FOR PLOT: D,CUM,DIALOG,CUMLOG,ERRLOG,AIRLOG
C
        WRITE (5,100)
        WRITE (5,120)
        WRITE (5,140)
        WRITE (5,150)
100     FORMAT ('1',72('*'))
120     FORMAT ('0',5X,'CUMULATIVE SIZE-FREQUENCY DISTRIBUTION')
140     FORMAT ('0',72('*'))
150     FORMAT ('0  DIAMETER',5X,'CUM. NO./AREA',5X,'LOG(DIAMETER)'
       1,5X,'LOG(CUM. NO./AREA)',5X,'LOG(ERROR LIMITS)')
        DO 200 K=1,J
        WRITE (5,180) DIA(K),CUM(K),DIALOG(K),CUMLOG(K),ERRLOG(K),AIRLOG(K)
180     FORMAT (' ',F10.3,8X,G10.3,4X,'!',4X,F10.3,13X,F10.3,3X,2F10.3)
        IF (AIRLOG(K).EQ.-9999.999) AIRLOG(K) = CUMLOG(K)
200     CONTINUE
C       .....................................................................
C       PREPARE DATA FOR PLOT
C
        CALL SQUEEZ(DIALOG,CUMLOG,J,NDIM,CUMPLT)
        CALL SQUISH(DIALOG,ERRLOG,AIRLOG,J,2*NDIM,BARCUM,JJ)
C       .....................................................................
C       PLOT DATA AND ERROR LIMITS
C
        WRITE (5,300)
        WRITE (5,320)
        WRITE (5,330)
300     FORMAT ('0X = LOG( DIAMETER (KM) )')
320     FORMAT (' Y = LOG( CUMULATIVE NUMBER OF CRATERS PER KM**2 )')
330     FORMAT (' PHI = ( CUM. NO. +- SQRT( CUM. NO. ) ) / AREA')
        CALL PLOT(CUMPLT,J,NDIM,BARCUM,JJ,2*NDIM,XAXIS1,XAXIS2,YAXIS1,YAXIS2)
C       .....................................................................
C       ASK FOR REPLOT OF GRAPH
C
490     WRITE (5,500)
500     FORMAT ('$WOULD YOU LIKE TO REPLOT THIS GRAPH?(0=NO,1=YES):')
        READ (5,505) NSER
505     FORMAT (I1)
        IF (NSER.EQ.0) GO TO 600
        WRITE (5,520)
520     FORMAT ('$LIST XMIN,XMAX,YMIN,YMAX: ')
        READ (5,525) XAXIS1,XAXIS2,YAXIS1,YAXIS2
525     FORMAT (4F10.5)
        CALL PLOT(CUMPLT,J,NDIM,BARCUM,JJ,2*NDIM,XAXIS1,XAXIS2,YAXIS1,YAXIS2)
        GO TO 490
600     RETURN
        END
```

```
C     ********************************************************************
C
C     SUBROUTINE CUMFRQ.FTN   (CALCULATES CUM-SIZE FREQUENCY VALUES)
C
C     ********************************************************************
C
C     MIKE BOTTS      1/31/79
C
C     CALCULATES VALUES NEEDED TO PLOT CUMULATIVE SIZE-FREQUENCY
C        DISTRIBUTIONS ACCORDING TO STANDARDS SUGGESTED BY
C        "STANDARD TECHNIQUES FOR PRESENTATION AND ANALYSIS OF
C        CRATER SIZE-FREQUENCY DATA" (NASA TM-79730).
C
C     INPUT:
C             D(N) = ARRAY OF MEASURED DIAMETERS (KM) OF N CRATERS
C             A = AREA (KM**2) OF TOTAL PICTURES COUNTED
C
C     OUTPUT:
C             DIA(J) = ARRAY OF DIAMETERS HAVING DIFFERENT VALUES
C             DIALOG(J) = LOG( DIA(J) )
C             CUM(J) = CUMULATIVE NO. OF CRATERS LARGER OR EQUAL TO
C                      DIA(J)
C             ERRLOG(J) AND AIRLOG(J) = LOG ( PHI(J) )
C                      PHI(J) = [CUM(J) +- SQRT( CUM(J) )] / A
C             J = TOTAL NO. OF CRATERS WITH DIFFERENT DIAMETERS
C
C     NOTE: ARRAY D MUST LIST DIAMETERS IN DECENDING ORDER FROM
C        D(1) TO D(N). USE SUBROUTINE SORTC.
C
C     NEGATIVE INFINITY MARKER = -9999.999 .
C
C     ------------------------------------------------------------------
      SUBROUTINE CUMFRQ(D,N,A,DIA,DIALOG,CUM,CUMLOG,ERRLOG,AIRLOG,J)
      DIMENSION D(N),DIA(N),DIALOG(N),CUM(N),CUMLOG(N),ERRLOG(N),AIRLOG(N)
      M=0
      DO 100 I=1,N
      IF (I.EQ.N) GO TO 60
      IF (D(I).EQ.D(I+1)) GO TO 100
60    M=M+1
C
C     CALCULATE VALUES FOR EACH DIFFERENT DIAMETER
      DIA(M) = D(I)
      DIALOG(M) = ALOG10(D(I))
      C = 1.0 * FLOAT(I)
      CUM(M) = C/A
      CUMLOG(M) = ALOG10(CUM(M))
      ERRLOG(M) = ALOG10((C + SQRT(C))/A)
      IF (I.GT.1) GO TO 90
      AIRLOG(M) = -9999.999
      GO TO 100
90    AIRLOG(M) = ALOG10((C- SQRT(C))/A)
100   CONTINUE
      J=M
      RETURN
      END
```

```
C     ***********************************************************************
C
C     SUBROUTINE SORTC.FTN    (SORTS COLUMNS OF AN ARRAY)
C
C     ***********************************************************************
C
C     MIKE BOTTS      1/31/79
C
C     SORTS ELEMENTS OF EACH COLUMN OF ARRAY A(N,M) INTO DESCENDING ORDER
C        FROM TOP TO BOTTOM AND RETURNS AS APRIME(N,M)
C
C     N = ACTUAL NUMBER OF ROWS IN ARRAY A
C     M = ACTUAL NUMBER OF COLUMNS IN ARRAY A
C     NDIM = ROW DIMENSION GIVEN ARRAY A IN MAIN PROGRAM
C
C     ---------------------------------------------------------------------
      SUBROUTINE SORTC(A,N,NDIM,M,APRIME)
      DIMENSION A(NDIM,M),APRIME(NDIM,M)
      DO 20 I=1,N
      DO 20 J=1,M
      APRIME(I,J) = A(I,J)
20    CONTINUE
      L=N-1
      DO 100 K=1,L
      DO 100 J=1,M
      DO 100 I=1,N
      IF(I.EQ.N) GO TO 100
      IF(APRIME(I,J).LE.APRIME(I+1,J)) GO TO 50
      GO TO 100
50    TEMP = APRIME(I,J)
      APRIME(I,J) = APRIME(I+1,J)
      APRIME(I+1,J) = TEMP
100   CONTINUE
      RETURN
      END


C     ***********************************************************************
C
C     SUBROUTINE SQUEEZ.FTN     (SQUEEZES 2 ARRAYS INTO 1 ARRAY)
C
C     ***********************************************************************
C
C     MIKE BOTTS      2/1/79
C
C     TURNS 2 ONE-COLUMN ARRAYS INTO 1 TWO-COLUMN ARRAY.
C          XY(I,1) = X(I)
C          XY(I,2) = Y(I)
C
C     I = ACTUAL NUMBER OF X AND Y VALUES
C     NDIM = ROW DIMENSION GIVEN XY IN MAIN PROGRAM
C
C     GOOD FOR PREPARING DATA FOR SUBROUTINE PLOTER.FTN.
C
C     ---------------------------------------------------------
      SUBROUTINE SQUEEZ(X,Y,I,NDIM,XY)
      DIMENSION X(I), Y(I), XY(NDIM,2)
      DO 100 J=1,I
      XY(J,1) = X(J)
      XY(J,2) = Y(J)
100   CONTINUE
      RETURN
      END
```

```
C     ***********************************************************************
C
C     SUBROUTINE SQUISH.FTN   (SQUISHES 2 UNEQUAL ARRAYS INTO 1 ARRAY)
C
C     ***********************************************************************
C
C     MIKE BOTTS      2/2/79
C
C     SPECIAL ROUTINE NEEDED TO PUT ERROR BAR DATA INTO A 2-COLUMN
C        REQUIRED BY SUBROUTINE PLOTER.FTN.
C
C     VALUE(J) = VALUE PLOTTED ON X AXIS (SAME AS X VALUE FOR REAL
C                   DATA POINTS).
C     ERR1(J) = ONE SET OF ERROR BAR LIMITS
C     ERR2(J) = OTHER SET OF ERROR BAR LIMITS
C     J = ACTUAL NUMBER OF 'VALUE' POINTS
C     NDIM = ROW DIMENSION GIVEN 'BAR' IN MAIN PROGRAM
C
C     RETURNS BAR(JJ,2) WHERE JJ = J*2 AND:
C             BAR(1,1) = VALUE(1),          BAR(1,2) = ERR1(1)
C             BAR(2,1) = VALUE(1)           BAR(2,2) = ERR2(1)
C             BAR(3,1) = VALUE(2)           BAR(3,2) = ERR1(2)
C             BAR(4,1) = VALUE(2)           BAR(4,2) = ERR2(2)
C                      .                             .
C                      .                             .
C                      .                             .
C             BAR(JJ,1) = VALUE(J)          BAR(JJ,2) = ERR2(J) .
C
C
C     USED BY MAIN PROGRAM CRPLOT.FTN (CRATER PLOT) WHICH PRODUCES
C        CRATER SIZE-FREQUENCY PLOTS WITH ERROR BARS.
C
C     ---------------------------------------------------------------
      SUBROUTINE SQUISH(VALUE,ERR1,ERR2,J,NDIM,BAR,JJ)
      DIMENSION VALUE(J),ERR1(J),ERR2(J),BAR(NDIM,2)
      JJ = J*2
      N=0
      DO 100 I=1,J
      N=N+1
      BAR(N,1) = VALUE(I)
      BAR(N,2) = ERR1(I)
      N=N+1
      BAR(N,1) = VALUE(I)
      BAR(N,2) = ERR2(I)
100   CONTINUE
      RETURN
      END
```

```
C       ********************************************************************
C
C       SUBROUTINE PLOT.FTN     (PLOTS 2 SETS OF DATA ON ONE GRAPH)
C
C       ********************************************************************
C
C       MIKE BOTTS      2/16/79
C
C       MODIFIED VERSION OF DAVIS' PLOTER.FTN #: GRAPH BOUNDARIES CAN NOW
C          BE GIVEN BY USER OR CALCULATED BY PROGRAM. IF CALCULATED BY
C          PROGRAM, ROUTINE NOT GUARANTEED TO GIVE "CLEAN" INTERVALS.
C       # (DAVIS, J.C. (1973),"STATISTICS & DATA ANALYSIS IN GEOLOGY",PG  211
C
C       PLOTS TWO VARIABLES ON ONE GRAPH. IF THE TWO VARIABLES CONSIST OF
C           DATA + ERROR LIMITS, IT IS SUGGESTED THAT THE DATA ARRAY = Q1,
C            AND THE ERROR ARRAY = Q2.
C
C       INPUT:
C               Q1 = FIRST SET OF VARIABLES TO BE PLOTTED, WHERE
C                       Q1(I,1) = VALUE PLOTTED IN X DIRECTION
C                       Q1(I,2) = VALUE PLOTTED IN Y DIRECTION
C               Q2 = SECOND SET OF VARIABLES TO BE PLOTTED
C               N1 = ACTUAL NUMBER OF ROWS OF Q1
C               N2 = ACTUAL NUMBER OF ROWS OF Q2 (SET = 0 IF ONLY ONE DATA
C                       SET IS TO BE PLOTTED)
C               N3 = ROW DIMENSION GIVEN Q1 IN MAIN PROGRAM
C               N4 = ROW DIMENSION GIVEN Q2 IN MAIN PROGRAM
C               XAXIS1 = LOWER BOUND OF X AXIS
C               XAXIS2 = UPPER BOUND OF X AXIS
C               YAXIS1 = LOWER BOUND OF Y AXIS
C               YAXIS2 = UPPER BOUND OF Y AXIS
C
C       NOTES:  IF YOU WISH BOUNDARIES CALCULATED FOR YOU , SET XAXIS1 AND
C                       XAXIS2 EQUAL TO 0.0 .
C               IF YOU WISH TO GIVE YOUR OWN BOUNDARIES, NOTE THAT :
C                       X INCREMENT = (XAXIS2 - XAXIS1)/100
C                       Y INCREMENT = (YAXIS2 - YAXIS1)/50 .
C
C       OUTPUT:
C               * = 1ST DATA SET
C               _ = 2ND DATA SET
C               O = OVERLAPPING POINT OF 1ST & 2ND SETS
C
C       ---------------------------------------------------------------------
        SUBROUTINE PLOT(Q1,N1,N3,Q2,N2,N4,XAXIS1,XAXIS2,YAXIS1,YAXIS2)
        DIMENSION Q1(N3,2),Q2(N4,2),IOUT(101),XX(11)
        DATA IBLNK/' '/,II/'I'/,IPLUS/'+'/,IBAR/'_'/,IMINUS/'-'/,ISTAR/'*'/
        DATA IO/'O'/
C
C       IF XAXIS1 AND XAXIS2 = 0.0 CALCULATE BOUNDARIES AND INCREMENTS
C
        NX1 = INT(XAXIS1).
        NX2 = INT(XAXIS2)
        IF (NX1.NE.0.OR.NX2.NE.0) GO TO 100
C       ...............................................................
C       IF BOUNDARIES NOT GIVEN, DETERMINE MAX & MIN
C
C       FIND MAXS AND MINS OF DATA SET Q1
C
        XAXIS1 = Q1(1,1)
        XAXIS2 = XAXIS1
        YAXIS1 = Q1(1,2)
        YAXIS2 = YAXIS1
        DO 50 J=1,N1
        IF (Q1(J,1).LT.XAXIS1) XAXIS1=Q1(J,1)
```

```
      IF (Q1(J,1).GT.XAXIS2) XAXIS2=Q1(J,1)
      IF (Q1(J,2).LT.YAXIS1) YAXIS1=Q1(J,2)
      IF (Q1(J,2).GT.YAXIS2) YAXIS2=Q1(J,2)
50    CONTINUE
      IF (N2.EQ.0) GO TO 100
C
C     FIND MAXS AND MINS OF DATA SET Q2
C
      DO 70 J=1,N2
      IF (Q2(J,1).LT.XAXIS1) XAXIS1=Q2(J,1)
      IF (Q2(J,1).GT.XAXIS2) XAXIS2=Q2(J,1)
      IF (Q2(J,2).LT.YAXIS1) YAXIS1=Q2(J,2)
      IF (Q2(J,2).GT.YAXIS2) YAXIS2=Q2(J,2)
70    CONTINUE
C     ..................................................................
C     CALCULATE INCREMENTS
C
100   DX = (XAXIS2 - XAXIS1)/100.
      DY = (YAXIS2 - YAXIS1)/50.
C     ..................................................................
C     GET GRAPH LINES AND DIVISIONS SET UP
C
      WRITE (5,103)
103   FORMAT ('0Y-AXIS',//)
      Y = YAXIS2
      DO 500 I=1,51
      IF (MOD(I-1,5).EQ.0) GO TO 120
      DO 110 J=1,101
      IOUT(J) = IBLNK
      IF (MOD(J-1,10).EQ.0) IOUT(J)=II
110   CONTINUE
      GO TO 140
120   DO 130 J=1,101
      IOUT(J) = IMINUS
      IF (MOD(J-1,10).EQ.0) IOUT(J) = IPLUS
130   CONTINUE
C     ..................................................................
C     PREPARE DATA SET Q1 FOR PLOTTING
C
140   DO 150 J=1,N1
      IY = NINT( (Q1(J,2) - YAXIS1)/ DY ) + 1
      IF ((52-I).NE.IY) GO TO 150
      IX = NINT( (Q1(J,1) - XAXIS1)/ DX ) + 1
      IOUT(IX) = ISTAR
150   CONTINUE
C     ..................................................................
C     PREPARE DATA SET Q2 FOR PLOTTING
C
      IF (N2.LE.0) GO TO 200
      DO 160 J=1,N2
      IY = NINT( (Q2(J,2) - YAXIS1)/ DY ) + 1
      IF ((52-I).NE.IY) GO TO 160
      IX = NINT( (Q2(J,1) - XAXIS1)/ DX ) + 1
      IF (IX.GT.100) IX = 100
      IF (IOUT(IX).EQ.IO) GO TO 160
      IF (IOUT(IX).EQ.ISTAR) GO TO 155
      IOUT(IX) = IBAR
      GO TO 160
155   IOUT(IX) = IO
160   CONTINUE
C     ..................................................................
C     PLOT ONE LINE OF PLOT
C
200   IF (MOD(I-1,5).NE.0) GO TO 300
      WRITE (5,250) Y,IOUT
250   FORMAT (1X,F10.5,1X,101A1)
```

```
      Y = Y-5.0*DY
      GO TO 500
300   WRITE (5,350) IOUT
350   FORMAT (12X,101A1)
500   CONTINUE
C     ..................................................................
C     PRINT BOTTOM LEGEND
C
      XXX = XAXIS1
      DO 600 I=1,11
      XX(I) = XXX
      XXX = XXX + 10.0*DX
600   CONTINUE
      WRITE (5,700) (XX(I),I=1,11,2)
700   FORMAT (8X,6(F10.5,10X))
      WRITE (5,800) (XX(I),I=2,10,2)
800   FORMAT (18X,5(F10.5,10X))
      WRITE (5,900)
900   FORMAT (50X,'X-AXIS')
      RETURN
      END
```

APPENDIX C

Crater Size-Frequency Data

Bulbous Ground : 72°N, 290°W

frames used : 538B03,538B05,538B08,538B09,538B12

total area : 5419.107 km^2

number of craters : 156

diameter (km)	cumulative no./area (km^{-2})
19.968	.133 X 10^{-3}
5.233	.266
2.319	.399
2.093	.532
2.092	.665
2.000	.798
1.943	.931
1.542	.106 X 10^{-2}
1.495	.133
1.469	.146
1.395	.160
1.345	.186
1.306	.200
1.248	.213
1.196	.240
1.175	.266
1.160	.279
1.121	.319
1.101	.333
1.077	.373
1.046	.399
1.015	.439
1.000	.452
.998	.466
.972	.546
.955	.599
.897	.652
.881	.719
.870	.732
.858	.745
.822	.785
.797	.798
.780	.812
.768	.825
.748	.905
.734	.971
.725	.102 X 10^{-1}
.702	.106
.692	.108
.691	.113
.673	.114

(continued)

diameter (km)	cumulative no./area (km^{-2})
.661	.121 X 10^{-1}
.652	.124
.624	.125
.615	.130
.614	.132
.609	.133
.598	.142
.587	.150
.580	.157
.538	.162
.523	.164
.514	.166
.507	.169
.468	.170
.462	.172
.461	.176
.449	.188
.441	.196
.435	.200
.390	.204
.385	.206
.384	.209
.374	.213
.367	.214
.362	.216
.312	.228
.308	.229
.307	.237
.299	.244
.294	.250
.290	.253
.234	.262
.231	.267
.230	.273
.224	.279
.220	.283
.217	.285
.159	.286
.156	.294
.154	.315
.149	.329
.147	.334
.145	.337
.077	.341
.075	.343
.072	.345

Bulbous Ground : 72°N, 59°W

frames used : 525B01 - 525B06

total area : 5400.687 km^2

number of craters : 97

diameter (km)	cumulative no./area (km^{-2})
3.166	.185 X 10^{-3}
2.174	.555
1.871	.741
1.594	.130 X 10^{-2}
1.295	.148
1.160	.185
1.151	.222
1.015	.259
1.007	.296
.870	.352
.725	.444
.720	.537
.580	.574
.576	.778
.435	.107 X 10^{-1}
.432	.122
.290	.137
.288	.156
.145	.167
.144	.180

Moderately-mantled Ground : 76°N, 90°W

frames used : 70B04, 71B61 - 71B64

total area : 24,344.584 km^2

number of craters : 71

diameter (km)	cumulative no./area (km^{-2})
12.878	.411 X 10^{-4}
10.231	.822
9.625	.123 X 10^{-3}
6.648	.164
6.576	.205
6.241	.246
5.540	.288
4.818	.329
3.942	.370
3.042	.411
2.847	.452
2.750	.493
2.466	.534
2.200	.575
2.063	.616
1.787	.657
1.650	.698
1.314	.822
1.095	.904
.962	.986
.876	.107 X 10^{-2}
.831	.111
.830	.115
.825	.119
.766	.127
.687	.131
.657	.152
.550	.156
.548	.168
.438	.177
.416	.181
.411	.185
.329	.189
.277	.205
.275	.209
.274	.230
.219	.271
.138	.275
.137	.283
.110	.292

Heavily-mantled Ground : 80°N, 65°W

frames used : 70B06 - 70B10, 70B27 - 70B34

total area : 55,120.613 km^2

number of craters : 9

diameter (km)	cumulative no./area (km^{-2})
8.157	.181 X 10^{-4}
4.456	.363
2.232	.544
2.108	.726
.830	.109 X 10^{-3}
.827	.127
.689	.145
.551	.163
.253	.181

1. Report No. NASA TM-81979	2. Government Accession No.	3. Recipient's Catalog No.
4. Title and Subtitle Advances in Planetary Geology		5. Report Date June 1980 6. Performing Organization Code SL-4
7. Author(s) Alex Woronow, Editor		8. Performing Organization Report No. 10. Work Unit No.
9. Performing Organization Name and Address Office of Space Science Planetary Division Planetary Geology Program		11. Contract or Grant No. 13. Type of Report and Period Covered Technical Memorandum
12. Sponsoring Agency Name and Address National Aeronautics and Space Administration Washington, DC 20546		14. Sponsoring Agency Code

15. Supplementary Notes

16. Abstract

Advances in Planetary Geology is a new series intended to serve the planetary geology community with a form for quick and thorough communications. There are no set lists of acceptable topics or formats, and submitted manuscripts will not undergo a formal review. All submissions should be in a camera-ready form, preferably single spaced, and submitted to the Editor.

17. Key Words (Suggested by Author(s))	18. Distribution Statement
Planetary Geology Planetology	Unclassified-Unlimited

19. Security Classif. (of this report)	20. Security Classif. (of this page)	21. No. of Pages	22. Price*
Unclassified	Unclassified	332	$12.00

For sale by the National Technical Information Service, Springfield, Virginia 22161

NASA-Langley, 1980

National Aeronautics and
Space Administration

Washington, D.C.
20546

Official Business
Penalty for Private Use, $300

SPECIAL FOURTH CLASS MAIL
BOOK

Postage and Fees Paid
National Aeronautics and
Space Administration
NASA-451

NASA

POSTMASTER: If Undeliverable (Section 158
Postal Manual) Do Not Return